Microwave Metamaterials for Compact Filters and Antennas

vorgelegt von
M.Sc
Merih Palandöken
aus Kahramanmaras

Von der Fakultät IV-Elektrotechnik und Informatik
der Technischen Universität Berlin
zur Erlangung des akademischen Grades

Doktor der Ingenieurwissenschaften
Dr.-Ing

genehmigte Dissertation

Promotionsausschuss:

Vorsitzender: Prof. Dr.-Ing. Klaus Petermann
Berichter: Prof. Dr.-Ing. Heino Henke
Berichter: Prof. Dr. Sergey I. Bozhevolnyi

Tag der wissenschaftliche Aussprache: 06. September 2012

Berlin 2012
D83

Acknowledgements

It is my pleasure to express my deepest gratitude and respect to Prof. Dr.-Ing Heino Henke for his invaluable guidance, helpful suggestions, endless support and patience. His personal and academic virtue shaped my academic personality and changed my approach to scientific study. I am very lucky to have the opportunity to study under his supervision. I would like to thank to the members of my thesis committee, Prof. Dr. Sergey I. Bozhevolnyi and Prof. Dr.-Ing. Klaus Petermann for reading the manuscript and commenting on the thesis.

I am very fortunate to have been a member of TET family, where I had a chance to work together and benefit from intelligent and excited people. I am very thankful to Dr.-Ing Manfred Filtz for motivating scientific discussions about the electromagnetic field theory, continuous support, patience and nice chance to be an evidence for his brilliant thinking approaches. Special and deep thanks to Dr. –Ing Heinrich Büssing for his incredible help, understanding and irreplaceable friend- and brothership during my research life. I would like to thank all members of TET family for their help in my doctorate period. I thank also very much to Dr.-Ing Tolga Tekin in the Department of Nano Interconnect Technology due to his help during and after my doctorate research.

I am also very thankful to Prof. Dr. Siddik Yarman, the Department Chair of Electrical and Electronics Engineering at Istanbul University for his continuous motivating advices and support during my doctorate research.

I would like to express my endless thanks to my mother and father for their love, encouragement and care.

Zusammenfassung

Werkstoffe mit gleichzeitig negativer Permittivität und Permeabilität in einem bestimmten Frequenzband wurden zuerst von Veselago im Jahr 1968 theoretisch untersucht. Er bezeichnet solche Medien als linkshändige Materie (LHM), weil die Vektoren des elektrischen Feldes, des Magnetfeldes und der Wellenausbreitungsrichtung ein linkshändiges System aufspannen. Weil solche Materialien in der Natur nicht vorkommen, konnten die vorhergesagten optischen und elektromagnetischen Konsequenzen aus Veselago‘s Arbeit erst ca. 30 Jahre nach deren Veröffentlichung beobachtet werden. Im Jahr 2000 wurde an einem künstlich zusammengesetzten Material, das auch als ein Metamaterial bekannt ist, und aus periodisch angeordneten negativen Permittivitäts- und Permeabilitätszellen in der Form von metallischen Drähten und Spaltringen aufgebaut ist, linkshändige Eigenschaft gezeigt. Weil die Abmessung der Drähte und Ringe klein im Vergleich zu der Wellenlänge sind, ist es möglich, die elektromagnetischen Eigenschaften dieser Strukturen durch eine effektive Permittivität und Permeabilität zu approximieren. In dieser Arbeit werden die grundlegenden Eigenschaften negativer Permeabilität, Permittivität und linkshändiger Materialien beim Entwurf von Antennen und Filtern als potenzielle Anwendungen in der Mikrowellentechnik erforscht.

Bei der Untersuchung grundlegender Eigenschaften und alternativer Design-Methoden von Metamaterialien, widmet sich diese Arbeit zunächst den künstlichen magnetischen Materialien. Diese künstlichen magnetischen Materialien liegen in Form von metallischen Zylindern mit oder ohne Spalten oder Spaltringresonatoren vor. Approximierte Formulierungen für die effektive Permeabilität werden abgeleitet. Die Berechnungen der Transmissions- und Reflexionsparameter von konzentrischen Zylindern mit Spalten werden auf analytischem Wege und auch numerisch durchgeführt. Die gute Übereinstimmung zwischen analytischen und numerischen Berechnungen wird bestätigt. Die Resonanzfrequenz der Spaltringresonatoren ist zusätzlich nach einem quasistationären Ansatz berechnet worden. Es wird gezeigt, dass die Ergebnisse der numerischen Berechnungen besser mit den Ergebnissen aus dem quasistationären Ansatz übereinstimmen. Das 1D-Dispersionsdiagramm der Spaltringresonatoren wird numerisch untersucht. Effektive Materialparameter werden extrahiert, um die Frequenzabhängigkeit der effektiven Permeabilität nach dem Lorentz-Modell zu bestätigen. Zur Untersuchung eines homogeneren Materialdesigns, wird ein fraktaler Spiralresonator als Einheitszelle mit negativer Permeabilität zum Einsatz gebracht. Es wird bestätigt, dass die effektive Permeabilität im gesamten Bereich zwischen der magnetischen Plasmafrequenz und der Resonanzfrequenz negativ ist und einen kapazitiven Wellenwiderstand aufweist. Eine zweite Art künstliche Materie, bestehend aus periodisch angeordneten metallischen Drähten, wird durch analytische und numerische Berechnungen untersucht. Es wird gezeigt, dass die effektive Permittivität einer solchen Drahtanordnung eine Frequenzabhängigkeit nach dem Drude-Modell aufweist und bei Frequenzen unterhalb der Plasmafrequenz negativ ist. Auch hier sind die Ergebnisse der numerischen und analytischen Rechnungen in guter Übereinstimmung. Um stärker homogenisierte Metamaterialien zu entwickeln, wird ein fraktaler Antispiralresonator (fractal anti-spiral-resonator) als Einheitszelle eines Materials mit negativer Permittivität untersucht. Es wird gezeigt, dass das Material zwischen der elektrischen Plasma- und Resonanzfrequenz negative Permittivität bei induktivem Wellenwiderstand aufweist.

Als letzte Untersuchung der Grundlagen von Metamaterialien, wird das Design linkshändiger Materialien erforscht. Die Eigenmodegleichung eines rechteckigen Hohlleiters, der periodisch mit Zellen negativer Permittivität und Permeabilität bestückt wird, wird analytisch und numerisch berechnet. Es wird gezeigt dass die Ergebnisse der analytischen und numerischen Rechnungen gut übereinstimmen. Darüber hinaus wird eine herkömmliche LHM Einheitszelle numerisch untersucht. Es wird bestätigt, dass das linkshändige Transmissionsband der Überlappungsbereich des negativen Permittivitäts- und Permeabilitätsbands ist.Eine kompakte Zellgeometrie, die auf Spiralresonatoren basiert, welche mit Drähten belastet werden, wird als Alternative zu den herkömmlichen Zelldesigns untersucht. Es wird aus numerischen Berechnungen abgeleitet, dass solche belasteten Resonatoren bei der Gestaltung von homogener LHM verwendet werden können.
Als nächstes werden zwei mögliche Anwendungsbereiche in der Mikrowellentechnik untersucht. Der erste Bereich ist Antennendesign. Zwei Meta-Antennen werden untersucht. Die erste Antenne ist eine breitbandige Dipolantenne, bei der die Dipolelemente durch LHM Einheitszellen in Form eines Arrays belastet werden. Die Breitbandigkeit dieser Antenne wird experimentell durch Messung und durch die Ergebnisse der numerischen Rechnung bestätigt. Es wird mit Hilfe der Oberflächenstromverteilung und Richtcharakteristik gezeigt, dass LHM Einheitszellen mit einem geringeren Strahlungsgewinn im Vergleich zu der Dipolantenne abstrahlen. Darüber hinaus ist aus den numerischen Ergebnissen abgeleitet, dass durch Anpassung der Phasendifferenz von Zelle zu Zelle die Abstrahlungseffizienz erhöht werden kann. Mögliche Methoden zur Verbesserung des Antennengewinns werden aufgezeigt, von denen eine im Design der zweiten Antenne verwendet ist. Die zweite Antenne ist eine Schlitzantenne, welche mit elektrischen und magnetischen Dipolen in Form von geschlitzten Metamaterialzellen im Abstrahlelement gestaltet wird. Es wird numerisch bestätigt, dass die Antenne schmalbandig mit hoher Abstrahlungseffizienz und Gewinn ist. Die zweite Anwendung ist der Filterentwurf. Zwei Meta-Filter sind untersucht. Der erste Filter ist ein kompakter Bandsperrfilter, welcher durch galvanische Kopplung von vier LHM Zellen in der Form von $\lambda/4$-Resonatoren mit Speiseleitung gestaltet wird. Die Wirkung der Bandsperre wird durch experimentelle und numerische Ergebnisse bestätigt. Das zweite Design ist ein kompakter Bandpassfilter, der durch Kopplung von zwei Elementarzellen, die direkt mit der Speiseleitung verbunden sind, entworfen ist. Es ist numerisch gezeigt, dass eine niedrige Einfügedämpfung und hohe Selektivität durch die Optimierung der Feld-Kopplung zwischen den Resonatoren erreicht werden kann. Ein Vorteil der beiden Filter ist, dass es keine Notwendigkeit für eine Anpassungsschaltung gibt, wodurch die Filtergröße deutlich reduziert wird.

Abstract

Materials with simultaneous negative permittivity and permeability in a certain frequency band were first studied by Veselago in 1968. He termed such media left-handed media due to the left-handed triad formed by the electric field, magnetic field and the phase propagation vector. Because of the inexistence of such materials in nature, the optical and electromagnetic consequences examined in Veselago's work could only be observed after nearly 30 years. In 2000, a composite material, also known as a metamaterial, consisting of periodic negative permittivity and permeability cells in the form of metallic wires and split rings was shown to exhibit left-handed properties. Because the dimension of the rods and rings are small compared to the operation wavelength, it is possible to approximately describe their bulk electromagnetic properties using an effective permittivity and permeability. In this thesis, the fundamental properties of negative permeability, permittivity and left-handed materials are explored in the antenna and filter design as potential microwave applications.

As an investigation on basic properties and alternative design methods of metamaterials, artificial magnetic materials are examined at first. Artificial magnetic materials in the form of metallic cylinders with/without splits and split ring resonators are studied. Approximate effective permeability formulations are derived. Numerical calculations for the transmission and reflection parameters of concentric cylinders with splits are carried out in addition to analytical calculations. The good agreement between analytical and numerical calculations is confirmed. The resonance frequency of split ring resonators is also approximated with an alternative formulation derived from quasi-static analysis. It is shown that the numerical calculations agree better with the derived formulation than the original formulation. 1D dispersion diagram of split ring resonators is also examined numerically. Effective material parameters are retrieved to confirm Lorentzian-type frequency dependence of permeability. As an investigation for more homogenous material design, a fractal spiral resonator is studied as a unit cell of negative permeability material. It is confirmed that the composite material has negative permeability between the magnetic plasma and resonance frequency with capacitive wave impedance. At second, artificial dielectrics composed of periodic metallic wires are examined with analytical and numerical calculations. It is shown that the effective permittivity of wire array has Drude type frequency dependence and is negative at the frequencies smaller than the plasma frequency. The numerical and analytical calculations are in good agreement. To design more homogeneous metamaterials, a fractal anti-spiral resonator is examined as a unit cell of negative permittivity material. It is pointed out that the composite material has negative permittivity between the electric plasma and resonance frequency with inductive wave impedance. As a last investigation on metamaterial fundamentals, the design of left-handed materials is explored. The eigenmode equation of a rectangular waveguide, which is periodically loaded with negative permittivity and permeability cells is analytically and numerically calculated. Both are in good agreement. In addition, a conventional LHM unit cell is numerically studied. It is confirmed that the LH transmission band is the overlapping region of negative permittivity and permeability bands. A compact cell geometry based on wire loading of spiral resonators is studied as an alternative to the conventional cell designs. It is deduced from the numerical calculations that it can be used in the design of more homogeneous LH materials.

Next, two potential microwave applications are explored. The first application is antenna design. Two meta-antennas are examined. The first antenna is a broadband dipole antenna, which is designed by loading the dipole element with LHM cells in an array form. The broadband operation is confirmed by experimental and numerical results. It is shown from the surface current distribution and radiation patterns that LHM cells are radiating with a lower gain in comparison to the dipole antenna. In addition, it is deduced from the numerical results that to adjust the phase difference per unit cell can be one solution to increase the radiation efficiency and antenna gain. Possible gain enhancement methods are pointed out, one of which is used in the design of the second antenna. It is a microstrip slot antenna. It is designed with electric and magnetic dipoles in the form of slotted metamaterial cells in the radiator. It is confirmed numerically that the antenna is narrowband with high radiation efficiency and gain.

The second application is the filter design. Two meta-filters are examined. The first filter is a compact band-stop filter. It is designed by directly connecting four LHM cells in the form of $\lambda/4$ resonators with the feeding line. The bandstop characteristics are confirmed by experimental and numerical results. The second design is a compact band-pass filter, which is designed by coupling two unit cells directly connected with the feeding line. It is shown numerically that low insertion loss and high selectivity can be achieved by optimizing the field coupling among the resonators. One advantage of both filters is that there is no need of a matching network, which therefore reduces the filter size significantly.

Contents

1. Introduction

Electromagnetic waves have important role in daily life, since the electromagnetism is the main driving phenomenon in many applications, including communication, imaging, sensing and devices like antennas, light sources, optical fibers, lenses, etc. Extending from extremely low frequencies up to Gamma rays, the electromagnetic wave phenomenon has received great interest. Researchers have widely studied on the interaction of electromagnetic waves with matter. This has led many technological applications and technical devices to be realized in diverse scientific disciplines. Transmission, reflection, refraction, diffraction and scattering are among many effects resulting from the interaction between the electromagnetic fields and materials. This electromagnetic interaction is determined by electromagnetic material parameters, dielectric permittivity (ε) and magnetic permeability (μ). Ordinary materials usually have positive values of ε and μ. However, the electromagnetic response of natural materials can be intentionally extended to the values that are not readily available by designing artificial materials, so called metamaterials. The phrase "Meta" is originating from Greek meaning "beyond". The ordinary materials are composed of atomic and molecular constituents that are much smaller than the wavelength. They are therefore termed as homogeneous materials. A similar interpretation could be analogically established with the artificial materials. In these materials, the basic building blocks, meta-atoms, are much smaller than the wavelength of interacting electromagnetic wave. The effective permittivity and permeability can therefore be similarly assigned to the whole composite medium as in natural materials. The motivating point in the metamaterials-based designs is the controllable engineering of the electromagnetic material parameters to obtain any desired value within the theoretical limits, even negative real values.

The progressive interest in metamaterial research started at the beginning of 21th century after the successful demonstration of artificial material with simultaneously negative permittivity and permeability [1]. However, it was more than 30 years ago in 1968 that a Russian physicist, Veselago, examined intensively the electromagnetic consequences of a conceptual material in which ε and μ had both negative real values [2]. He has termed this material as left-handed material (LHM) because the electric field, magnetic field, and wave propagation direction form a left-handed system. In addition, the negative material parameters result the effective refractive index to be negative. This is not achievable with known conventional materials [2-4]. Negative electromagnetic parameters result alternative design methodologies to be implemented in the component design. Novel microwave components with improved performances are therefore realized. Large number of scientific papers on the analytical, numerical and experimental investigations of peculiar metamaterial effects and metamaterial-based components are published [3-6].

1.1 Motivation

Metamaterials offer a wide range of exciting physical phenomena to be observed, which are not attainable with ubiquitous materials. Artificial magnetism is one of these exotic electromagnetic properties. Resonant magnetic response can be achieved from the periodic arrangement of non-magnetic inclusions. These inclusions can be designed as electrically small resonators with distributed capacitive and inductive elements. A split-ring resonator (SRR) is an original example of this type [7].

The resonant permeability can be tailored to any desired value including negative values between the magnetic resonance and plasma frequency. On the other hand, an effective negative permittivity over a desired frequency band can be obtained with the regular lattice of conducting wires [8,9]. This periodic structure exhibits plasma-like permittivity response for the wavelength larger than the lattice period. Therefore, the negative permeability and permittivity materials can be engineered in a controlled manner to obtain any value of refractive index within a desired frequency range [1], [3-6]. Some possible applications of metamaterials are shown in Figure 1.1.

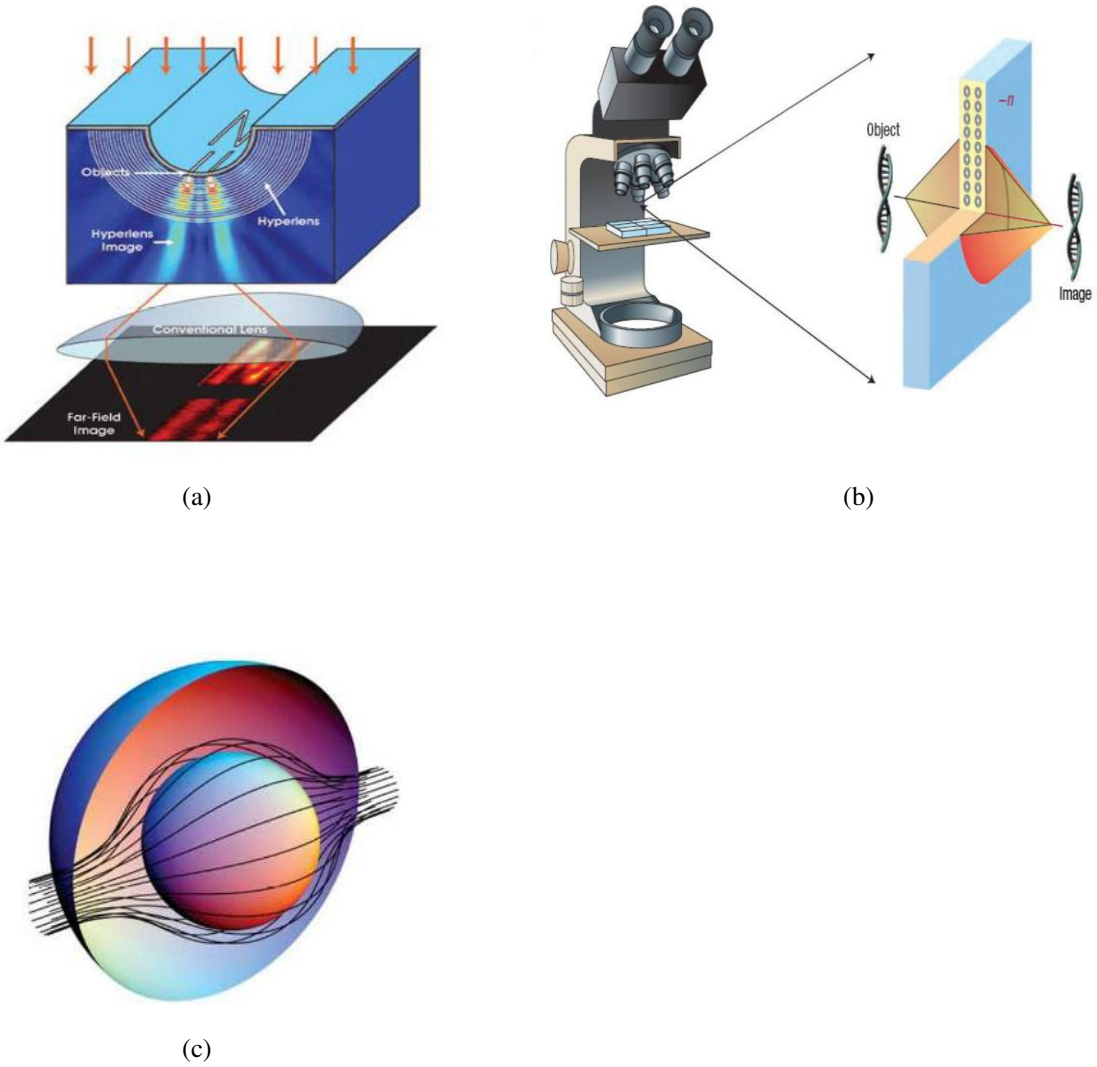

(a) (b)

(c)

Figure 1.1. Metamaterial applications (a) magnifiying hyperlens [10] (b) superlens [11] (c) cloaking device [12]

There are some engineering applications derived from the metamaterial concept such as phase compensation [4,5] and electrically small resonators [6], [13], compact high selective microwave filters [3],[14], subwavelength waveguides with lateral dimensions below diffraction limits [15,16], enhanced focusing [17,18], backward wave antennas [5],[19] and enhanced electrically small antennas [20-23]. Because the metamaterials are geometrically scalable structures, they offer the same operation and design principles to be conveniently implemented at higher/lower frequencies. Different metamaterial designs in wide range of operation frequencies are explained in detail [24-30].

1.2 Thesis Work

In this thesis, the fundamental properties of negative permeability, negative permittivity and LHM at microwave frequencies are analytically and numerically studied. How to utilize these electrically small cells in the design of compact antennas and filters is experimentally and numerically investigated with two meta-antenna and two meta-filter designs.

In the second chapter, how to tailor and overcome the restrictions in electromagnetic material parameters are introduced. Artificial dielectric, magnetic and left-handed materials are explained shortly. The fundamental electromagnetic properties are studied with the analytical and numerical calculations in detail in the next chapters.

The third chapter is dedicated to the main principles of non-resonant and resonant artificial magnetism. The artificial diamagnetism obtained from periodic infinitely long cylinders is addressed at first. It is important to understand non-resonant magnetism in 2D. Two concentric cylindrical sheets with opposite splits are then investigated. They are important to obtain resonant magnetic permeability with negative permeability region. SRR is studied next. The numerical calculations are done to confirm the negative permeability phenomenon in SRR-based materials. The effective electromagnetic parameters are retrieved. Dispersion relation is studied. Negative permeability band is determined. At the end of the chapter, a novel unit cell based on fractal spiral resonator is proposed. The material parameters, Bloch impedance and propagation constant are extensively studied. This magnetic cell can be used to design more homogeneous materials with negative permeability.

In Chapter 4, the fundamental principles of negative permittivity materials are explained in detail. The analytical calculations on periodic wire array in Pendry's original work [8,9] are revised. A more generalized formulation is obtained. The plasma-like permittivity response is analytically calculated. The effect of periodic wire loading on effective permeability is also pointed out. More homogeneous alternative designs are referenced. The numerical calculations are performed for a wire strip model. The effective material parameters are retrieved. 1D dispersion relation is studied. The plasma frequency and negative permittivity band are determined. At the end of the chapter, a unit cell based on fractal antispiral resonator is proposed to design more homogeneous materials with negative permittivity.

LHMs are then explained in Chapter 5. They are basically composed of both negative permittivity and permeability unit cells in the same host medium. The eigenmode equation of periodically loaded negative permittivity and permeability materials is analytically and numerically calculated. This analytical study is important to understand the subwavelength resonance feature and negative phase velocity in LHMs. The numerical calculations are done for a conventional LHM cell. The wave propagation in the frequency band of both negative permeability and permittivity is confirmed. The effective parameters are retrieved. Dispersion relation is also studied to determine the frequency band of negative refractive index. At the end of the chapter, an LHM cell based on wire-loaded spiral resonator is numerically investigated for the design of more homogeneous LHMs.

One potential application of artificial materials in microwave systems is antenna design. Metamaterials-based antenna design is therefore explained in Chapter 6. Basic concepts in small antennas are addressed first to understand the fundamental performance limitations. As a next step, a broadband LHM-loaded dipole antenna is designed. It is studied numerically and experimentally. The reflection parameter of the fabricated prototype is measured to confirm the numerical results. This design is a good representative example how to exploit artificial materials in broadband antenna design.

As a second design, a higher profile meta-antenna is designed. In this antenna, electrically small cells are used in the design of a slot radiator to enhance the antenna gain.
In Chapter 7, the basic design approaches of metamaterials-based filters are explained. They are addressed with some filter examples in the literature. Compact narrowband / broadband bandpass filters are illustrated in addition to the alternative wideband filters. As a first meta-filter example, a compact band-stop filter is designed. The filter performance is studied numerically and experimentally in detail. As a second example, a compact band-pass filter is designed with the same resonator geometry. The important geometrical parameters are pointed out to optimize and tune the filter operation frequencies and performance parameters.
Chapter 8 concludes the results and implications of various aspects of this research.

2. Metamaterials Short Overview

There are some restrictions on the electromagnetic material parameters of naturally available materials. These materials have lossy frequency dependent material parameters. In addition, it is sometimes difficult to find a suitable material with desired material parameters for some applications. However, the electromagnetic material parameters of natural materials can be tailored artificially in a controlled manner to obtain desired frequency dispersion. The resulting artificial materials with engineered material parameters are termed as 'metamaterials'. Three basic types of metamaterials are introduced shortly in the next sections.

2.1 Artificial Dielectric Materials

Artificial dielectrics are the first ever known artificial materials. They are composed of artificially created 'meta-molecules' or 'meta-atoms' in the form of dielectric or metallic inclusions of a certain shape. These inclusions can be arranged either periodically or aperiodically in the host material. The 'meta-molecules' size and lattice distances are assumed to be very small in comparison to the operation wavelength. Therefore, the macroscopic interaction of the electromagnetic wave with the artificial material can be described in terms of effective material parameters as in the case of homogeneous materials. The first artificial dielectric was proposed by W.E.Kock [31] for the design of light weight microwave lens. The main advantage of artificial dielectrics is to have the design possibility of high permittivity, low loss dielectric material. The material losses can be intentionally increased in a controlled manner to design light weight absorbers. Another important application is to design light weight materials with plasma-like permittivity response at the microwave frequencies. These materials can be realised from the periodic conducting wires with smaller radii as compared to the lattice periods as shown in Figure 2.1.

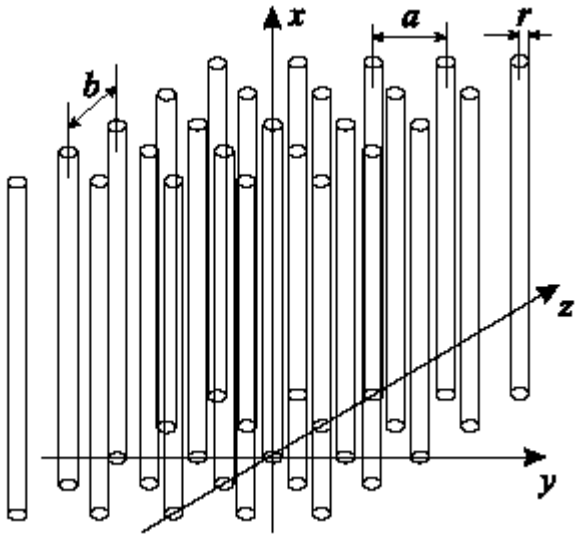

Figure 2.1. Wire medium geometry [9]

The wire medium is often called ‘artificial plasma’. They were even used in the plasma simulations and high-impedance surface design at microwaves [6],[32,33]. Negative permittivity materials are explained in more detail in Chapter 4.

2.2 Artificial Magnetic Materials

The artificial magnetic materials in the present time are basically in the form of diamagnetic and resonant magnetic materials in 2D and 3D [7].Their design approach is based on the periodic arrangement of electrically small resonators to obtain strong magnetic response. The typical resonant elements are split-ring resonators (SRR) in 3D and Swiss rolls in 2D. They are shown in Figure 2.2. Magnetic materials made up of periodic SRRs in 3D and Swiss rolls in 2D have negative permeability within a narrow frequency band between the magnetic resonance and plasma frequencies [7],[3]. Actually, the design logic of SRR dates back to the slotted tube resonators in the detection system of nuclear magnetic resonance spectroscopy [34].

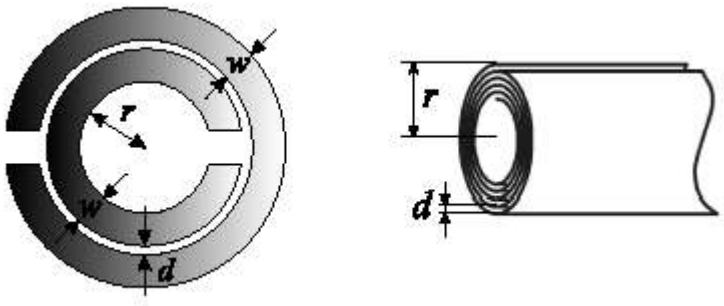

Figure 2.2 Split-ring resonator and Swiss Roll Structure geometry

However, Swiss Roll structures are more effective than SRRs with the design possibility of compact RF lens and flux guiding elements for MRI systems [35-37]. Negative permeability materials are explained with alternative homogeneous realizations in Chapter 3.

2.3 Left-Handed Materials

The left-handed concept is first introduced by V.G. Veselago. He examined theoretically the electromagnetic consequences of plane wave propagating in a material with simultaneous negative permittivity and permeability in 1968 [2]. He has termed this material as ‘left-handed material’ because electric field, magnetic field and wave vector form a left-handed triad rather than right-handed triad in the conventional materials. LH media have interesting possible applications such as the possibility of perfect lens construction predicted by Pendry [18], a sub-wavelength cavity resonator invented by Engheta [13], compact high gain resonant antennas [20], backward wave antennas [19], compact phase shifters [38], compact high selective filters [14], directional couplers with arbitrary coupling strength [39], subwavelength waveguides [15,16], cloaking [12]. The uniaxial version of first LHM is realized by Smith in 2000 [1]. It is composed of periodic arrangement of thin wires and split-ring resonators proposed by Pendry. It is shown in Figure 2.3.

Figure 2.3. LHM geometry

In this design, the periodic wires (wire medium) exhibits negative permittivity and the periodic split-ring resonators exhibits negative permeability. However, LH structures presented originally were less practical for microwave applications because of their lossy and narrow bandwidth characteristics. Therefore, a transmission line (TL) approach of LH materials based on nonresonant components is introduced to realize an artificial LH-TL with low losses and broad bandwidth [4,5]. Several microwave components with improved performances have been realized with this design method [4-6]. In Chapter 5, resonant type LHM materials are explained in detail.

3. Negative Permeability Metamaterials

3.1 Introduction

This chapter explains the main principles of artificial magnetism. The artificial diamagnetism is addressed at first with the analytical calculations on infinitely long metallic cylinders. This analytical study is important to understand how to obtain controllable nonresonant magnetism in 2D. Then two concentric cylindrical sheets with opposite splits are introduced as artificial magnetic inclusion. This cell geometry is important to obtain resonant magnetic permeability with negative permeability region. Split-ring resonator (SRR), which is proposed by Pendry, is addressed next to design 3D artificial materials. The numerical calculations are performed for a specific SRR model. The negative permeability phenomenon is confirmed with retrieved material parameters. The effect of electromagnetic coupling among the cells on the resonance frequency is investigated. 1D dispersion relation is studied. At the end of the chapter, a unit cell based on fractal spiral resonator is proposed to design more homogenous negative permeability materials.

3.2 Theoretical Analysis

The response of natural materials to the magnetic field is determined by the permeability. The bulk permeability is a macroscopic description of how readily the material experiences the magnetization when an external magnetic field is applied. Magnetization is the measure of total magnetic moment resulting from the parallel or anti-parallel alignment of orbital and spin motion of moving charges to the magnetic field. The lack of magnetic charge leads the permeability of natural materials to be positive. This makes them not to be useful in LHM design. However, the effective electromagnetic parameters of any material can be engineered in a controlled manner by embedding electrically small inclusions into the host material. This is the main design strategy to be used in the design of negative permeability materials. On the other hand, there must be some restrictions on the cell size. If macroscopic electromagnetic parameters are to be assigned as in homogenous materials, the operation wavelength has to be much larger than the cell size. This results the internal composite nature of the medium not be identified by the electromagnetic wave. In other words, long wavelength radiation is too myopic to detect the internal structure. In this limit, to assign an effective permittivity and permeability is a valid concept even for the inhomogeneous material. If this condition were not obeyed, there would be the possibility that internal structure could diffract as well as scatter the radiation. This invalidates the effective material definition [3-5],[7]. As a rule of thumb, the composite materials, made up of metallic inclusions with period p can be treated as effective homogeneous materials under an effective homogeneity condition. It is stated as [5]

$$p \leq \frac{\lambda_g}{4} \tag{3.1}$$

where λ_g is the guided wavelength.

3.2.1 Periodic Array of Cylindrical Metallic Sheets

In 1999, Pendry *et al.* introduced several configurations of conducting scattering elements as the unit cells of artificial magnetic materials. In this section, the first structure in Pendry's work is studied. It is shown in Figure 3.1.

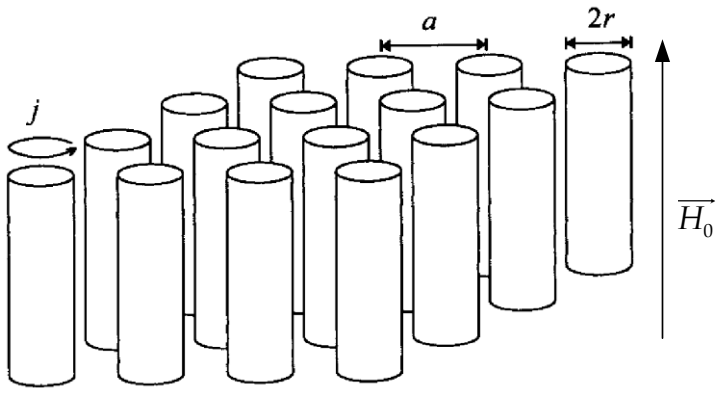

Figure 3.1 Periodic arrangement of infinitely long cylindrical sheets excited by axial magnetic field $\overrightarrow{H_0}$ [7]

This bulk material is composed of periodic infinitely long metallic cylinders in 2D. The period and radius are a and r, respectively. In terms of effective medium approach, these sheets can be attributed as electrically small constituents of the host material. The sheet thickness is comparably smaller than the skin depth at the frequency of interest. The magnetic response to the axial magnetic field can be calculated by the quasi-static analysis in the following manner. The external time-varying magnetic field induces current in the cylinder. The induced current generates in turn magnetic field inside the cylinder opposing to the time variation of external magnetic field. The φ-directed current leads the magnetic field to change by a factor of S. S can be regarded as a magnetization factor. The induced voltage on the cylinder surface is calculated by Faraday's induction law as

$$\oint_C \vec{E}.\overrightarrow{dl} = -j\omega \int_F \vec{B}.\overrightarrow{dF}$$
$$\oint_C \vec{E}.\overrightarrow{dl} = -j\omega\mu_o \int_F S\overrightarrow{H_0}.\overrightarrow{dF} \quad . \tag{3.2}$$

Because cylinder thickness, Δr is much smaller than cylinder radius and operation wavelength, the current can be approximated as a surface current. The surface current, $\overrightarrow{J_F}$, is calculated from the magnetic field difference between the inner and outer cylinder regions as

$$\overrightarrow{J_F} = (S-1)H_0\overrightarrow{e_\varphi} \quad . \tag{3.3}$$

(3.2) can be alternatively formulated in terms of $\overrightarrow{J_F}$ as

$$\frac{J_F}{\Delta r \kappa} 2\pi r = -j\omega\mu_0 S H_0 \pi r^2 \tag{3.4}$$

where κ is the electric conductivity.
S can then be calculated by the substitution of (3.3) into (3.4) as

$$S = \frac{1}{1 + \frac{j\omega\kappa\mu_0 r\Delta r}{2}} = \frac{j\delta_s^2}{j\delta_s^2 - r\Delta r} \tag{3.5}$$

where δ_s is the skin-depth.
The magnetization vector, $\overrightarrow{M}$ can then be formulated in terms of $\overrightarrow{H_0}$ and effective magnetic susceptibility, χ_m as

$$\overrightarrow{M} = \frac{\pi r^2}{a^2} J_F \overrightarrow{e_z} = \frac{\pi r^2}{a^2} \frac{r\Delta r}{j\delta_s^2 - r\Delta r} \overrightarrow{H_0} = \chi_m \overrightarrow{H_0} \ . \tag{3.6}$$

The effective permeability is calculated in the form of

$$\mu_{eff} = \mu_0(1 + \chi_m)$$
$$\mu_{eff} = \mu_0\left(1 - \frac{\pi r^2}{a^2} \frac{r\Delta r}{-j\delta_s^2 + r\Delta r}\right) . \tag{3.7a}$$

In (3.7a), for infinite conductivity or in the high frequency limit, μ_{eff} is reduced by the ratio of the cylinder surface to the cell surface. This surface ratio is an important factor in the permeability calculation of further alternative forms of this model. An important remark is that μ_{eff} can never be less than zero or greater than μ_0. It has a nonresonant diamagnetic frequency dependence.
The same formulation can be alternatively derived for the finite cylinders of length, $l_{cyr.}$ and inductance, L as an approximation to the present model (see Appendix A)

$$\mu_{eff} = \mu_0\left(1 + \frac{(\pi r^2)^2}{a^2} \frac{-j\omega\mu_0}{\frac{2\pi r}{\kappa\Delta r} + j\omega L\, l_{cyr.}}\right) \quad . \tag{3.7b}$$

In (3.7b), if L is loaded with a series capacitance, C in the form of longitudinal slots along the cylinder axis, this array exhibits resonant magnetic response with a negative permeability region in a certain frequency band. This point can be better understood after the substitution of $L\left(1 - \frac{1}{\omega^2 LC}\right) = L\left(1 - \frac{\omega_0^{\ 2}}{\omega^2}\right)$ into L in (3.7b). The effective permeability in (3.7b) is then in the form of

$$\mu_{eff} = \mu_0(1 + \frac{(\pi r^2)^2}{a^2} \frac{-j\omega\mu_0}{\frac{2\pi r}{\kappa\Delta r} + j\omega L\, l_{cyr.} + \frac{1}{j\omega C'}}) = \mu_0(1 + \frac{(\pi r^2)^2}{a^2} \frac{-j\omega\mu_0}{\frac{2\pi r}{\kappa\Delta r} + j\omega L(1 - \frac{\omega_0^2}{\omega^2})\, l_{cyr.}}) \tag{3.8}$$

$$\mu_{eff} = \mu_0\left(1 + \frac{-F\omega^2}{-\omega_0^2 + \omega^2 - j\omega\Gamma}\right)$$

where C´ is the series capacitance per unit length, $C/l_{cyr.}$., ω_0 is the magnetic resonance frequency, F is the filling factor and Γ is the loss factor.
These parameters can be defined as

$$F = \frac{\pi r^2}{a^2}, \quad \Gamma = \frac{2}{\mu_0 \kappa r \Delta r}, \quad \omega_0 = \sqrt{\frac{1}{LC}} \quad . \tag{3.9}$$

The generic form of relative permeability is shown in Figure 3.2 for F= 1/3, f_0 = 2GHz and Γ =20 MHz.

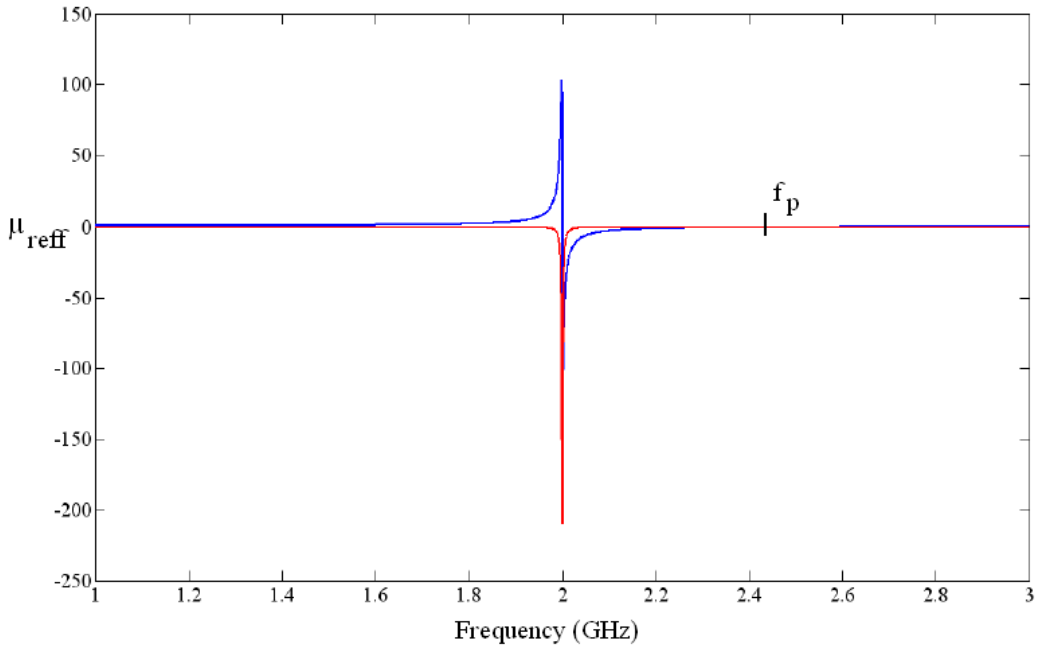

Figure 3.2 Real (blue) and imaginary (red) part of effective relative permeability

In Figure 3.2, the effective relative permeability exhibits Lorentzian type frequency dependence with the resonance frequency, f_0. In addition, the resonance phenomenon results the artificial material to be highly magnetized and demagnetized just below and above f_0. There is a negative permeability region between f_0 and f_p. f_p is defined as the magnetic plasma frequency at which the effective permeability is zero analogous to the electric plasma frequency of metals, ionic molecular and atomic gases. f_p is calculated as

$$f_p = f_0\sqrt{\frac{1}{1-F}} \tag{3.10}$$

3.2.2 Periodic Array of Concentric Cylindrical Metallic Sheets with Splits

In order to design more homogeneous medium, the resonance frequency has to be reduced with the larger capacitive loading in the same cell. One cell of this type is proposed by Pendry. It is composed of two concentric metallic cylinders with the splits at the opposite ends as shown in Figure 3.3.

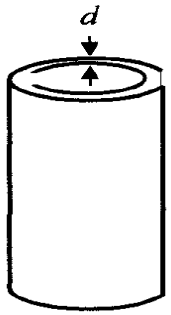

Figure .3.3. One unit cell of square array of concentric metallic sheets divided into a "split ring" structure and separated from each other by a distance d [7]

In Figure 3.3, the large capacitance between two rings enables the current to flow from one ring to the other ring in the form of displacement current. The ring inductance is then loaded by the gap capacitance between the outer and inner rings with a result of resonant magnetic response. Therefore, due to the current interrupted by the splits, in the equivalent circuit modeling, the first and second half of the total gap capacitance without splits are connected in series manner [3],[40,41]. The equivalent circuit model is shown in Figure 3.4 where C_0 is the capacitance of two concentric cylinders without splits. The effective permeability can be calculated by substituting the equivalent capacitance per unit length into the formulation in (3.8). The capacitance per unit length, C´ and inductance, L are approximately (see Appendix A)

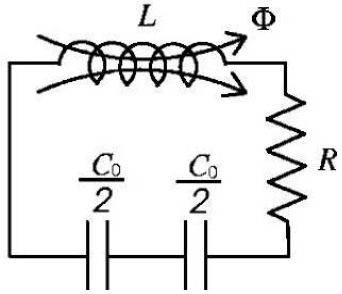

Figure 3.4. Equivalent circuit model of concentric cylindrical sheets with opposite splits [40]

$$C' = \frac{C_0}{4l_{cyr.}} = \frac{\pi\varepsilon_0}{2\ln(\frac{r+d}{r})}$$

$$L = \frac{\mu_0 \pi r^2}{l_{cyr.}} \qquad (3.11)$$

Therefore, the effective permeability has the form of

$$\mu_{eff} = \mu_0\left(1 + \frac{(\pi r^2)^2}{a^2}\frac{-j\omega\mu_0}{\frac{2\pi r}{\kappa\Delta r} + j\omega\mu_0\pi r^2 + \frac{2\ln(\frac{r+d}{r})}{j\omega\pi\varepsilon_0}}\right) = \mu_0\left(1 - \frac{\pi r^2}{a^2}\frac{1}{-\frac{j2}{\omega\mu_0\kappa r\Delta r} + 1 - \frac{2\ln(\frac{r+d}{r})}{(r\omega\pi)^2\varepsilon_0\mu_0}}\right). \qquad (3.12)$$

It can be expressed as in (3.8) with the respective parameters,

$$F = \frac{\pi r^2}{a^2}, \quad \Gamma = \frac{2}{\mu_0 \kappa r \Delta r}, \quad \omega_0 = \sqrt{\frac{2\ln(\frac{r+d}{r})}{(r\pi)^2 \varepsilon_0 \mu_0}} \quad . \tag{3.13}$$

In order to verify the analytical formulation in (3.12), the electromagnetic response of the cell model in Figure 3.3 is numerically calculated under plane wave excitation. The perfect electric (PEC) and magnetic (PMC) boundary conditions are imposed at two y-planes and z-planes, respectively. They are also important to satisfy the transversal periodicity with one unit cell. The numerical calculations are done with FEM based full-wave EM simulator HFSS. The numerical model is shown in Figure 3.5. The geometrical parameters are tabulated in Table 3.1. The transmission and reflection parameters are also calculated analytically to compare the analytical and numerical calculations. They are shown in Figure 3.6. and in reasonable agreement.

Table 3.1. Geometrical parameters of infinitely extended concentric cylinders with opposite splits

Geometrical Parameters		(mm)
radius of inner cylinder	(r_{in})	2.9
radius of outer cylinder	(r_{out})	3.3
gap distance	(d)	0.3
split width	(w_s)	0.2
metal width	(w)	0.1
lattice period	(a)	10

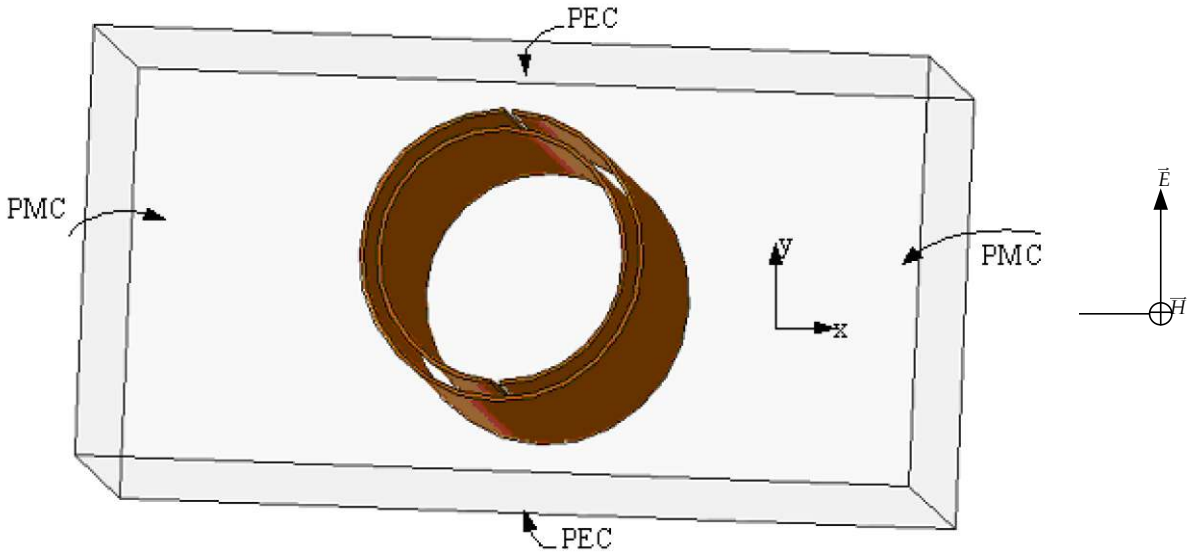

Figure 3.5. Numerical model of infinitely extended concentric cylindrical sheets with opposite splits and boundary conditions

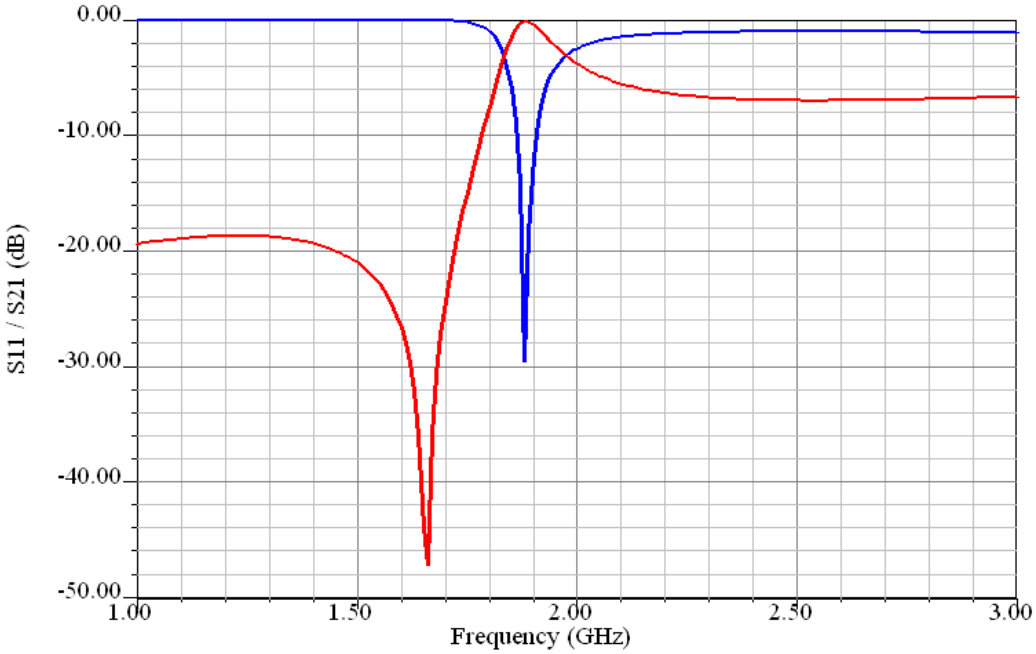

Figure 3.6.a: Numerically calculated transmission (blue) and reflection (red) parameters of infinitely extended cylinders with opposite splits

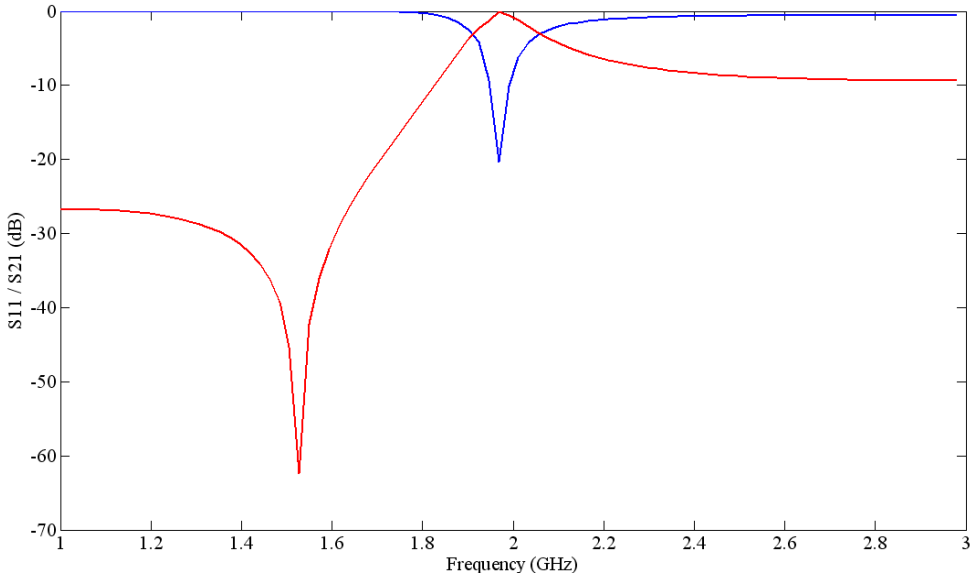

Figure 3.6.b: Analytically calculated transmission (blue) and reflection (red) parameters of infinitely extended cylinders with opposite splits

In the analytical calculations, due to the finite cylinder thickness, resonance frequency, filling factor and loss parameter in (3.13) are modified as

$$F = \frac{\pi r_{out}^2}{a^2}, \quad \Gamma = \frac{2}{\mu_0 \kappa r_{out} \delta_s}, \quad \omega_0 = \sqrt{\frac{2\ln\left(\frac{r_{in}+w+d}{r_{in}+w}\right)}{\left(r_{out}\pi\right)^2 \varepsilon_0 \mu_0}} \quad . \tag{3.14}$$

In the numerical calculation, the resonance frequency is 1.88 GHz. In the analytical calculation, it is 1.95 GHz. The resonance frequency formulated by Pendry for the same structure [7] is 2.92 GHz. (3.12) estimates the resonance frequency better than the original one with 3.72 % error. The cell size is 10 mm, which is 1/14.5 of the free space wavelength at the resonance frequency.

Therefore, this one cell thick periodic array can be attributed as a resonant magnetic material. The wave impedance is also analytically calculated and shown in Figure 3.7. It is increasing monotonically from low frequencies up to the resonance frequency. At the lower edge of the resonance frequency, it is high and then capacitive in the negative permeability band between the magnetic resonance and plasma frequencies.

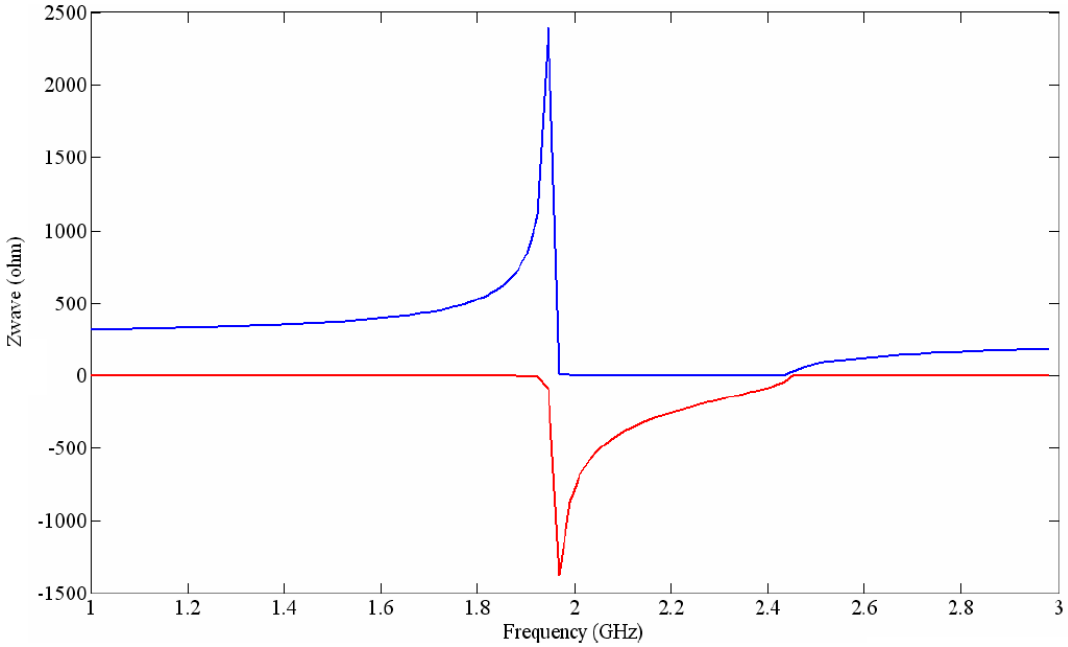

Figure 3.7 Analytically calculated real (blue) and imaginary (red) part of effective wave impedance of infinitely extended cylinders with opposite splits

3.2.3 Periodic Array of Split- Ring Resonators

As stated in the previous section, the periodic concentric cylinders with the opposite splits exhibit resonant magnetic response. However, the magnetic resonance is only valid for the exciting magnetic field aligned along the cylinder axis. In addition, they exhibit nonresonant electric response to the axially polarized wave with low transmission. This polarization dependency of the material parameters makes 2D magnetic materials not to be useful in some applications. Therefore, Pendry proposed one unit cell geometry in the form of split-ring resonator (SRR) to design 3D isotropic magnetic materials. The material isotropy can be potentially restored by printing one SRR cell on each of six surfaces of a cubic magnetic material as in [7].

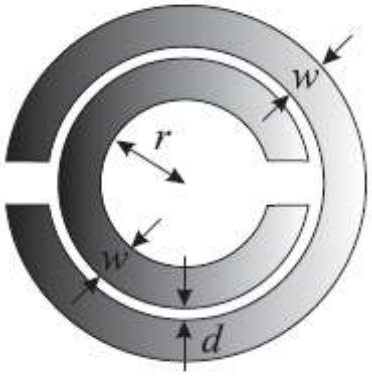

Figure 3.8a. Split-ring resonator geometry as negative permeability material

The resonance frequency can be sufficiently good estimated in the same manner as in Section 3.2.2 (see Appendix A). The resonance frequency, filling and loss factors can be calculated as

$$F = \frac{\pi r_{out}^2}{a^2}, \quad \Gamma = \frac{2}{\mu_0 \kappa r_{out} \delta_s}, \quad \omega_0 = c_0 \sqrt{\frac{2a_z}{r_{out}^2 \ln(1+\frac{2w}{d}) r_{av} \pi (1+\varepsilon_r)}},$$

$$r_{av} = r + \frac{3w}{2} + \frac{d}{2}$$
$$r_{out} = r + 2w + d \qquad (3.15)$$

where ε_r is the substrate relative permittivity and a_z is the period in the axial direction.
A 2D SRR array with the geometrical parameters in Table 3.2 is numerically calculated. It is shown in Figure 3.8b.

Table 3.2. Geometrical parameters of SRR

Geometrical Parameters	mm
inner ring radius (Ri)	2.4
outer ring radius (Ro)	3.1
width of each ring (w)	0.6
spacing between ring edges (d)	0.1
split width	0.2
a_x	10
a_y	10
a_z	1
ε_r	1

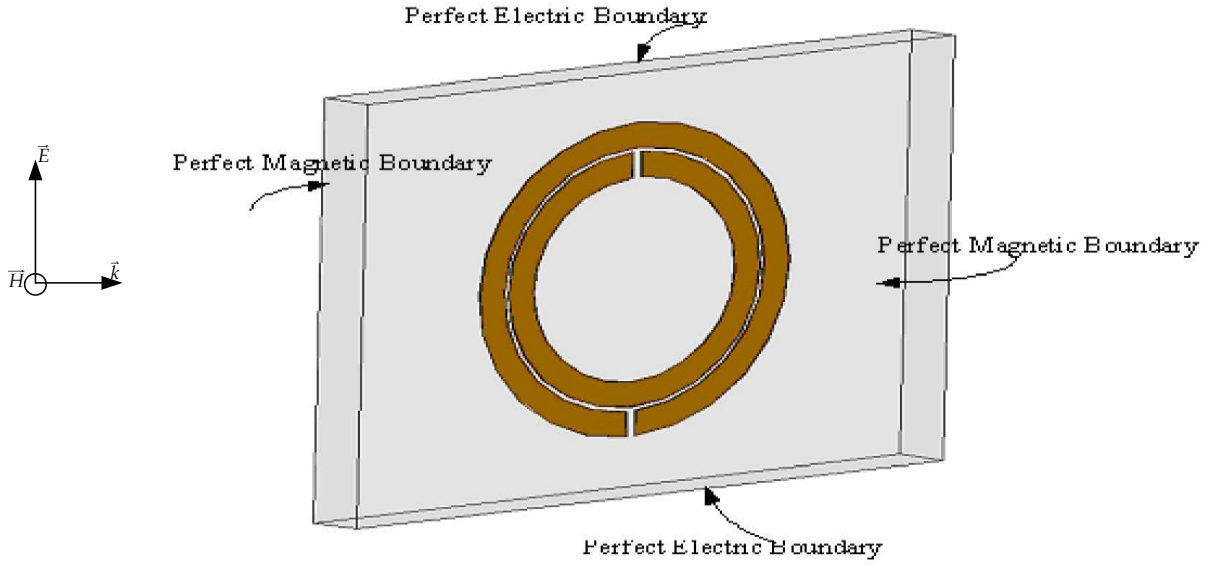

Figure 3.8b Split-ring resonator model with boundary conditions

In the numerical calculation, the resonance frequency is 2.58 GHz. In the analytical calculation, it is 2.48 GHz. The percentage error is 3.87%. In the work of Pendry, it is highly overestimated as 8 GHz.

The resonance frequency can be better estimated from alternative analytical formulations. In [42, 43], the resonance frequency is calculated from the solution of a set of differential equations, which are formulated in terms of ring currents. In [44], there is one improved analysis, which is based on the treatment of doubly-split double rings as two coupled split rings for resonance frequency calculation. In [41,45], the equivalent circuit models are derived from the quasistatic calculations on the modified forms of SRRs. In these circuit models, the average inductance is numerically calculated from the variational formulation and the capacitance per unit length is calculated from the closed form expressions in [46].

Modified geometries of SRRs are also studied [47-49]. They are important to understand how SRRs with multiple splits can be effectively used to tune the resonance frequency towards higher frequencies. Alternative cell geometries are also proposed to squeeze the resonant electrical size for the design of homogeneous magnetic materials [50-54]. An intuitive method to reduce the electrical size without increasing the resonator area is to use multiple split-ring resonators [3,55]. This cell design is extensively studied and equivalent circuit model is derived in [55].

3.3 Numerical Simulations

3.3.1 Resonance Frequency of SRR Periodic Array

In this section, the electromagnetic response of one cell thick SRR array is numerically calculated under plane wave excitation. The unit cell is shown along with the boundary conditions in Figure 3.9. The geometrical parameters are tabulated in Table 3.3.

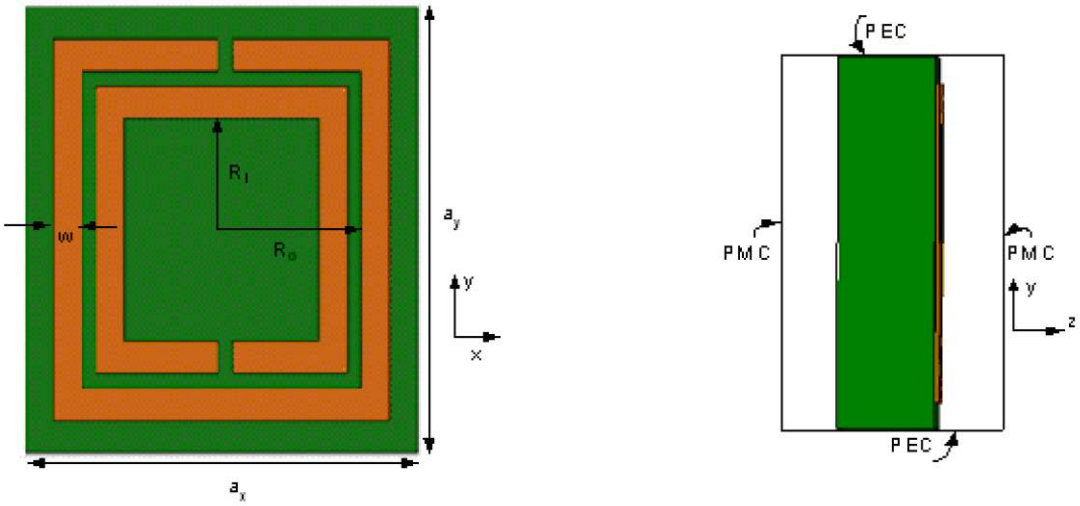

(a) (b)

Figure 3.9 (a) One unit cell of SRR geometry (b) boundary conditions imposed on the edges of one unit cell

Table 3.3 Geometrical parameters of one unit cell of SRR array

Geometrical Parameters	mm
inner ring radius (Ri)	0.7
outer ring radius (Ro)	1
width of each ring (w)	0.2
spacing between ring edges (d)	0.1
split width	0.1
substrate thickness	0.5
a_x	2.8
a_y	2.8
a_z	2

PEC is imposed on two y-planes at the edges of the unit cell as shown in Figure 3.9b. It couples the periodic cells along y-direction electrically. In the same manner, PMC is imposed on two z-planes at the edges to couple the periodic cells along z-direction magnetically. Under these boundary conditions, one cell thick SRR array can be excited by y-polarized in x-direction propagating plane wave. TEM wave is the fundamental mode of the surrounding PEC-PMC guiding structure. The substrate is Rogers/RT duroid 5870. The relative permittivity and tan(δ) are 2.33 and 0.0012, respectively. The transmission and reflection parameters are numerically calculated with FEM based software HFSS. They are shown in Figure 3.10.

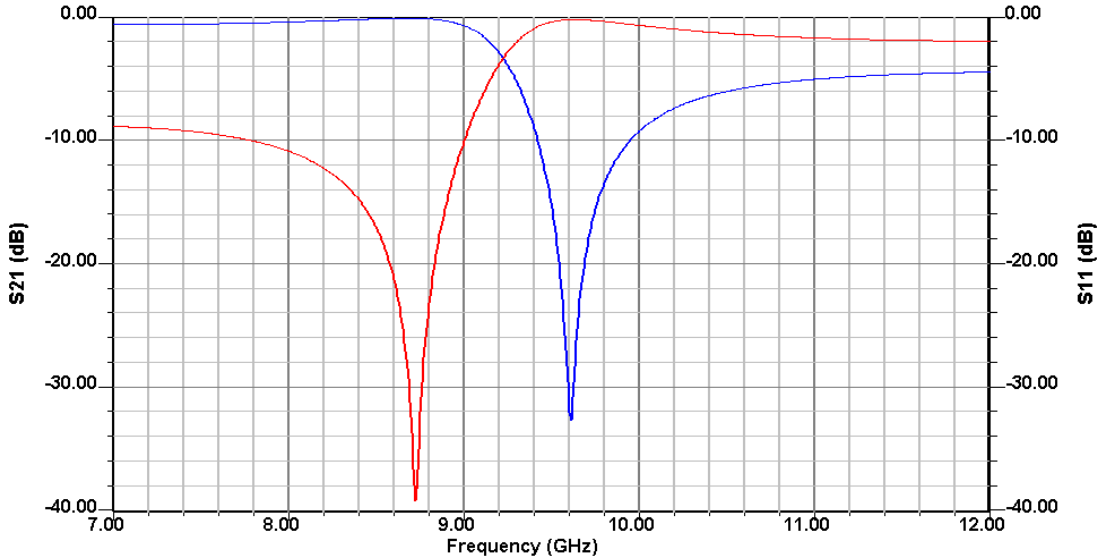

Figure 3.10 Reflection (red) and transmission (blue) parameters of one unit cell thick SRR sample

The magnetic resonance frequency is 9.61 GHz. The operation wavelength is 31.21 mm. It is approximately 11 times larger than the cell size. Thus, one cell thick SRR array can be considered as an effectively homogeneous material. At the resonance frequency, the wave transmission is highly degraded as explained in Section 3.2.2. The transmission between the magnetic resonance and plasma frequency is also low as a result of wave attenuation and impedance mismatch due to negative permeability. However, it is high at the resonance frequency of 8.7GHz due to increasing effective permeability near the magnetic resonance frequency as in Figure 3.2 and resulting impedance match with the port impedance. These points are confirmed from the effective material parameters and wave impedance. The magnetic field, electric field and surface current distribution at the magnetic resonance frequency are shown in Figure 3.11.

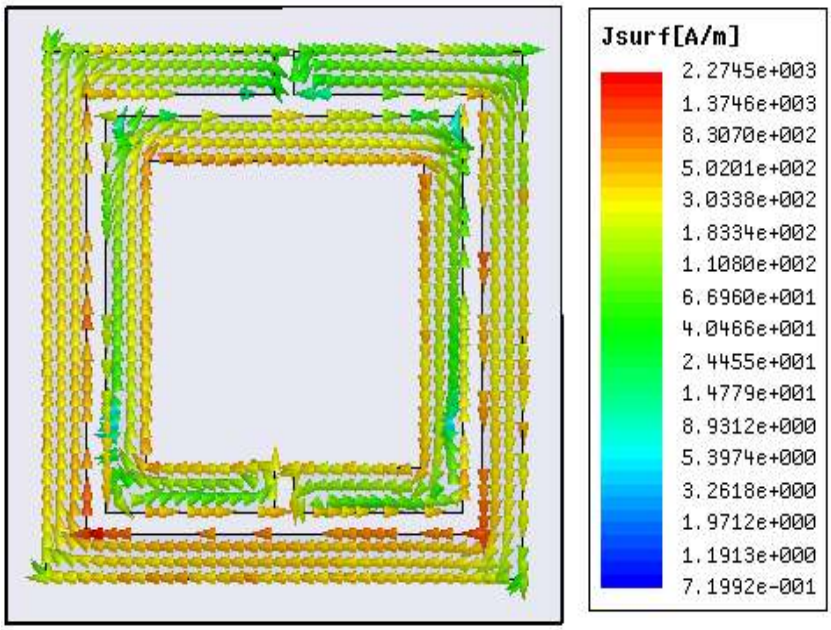

Figure 3.11a Surface current distribution of one unit cell at the magnetic resonance frequency

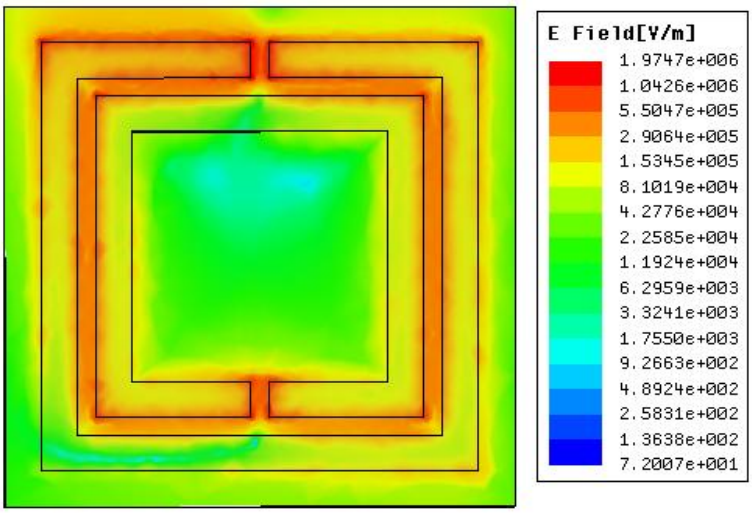

Figure 3.11b Magnitude of electric field distribution of one unit cell at the magnetic resonance frequency

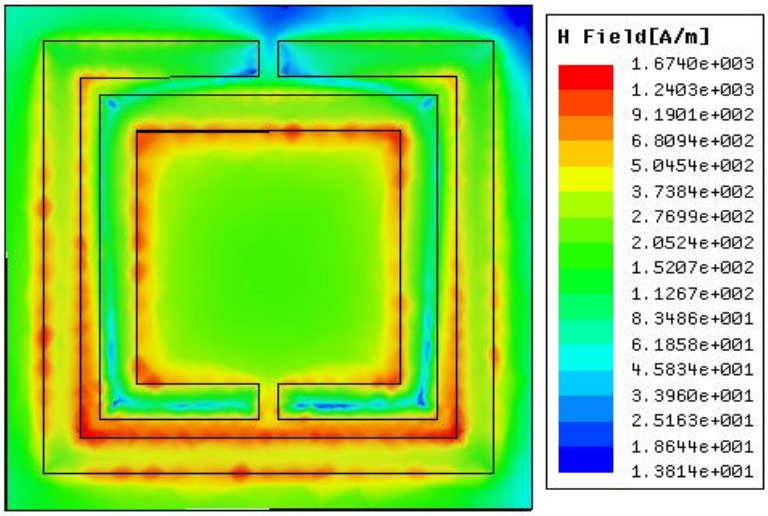

Figure 3.11c Magnitude of magnetic field distribution of one unit cell at the magnetic resonance frequency

The electric and magnetic field distributions are unsymmetrical despite geometrical symmetry of unit cell. This is mainly because of finite metallic loss inside the cell and resulting nonzero transmission at the magnetic resonance frequency. In addition to the resonant field distributions, the effect of transversal periods on the resonance frequency has to be investigated. It is important in order to figure out the role of electric and magnetic coupling among the neighboring cells on the material parameters. Therefore, the transmission parameter of one cell thick sample is numerically calculated for different periods in the transversal directions. The effect of electric coupling among y-direction oriented cells is shown in Figure 3.12a. The lower electric coupling resulting from the larger period in y-direction, a_y increases the resonance frequency. The transversal periodicity in y-direction has however minor effect. It is because the electric field is mainly concentrated in the split region of the rings and the gap region between the split rings as shown in Figure 3.11b. The resonant magnetic polarizability of SRR cell results the neighboring cells to couple magnetically in more effective manner. This can be implied from the effect of magnetic coupling among z-direction oriented cells on the resonance frequency. It is shown in Figure 3.12b for the different periods in z-direction, a_z. Because the magnetic field is mainly axially directed, the larger a_z reduces SRR inductance due to lower magnetic coupling between axially oriented cells. This is the reason why the resonance frequency is lower for the larger a_z.

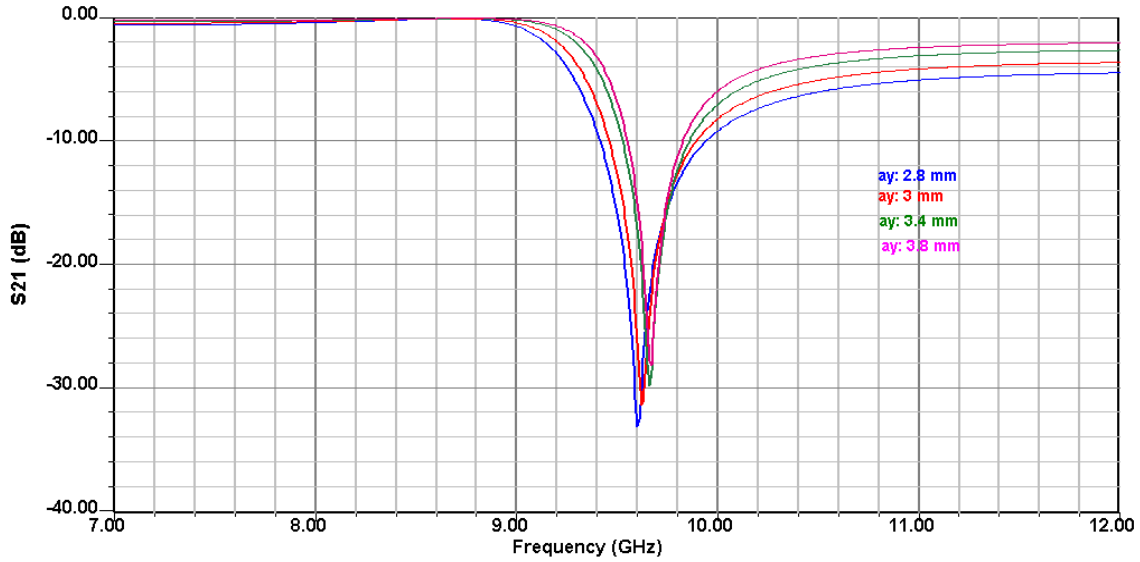

Figure 3.12a Transmission parameter with different transversal periodicity in y- direction

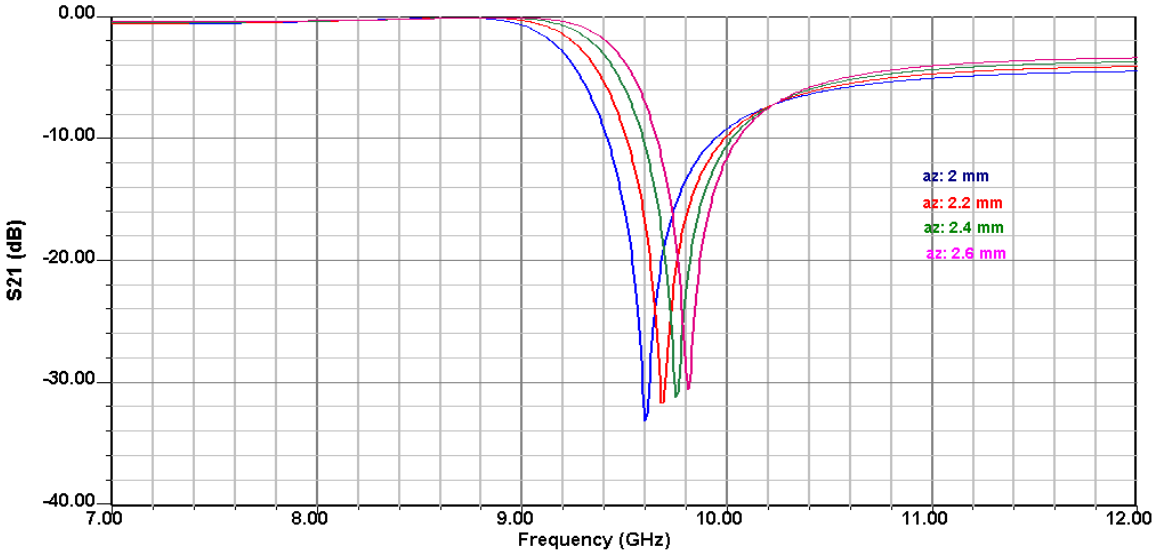

Figure 3.12b Transmission parameter with different transversal periodicity in z- direction

3.3.2 Dispersion Relation of SRR Periodic Array

In this section, 1D Brillion diagram is numerically studied to investigate the passband and stopband of SRR array. In the numerical model, eigenfrequencies are calculated with the periodic boundary conditions in the propagation direction with different phase shifts. The same PEC and PMC on the transversal y- and z-planes in the port mode simulation are imposed. The dispersion diagram of two lowest bands is shown in Figure 3.13. In Figure 3.13, SRR array can be regarded as a transmission medium. The lower frequency band is from 0 to 9.05 GHz. The higher frequency band is from 11.1 GHz to 22.41 GHz. However, it can not be attributed as an effective material for the higher frequencies of second band. It can only be regarded as an effective material in the first band. This is because the unit cell size is comparable with the free space wavelength at the higher frequencies in the second band. On the other hand, there is no wave propagation between the higher end of first band, 9.05 GHz and lower end of second band, 11.1 GHz. In this bandgap, it exhibits magnetic resonance and negative permeability behavior. This is verified from the effective parameter retrieval procedure in the next section.

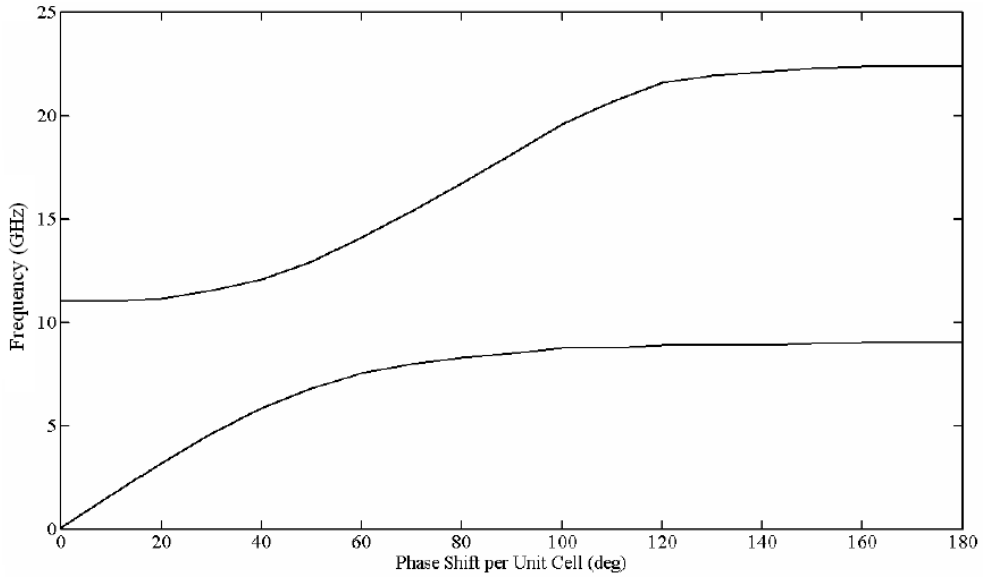

Figure 3.13 Dispersion diagram of SRR with periodic boundary conditions of different phase shifts in propagation direction

3.3.3 Effective Material Parameters of SRR Periodic Array

In this section, the effective material parameters are retrieved to confirm the negative permeability. There are a number of proposed analytical methods for the material parameter extraction in the literature [56-60]. The common point of these approaches is to calculate the transmission and reflection parameters of one cell thick sample under plane wave excitation. The wave impedance and propagation constant are then calculated from transmission and reflection data. Effective permittivity and permeability are then retrieved from the wave impedance and propagation constant. In these retrieval procedures, one cell thick sample in the propagation direction is assumed to be sufficient for effective parameter assignment due to electrically small cell size [56-60]. Instead of using conventional retrieval procedures, an alternative extraction method is introduced. In this method, the longitudinal cell periodicity in the propagation direction is included in the parameter extraction by using Bloch Theorem unlike in conventional procedures. The common point is that the transmission and reflection parameters have to calculated only for the fundamental mode in the extraction procedure as a first step. These parameters have to be then deembedded upto the left and right surface of the cell. As a second step, S parameters have to be transformed into Z parameters. ABCD parameters of one unit cell are then calculated from Z parameters in order to use Bloch Theorem in the following manner,

$$A=\frac{Z_{11}}{Z_{21}},\ B=\frac{Z_{11}Z_{22}-Z_{21}^2}{Z_{21}},\quad C=\frac{1}{Z_{21}},\quad D=\frac{Z_{22}}{Z_{21}}\ . \tag{3.16}$$

The complex propagation constant, γ and Bloch impedance, Z_B are calculated from ABCD parameters by Bloch Theorem as

$$\gamma=\frac{\operatorname{arccosh}\left(\frac{A+D}{2}\right)}{a_x},\quad Z_B=\frac{Be^{-\gamma d}}{1-Ae^{-\gamma d}},\ \gamma=\alpha+j\beta \tag{3.17}$$

where β and α are the phase and attenuation constants, respectively.
As a last step, effective relative permeability and permittivity are calculated from γ and Z_B in the form of

$$\mu_{reff} = \frac{-j\gamma Z_B}{Z_{line} k_o}, \quad \varepsilon_{reff} = \frac{-j\gamma Z_{line}}{Z_B k_o}, \quad Z_{line} = Z_o \frac{a_y}{a_z} \tag{3.18}$$

where k_o is the free space wave number and Z_{line} is the line impedance.
The effective material parameters, complex propagation constant and characteristic impedance of SRR array are retrieved by the above procedure. They are shown in Figure 3.14.

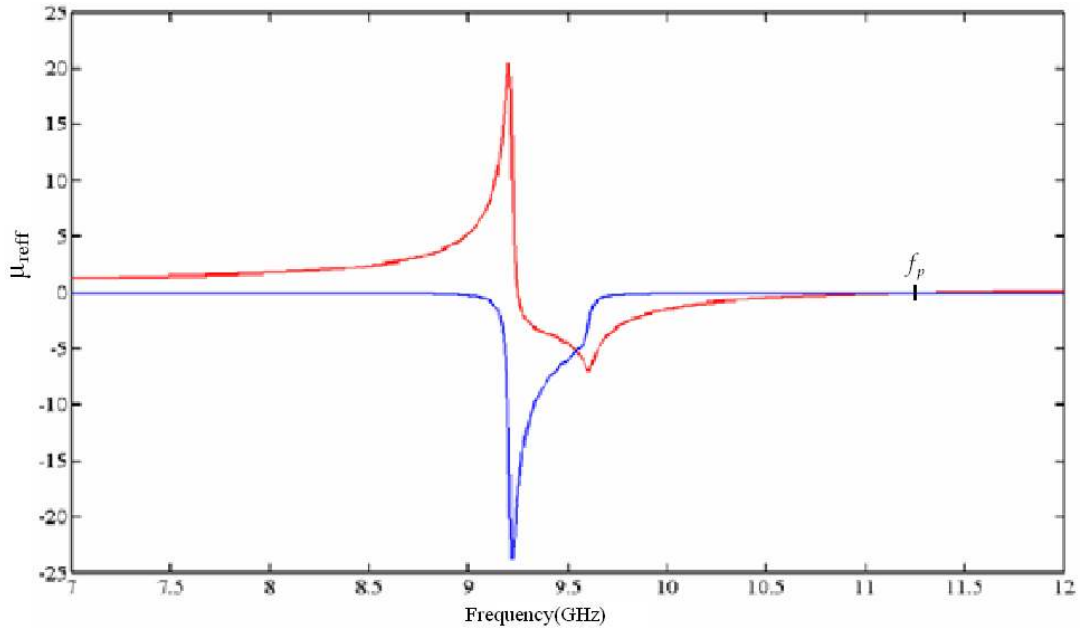

Figure 3.14a. Real (red) and imaginary (blue) part of effective relative permeability of SRR periodic array

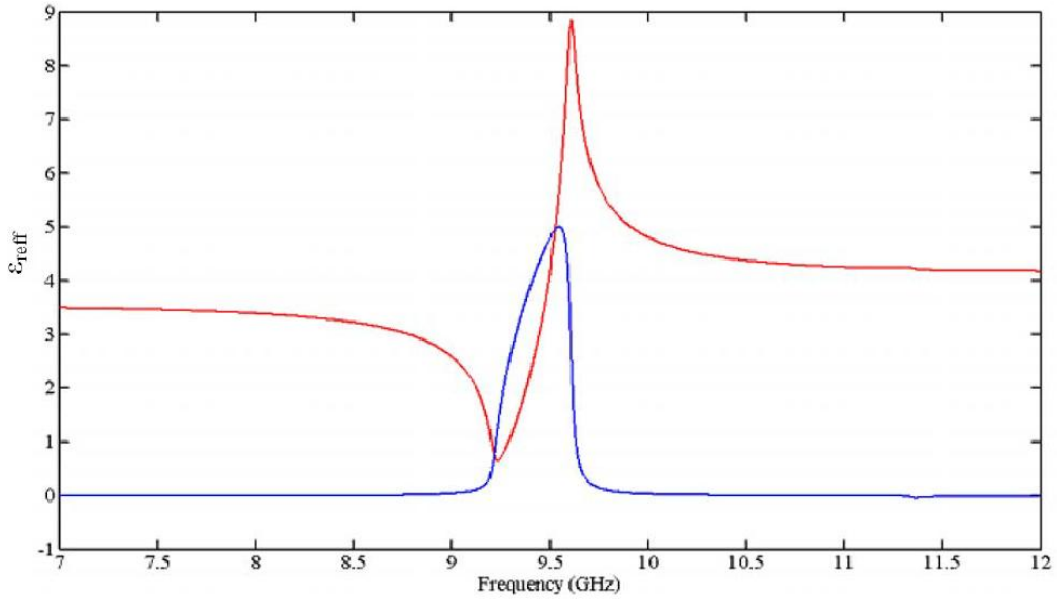

Figure 3.14b. Real (red) and imaginary (blue) part of effective relative permittivity of SRR periodic array

In Figure 3.14a, SRR array exhibits magnetic resonance at 9.22 GHz. The relative permeability has negative real part between magnetic resonance and plasma frequency, 11.36 GHz. The imaginary part is negative and minimum near the resonance frequency. Small amount of power is transmitted through SRR array due to high field attenuation. In addition, SRR cell has largest current distribution at this frequency due to high field concentration. This increases ohmic loss in the metallic parts. It is the natural consequence of field enhancement with accompanying high loss at the resonance frequency. The negative permeability frequency band is in the bandgap region of the dispersion diagram in Figure 3.13. On the other hand, relative permittivity is positive as expected. However, the imaginary part is positive between 9.2 GHz and 9.7 GHz. This is a nonphysical artifact for the passive materials. There are typically three main reasons for this unphysical effect. The first reason is the possible neglection of the effect of higher order modes excited by SRR. The higher order modes are exponentially decaying evanescent fields. Even though no real power is transported by the evanescent waves, the total reactive power in the near field has effect on the reactive part of Z parameters. The second reason is the neglection of reactive intercoupling of each cell with the adjacent cell by higher order modes even though the longitudinal cell periodicity is taken into account. This is the common point, which is lacking in alternative retrieval procedures [57-59]. The third reason is although the cell size is smaller than the operation wavelength, the wavelength to cell size ratio is not sufficiently large to regard SRR array as an ideal homogeneous material.

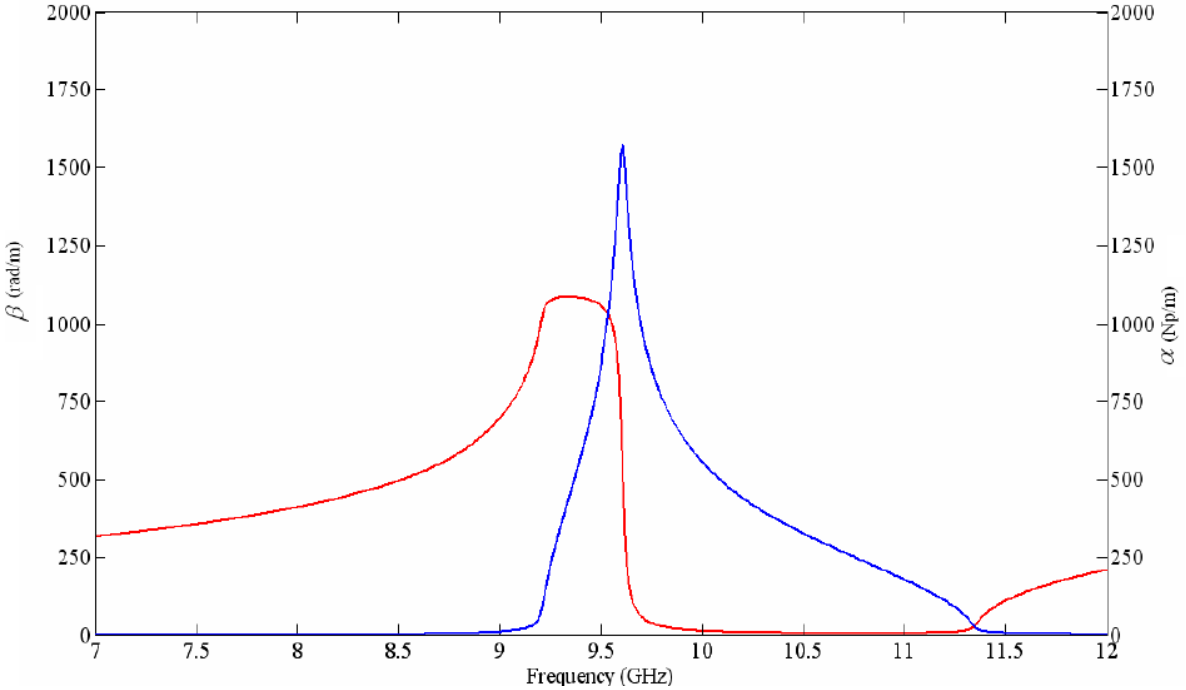

Figure 3.14c. Attenuation (blue) and phase (red) constant of SRR periodic array

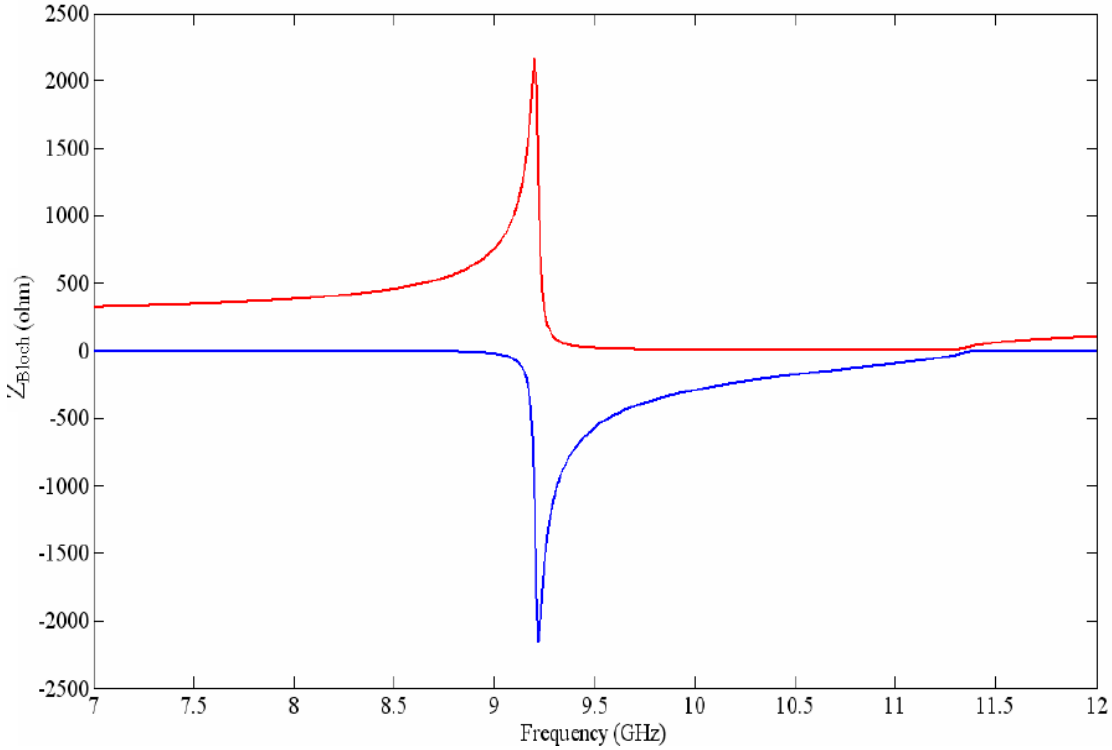

Figure 3.14d. Real (red) and imaginary (blue) part of wave impedance of SRR periodic array

In Figure 3.14c, the attenuation constant is positive between 9.22 GHz and 11.36 GHz. It corresponds well with the bandgap region of dispersion diagram in Figure 3.13. In addition, this frequency band coincides with the negative permeability band. The wave attenuation is maximum at 9.7GHz, which is the frequency of minimum negative permeability in Figure 3.14a. The wave impedance is capacitive in the bandgap region. Therefore, the field transmission is highly degraded due to wave attenuation and high reflection resulting from the impedance mismatch. On the other hand, SRR array responds to the exciting field as a high impedance surface at 9.2 GHz as shown in Figure 3.14d. This feature has a potential application in the design of high efficient directive antennas [4-6]. The reactive impedance in the negative permeability band can be implied from the wave impedance formulation of homogeneous materials

$$Z_{wave} = \sqrt{\frac{\mu_{eff}}{\varepsilon_{eff}}} = \sqrt{\frac{-|\mu_{eff}|}{\varepsilon_{eff}}} = -j\sqrt{\frac{|\mu_{eff}|}{\varepsilon_{eff}}} \quad . \tag{3.19}$$

As a result, analytical and numerical results prove the effective negative permeability of SRR array. However, effective material parameters can only be assigned to the composite materials if the unit cell size is much smaller than the wavelength. Therefore, it is important to investigate alternative designs for the miniaturization of unit cells for more homogeneous materials [3-4],[50-55]. In the next section, one electrically small negative permeability cell is proposed for the design of more homogeneous materials.

3.4 Fractal Spiral Resonator as Magnetic Metamaterial

As a further step in more homogeneous material realization, an artificial magnetic unit cell based on spiral fractal geometry is proposed [51]. The cell geometry is explained first in Section 3.4.1. The magnetic resonance is illustrated from the numerically calculated field pattern in Section 3.4.2. The effective permeability is analytically calculated from the numerical data. The dispersion diagram and Bloch impedance are illustrated in Section 3.4.3.

3.4.1 Structural Description

The unit cell is shown in Figure 3.15. The resonator is basically formed by connecting two fractal ring resonators in a spiral form. Upper half of the inner and outer rings is the mirror image of the lower half. It is in the form of first order Hilbert fractal. These two concentric rings are then connected at one end to obtain the spiral form. The marked inner section is the extension of the inner curve. It is important in order to decrease the resonance frequency due to inductive and capacitive coupling among the different sections. The substrate is 0.5 mm thick FR4 with dielectric constant 4.4 and tan(δ) 0.02. The metallization is copper. The copper line width and minimum distance between any two lines are 0.2 mm. The other geometrical parameters are L_1= 2.2mm, L_2= 0.8mm and L_3= lmm. The unit cell size is a_x= 5mm, a_y = 2mm, a_z = 5mm. Only one side of the substrate is structured with the prescribed fractal geometry.

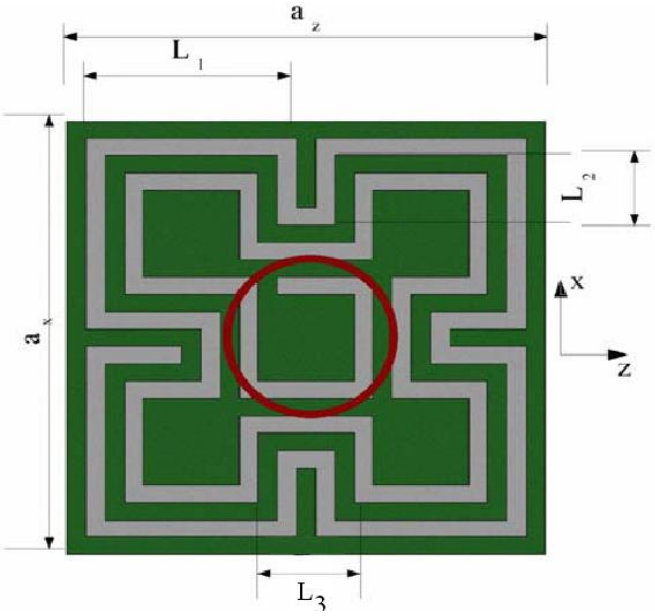

Figure 3.15 Geometry of a fractal spiral resonator

3.4.2 Simulation Results

In order to obtain the magnetic resonance, the fractal spiral resonator array has to be excited with out-of-plane directed magnetic field of the plane wave. Therefore, PEC at two x-planes and PMC at two y-planes are imposed at the edges of the unit cell. These boundary conditions are necessary to excite the array with x-direction polarized and z-direction propagating plane wave.

The numerically calculated S-parameters are shown in Figure 3.16. The resonance frequency is 1.52 GHz. The unit cell size is 1/40 of free space wavelength. Therefore, the composite material made up of fractal spiral resonators can be regarded as a more homogeneous material than SRRs-based materials. The magnetic field and surface current distribution at the resonance frequency are shown in Figure 3.17a and Figure 3.17b.

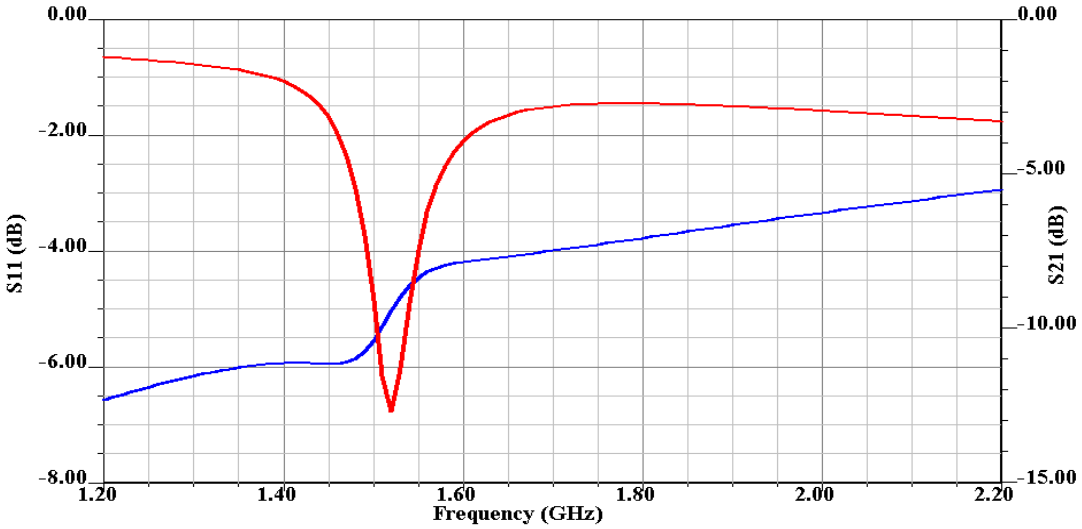

Figure 3.16 Transmission (red) and reflection (blue) parameters of fractal spiral resonator

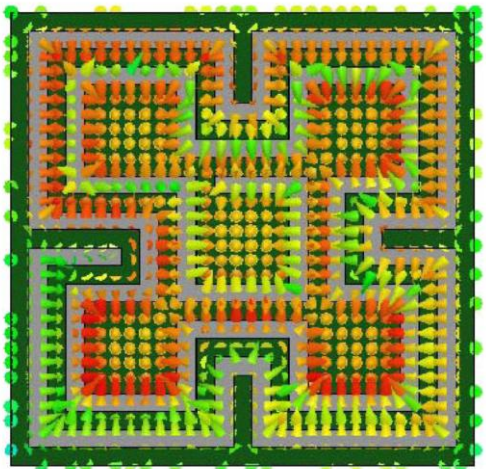

Figure 3.17a Magnetic field distribution of fractal spiral resonator at the resonance frequency

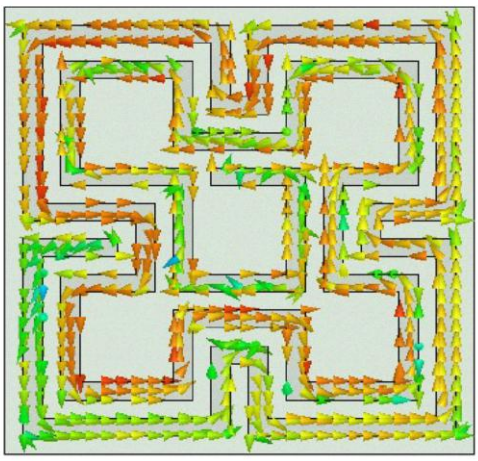

Figure 3.17b Surface current distribution of fractal spiral resonator at the resonance frequency

Due to the spiral form of surface current and resulting out-of-plane directed magnetic field, the magnetic resonance is confirmed. Therefore, this electrically small cell can be considered as a resonant magnetic dipole. The low transmission in Figure 3.16 is the result of demagnetization effect of resonant inclusion to the exciting magnetic field in the negative permeability band. This is the reason why this unit cell can be used in the realization of negative permeability materials.

3.4.3 Effective Parameters

As a next step, the effective material parameters are retrieved to confirm the negative permeability and justify the above-mentioned remarks. The extraction method explained in Section 3.3.3 is exploited to calculate the propagation constant, Bloch impedance and effective relative permeability. They are shown in Figure 3.18.

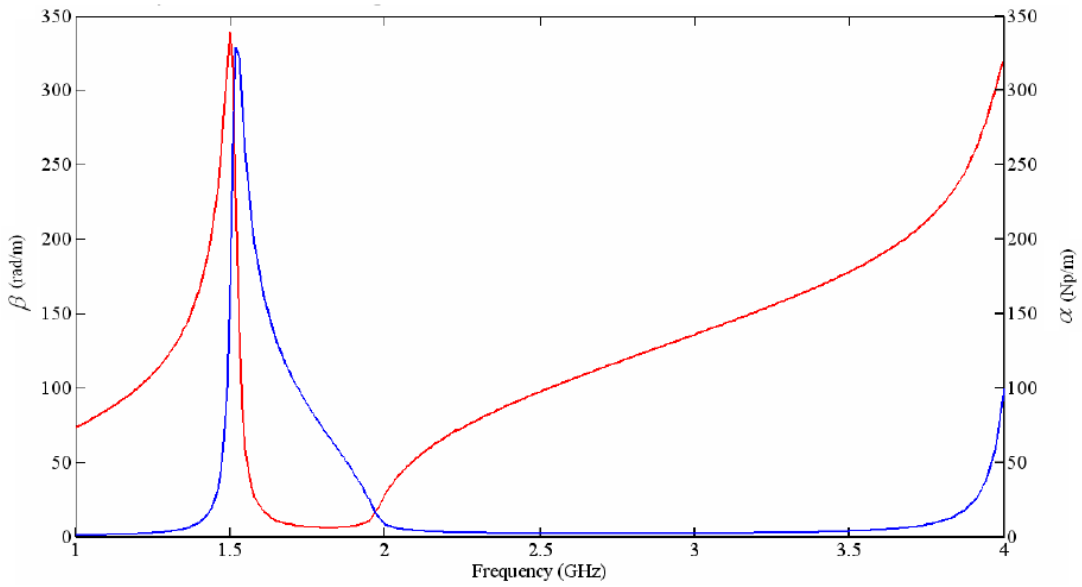

Figure 3.18a Phase (red) and attenuation (blue) constant of fractal spiral resonator array

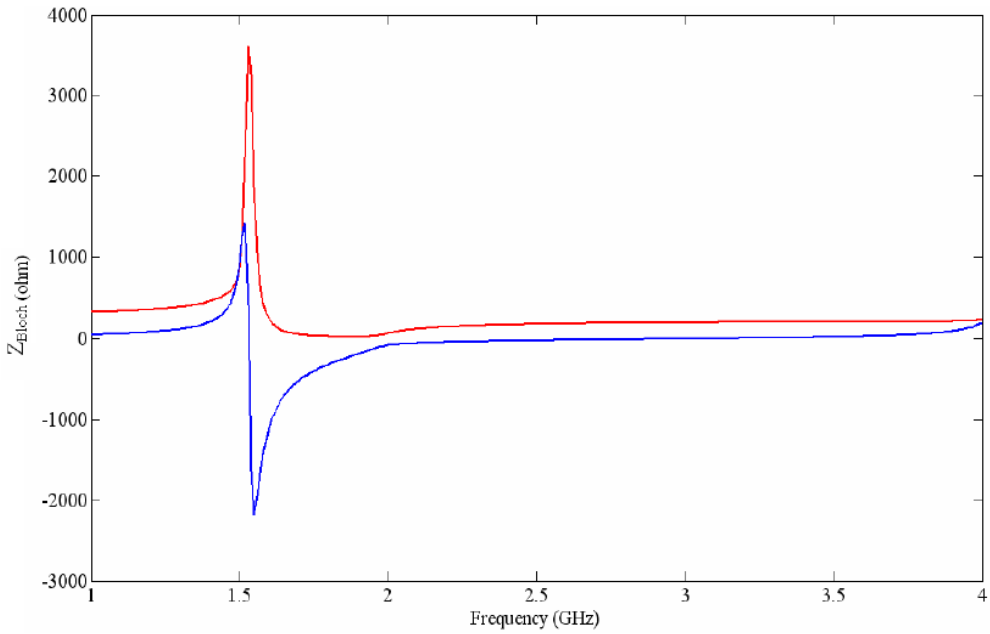

Figure 3.18b Real (red) and imaginary (blue) part of Bloch impedance of fractal spiral resonator array

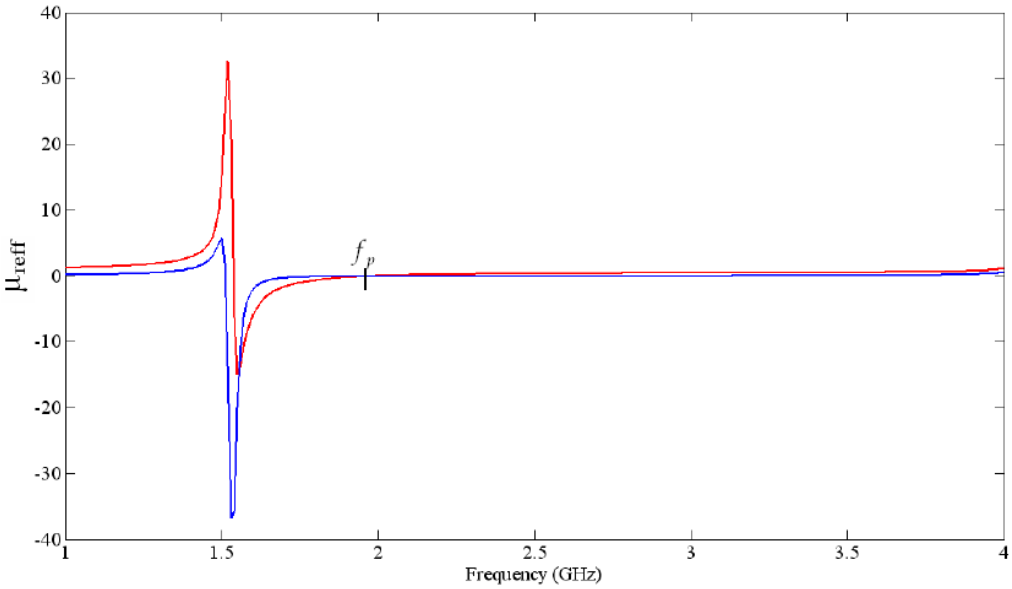

Figure 3.18c Real (red) and imaginary (blue) part of effective relative permeability of fractal spiral resonator array

In the frequency band of high field attenuation in Figure 3.18a, the wave impedance is capacitive as shown in Figure 3.18b. This bandgap region is between 1.52GHz and 1.95GHz. The wave impedance has its highest value at the lower edge of magnetic resonance frequency, 1.52GHz. The wave attenuation is therefore maximum at this frequency, which is the reason of lowest transmission in Figure 3.16. The reason of low transmission between 1.4 GHz and 1.52 GHz is the impedance mismatch resulting from increasing wave impedance rather than negative permeability. The magnetic resonance is also implied from Figure 3.18c. In Figure 3.18c, the fractal spiral resonator exhibits negative permeability between the resonance and plasma frequency, 1.96GHz. As a result, numerical simulations confirm the magnetic resonance and negative permeability.

3.5 Chapter Conclusion

In this chapter, the artificial magnetism obtained from periodic metallic cylinders and SRRs is explained to introduce the design approach of negative permeability materials. The effective permeability is analytically formulated for the plane wave excitation with axially directed magnetic field. The transmission and reflection parameters are calculated. The numerical calculations are additionally done to verify the analytical calculations. They are in good agreement. The effective permeability formulations are compared with the original formulations of Pendry. The analytical formulations in this chapter estimate the resonance frequency better than the analytical formulations of Pendry.

A typical SRR model is numerically analyzed. The transmission and reflection parameters are calculated. The surface current, electric and magnetic field distributions are presented. The main reason in the demagnetization of incoming magnetic field is the excitation of electrically small magnetic dipoles in the cells. They are formed from circular form of surface currents on the metallic rings. 1D Brillion diagram is numerically calculated. The bandgap region is determined. In the bandgap, the composite material has negative permeability and capacitive wave impedance. An alternative parameter retrieval method is proposed. It is based on the calculation of the effective material parameters of 3D array as a result of periodic continuation of one cell in the propagation direction by Bloch Theorem.

The effective material parameters, Bloch impedance and dispersion diagram are calculated.

At the end of the chapter, a unit cell based on fractal spiral resonator is proposed. It is numerically investigated in terms of effective permeability, Bloch impedance and complex propagation constant. The numerical calculations confirm the effectiveness of the resonant inclusion in the design of more homogeneous composite materials.

4. Negative Permittivity Metamaterials

4.1 Introduction

This chapter explains the basic principles of negative permittivity materials starting with the periodic wire array. This was originally proposed by Pendry [8,9]. The plasma-like permittivity response obtained from the periodic long wires is analytically calculated. This calculation is important to understand the fundamental principle of nonresonant electric depolarization in 2D. The effect of wire loading on effective permeability is also addressed. Alternative designs are also pointed out for more homogeneous realizations. The numerical calculations are conducted for a wire strip model structured on a low loss substrate as a microwave realization of negative permittivity materials. The effective material parameters are retrieved. 1D dispersion relation is studied to determine the plasma frequency and negative permittivity band. At the end of the chapter, a unit cell based on fractal antispiral resonator is proposed for the design of more homogeneous negative permittivity materials.

4.2 Theoretical Analysis

The response of natural materials to the electric field is determined by the permittivity. The electric permittivity quantifies the polarisability strength of molecules and atoms in the microscopic scale with the resulting dipole moment. The relative permittivity of natural dielectrics is positive and larger than 1. On the other hand, the relative permittivity of metals and dilute gases, plasmas can be negative. The electromagnetic response of metals is determined by the dissipation at low frequencies below infrared. The metals respond to the electromagnetic fields with the negative permittivity at the frequencies smaller than the plasma frequency [6],[8,9], which is in the visible and UV frequency regions. To achieve negative permittivity at lower frequencies in the microwave regime, periodic metallic wires are proposed by Pendry. It is shown in Figure 4.1 [8,9]. Pendry examined how the magnetic field of wire electrons increase the electron momentum in the wire array under plane wave excitation [8,9]. The larger electron momentum can be described by the larger effective mass of wire electrons. This larger effective mass reduces the plasma frequency from the range of UV to the microwave regime. However, in Pendry's formulation, the effective permittivity is calculated under the assumption of Drude type permittivity response without any high frequency field calculations. The generic form of Drude type permittivity is expressed in (4.1) with the plasma frequency, ω_p and dissipation factor, Γ

$$\varepsilon_r(\omega) = 1 - \frac{\omega_p^2}{\omega^2 - j\Gamma\omega} \ . \tag{4.1}$$

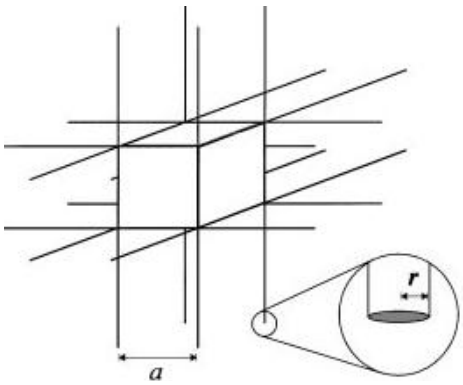

Figure 4.1. One unit cell of periodic structure composed of infinitely long wires in a simple cubic lattice [9]

In (4.1), the real part of relative permittivity is negative at the frequencies smaller than ω_p for small Γ. For larger Γ, the frequency at which the real part is zero, is calculated as

$$\omega_{new} = \sqrt{\omega_p^2 - \Gamma^2} \ . \tag{4.2}$$

In this section, the effective permittivity of periodic infinitely long wires of width w is calculated under plane wave excitation. This formulation is more generalized than Pendry's formulation [8,9]. The equivalent model to be used in the analytical calculation is shown in Figure 4.2.

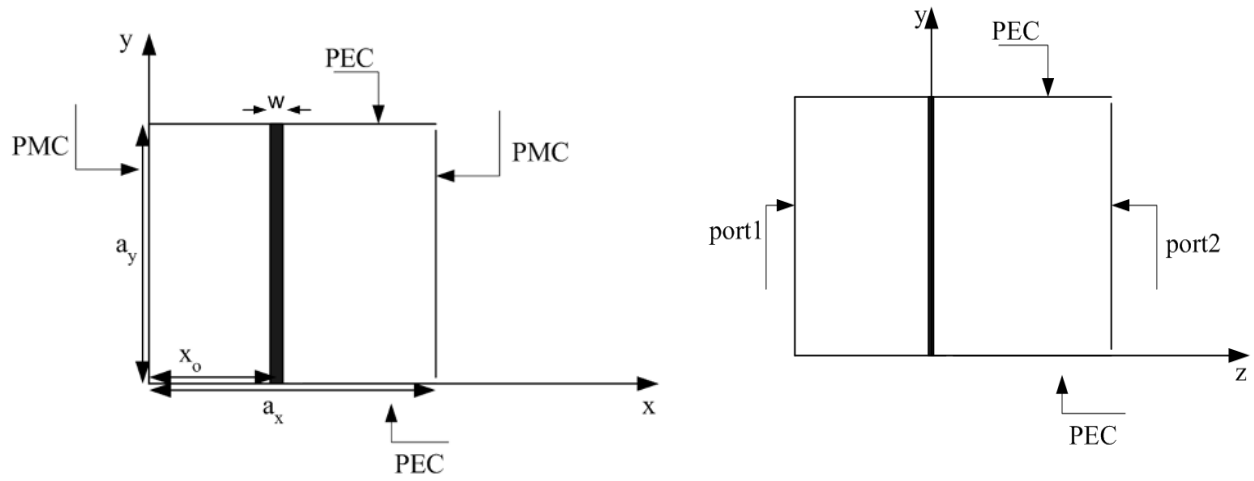

Figure 4.2. Excitation and boundary conditions of equivalent model of infinitely long wire array (a) on x-y plane (b) on y-z plane

In this model, PEC boundary conditions are imposed at two y-planes to extend the wire length to infinity. Because of infinite extension in y-direction and y-independency of the incoming wave, the scattering parameters, Bloch impedance, complex propagation constant and effective parameters are independent of the periodicity in y-direction, a_y. In a similar manner, PMC boundary conditions are imposed at two x-planes to excite the plane wave mode of PEC-PMC guiding medium. This boundary condition extends the wire strip periodically in x-direction. Thus, these boundary conditions model 1D wire array with one unit cell in the propagation direction. This array has to be excited by y-polarized z-direction propagating plane wave.

However, due to the material inhomogenity in x-direction, TE waves are also excited in addition to TEM wave. Therefore, TE wave components, which are y-independent, have to be calculated, as well. They are formulated as,

TE wave field components:

$$
\begin{aligned}
E_y^{TE} &= -A^{TE}\cos(k_x x)e^{-jk_z z} \\
H_x^{TE} &= A^{TE}\frac{k_z}{\omega\mu}\cos(k_x x)e^{-jk_z z} \\
H_z^{TE} &= jA^{TE}\frac{\left(k^2-k_z^2\right)}{\omega\mu k_x}\sin(k_x x)e^{-jk_z z}
\end{aligned}
\tag{4.3}
$$

The resulting field components can be described as the superposition of field components of incoming plane wave and all excited modes of TE wave. They are formulated for $z \leq 0$ as,

$$
\begin{aligned}
E_y^{TE} &= -\sum_{m=0,1,2,3\ldots} A_m^{TE}\cos(\frac{m\pi}{a_x}x)e^{jk_{zm}z} + E_0 e^{-jk_0 z} \\
H_x^{TE} &= -\sum_{m=0,1,2,3\ldots} A_m^{TE}\frac{k_{zm}}{\omega\mu}\cos(\frac{m\pi}{a_x}x)e^{jk_{zm}z} + \frac{-E_0}{Z_o}e^{-jk_0 z} \\
H_z^{TE} &= \sum_{m=0,1,2,3\ldots} jA_m^{TE}\frac{\left(k_o{}^2-k_{zm}^2\right)}{\omega\mu\frac{m\pi}{a_x}}\sin(\frac{m\pi}{a_x}x)e^{jk_{zm}z}
\end{aligned}
\tag{4.4}
$$

with $k_x = \frac{m\pi}{a_x}$, $k_{zm} = \sqrt{k_o^2 - \left(\frac{m\pi}{a_x}\right)^2}$ and $k_o = \frac{\omega}{c_0}$, where a_x is the cell size in x-direction.

In (4.4), the first terms are the field components excited by the current on the wire at z=0. The field components for *m*=0 are the plane wave components of the reflected wave. The second terms are the field components of incoming plane wave. To calculate the reflection coefficient, unknown modal constants, A_m^{TE} have to be determined. A_m^{TE}s can be calculated by setting the total electric field on the wire surface to zero. This boundary condition can be easily satisfied at one point on the wire instead of whole wire surface from x_o-w/2 to x_o+w/2 if w is much smaller than free space wavelength. Therefore, to take one point on the wire surface as the field calculation point is a sufficiently good approximation with negligible deviations in the calculated A_m^{TE}s. The relation between A_m^{TE}'s and E_o can then be obtained as

$$
A_0^{TE} + \sum_{m=1,2,3\ldots} A_m^{TE}\cos\left(\frac{m\pi}{a_x}(x_o + \frac{\mathrm{w}}{2})\right) = E_0 \quad . \tag{4.5}
$$

The reflection coefficient, R is defined as

$$
R = -\frac{A_0^{TE}}{E_0} \quad . \tag{4.6}
$$

An additional relation between A_o^{TE} and E_0 has to be derived to calculate R. This relation can be obtained if the wire current, I_{wire} is expressed in terms of A_m^{TE}. I_{wire} can be calculated from the tangential magnetic field at $x=x_0$ and $z=0$ as

$$\sum_{m=0,1,2,3...} 2A_m^{TE}\frac{k_z}{\omega\mu}\cos(\frac{m\pi}{a_x}x) = I_{wire}\delta(x-x_o)\,. \tag{4.7a}$$

In the above expression, the current distribution is assumed to be concentrated at $x=x_0$. A_m^{TE}'s can be calculated from (4.7a) by the infinite series expansion of the current distribution in terms of modal magnetic field as

$$A_m^{TE} = I_{wire}\cos(\frac{m\pi}{a_x}x_o)\frac{\omega\mu}{a_x k_{zm}} \qquad \text{m=1,2,3...}$$
$$A_0^{TE} = \frac{I_{wire}}{2}\frac{\omega\mu}{a_x k_0}\quad . \tag{4.7b}$$

By the substitution of A_m^{TE}'s in (4.7b) into (4.5), I_{wire} can be calculated in terms of E_0 in addition to R as

$$I_{wire} = \frac{\frac{E_0 a_x}{\omega\mu}}{\frac{1}{2k_0} + \sum_{m=1,2,3...}\frac{\cos\left(\frac{m\pi}{a_x}x_o\right)\cos\left(\frac{m\pi}{a_x}(x_o+\frac{w}{2})\right)}{\sqrt{k^2-\left(\frac{m\pi}{a_x}\right)^2}}} \tag{4.8a}$$

$$R = \frac{-1}{1+\sum_{m=1,2,3...}\frac{2k_0\cos\left(\frac{m\pi}{a_x}x_o\right)\cos\left(\frac{m\pi}{a_x}(x_o+\frac{w}{2})\right)}{\sqrt{k_0^2-\left(\frac{m\pi}{a_x}\right)^2}}}. \tag{4.8b}$$

After the calculation of R, an equivalent circuit model can be built for the wire loaded PEC-PMC guiding medium. As implied from Figure 4.2, the equivalent circuit can be conveniently modeled as two transmission line sections of length, $\frac{a_z}{2}$ loaded with a shunt inductance, L_{wire}. It is shown in Figure 4.3.

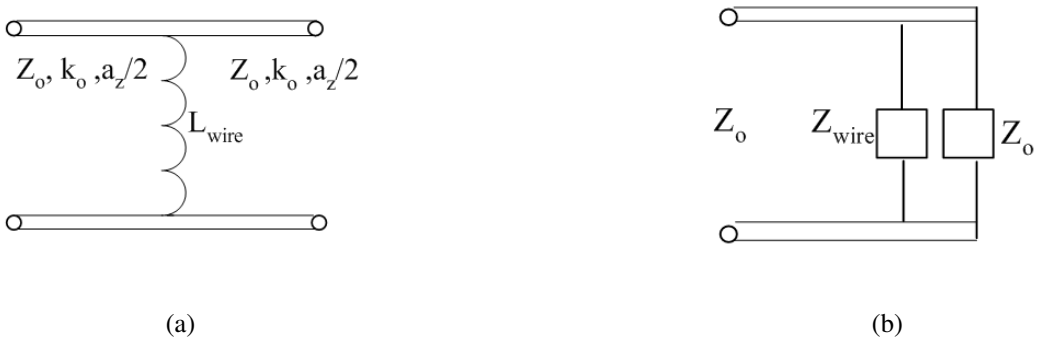

Figure 4.3. (a) Equivalent circuit and (b) impedance model of one cell thick long wire array

k_o and Z_0 are the free space propagation constant and wave impedance, respectively. The wire inductance per unit length is calculated from the equivalent impedance in Figure 4.3b as

$$L_{wire} = -\frac{Z_o}{j\omega a_y}\frac{(1+R)}{2R} \quad . \tag{4.9}$$

In order to validate the equivalent circuit model, the transmission and reflection parameters of wire array are numerically calculated. The model is shown in Figure 4.4 with the boundary conditions. The important issue in the analytical modeling is that two successive wire elements do not have to be equally spaced in x-direction. However, in the original work of Pendry, the wires are equally spaced in 2D array [8,9]. In addition, the above analytical modeling allows two wires to be located inside the same cell in a more generalized form.

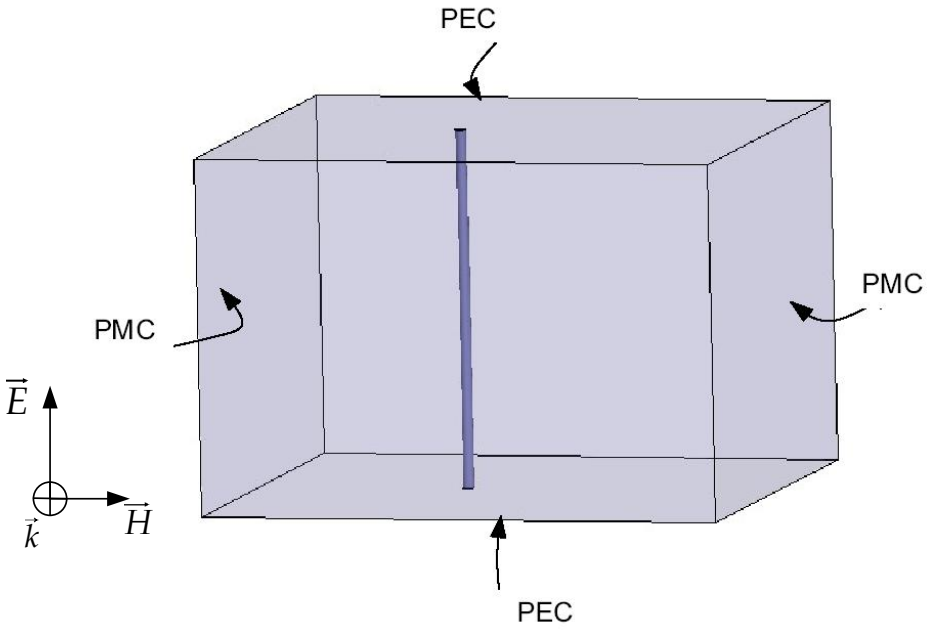

Figure 4.4. Numerical model of infinitely extended wire array with PEC and PMC boundary conditions

In the model, the wire radius is 0.05 mm. The wire is located at a separation distance of 2 mm from the left PMC wall. The separation distance of two PMC walls is 5 mm. The wire length between two PEC walls is 2.8 mm. The cell size in the propagation direction is 5mm. In the modeling, the cutoff frequency of first propagating TE mode has to be larger than the largest frequency in the interested band. This condition imposes the cell size to be smaller than the operation wavelength. This is an important requirement to fulfill the effective homogeneity condition. The numerically calculated scattering parameters are compared with the analytical calculations. The results are shown in Figure 4.5. The agreement is very good. The wire inductance per unit length is also calculated. It is shown in Figure 4.6.

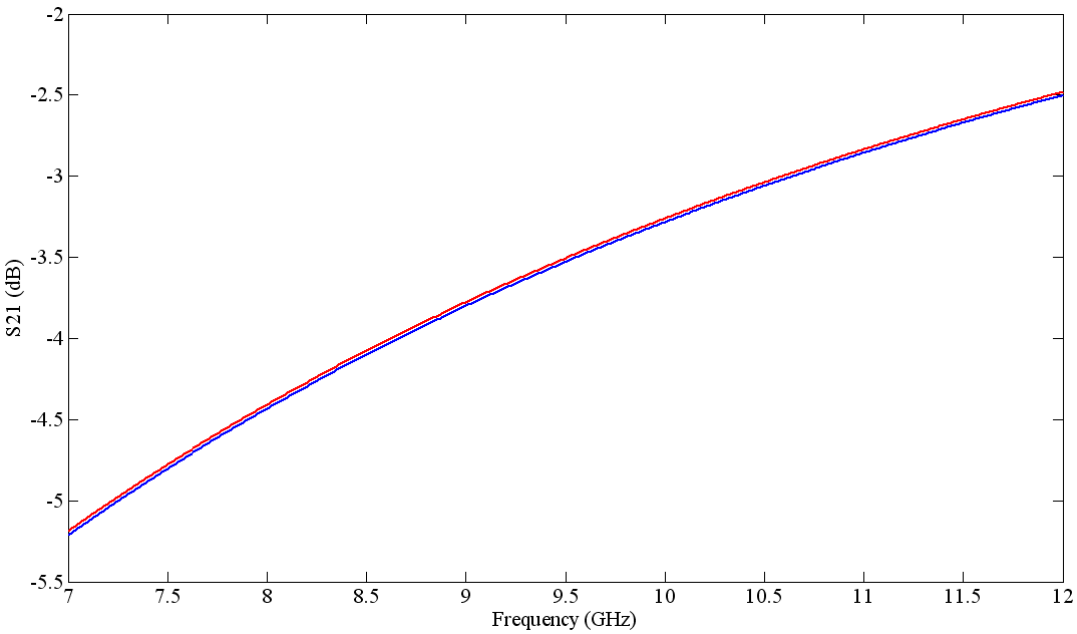

Figure 4.5a. Magnitude of analytically (red) and numerically(blue) calculated transmission parameters

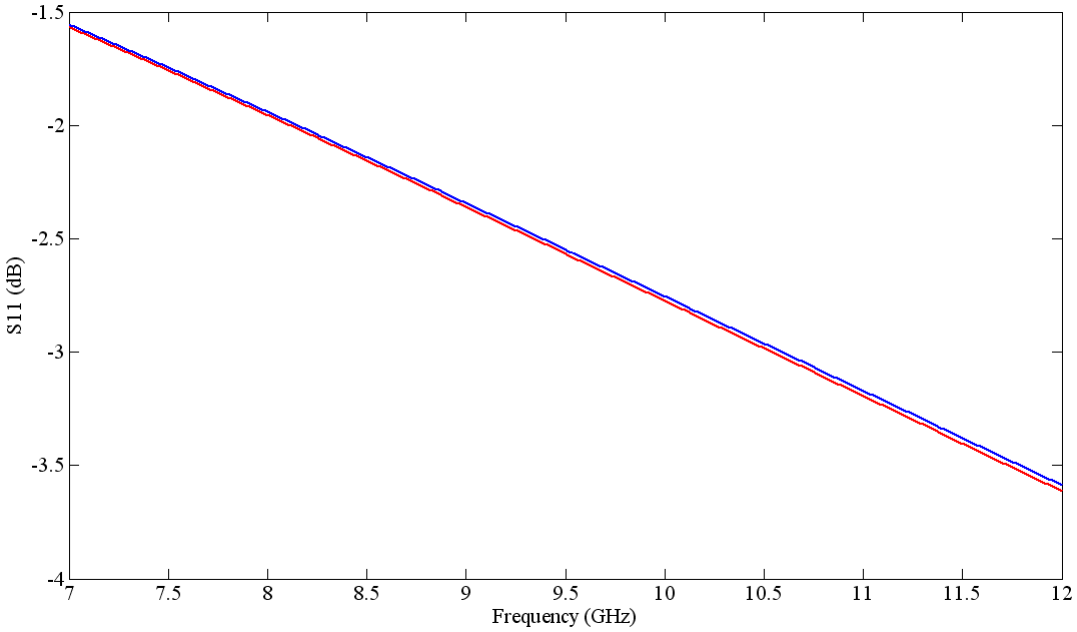

Figure 4.5b. Magnitude of analytically (red) and numerically(blue) calculated reflection parameters

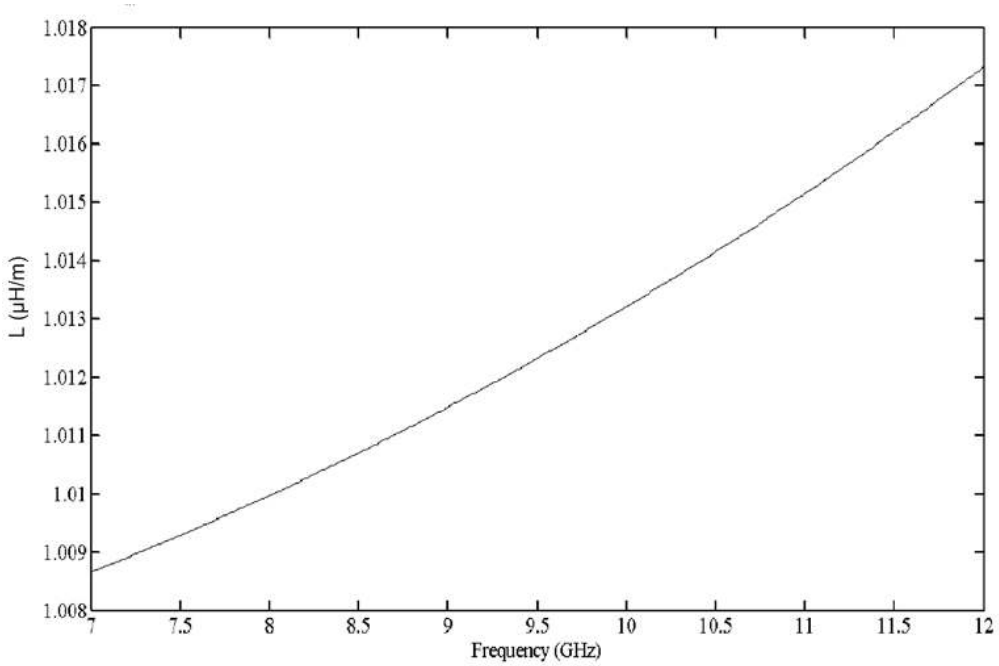

Figure 4.6. Analytically calculated per-unit-length inductance of wire array

In Figure 4.6, the inductance is approximately constant as expected with a maximum change smaller than 1%. This result confirms the validity of the wire modeling with the equivalent circuit in Figure 4.3. However, there is no periodicity in the propagation direction. Therefore, this 1D wire array has to be extended periodically in the propagation direction for 2D wire array modeling. To retrieve the effective material parameters of 2D wire array, the equivalent ABCD matrix of the unit cell in Figure 4.3 has to be calculated. ABCD matrix of transmission line section of length $a_z/2$ is expressed as

$$M_{ABCD\_trline} = \begin{bmatrix} \cos(k_o \frac{a_z}{2}) & jZ_0 \sin(k_o \frac{a_z}{2}) \\ j\frac{\sin(k_o \frac{a_z}{2})}{Z_0} & \cos(k_o \frac{a_z}{2}) \end{bmatrix}. \tag{4.10a}$$

ABCD matrix of L_{wire} is expressed as

$$M_{ABCD\_shuntL} = \begin{bmatrix} 1 & 0 \\ -j\frac{1}{\omega L} & 1 \end{bmatrix}. \tag{4.10b}$$

Therefore, the ABCD matrix of one wire cell is calculated as in (4.10c) with the matrix elements in (4.10d)

$$M_{ABCD\_cell} = \begin{bmatrix} \cos(k_o \frac{a_z}{2}) & jZ_0 \sin(k_o \frac{a_z}{2}) \\ j\frac{\sin(k_o \frac{a_z}{2})}{Z_0} & \cos(k_o \frac{a_z}{2}) \end{bmatrix} \begin{bmatrix} 1 & 0 \\ -j\frac{1}{\omega L} & 1 \end{bmatrix} \begin{bmatrix} \cos(k_o \frac{a_z}{2}) & jZ_0 \sin(k_o \frac{a_z}{2}) \\ j\frac{\sin(k_o \frac{a_z}{2})}{Z_0} & \cos(k_o \frac{a_z}{2}) \end{bmatrix} \tag{4.10c}$$

$$M_{ABCD\_cell} = \begin{bmatrix} A & B \\ C & D \end{bmatrix}$$

$$\begin{aligned} A &= \cos^2(k_o a_z / 2) + \frac{Z_o}{2\omega L}\sin(k_o a_z) - \sin^2(k_o a_z / 2) \\ B &= jZ_o \sin(k_o a_z) + j\frac{Z_0^2}{\omega L}\sin^2(k_o \frac{a_z}{2}) \\ C &= j\frac{1}{Z_o}\sin(k_o a_z) - j\frac{1}{\omega L}\cos^2(k_o \frac{a_z}{2}) \\ D &= A \end{aligned} \tag{4.10d}$$

The complex propagation constant, $\gamma_{per} = \alpha + j\beta$ follows from Bloch theorem together with (4.10c) as

$$\cos(k_o a_z) + \frac{Z_o}{2\omega L}\sin(k_o a_z) = \cosh(\gamma_{per} a_z) \ . \tag{4.11a}$$

where α and β are the attenuation and phase constants, respectively. a_z is the cell period in the propagation direction.
The Bloch impedance is then calculated in the form of

$$\begin{aligned} Z_{Bloch} &= \frac{Be^{-\gamma_{per} a_z}}{-Ae^{-\gamma_{per} a_z} + 1} \\ Z_{Bloch} &= \frac{\left(jZ_o \sin(k_o a_z) + j\frac{Z_0^2}{\omega L}\sin^2(k_o \frac{a_z}{2}) \right) e^{-\gamma_{per} a_z}}{-\left(\cos(k_o a_z) + \frac{Z_o}{2\omega L}\sin(k_o a_z) \right) e^{-\gamma_{per} a_z} + 1} \ . \end{aligned} \tag{4.11b}$$

The effective relative permittivity and permeability are calculated from Bloch impedance and complex propagation constant as in Section 3.3.3. They are shown in Figure 4.7 along with Bloch impedance and complex propagation constant.

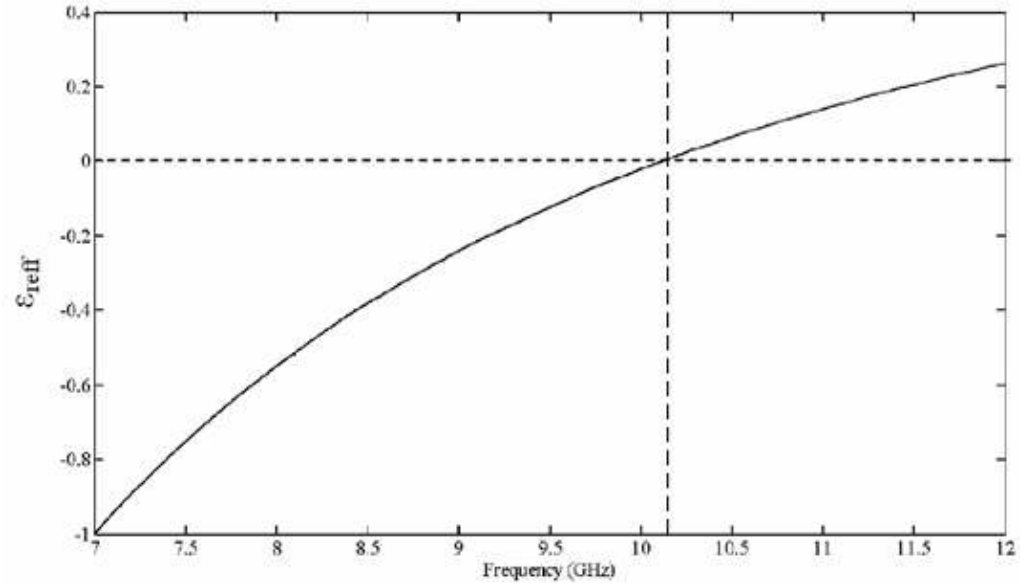

Figure 4.7a Effective relative permittivity of analytically calculated periodic wire array

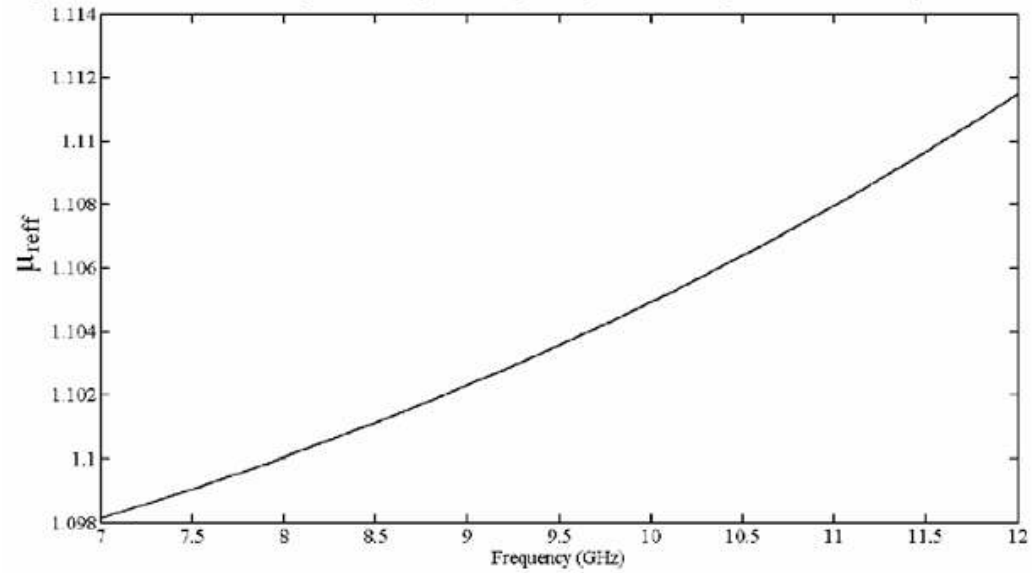

Figure 4.7b Effective relative permeability of analytically calculated periodic wire array

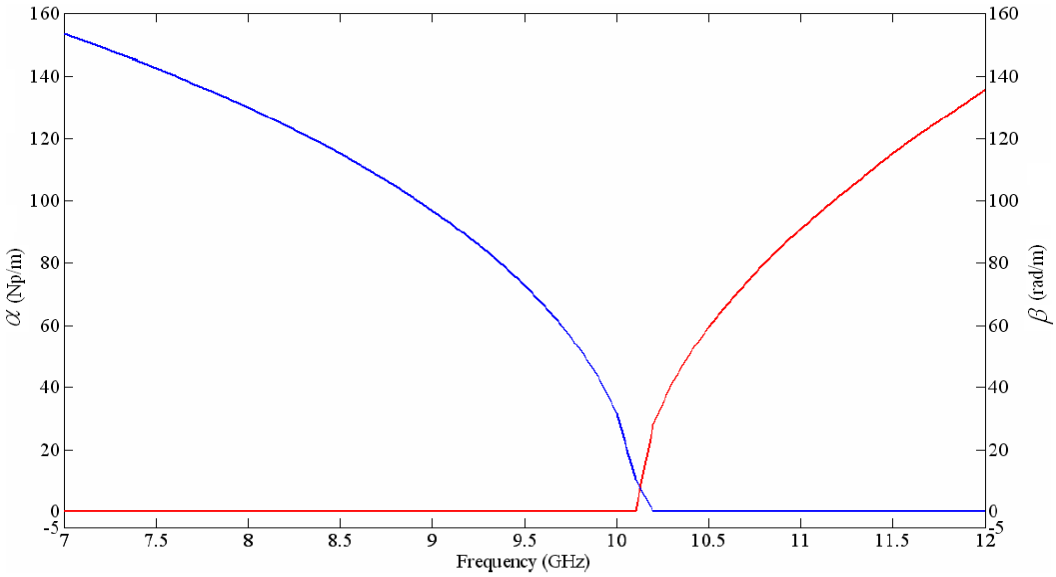

Figure 4.7c Attenuation (blue) and phase constant (red) of analytically calculated periodic wire array

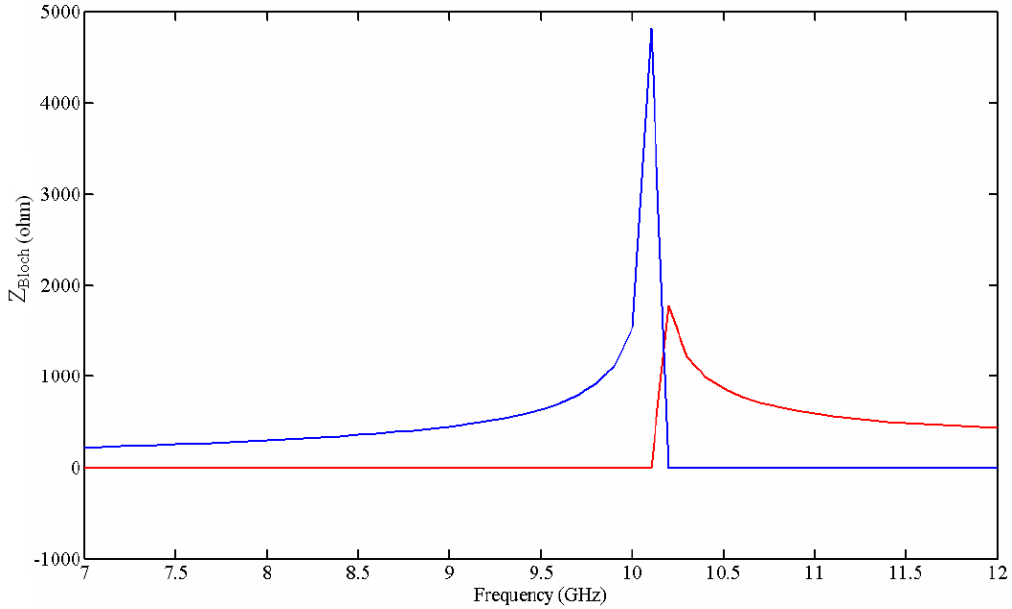

Figure 4.7d Real (red) and imaginary (blue) part of Bloch impedance of analytically calculated periodic wire array

In Figure 4.7a, the wire array exhibits Drude type permittivity response as in dilute plasmas and metals. The plasma frequency is 10.11 GHz. The part of the dielectric loss due to metallic loss is neglected in the analytical modeling. On the other hand, the relative permeability is positive as expected and approximately 1.106. It is larger than 1 due to the inductive loading of shunt wires between two PEC surfaces. In Figure 4.7c, the attenuation constant is positive below the plasma frequency as expected. This is the band of high field attenuation with low transmission. The incoming wave is also reflected due to the inductive wave impedance shown in Figure 4.7d. For the higher frequencies than the plasma frequency, the wire array is a frequency dispersive transmission medium as shown in Figure 4.7c. This can also be implied from the nonlinear dependence of γ_{per} on the frequency in (4.11a). However, it tends to be less dispersive at higher frequencies due to the reducing effect of inductive loading with increasing frequency. There is one important issue in the wire array modeling. The pure inductive modeling of wire loading in Figure 4.3 is an approximation with a maximum change smaller than 1%. Due to frequency dependency of inductance, the shunt impedance has to be modeled with the insertion of a capacitance in parallel with the inductance to take the frequency dependence as in Fig. 4.6 into account [4-6].

For the realization of negative permittivity materials, the wire array has to be long enough to have similar electromagnetic response of infinitely long array. However, Lorentzian type permittivity response is obtained instead of Drude type response due to finite wire length. In this case, the wire length is then comparable with the wavelength. Because the effective homogeneity condition is invalidated, electromagnetic properties of such artificial materials change according to the block size in the transversal and longitudinal directions. This causes important dispersion and application problems in the composite materials made up of these unit cells. Therefore, some more homogenous alternatives are also introduced such as meander line or its modified forms and fractal based designs. They are valid design strategies to obtain more homogeneous designs [4-6],[61,62]. An intuitive approach in the cell miniaturization is the use of complementary designs of negative permeability materials by invoking the concept of duality and complementarity [3-6]. The complementary SRR (CSRR) is the negative image of SRR.

It is structured as the slotted form of SRR by etching the slots in the ground plane or in the conductor strip of the transmission line [3]. The magnetic dipole of negative permeability materials is replaced by the electric dipole of negative permittivity materials [3]. Multiple slotted circular or rectangular rings and fractal resonators are well-known complementary modifications of SRRs to design negative permittivity materials [51-53],[63].

4.3 Numerical Simulations

4.3.1 Frequency Response of a 1D Wire Array

In this section, the scattering parameters of one cell thick sample are numerically calculated under plane wave excitation. The unit cell and imposed boundary conditions are shown in Figure 4.8. The geometrical parameters are tabulated in Table 4.1.

(a) (b)

Figure 4.8. (a) One unit cell of wire strip geometry (b) boundary conditions imposed on the edges of one unit cell

Table 4.1. Geometrical parameters of one unit cell of periodic wire array

Geometrical Parameters	mm
Wire width	0.2
Wire length (a_y)	2.8
a_x	2.8
a_z	2

PEC and PMC are imposed on two y- and z-planes, respectively. The wire array can then be excited by y-polarized x-direction propagating plane wave under these boundary conditions. The substrate is 0.5mm thick Rogers/RT duroid 5870 with the relative permittivity of 2.33 and tan(δ) 0.0012. The transmission and reflection parameters are shown in Figure 4.9.

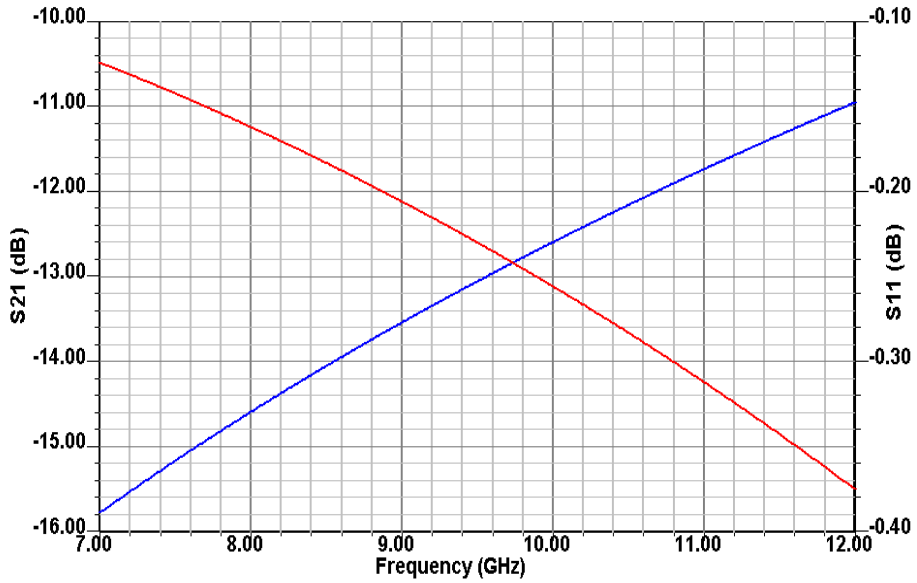

Figure 4.9 Reflection (red) and transmission (blue) parameters of one unit cell thick wire array

They have quite similar frequency dependence as the theoretical results in Figure 4.5. As shown in Figure 4.10a, there is no resonant current distribution. Therefore, PEC boundary condition extends the unit cell infinitely in y-direction to model the wires with no y-dependence. This 1D array can only have higher transmission in the same frequency band if it is extended in the propagation direction as 2D array. For this case, the transmission peaks are resulting from the periodic arrangement in the propagation direction. The resonance wavelength is therefore comparable with the cell period, which makes the effective homogeneity condition invalid. This causes the material parameters to be dependent on the number of cells in the propagation direction.
As stated in Section 4.2, the wire strip loads the guiding medium inductively. This results accordingly the effective permittivity to be negative. These are the main reasons why there is low transmission through the wire medium as shown in Figure 4.9. The magnetic field, electric field and surface current distribution at 9.6 GHz are shown in Figure 4.10.

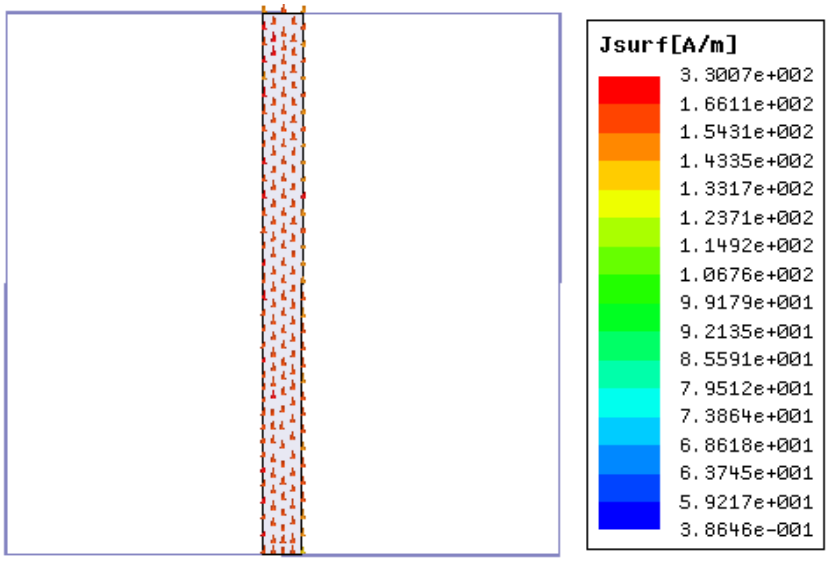

Figure 4.10a. Surface current distribution of one unit cell at 9.6 GHz

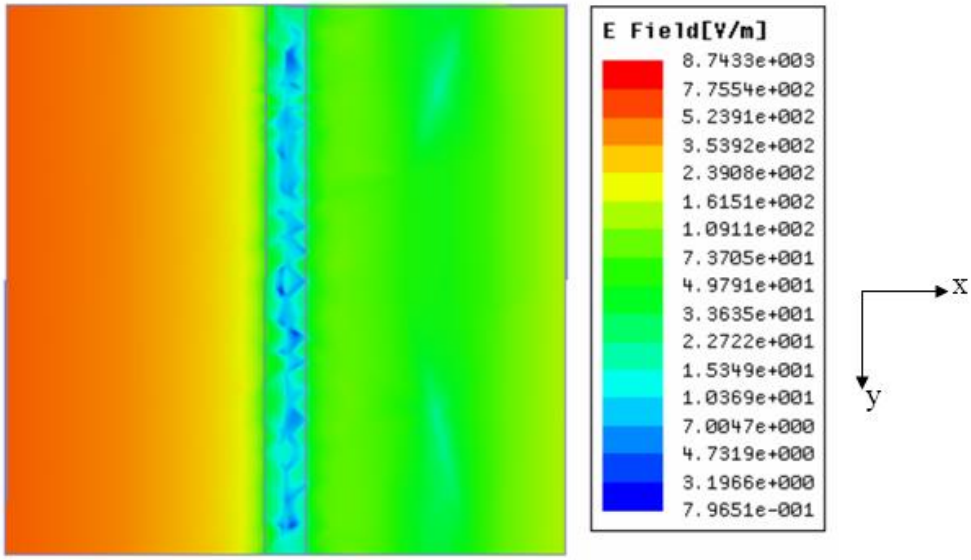

Figure 4.10b. Magnitude of electric field distribution of one unit cell at 9.6 GHz

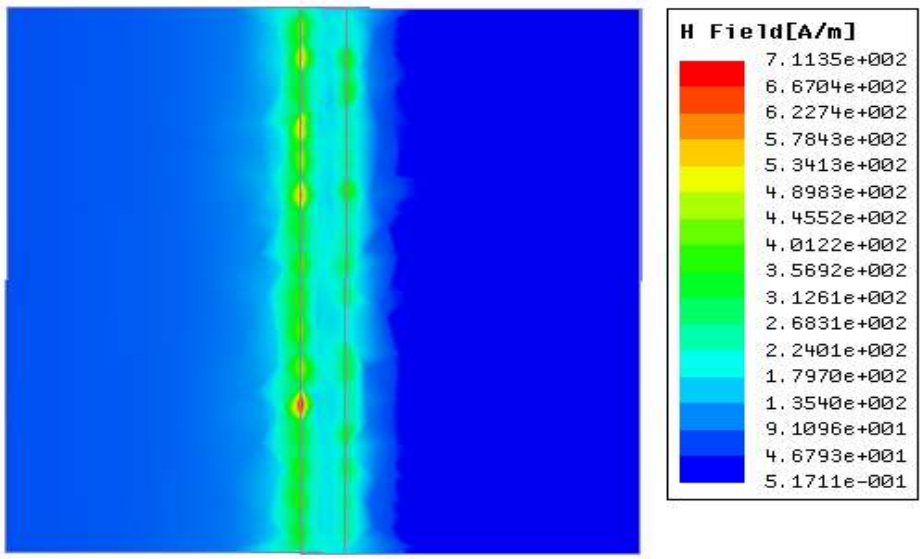

Figure 4.10c. Magnitude of magnetic field distribution of one unit cell at 9.6 GHz

The field distributions are calculated at 9.6 GHz. It is because 9.6 GHz is the frequency at which minimum negative permeability of SRR array is analytically retrieved in Section 3.3.3. In the next chapter, it is confirmed that 9.6 GHz is in the LH band where negative permittivity of wire and negative permeability of SRR array are simultaneously obtained.
As in Chapter 3, the effect of electric and magnetic coupling between the neighboring cells on the plasma frequency has to be figured out. This study is important in order to engineer the effective material parameters with different coupling levels. The shift of plasma frequency to lower frequencies can be deduced from how effectively the plane wave is transmitted. It is because the wave has a higher attenuation for a higher plasma frequency. Therefore, the transmission parameter of one cell thick sample with different periodicities in the transversal directions is numerically calculated. There is no effect of electric coupling among the cells in y-direction as expected. The magnetic coupling among the cells in z-direction has an important effect due to the dependence of plasma frequency on cell periodicity. As in the analytical formulations [8,9], the plasma frequency decreases with increasing wire separation in z-direction.

4.3.2 Dispersion Relation of Periodic Wire Array

As a next step, the eigenfrequencies of one cell with periodic boundary conditions of different phase shifts in the propagation direction are numerically calculated. The PEC and PMC on the transversal y- and z-planes are imposed as in Figure 4.8. 1D dispersion diagram of first two bands is shown in Figure 4.11. In Figure 4.11, there is no transmission through wire medium in the frequency band of 7-12 GHz. The incoming field is attenuated due to the negative permittivity and reflected due to the resulting inductive wave impedance. This remark will be confirmed from the effective material parameters to be retrieved in the next section. On the other hand, there is one important issue to be explained about the eigenmode calculation. In the eigenmode calculation, all propagating modes are taken into account to satisfy the phase shift along the propagation direction. Therefore, also higher TE and TM modes are present in the high frequency band. This is the reason why Brillouin diagram tends to be smoother for the phase shifts larger than 140° in the first band. These are frequencies at which higher order modes with y-dependence are propagating, which is not physically true for infinitely long wires.

However, the calculated eigenfrequencies and modes are correct. In other words, this is a modeling artifact due to the finite cell size in y-direction for the frequencies higher than the lowest cutoff frequency of PEC-PMC medium. This problem can be solved by decreasing the cell size in y-direction or taking the frequencies in the second band as the extension of the first band. In addition, the wire medium exhibits left-handed (LH) behavior for the phase shifts larger than 150° in the first band. This is because of the capacitive coupling of successive cells in the propagation direction under the excitation of higher order modes.

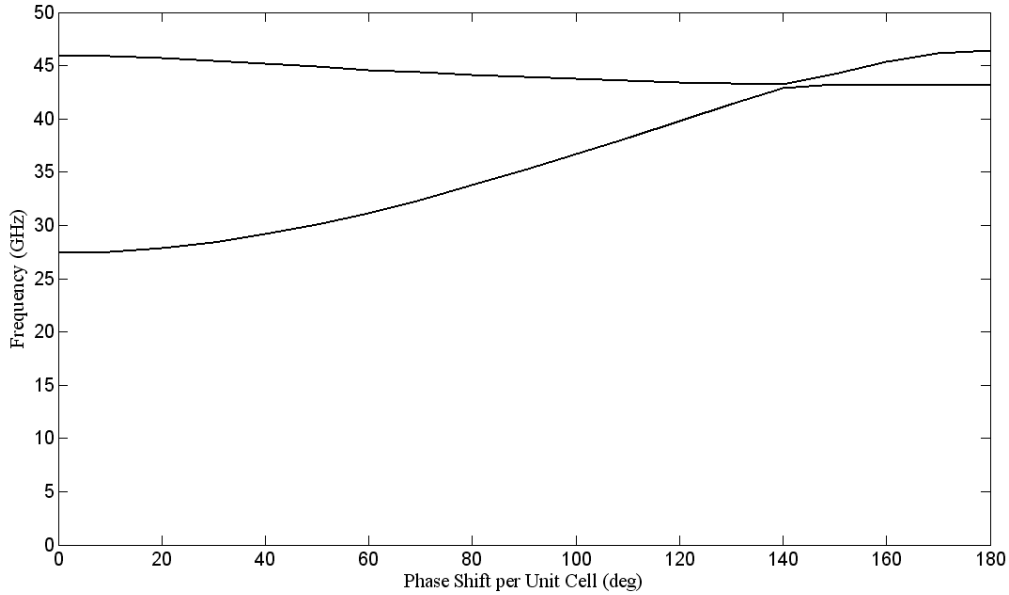

Figure 4.11 Dispersion diagram of wire strip with periodic boundary conditions of different phase shifts in propagation direction

4.3.3 Effective Parameters of Periodic Wire Array

In this section, the effective relative permittivity and permeability are retrieved to confirm the negative permittivity and positive permeability. The retrieval procedure in Section 3.3.3 is implemented. The effective material parameters, complex propagation constant and characteristic impedance are shown in Figure 4.12.

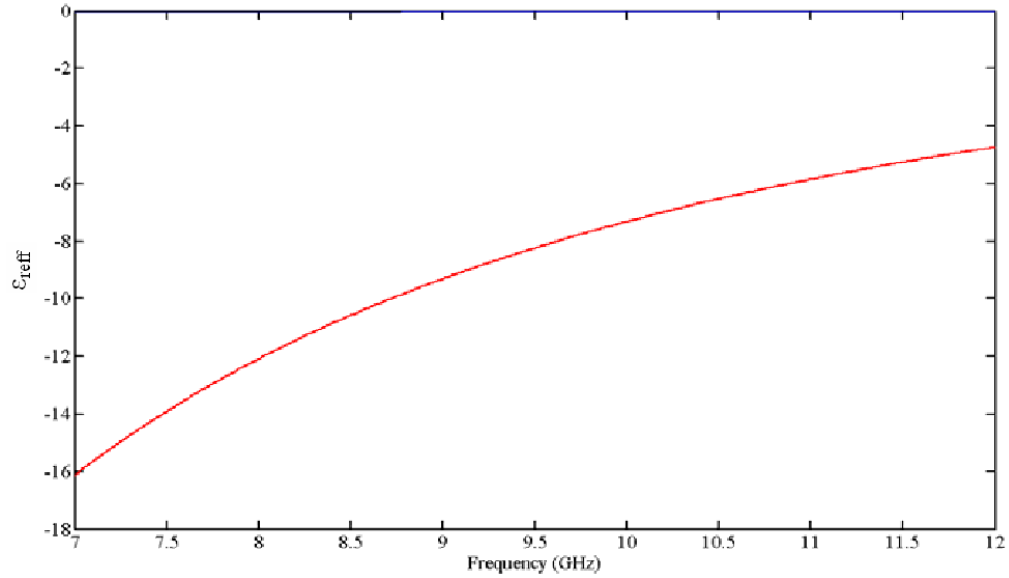

Figure 4.12a. Real (red) and imaginary (blue) part of effective relative permittivity of periodic wire array

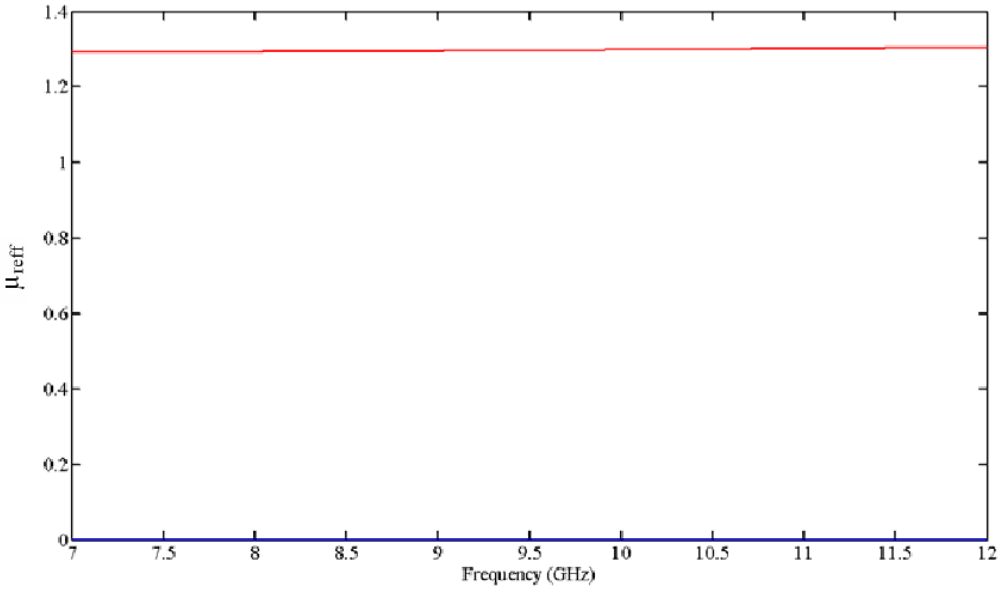

Figure 4.12b. Real (red) and imaginary (blue) part of effective relative permeability of periodic wire array

In Figure 4.12a, the wire array exhibits Drude type permittivity response. The relative permittivity has negative real part in the frequency band of 7-12 GHz. The imaginary part is negligibly small in comparison to the real part. It is in the range of 0.05. The plasma frequency can be estimated with an approximate calculation. The relative permittivity values in Figure 4.12a can be fit analytically into Drude type permittivity formulation in (4.1). This analytic formulation estimates the plasma frequency as 28.56GHz. The lowest frequency of the first band in Figure 4.11 corresponds quite well with this estimated frequency. On the other hand, relative permeability is positive. The magnetic loss is in the range of 8.10^{-4}. The real part is greater than 1 and approximately 1.3. It is because of the inductive loading of the wire strip as explained in Section 4.2.

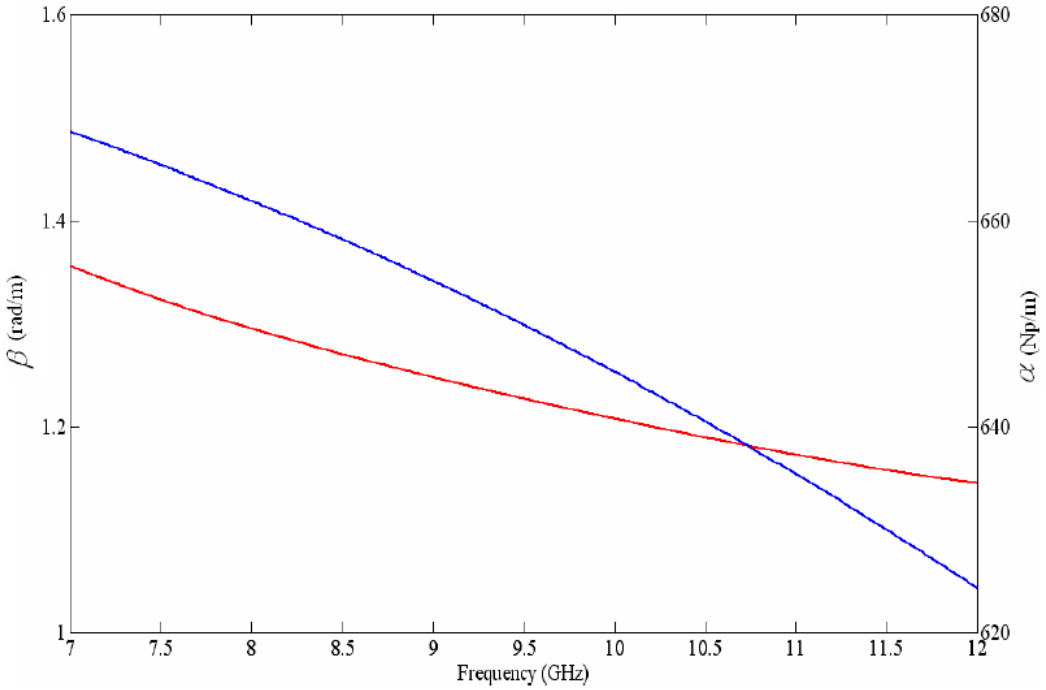

Figure 4.12c. Attenuation (blue) and phase (red) constant of periodic wire array

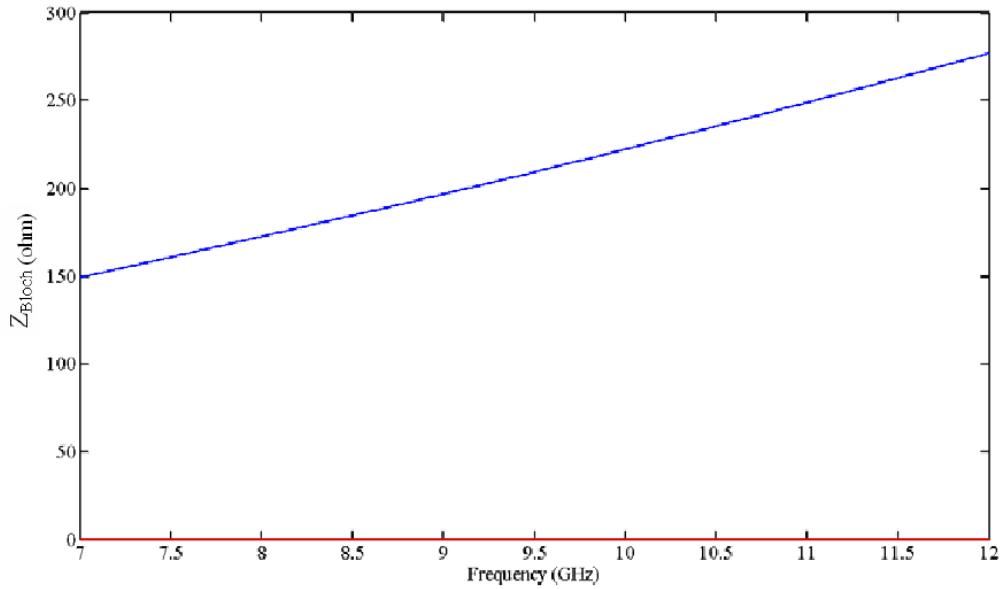

Figure 4.12d. Real (red) and imaginary (blue) part of wave impedance of periodic wire array

The wave impedance is inductive with a negligible resistive part in the range of 0.25Ω. Thus, the field transmission is highly degraded due to the wave attenuation and reflection resulting from the impedance mismatch at the port. As a result, the numerical and analytical results prove effective negative permittivity of wire array.
In the next section, a special negative permittivity cell is proposed. This design illustrates how to decrease the effect of material inhomogenity with electrically small cell sizes. To investigate such alternative designs for miniaturized cells is an important task in artificial material design.

4.4 Fractal Anti-Spiral Resonator as Dielectric Metamaterial

In this section, a unit cell based on fractal spiral resonator is proposed for the design of negative permittivity materials [62]. The cell geometry is explained at first. The electric resonance is illustrated from the numerically calculated field pattern. The effective permittivity is calculated from the numerical data in addition to the complex propagation constant and Bloch impedance.

4.4.1 Structural Description

The geometry of one unit cell is shown in Figure 4.13. The red marked section is a second order fractal Hilbert curve with modified side length ratio. It is surrounded closely with another Hilbert curve in order to decrease the resonance frequency by capacitive coupling inbetween. The design is similar to the magnetic metamaterial in Section 3.4. The important difference is how first half of Hilbert curve is connected with the second half. The second half is the mirror image of the first half. The substrate material is 0.5 mm thick FR4 with dielectric constant 4.4 and tan(δ) 0.02. The metallization is copper. The copper line width and minimum distance between any two lines are 0.2 mm. The other geometrical parameters are L1 = 0.6 mm, L2 = 2 mm and L3 = 2 mm. The unit cell size is a_x = 2 mm, a_y = 5 mm, a_z = 5 mm. Only one side of the substrate is structured with the prescribed fractal geometry.

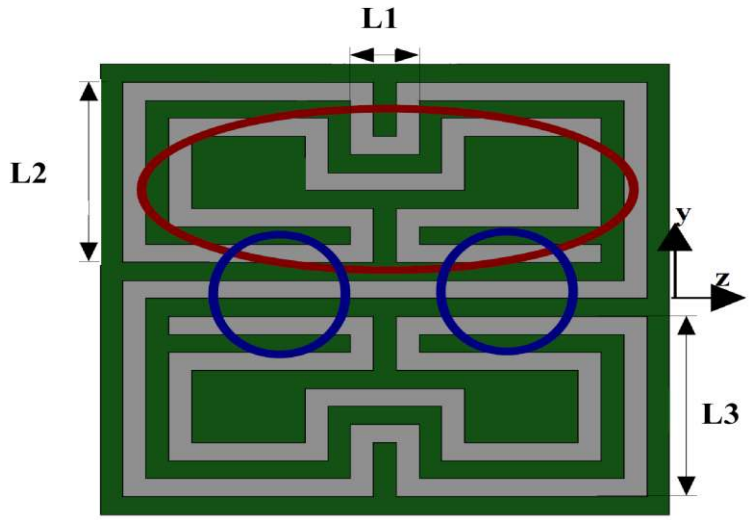

Figure 4.13. Geometry of fractal anti-spiral resonator as artificial dielectric material

4.4.2 Simulation Results

In order to obtain resonant negative permittivity, this structure is excited by a y-direction polarized, z-direction propagating plane wave. The blue marked overlapping sections in Figure 4.13 show the enhanced capacitively coupled sections to reduce the resonance frequency. In the numerical model, PEC at two y-planes and PMC at two x-planes are imposed on one unit cell. The simulated S parameters are shown in Figure 4.14.

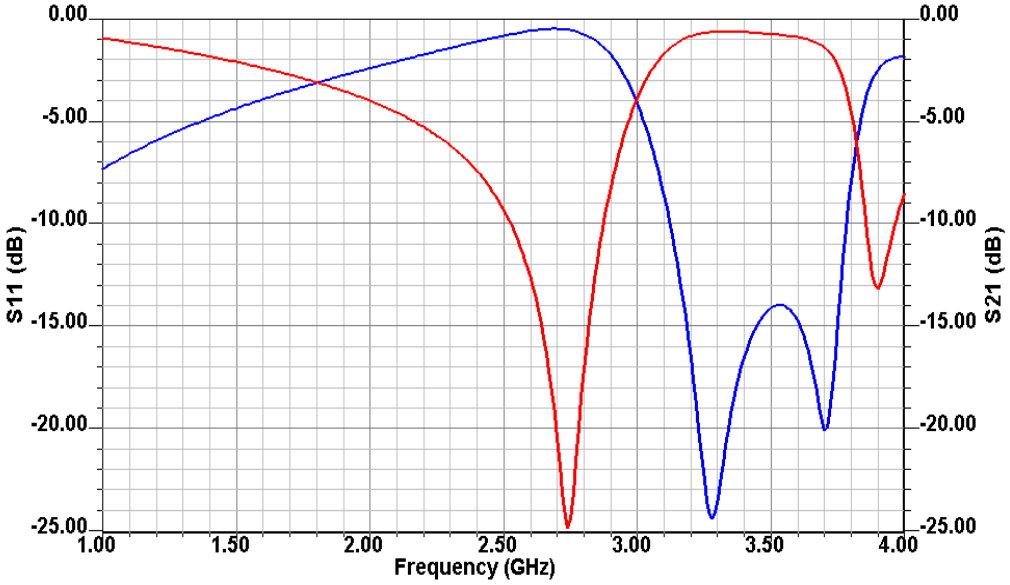

Figure 4.14. Transmission (red) and reflection (blue) parameters of fractal anti-spiral resonator

It is important to note that to determine the right polarization and propagation direction for the cell excitation, additional S parameter calculations are done for both x- and z-polarized plane waves with the corresponding boundary conditions and port locations. Electric resonance was obtained at the lowest frequency and therefore, the above mentioned y-direction polarized, z-direction propagating plane wave corresponds to the right excitation.
In Figure 4.14, the resonance frequency is 2.74 GHz. In order to understand why the electric resonance is more effectively excited, the current distribution is investigated along with the electric field distribution at the resonance frequency.

In Figure 4.15a, the current distributions on the upper and lower half are nearly anti-symmetrical. The induced magnetic fields are thus oppositely directed. This results into a small net out-of-plane magnetic dipole moment.

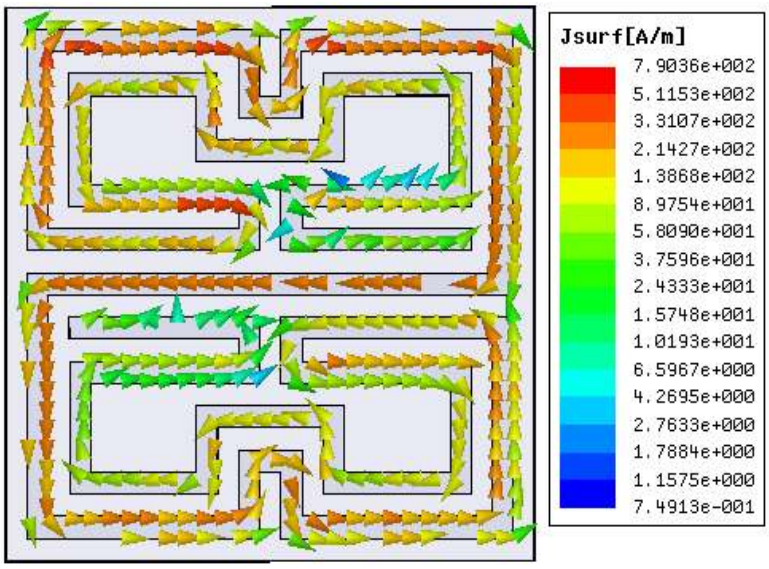

Figure 4.15a. Surface current distribution of fractal anti-spiral resonator at the resonance frequency

However, in Figure 4.15b, due to the electrically coupled sections in the middle part, the y-directed electric field has a similar field distribution as a resonant y-directed electric dipole. The transmission minimum is due to the depolarization effect of the excited dipole on the incoming electric field. It can be noticed from the weaker field distribution on the right-hand side than that on the left-hand side as in Figure 4.15b. Therefore, this artificial material is regarded as a negative permittivity material in a certain frequency band. On the other hand, the excited electric dipole is an in-plane dipole rather than out-off plane dipole. This is an important difference between the proposed design and conventional CSRR-based designs. In CSRR-based designs, slots etched in the ground plane excite out-off plane directed dipoles. Thus, this design method has the advantage of exciting the structure effectively with an in-plane feeding line on the same substrate layer [3-5], which is not preferred for CSRR-based designs.

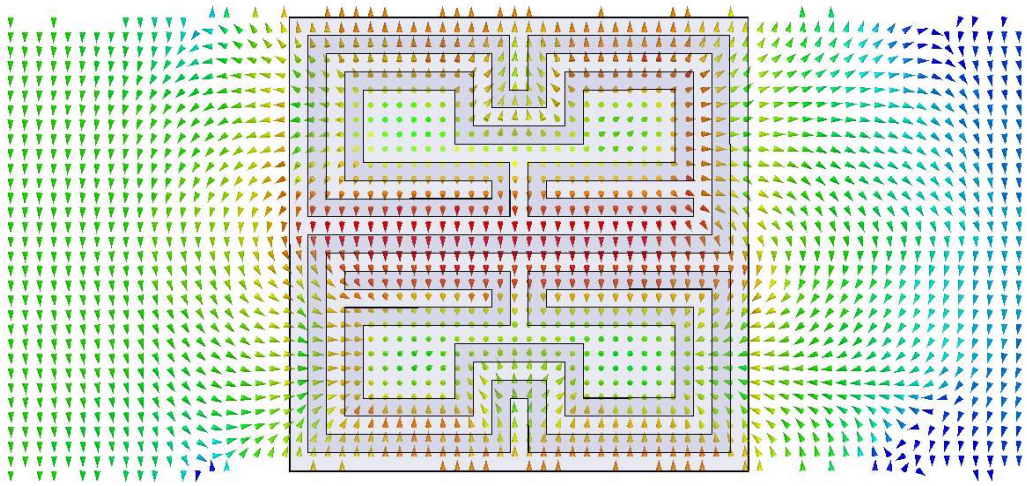

Figure 4.15b. E-field distribution of fractal anti-spiral resonator at the resonance frequency

4.4.3 Effective Parameters

As a next step, the effective permittivity is retrieved. The complex propagation constant and Bloch impedance are also illustrated. They are shown in Figure 4.16.

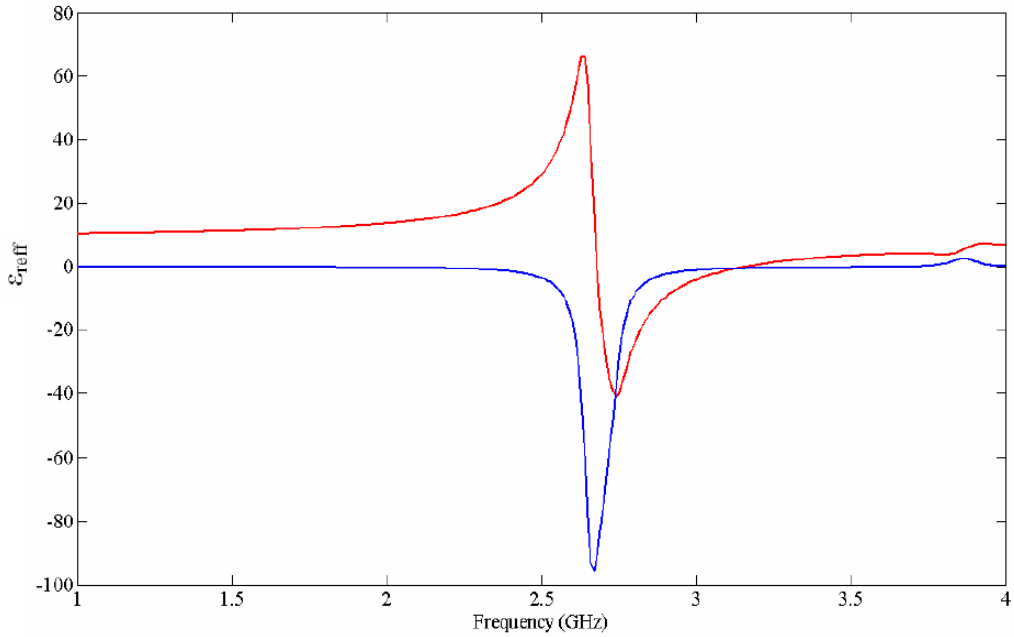

Figure 4.16a. Real (red) and imaginary (blue) part of effective relative permittivity of fractal anti-spiral resonator array

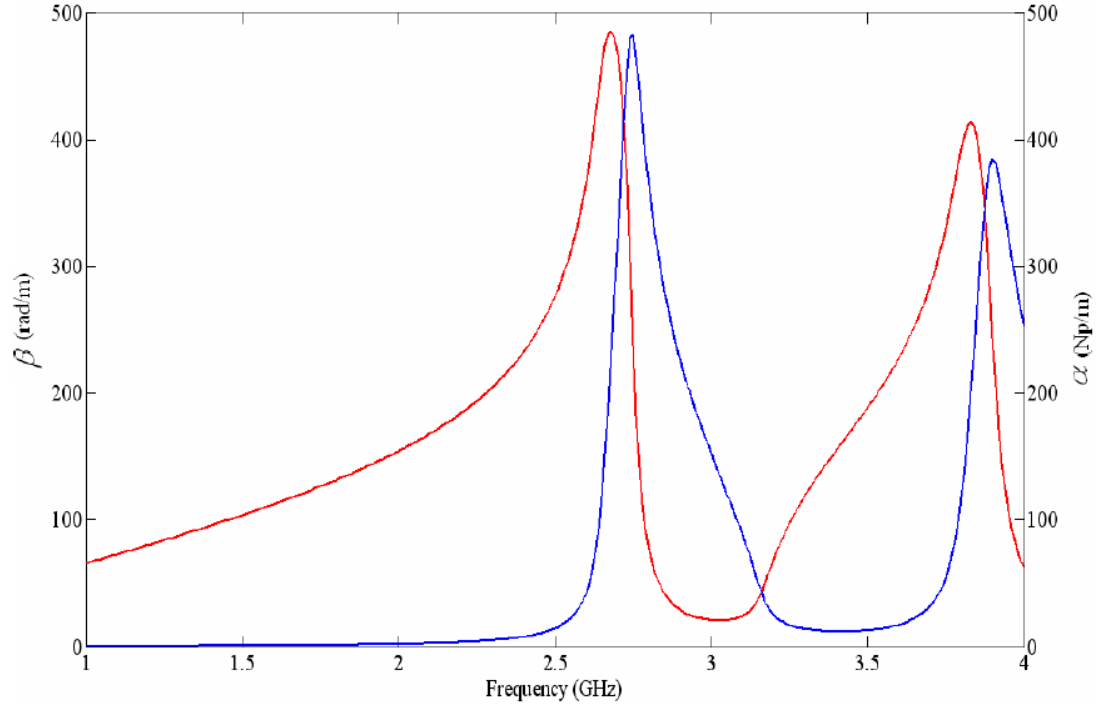

Figure 4.16b. Phase (red) and attenuation (blue) constant of fractal anti-spiral resonator array

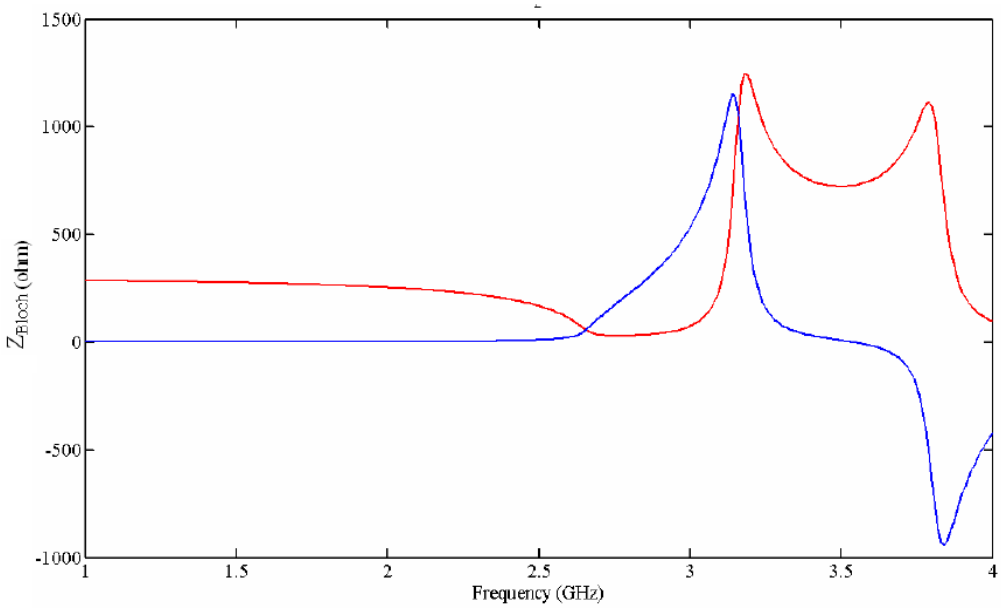

Figure 4.16c. Real (red) and imaginary (blue) part of Bloch impedance of fractal anti-spiral resonator array

In Figure 4.16a, the effective permittivity has Lorentzian type dispersion characteristics. The plasma frequency is 3.13 GHz. The negative permittivity band extends from 2.67 GHz to 3.13 GHz with the bandwidth of 460 MHz. The transmission minimum is at the frequency of lowest negative permittivity, 2.74 GHz. It is 70 MHZ shifted from the electric resonance frequency due to the metallic and substrate losses. In the negative permittivity band, the attenuation constant is high and the wave impedance is inductive.
As a result, the numerical simulations confirm the electric resonance and negative permittivity of fractal anti-spiral resonator. The unit cell size is 1/22 of free space wavelength. It can be used to design more homogeneous dielectric metamaterials.

4.5 Chapter Conclusion

In this chapter, artificial dielectrics based on periodic metallic wires are first addressed. The fundamental approach in the design of negative permittivity materials is introduced. The effective permittivity is analytically formulated under plane wave excitation. The electric field has to be directed parallel to the wire axis to obtain Drude type permittivity response. The transmission and reflection parameters are analytically and numerically calculated. They have quite good agreement. The equivalent circuit model is derived. The effective material parameters are then analytically calculated from the equivalent circuit by Bloch's Theorem. The effective permittivity formulation has Drude type frequency dispersion as expected from the original formulations of Pendry. The analytical calculations in this chapter do not use any assumptions on the frequency dependency of wire array unlike in the analytical formulation of Pendry. A wire model structured on low loss substrate is numerically analyzed. The transmission and reflection parameters are calculated. Surface current, electric and magnetic field distributions are presented. They are important to understand the main driving principle of negative permittivity. The reason why the incoming electric field is depolarized, is the excitation of electrically small electric dipoles, formed from the wire currents. Thus, the wire array has an inductive impedance in the negative permittivity region as in the case of short-circuited transmission line. 1D Brillion diagram is numerically calculated. The bandgap region and plasma frequency are determined.

The effective material parameters, Bloch impedance and complex propagation constant are calculated. At the end of the chapter, a unit cell based on fractal anti-spiral resonator is proposed and numerically investigated. The effective permittivity, Bloch impedance and complex propagation constant are retrieved. The numerical calculations confirm the effectiveness of this electrically small cell in the design of more homogeneous negative permittivity materials.

5. Left-Handed Metamaterials

5.1 Introduction

In this chapter, a third class of artificial materials, 'Left-handed Metamaterials' (LHM) is explained. LHMs are realized by embedding negative permittivity and permeability unit cells into same host medium to obtain artificial magnetism and dielectricity in the same frequency band. The eigenmode equation of periodically loaded negative permittivity and permeability materials is therefore first analytically calculated. This calculation is also important to confirm subwavelength resonance and negative phase velocity in LHMs. The numerical calculations are additionally done for a specific LHM cell geometry. This unit cell is composed of same SRR geometry in Chapter 3 and wire geometry in Chapter 4. The main reason to use same cell geometries is to confirm LH propagation in the frequency band of both negative permeability and permittivity. The effective parameters are retrieved. Dispersion relation is studied. The frequency band of negative refractive index is determined. At the end of the chapter, a unit cell based on thin wire loaded spiral resonator is studied to realize more homogeneous LH materials.

5.2 Theoretical Analysis

The theoretical research on LHM was initiated by Veselago in 1968 [2]. He considered electromagnetic wave propagation through a homogenous isotropic material in which both permittivity and permeability were negative. Because the direction of Poynting vector is opposite to that of phase velocity in this material, he referred to this medium as a left-handed medium. Due to the natural inexistence of such exotic materials, his ideas have received little attention in scientific community. However, the work of Pendry on electromagnetic engineering of permeability and permittivity of a host material has made Veselago's ideas realisable [7-9]. In 2000, Smith constructed a composite LH medium with periodic metallic wires and SRRs in the microwave regime [1]. He demonstrated negative refraction at the interface of LH medium and air. There have now been several theoretical and experimental studies confirming negative refractive index [56-59], [64-69]. The negative refractive index in LHMs can be simply understood from a similar procedure in Section 3.3 and Section 4.3 by calculating wave impedances of LHM filled waveguide. H- and E-wave impedances are calculated as

$$
\begin{aligned}
Z_{Hmn} &= \frac{\omega\mu}{k_{zmn}} = -\frac{\omega|\mu_{LHM}|}{k_{zmn}} \\
Z_{Emn} &= \frac{k_{zmn}}{\omega\varepsilon} = -\frac{k_{zmn}}{\omega|\varepsilon_{LHM}|} \\
n_{eff} &= \frac{k_{zmn}}{k_0}
\end{aligned}
\qquad (5.1)
$$

where k_{zmn} is phase constant at the operation frequency, ω . μ and ε are negative permeability and permittivity of LHM, respectively.

Because the wave impedance is always positive, k_{zmn} has to be negative in the impedance formulation. This makes LHM to have negative refractive index. This is an alternative explanation to understand why the refractive index is negative in LHMs. The effective electromagnetic parameters can also be retrieved experimentally and numerically [56-59]. There are also engineering applications derived from this concept in addition to negative refraction. Some of them are electrically small resonators [13], sub-wavelength waveguides [15],[70-72], enhanced focusing [17,18], backward wave antennas [19], enhanced electrically small antennas [20], compact filters [14], [73] and improved microwave components [3,4],[6].
In this section, eigenmode equation of H-waves in a rectangular waveguide, which is periodically loaded with negative permittivity and permeability materials is analytically calculated [73]. The eigenmode equation of E-waves can be similarly calculated by replacing H-wave impedance with E-wave impedance in ABCD matrix formulation. The analytic model is shown in Figure 5.1.

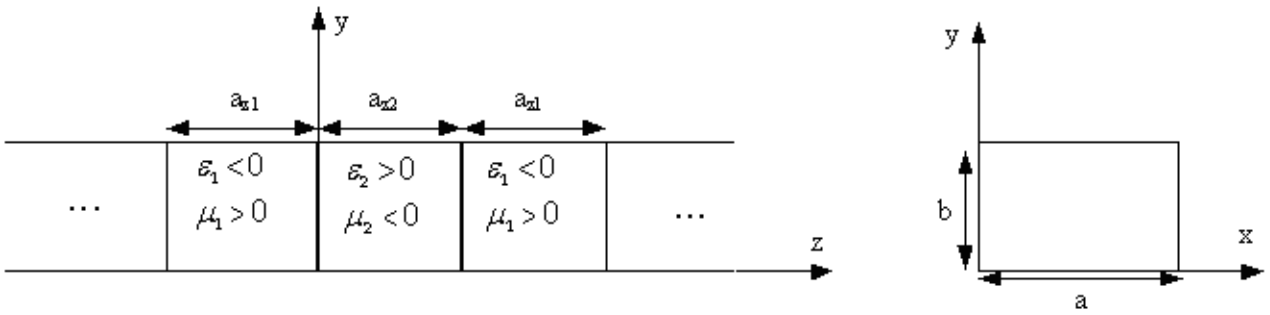

Figure 5.1. Analytical model of periodically loaded negative permeability and permittivity materials

ABCD matrix of negative permittivity material of length a_{z1} is formulated with H-wave impedance, Z_{H1} and phase constant, k_{z1} as

$$M_{ABCD\_negeps} = \begin{bmatrix} \cos(k_{z1}a_{z1}) & jZ_{H1}\sin(k_{z1}a_{z1}) \\ j\dfrac{\sin(k_{z1}a_{z1})}{Z_{H1}} & \cos(k_{z1}a_{z1}) \end{bmatrix} \tag{5.2a}$$

$$k_{z1} = \sqrt{\omega^2\mu_1\varepsilon_1 - (\frac{m\pi}{a})^2 - (\frac{n\pi}{b})^2}$$

$$Z_{H1} = \frac{\omega\mu_1}{k_{z1}}$$

where a and b are the waveguide side lengths in x- and y-directions, respectively.
In the same manner, ABCD matrix of negative permeability material of length a_{z2} is formulated with H-wave impedance, Z_{H2} and phase constant, k_{z2} as

$$M_{ABCD\_negmu} = \begin{bmatrix} \cos(k_{z2}a_{z2}) & jZ_{H2}\sin(k_{z2}a_{z2}) \\ j\dfrac{\sin(k_{z2}a_{z2})}{Z_{H2}} & \cos(k_{z2}a_{z2}) \end{bmatrix}$$

$$k_{z2} = \sqrt{\omega^2\mu_2\varepsilon_2 - (\frac{m\pi}{a})^2 - (\frac{n\pi}{b})^2} \tag{5.2b}$$

$$Z_{H2} = \frac{\omega \mu_2}{k_{z2}}$$

Thus, ABCD matrix of one cell of length, $a_{z1}+a_{z2}$ is calculated by cascading ABCD matrices as

$$M_{ABCD\_cell} = \begin{bmatrix} \cos(k_{z2}\frac{a_{z2}}{2}) & jZ_{H2}\sin(k_{z2}\frac{a_{z2}}{2}) \\ j\frac{\sin(k_{z2}\frac{a_{z2}}{2})}{Z_{H2}} & \cos(k_{z2}\frac{a_{z2}}{2}) \end{bmatrix} \begin{bmatrix} \cos(k_{z1}a_{z1}) & jZ_{H1}\sin(k_{z1}a_{z1}) \\ j\frac{\sin(k_{z1}a_{z1})}{Z_{H1}} & \cos(k_{z1}a_{z1}) \end{bmatrix} \begin{bmatrix} \cos(k_{z2}\frac{a_{z2}}{2}) & jZ_{H2}\sin(k_{z2}\frac{a_{z2}}{2}) \\ j\frac{\sin(k_{z2}\frac{a_{z2}}{2})}{Z_{H2}} & \cos(k_{z2}\frac{a_{z2}}{2}) \end{bmatrix}$$

$$M_{ABCD\_cell} = \begin{bmatrix} A & B \\ C & D \end{bmatrix} \tag{5.2c}$$

where the matrix elements are calculated in (5.2.d).

$$\begin{aligned} A &= \cos(k_{z1}a_{z1})\cos(k_{z2}a_{z2}) - \frac{1}{2}\left(\frac{Z_{H2}}{Z_{H1}} + \frac{Z_{H1}}{Z_{H2}}\right)\sin(k_{z1}a_{z1})\sin(k_{z2}a_{z2}) \\ B &= jZ_{H2}\cos(k_{z1}a_{z1})\sin(k_{z2}a_{z2}) + j\frac{\sin(k_{z1}a_{z1})}{2Z_{H1}}\left(\left(Z_{H1}^2 - Z_{H2}^2\right) + \left(Z_{H1}^2 + Z_{H2}^2\right)\cos(k_{z2}a_{z2})\right) \\ C &= j\frac{1}{Z_{H2}}\cos(k_{z1}a_{z1})\sin(k_{z2}a_{z2}) + j\frac{\sin(k_{z1}a_{z1})}{2Z_{H1}Z_{H2}^2}\left(\left(-Z_{H1}^2 + Z_{H2}^2\right) + \left(Z_{H2}^2 + Z_{H1}^2\right)\cos(k_{z2}a_{z2})\right) \\ D &= \cos(k_{z1}a_{z1})\cos(k_{z2}a_{z2}) - \frac{1}{2}\left(\frac{Z_{H2}}{Z_{H1}} + \frac{Z_{H1}}{Z_{H2}}\right)\sin(k_{z1}a_{z1})\sin(k_{z2}a_{z2}) \end{aligned} \tag{5.2d}$$

The dispersion relation can then be calculated from ABCD parameters to determine complex propagation constant, γ_{eff} as

$$\cosh(\gamma_{eff}(a_{z1}+a_{z2})) = \cos(k_{z1}a_{z1})\cos(k_{z2}a_{z2}) - \frac{1}{2}\left(\frac{Z_{H1}}{Z_{H2}} + \frac{Z_{H2}}{Z_{H1}}\right)\sin(k_{z1}a_{z1})\sin(k_{z2}a_{z2}) \tag{5.2e}$$

It can be formulated in an alternative form for lossless negative material parameters as

$$\cosh(\gamma_{zeff}(a_{z1}+a_{z2})) = \cosh(\alpha_{z1}a_{z1})\cosh(\alpha_{z2}a_{z2}) - \frac{1}{2}\left(\frac{Z_1}{Z_2} + \frac{Z_2}{Z_1}\right)\sinh(\alpha_{z1}a_{z1})\sinh(\alpha_{z2}a_{z2}) \tag{5.3.a}$$

where $Z_{1,2}$ are the wave reactances and $\alpha_{z1,2}$ are the attenuation constants of negative permittivity and permeability medium, respectively. The wave reactances and attenuation constants are calculated from (5.2a) and (5.2b) as

$$Z_{H1} = \frac{\omega\mu_1}{-j\sqrt{\omega^2\mu_1|\varepsilon_1| + (\frac{m\pi}{a})^2 + (\frac{n\pi}{b})^2}} = jZ_1$$
$$Z_{H2} = \frac{\omega|\mu_2|}{j\sqrt{\omega^2|\mu_2|\varepsilon_2 + (\frac{m\pi}{a})^2 + (\frac{n\pi}{b})^2}} = -jZ_2 \quad (5.3b)$$

$$\alpha_{z1} = \sqrt{\omega^2|\varepsilon_1|\mu_1 + (\frac{m\pi}{a})^2 + (\frac{n\pi}{b})^2}$$
$$\alpha_{z2} = \sqrt{\omega^2\varepsilon_2|\mu_2| + (\frac{m\pi}{a})^2 + (\frac{n\pi}{b})^2}\,. \quad (5.3c)$$

There are important issues to be discussed about the eigenmode equation. In (5.3b), the wave impedances of negative permittivity and permeability materials are inductive and capacitive, respectively. Thus, the wave propagation can be in principle obtained at any frequency by engineering the material parameters and adjusting the slab thicknesses. In addition, in (5.3a), the eigenmode equation is dependent on the monotonically increasing hyperbolic functions. Therefore, due to lack of periodic functions in (5.3a) unlike in the eigenmode equation of RHM and LHM loaded waveguides, one resonance frequency may be calculated at a certain phase shift per cell for each mode. The same conclusion is also valid for the parallel plate waveguides which are loaded with negative permittivity and permeability materials in the transverse plane [15]. Another important issue is the design possibility of compact LHM and RHM loaded cavity resonators with the resonance frequencies dependent on the ratio of each slab thickness [13]. The main reason is the phase compensation feature of LHM in RHM-based transmission lines and resulting zeroth order resonance unlike in the conventional resonators [5],[73,74]. Thus, compact transmission media and resonators can be realised by pairing any slab thickness of LHM with RHM [13],[75]. The design possibility of subwavelength guided wave structures with lateral dimensions below diffraction limits is analysed in [15,16].

As a case study, one ε-negative material with Drude type permittivity response is periodically loaded with another μ-negative material with Lorentzian type permeability response inside a rectangular waveguide. The eigenfrequencies of H_{10} mode are calculated. The slab lengths of negative permittivity and permeability materials in the propagation direction are a_{z1}= 1mm and a_{z2}=2mm, respectively. The side lengths of waveguide are a=10mm and b=5mm. The magnetic resonance, magnetic plasma frequency and loss parameter are 2.10 GHz, 2.21 GHz and 100 Hz. The electric plasma frequency and loss parameter are 10 GHz and 100 Hz. The dispersion diagram and Bloch impedance are analytically calculated. They are shown in Figure 5.2 between the magnetic resonance and magnetic plasma frequencies along with numerically calculated eigenfrequencies at certain phase shifts. The analytical and numerical results are in good agreement with maximum error smaller than 1%.

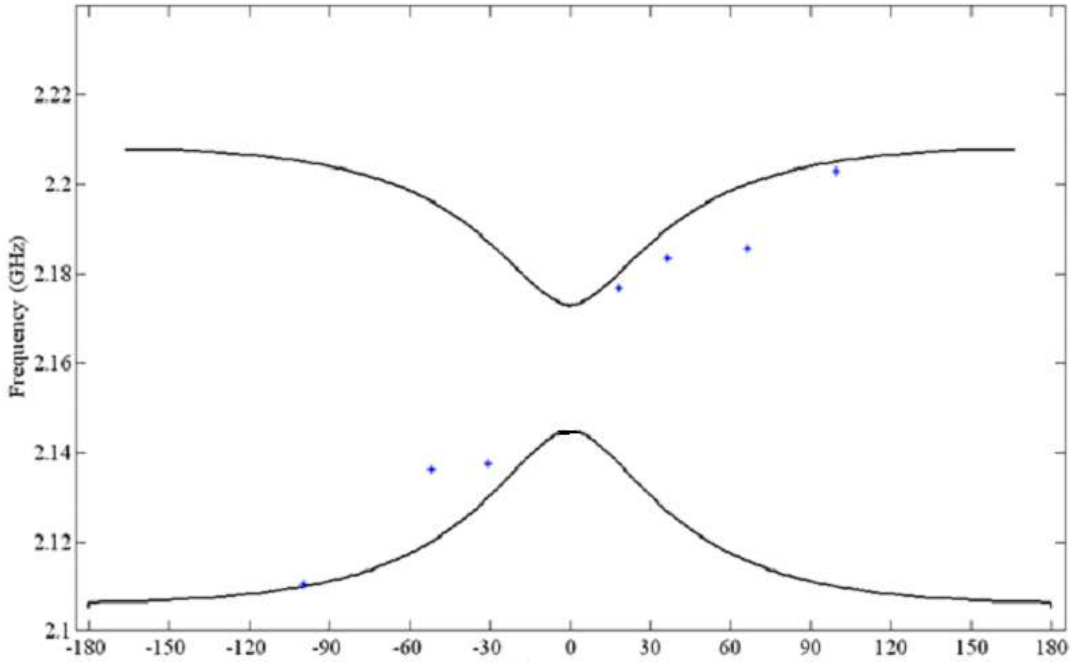

Figure 5.2a. (*) Numerically and (solid)analytically calculated 1D dispersion diagram of periodically arranged negative permeability and permittivity materials

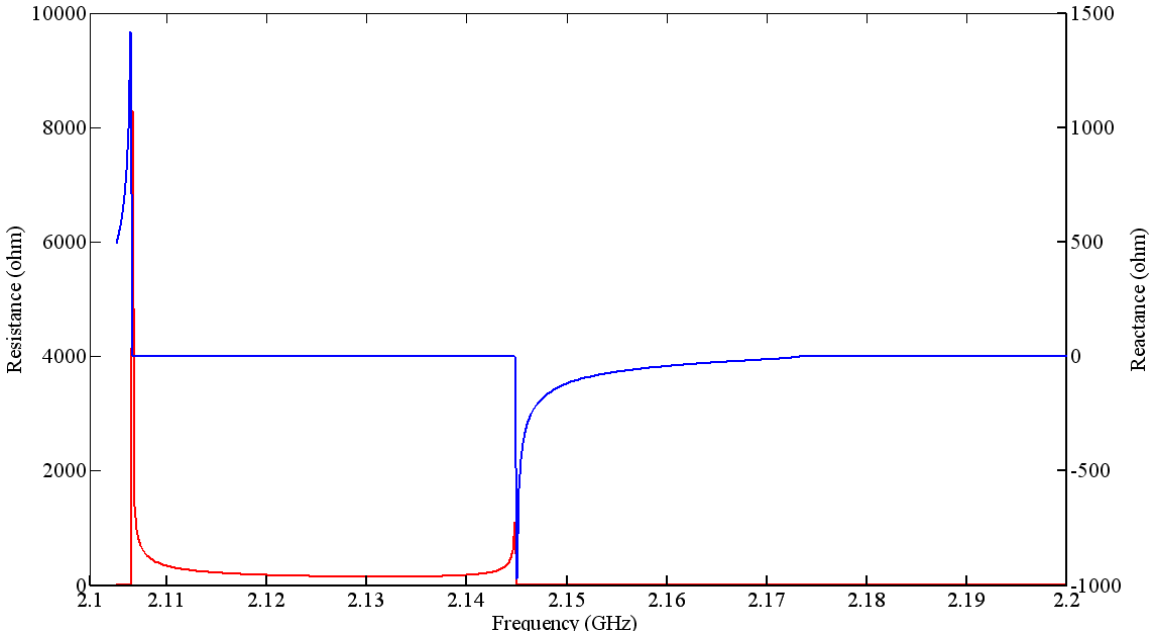

Figure 5.2b. Resistance (red) and reactance (blue) of periodically arranged negative permeability and permittivity materials

In Figure 5.2a, the propagation constant is negative between 2.106 GHz and 2.146 GHz with 40 MHz bandwidth. However, in addition to LH band, RH band is also obtained between 2.173 GHz and 2.21GHz with 37 MHz bandwidth. In both LH and RH bands, the transmission loss is negligibly small due to low dissipation factors assumed in the permeability and permittivity formulations. There is 27 MHz bandgap between LH and RH bands. It extends from 2.146 GHz to 2.173 GHz. In Figure 5.2b, in the bandgap, Bloch impedance is low ohmic with capacitive reactive part. However, there is no reactive part as in the case of resonant circuits at the frequencies of band edges.

Thus, the composite material can be modeled as a combination of parallel and series resonant circuits with the resonance frequencies of 2.146 GHz and 2.173 GHz, respectively. The equivalent circuit models of negative permittivity and permeability materials are illustrated in Figure 5.3 to confirm the emergence of RH band at the higher frequencies [4-6].

(a) (b)

Figure 5.3. Equivalent circuit model of one unit cell of (a) negative permittivity and (b) negative permeability materials

The periodic loading of negative permittivity and permeability materials can be modeled with a unit cell shown in Figure 5.4.

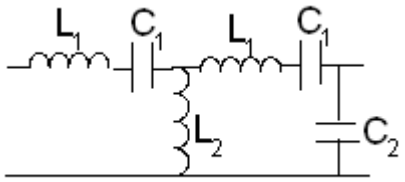

Figure 5.4. Equivalent circuit model of one unit cell of periodically loaded negative permittivity and permeability materials

In Figure 5.4, for the frequencies higher than the series resonance frequency, the impedance of series branches is inductive. The impedance of parallel branches is capacitive for the frequencies higher than the parallel resonance frequency. Thus, this unit cell can be modeled as a series inductor loaded with a shunt capacitor for the frequencies larger than the parallel and series resonance frequencies. This is the equivalent circuit model of conventional RH transmission lines. It is the main reason why this material has an additional RH band at the frequencies higher than LH band. The equivalent circuit model of LH materials can be similarly derived from same circuit model for the frequencies lower than the parallel and series resonance frequencies. For this case, the circuit model has an equivalent form of a series capacitor loaded with a shunt inductor. It is the dual of RH circuit model. One important remark is therefore the negative permittivity and permeability materials can be alternatively designed without relying on high lossy resonance phenomenon. In other words, low loss LHMs can also be realized by periodic loading of conventional microstrip transmission lines with series capacitors and shunt inductors in planar microwave technology [4,5]. Many microwave circuits have been implemented by using this methodology such as compact broadband couplers [4], broadband phase shifters [5], compact wideband filters [3],[14], compact resonant antennas [21-23],[76].

5.3 Numerical Simulations

5.3.1 Resonance Frequency of LHM Periodic Array

In this section, transmission and reflection parameters of one cell thick LHM array is numerically calculated under plane wave excitation. The unit cell is shown in Figure 5.5 along with the boundary conditions. The geometrical parameters of SRR and wire are the same as the ones of SRR in Section 3.3 and of wire in Section 4.3.

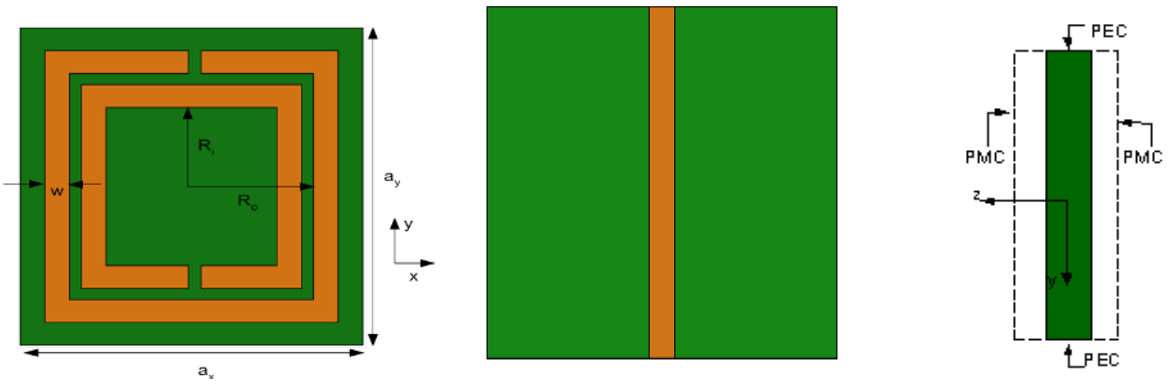

(a) (b) (c)

Figure 5.5. (a) Top and (b) bottom view of one unit cell of LHM geometry (c)PEC and PMC boundary conditions

In Figure 5.5, PEC is imposed on two y-planes at the edges to excite the wire by y-polarized plane wave. This boundary condition is important to obtain Drude type permittivity response. In the same manner, PMC is imposed on two z-planes to excite SRR with z-directed magnetic field. It is important to obtain Lorentzian type permeability response. In addition, these boundary conditions result the cells in y- and z-direction to be coupled electrically and magnetically, respectively. The unit cell can then be excited by y-polarized x-direction propagating plane wave. The substrate is 0.5mm thick Rogers/RT Duroid 5870. The relative permittivity and tan(δ) are 2.33 and 0.0012, respectively. The transmission and reflection parameters of LHM model are numerically calculated with HFSS. They are shown in Figure 5.6.

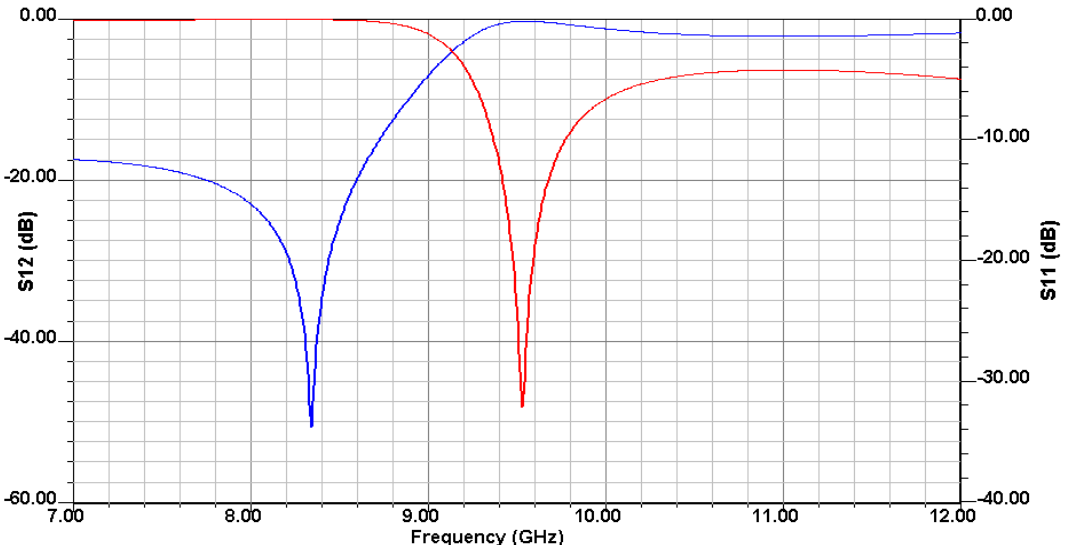

Figure 5.6. Reflection (red) and transmission (blue) parameters of one unit cell thick LHM sample

The resonance frequency is 9.58GHz. The resonance wavelength is 31.48 mm. It is approximately 11 times larger than the cell size. The cell size is sufficiently small to attribute the composite material as a homogeneous material. The resonance frequency agrees well with the magnetic resonance frequency of SRR array in Section 3.3.1 with only 30 MHz frequency shift. As explained in Section 3.3 and 4.3, there is low amount of power transport through SRR and wire array due to negative permeability and permittivity, respectively. However, the wave can propagate through LHM slab at the overlapping frequency band of negative permeability and permittivity. This is because the capacitive impedance of SRR array is compensated with the inductive impedance of wire array at LHM band. This issue is confirmed from the extracted material parameters in the next section. The magnetic field, electric field and surface current distribution at the resonance frequency are shown in Figure 5.7.

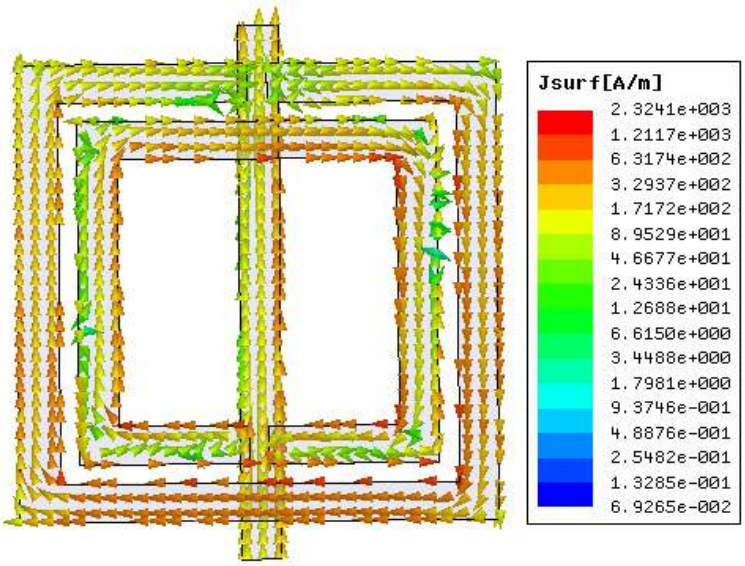

Figure 5.7a Surface current distribution of one unit cell at the resonance frequency

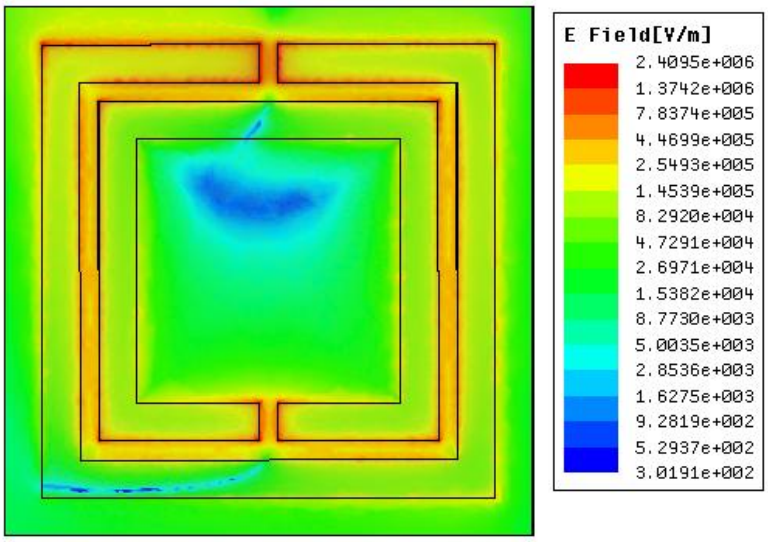

Figure 5.7b Magnitude of electric field distribution of one unit cell at the resonance frequency

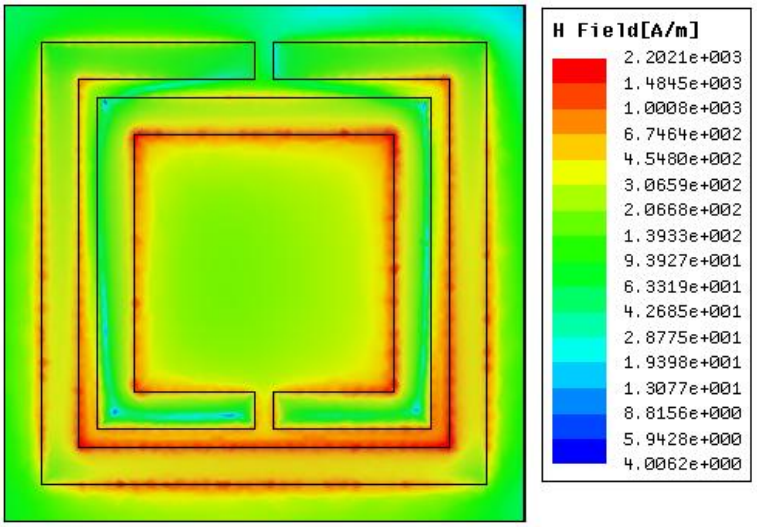

Figure 5.7c Magnitude of magnetic field distribution of one unit cell at the resonance frequency

The coupling between SRR and wire is important to determine the optimum wire position for maximum LH transmission. The transmission and reflection parameters for different wire positions with respect to SRR symmetry axis are numerically calculated. They are shown in Figure 5.8. In Figure 5.8, the highest transmission is obtained for the wire position at the symmetry axis of SRR. The resonance frequency is quite near to the magnetic resonance frequency of SRR array with 30MHz frequency shift. The first reason of this frequency overlap is ineffective magnetic coupling between SRR and wire because of no net magnetic flux penetrating through SRR at this position. The second reason is the negligible electrical coupling between SRR and wire since there is no y-directed electric field along SRR symmetry axis. Therefore, maximum transmission is quite near to the magnetic resonance frequency. In other words, the wire and SRR are excited almost independently from each other with negligible field coupling inbetween.

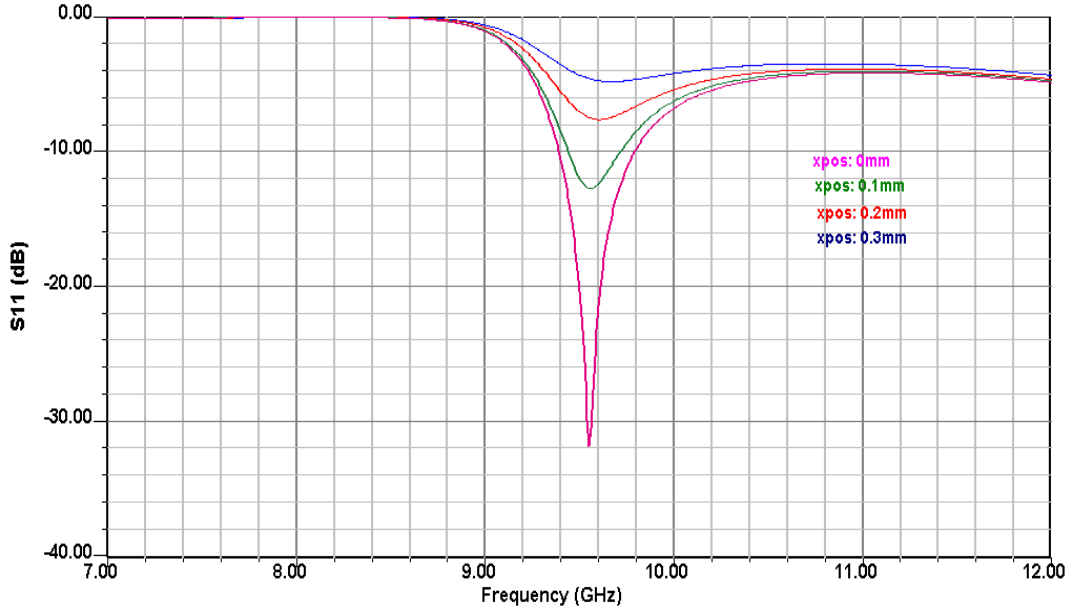

Figure 5.8a Reflection parameter of one unit cell thick LHM medium for different wire positions

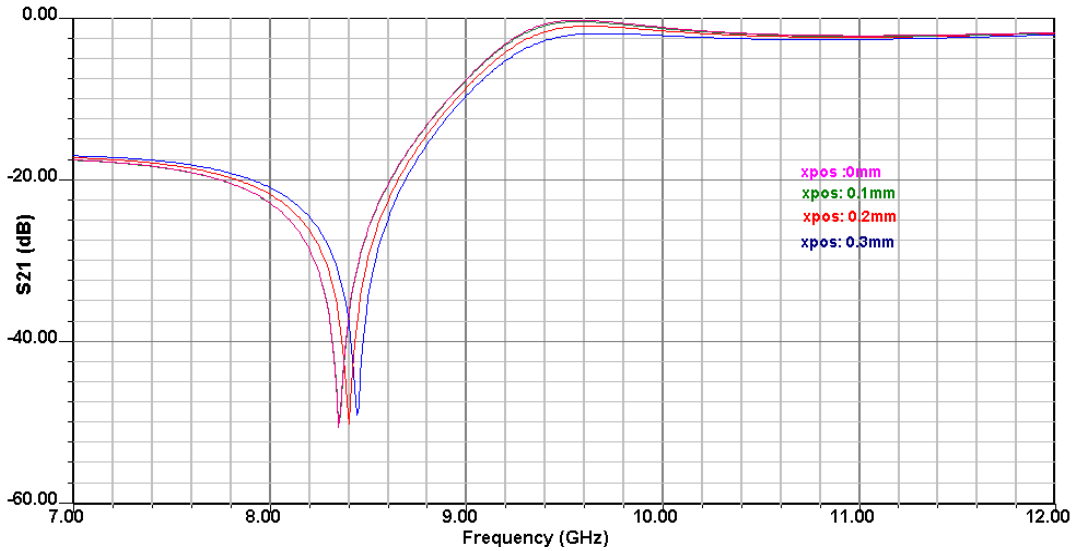

Figure 5.8b Transmission parameter of one unit cell thick LHM medium for different wire positions

In Figure 5.8a, LH resonance is not so noticeable for increasing wire displacement from SRR symmetry axis. The electrical coupling between SRR and wire at increasing distances reduces the magnetic flux penetrating through SRR. This degrades the demagnetization effect of SRR in negative permeability band with the result of low LH transmission. The effect of electric and magnetic coupling among the cells is also investigated in Chapter 3 and Chapter 4. The lower electric coupling along y-direction increases the resonance frequency slightly as in Section 3.3.1. The lower magnetic coupling along z-direction increases the magnetic resonance frequency and decreases the electric resonance frequency as in Section 3.3.1 and Section 4.3.1.

5.3.2 Dispersion Relation of LHM Periodic Array

In this section, 1D Brillouin diagram of LHM cell is numerically studied. In the numerical model, eigenfrequencies of one unit cell with periodic boundary conditions in the propagation direction is numerically calculated for different phase shifts. PEC and PMC on the transversal planes are imposed as in the case of port mode calculation. The dispersion diagram of two lowest bands is shown in Figure 5.9. Because the phase velocity and group velocity are oppositely directed in the first band, this band is LH band. LH band coincides quite well with the stop band of only SRR array. LH resonance at 9.53 GHz in Figure 5.6 is the result of pure real Bloch impedance of LHM array, which matches with the line impedance of PEC-PMC medium. These periodic cells can thus be regarded as LH and RH transmission medium in the first and second band, respectively. The lower band is from 9.2 GHz to 11.16 GHz, whereas the higher band is from 14.42 GHz to 22.43 GHz. There is no transmission between the higher end of first band and lower end of second band. The bandgap is 3.26 GHz.

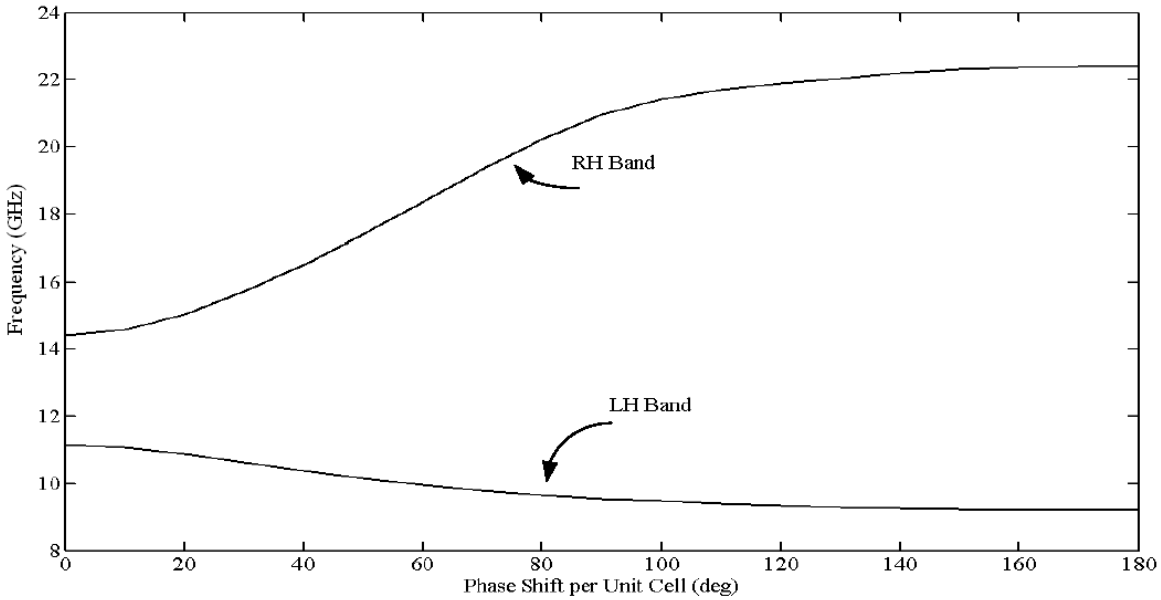

Figure 5.9. Dispersion diagram of LHM with periodic boundary conditions of different phase shifts in propagation direction

The effective refractive indices are calculated from the dispersion diagram as

$$n_{\text{eff}} = \frac{\Delta\Phi}{p}\frac{c_o}{2\pi f} \tag{5.4}$$

where $\Delta\Phi$ is phase shift per unit cell, p is cell period, c_o is speed of light in free space and f is eigenfrequency. They are shown in Figure 5.10 and are negative in LH band and positive in RH band. They are decreasing in magnitude with increasing frequency for LH band. This results the composite LH medium to be more homogeneous for the higher frequencies because of smaller phase shift per unit cell unlike in RH medium.

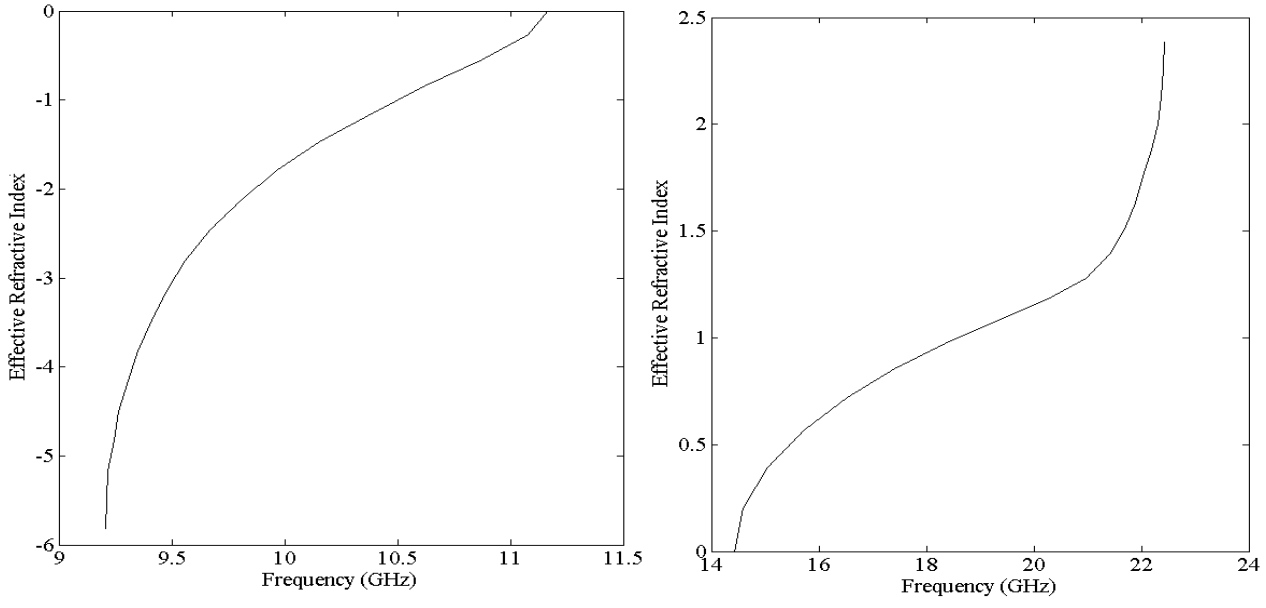

(a) (b)

Figure 5.10. Effective refractive index of one unit cell thick LHM medium in (a) LH band and (b) RH band

In addition to the refractive indices, Q factors are numerically calculated at each frequency in LH and RH band. They are shown in Figure 5.11. In Figure 5.11a, the larger metallic losses result Q factor in LH band to decrease with increasing frequency. Q factor in RH band is larger than Q factor in LH band upto 18.8 GHz. However, for the larger frequencies than 18.8 GHz, the metallic losses are more effective than the total stored energies inside the cell. Therefore, Q factor tends to decrease rapidly.

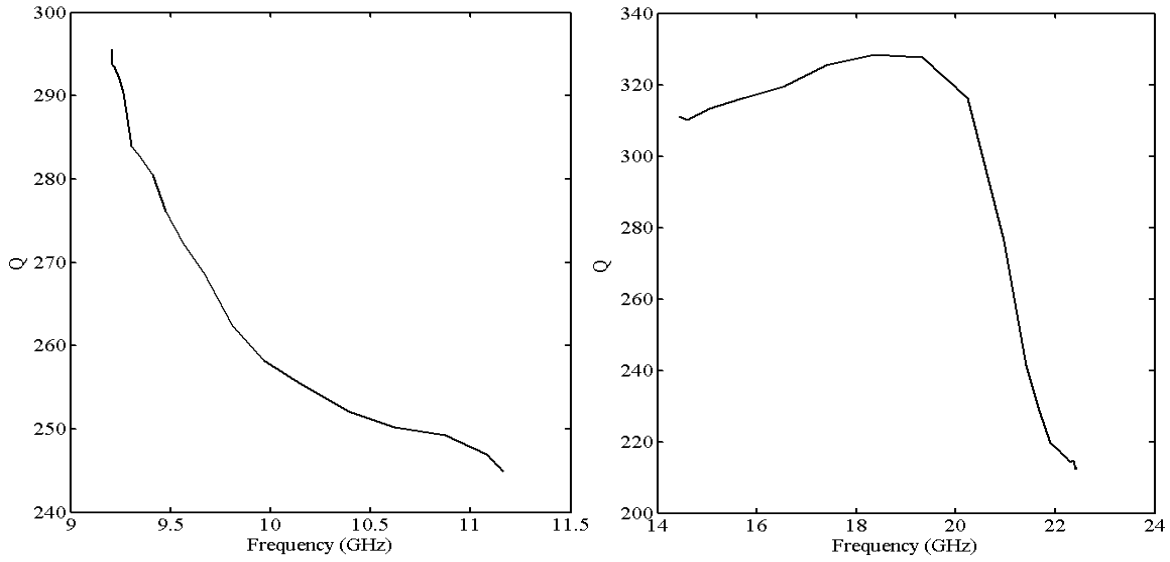

(a) (b)

Figure 5.11. Q factor of one unit cell thick LHM array in (a) LH and (b) RH band

5.3.3 Effective Parameters of LHM Periodic Array

In this section, the effective permeability and permittivity are retrieved with the procedure of Section 3.3.3. They are shown in Figure 5.12 along with Bloch impedance, complex propagation constant and effective refractive index.

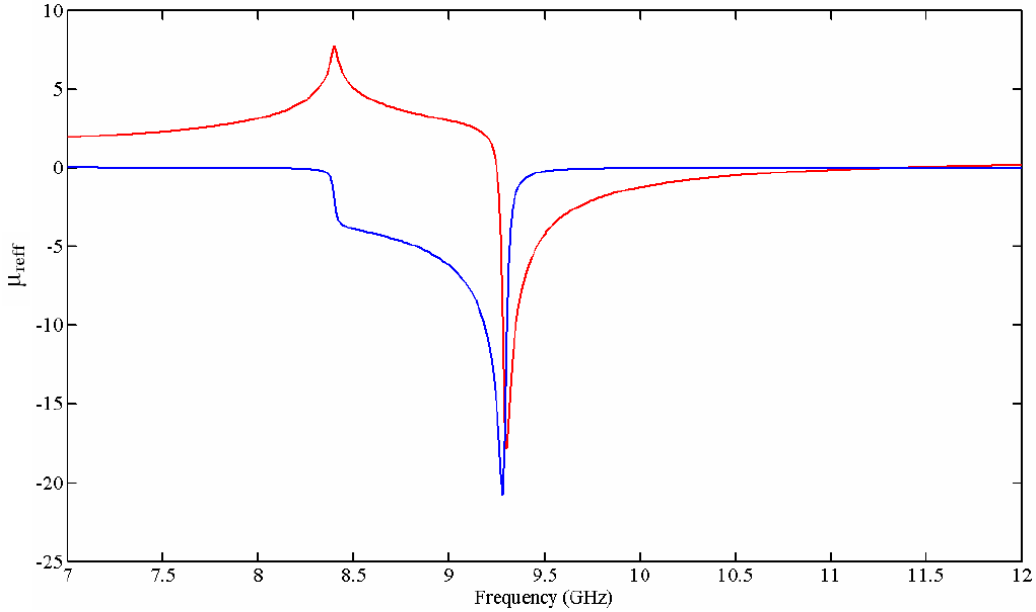

Figure 5.12a. Real (red) and imaginary (blue) part of effective relative permeability of LHM periodic array

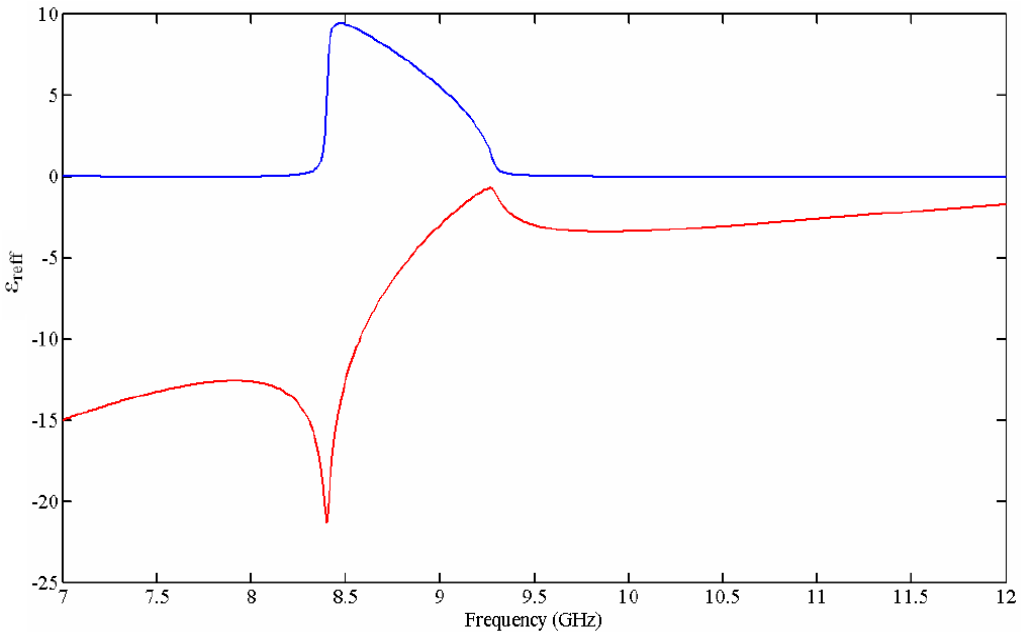

Figure 5.12b. Real (red) and imaginary (blue) part of effective relative permittivity of LHM periodic array

In Figure 5.12a, LHM array exhibits resonant permeability response. The real part of effective permeability is negative between the magnetic resonance, 9.38GHz and plasma frequency, 11.4 GHz. The imaginary part is negative. The highest magnetic loss is obtained near the magnetic resonance frequency. The magnetic resonance frequency of LHM array is quite near the magnetic resonance frequency of only SRR array with 160 MHz frequency shift. This 1.7 % frequency shift points out the negligible magnetic coupling between the wire and SRR. Therefore, the material parameters of LHM array can be controlled independently due to the electromagnetic decoupling of two metallic inclusions.
On the other hand, relative permittivity has Drude type response between 8.4 GHz and 9.28 GHz as expected. However, the imaginary part is positive between 8.47 GHz and 9.28 GHz. This is a nonphysical artifact for the passive materials with the possible reasons as explained in Section 3.3.3. This phenomenon has also been observed and pointed out in [57],[77].

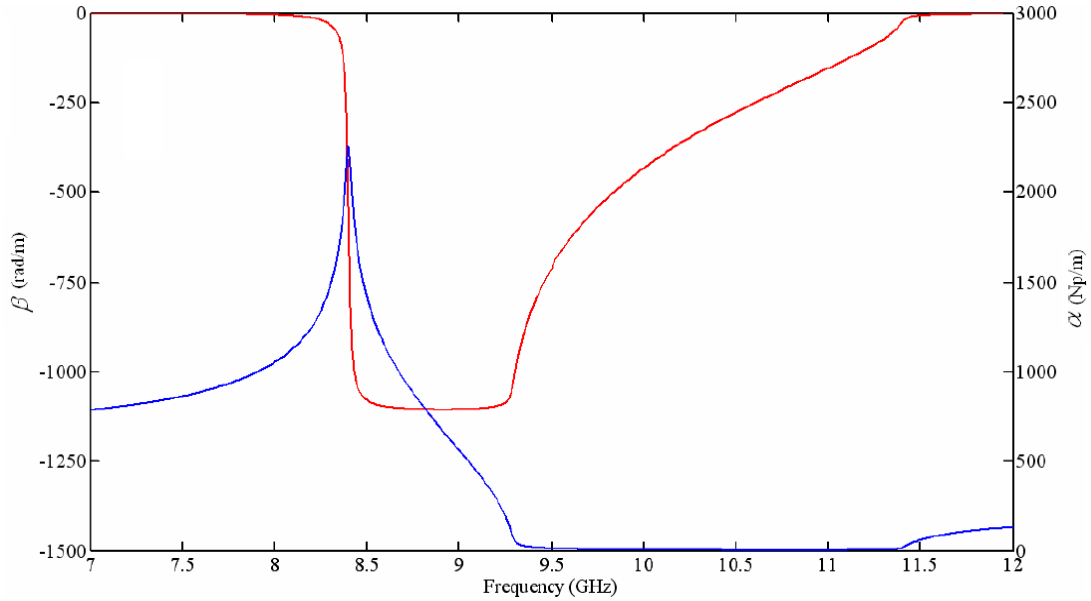

Figure 5.12c. Attenuation (blue) and phase (red) constant of LHM periodic array

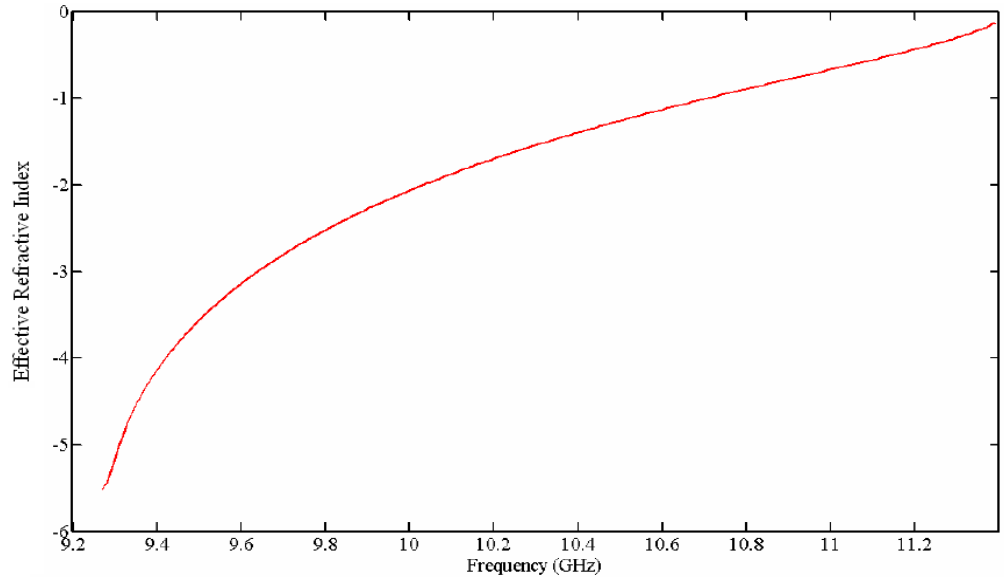

Figure 5.12d. Effective refractive index of LHM periodic array

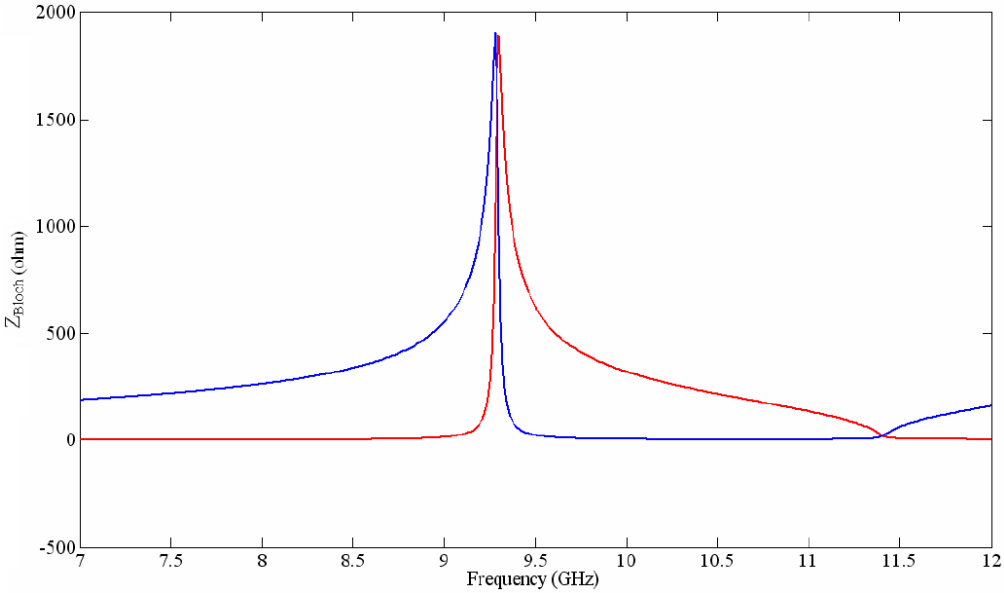

Figure 5.12e. Real (red) and imaginary (blue) part of wave impedance of LHM periodic array

In Figure 5.12c, the attenuation constant is positive at the frequencies lower than 9.3 GHz and higher than 11.4 GHz. The retrieved LH cutoff frequencies are higher than LH cutoff frequencies in the dispersion diagram in Figure 5.9. This is possibly due to the neglection of cell intercoupling in the retrieval method whereas cell intercoupling is not neglected in the eigenmode calculation. The phase constant is real and negative as expected from 1D dispersion relation. The refractive index is shown in Figure 5.12d. It has quite similar form with the one calculated from the dispersion diagram in Figure 5.10.

In Figure 5.12e, the wave impedance is inductive for the frequencies, which are not in LH band. Because SRR is not excited as a magnetic dipole in this bandgap, the wire loading yields an inductive wave impedance. The wave impedance is real between 9.3 GHz and 11.4 GHz, which are the lowest and highest LH frequencies, respectively. LH material has high impedance at 9.3 GHz and low impedance at 11.4 GHz, which is typical for LH materials.

As a result, analytical and numerical calculations prove effective negative permeability and permittivity of periodic LHM arrays. In the next section, an LHM unit cell is proposed for the design of more homogeneous negative index materials.

5.4 Wire loaded Spiral Resonator as LHM

In this section, an alternative LHM cell is proposed [76]. The design principle is based on the wire loading of spiral resonator (SR) on both sides of the unit cell. Because the resonance frequency of SR is one half of SRR resonance frequency, LHM cell design with the spiral resonator is an alternative miniaturization strategy to the fractal based designs in Chapter 3 and Chapter 4. The cell geometry is introduced first to explain how to obtain LH behavior. The reflection and transmission parameters of one cell thick LHM array are numerically calculated with 1D dispersion diagram. The effective parameters are analytically retrieved from the numerical data as a last step to illustrate the negative material parameters.

5.4.1 Structural Description

The negative material parameters are synthesized by the simultaneous excitation of electric and magnetic dipoles in LHM unit cell. The nonresonant electric and resonant magnetic dipoles are obtained by the excitation of wires and SRRs, respectively. As an alternative model to the conventional designs, more homogeneous LHM cell can be designed by the same methodology as shown in Figure 5.13. The geometrical parameters are tabulated in Table 5.1.

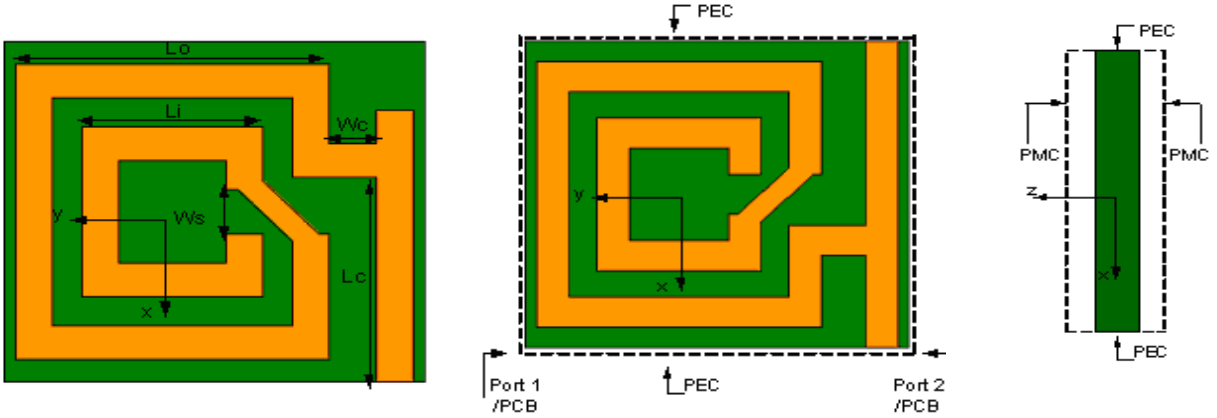

(a) (b) (c)

Figure 5.13. (a) Front and (b)back side of one LHM unit cell with indicated geometrical parameters and boundary conditions

The substrate is FR4-Epoxy with the relative permittivity of 4.4 and loss tangent of 0.02. In Figure 5.13a, the inner ring of SR is connected to the outer one with a 0.2 mm wide line. The line width is selected so as not to cause unwanted overlapping of the corner points of the inner and outer rings because of poor resolution in the fabrication process. SR is used as an alternative magnetic material to SRR because SR resonance frequency is one half of SRR resonance frequency [40]. The wire strips and SR are directly connected with each other on both sides of the substrate. This design method enhances electromagnetic coupling between wire strips and SRs on each substrate side by increasing the electrical length effectively in small cell size.

Table 5.1. Geometrical parameters of LHM unit cell (mm)

Length of outer SR ring (Lo)	2.6
Length of inner SR ring (Li)	1.5
Width of SR and wire strip	0.3
Gap between inner and outer ring of SR	0.25
Split length of inner/outer ring of SR (Ws)	0.4
Unit cell size (x)	3
Unit cell size (y)	3.5
Unit cell size (z)	2
Wire strip – SR coupling width (Wc)	0.4
Wire strip – SR coupling length (Lc)	1.7
Distance from substrate edge (x)	0.2
Distance from substrate edge (y)	0.1

The geometrical parameters of the front and back side cells are same except 0.6 mm shorter wire length on the front side. Different wire lengths decrease the resonance frequency and increase the bandwidth, as discussed in Section 5.4.3. In order to prove this issue, in addition to the proposed model, two different alternative designs are also investigated to determine the optimum LHM geometry. The first and second alternative models are LHM cell designs with the identical resonator geometry in Figure 5.13a and Figure 5.13b on both front and back sides, respectively. The opposite direction of group and phase velocity in LHMs is verified for each of three models from the eigenmode calculations. However, the validity of proposed LHM model in Figure 5.13 is confirmed by retrieving the effective material parameters from S parameters in addition to eigenmode calculations.

5.4.2 Numerical Simulations

5.4.2.1 Transmission and Reflection Parameters of Wire loaded Spiral Resonator

In order to determine the resonance frequency, scattering parameters of one cell thick LHM array are numerically calculated under plane wave excitation. PEC and PMC are imposed at two x- and z-planes, respectively. These boundary conditions result the cell to be excited by x-polarized y-direction propagating plane wave. The boundary conditions are shown along with the port settings in Figure 5.13. The reflection and transmission parameters are shown in Figure 5.14.

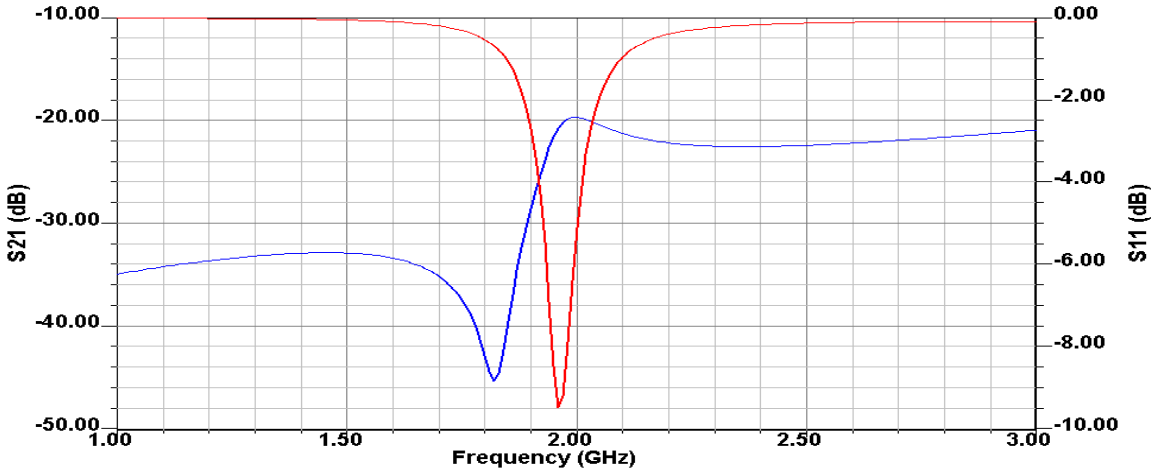

Figure 5.14. Reflection (red) and transmission (blue) parameters of one unit cell thick wire loaded spiral resonator

The resonance frequency is 1.96GHz. The resonance wavelength is 153.06 mm. It is approximately 43.73 times larger than the cell size. The transmission and reflection at the resonance frequency are approximately -20 dB and -9.5dB, which are worse than the reflection and transmission parameters of LHM model in the previous section. This is the natural consequence of the resonance phenomenon. In this cell model, the high current and field concentration at the resonance frequency increase the metallic and dielectric losses with the result of low transmission. The transmission and reflection parameters can be enhanced by the cell design with one sided metallization or low loss substrate as in Section 5.3.1. As a result, the wire loading of spiral resonator on both substrate sides reduces the resonance frequency. However, it increases the transmission loss and decreases Q at the resonance frequency. The numerical results point out this trade off between lower resonance frequency and higher losses. As a next step, 1D dispersion relation is studied to confirm LH behavior.

5.4.2.2 1D Brillouin Diagram of Wire loaded Spiral Resonator

1D Brillouin diagram is studied in this section. In order to obtain the dispersion relation, LHM cells are excited with the magnetic field perpendicular to the SR plane (z-direction), and the electric field in the direction of wires(x-direction) as in Figure 5.13b. Unlike in the port mode calculation, periodic boundary conditions are imposed in the propagation direction with different phase shifts. The dispersion diagram is shown in Figure 5.15. Oppositely directed phase and group velocities are observed in the first two bands between 2.15–2.56 GHz with 410 MHz bandwidth and 5.10-5.48GHz with 380MHz bandwidth.

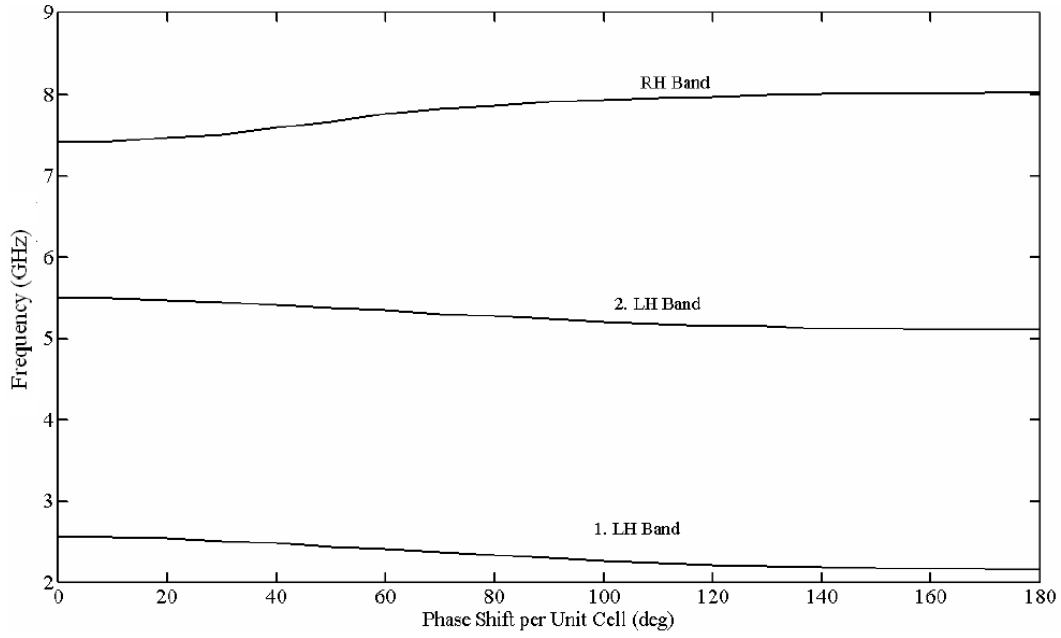

Figure 5.15 Dispersion diagram of LHM with periodic boundary conditions of different phase shifts in propagation direction

The resonance frequencies in the first LH band can be estimated from the total length of spiral resonator and wire strip. In the first band, the open-circuited end of spiral resonator is transformed to the short-circuited end of wire strip as in $\lambda/4$ transmission lines.

Similarly, the resonance frequencies in the second LH band are resulting from λ/2 resonance between spiral resonator and wire ends. The current direction at λ/2 resonance is same as the current direction at λ/4 resonance. This is the main reason why LH feature is obtained in first two bands and not in the third band. The eigenfrequencies of alternative LH geometries mentioned in Section 5.4.1 are also numerically calculated. LH band of first alternative model is between 3.21-3.25GHz with 40MHz bandwidth. LH band of the second model is between 2.72–3.03 GHz with 310MHz bandwidth. The second model is better than the first model. However, the proposed model has lower eigenfrequencies and broader bandwidth than those of the alternative designs. These additional calculations point out why the proposed cell is selected in LHM design instead of two alternative forms.

5.4.3 Effective Parameters

Even though the left-handedness is proved with the opposite phase and group velocities in Figure 5.15, the values and sign of the effective parameters have to be determined. Therefore, effective material parameters are retrieved from the scattering parameters of one cell thick LHM array. The effective relative permittivity, permeability, complex propagation constant and wave impedance are shown in Figure 5.16. There is one important remark on the exploited extraction method. Even though there are alternative retrieval methods, one reason why to exploit this method is the cell asymmetry. Because the effective parameters are retrieved from the transmission and reflection data, there is one inherent problem in the parameter extraction of asymmetric cells [56-59]. In these cells, the reflection parameter at the first port is different from the one at the second port. In order to solve this problem, the geometrical mean of two reflection parameters is used as an effective reflection parameter in the conventional retrieval methods [57]. On the other hand, this is not necessary in the proposed retrieval procedure. This is an important advantage.

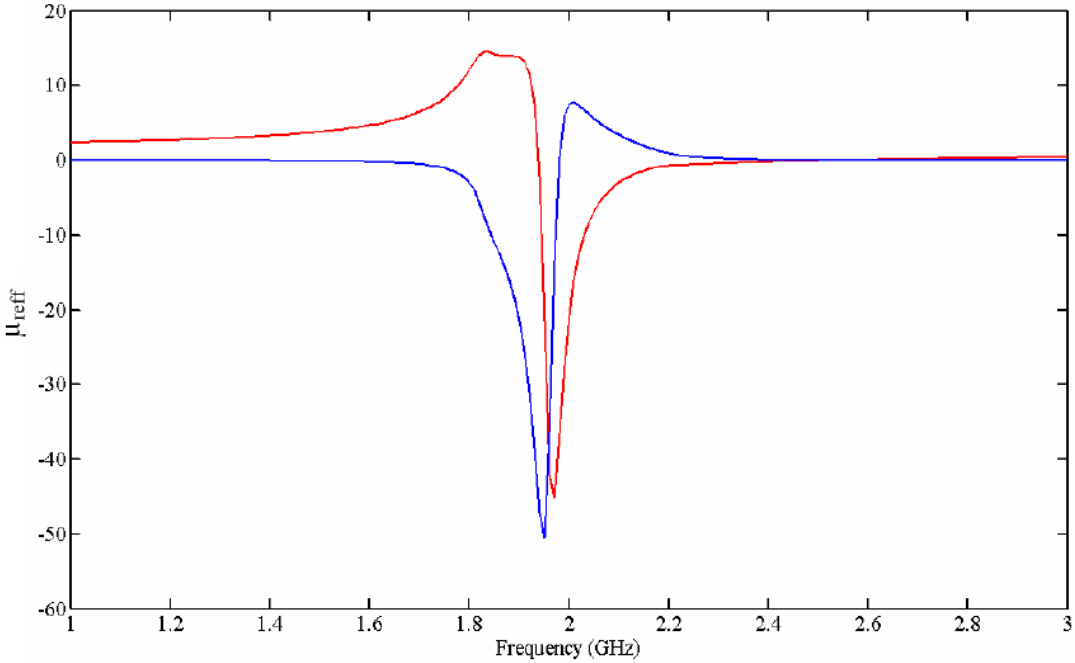

Figure 5.16a. Real (red) and imaginary (blue) part of effective relative permeability of wire loaded SR

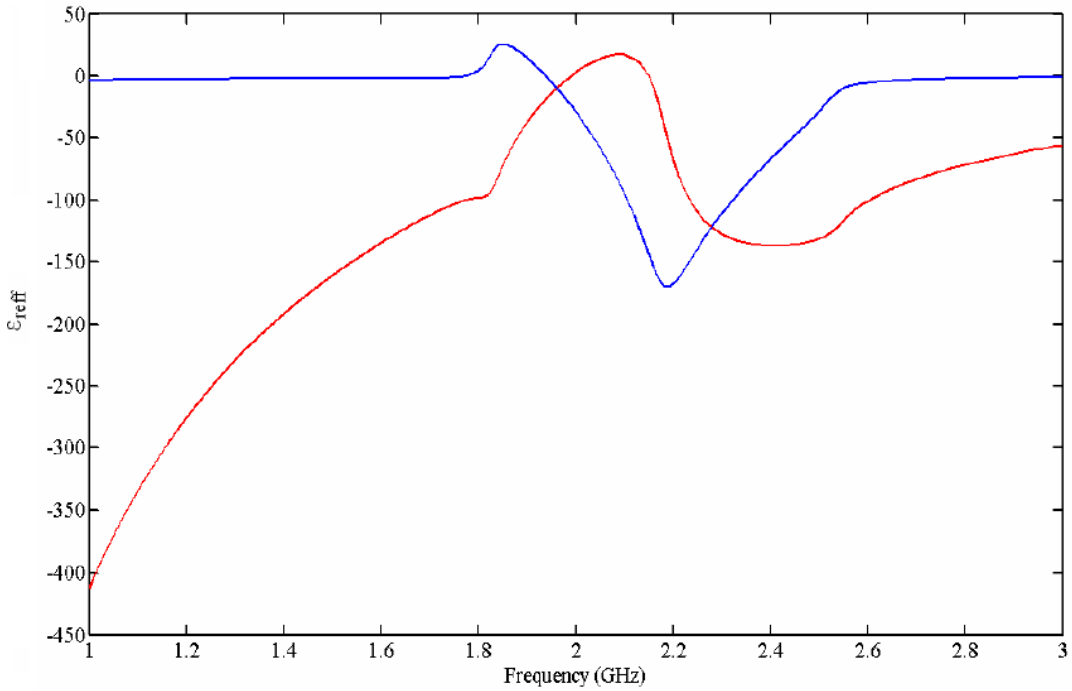

Figure 5.16b. Real (red) and imaginary (blue) part of effective relative permittivity of wire loaded SR

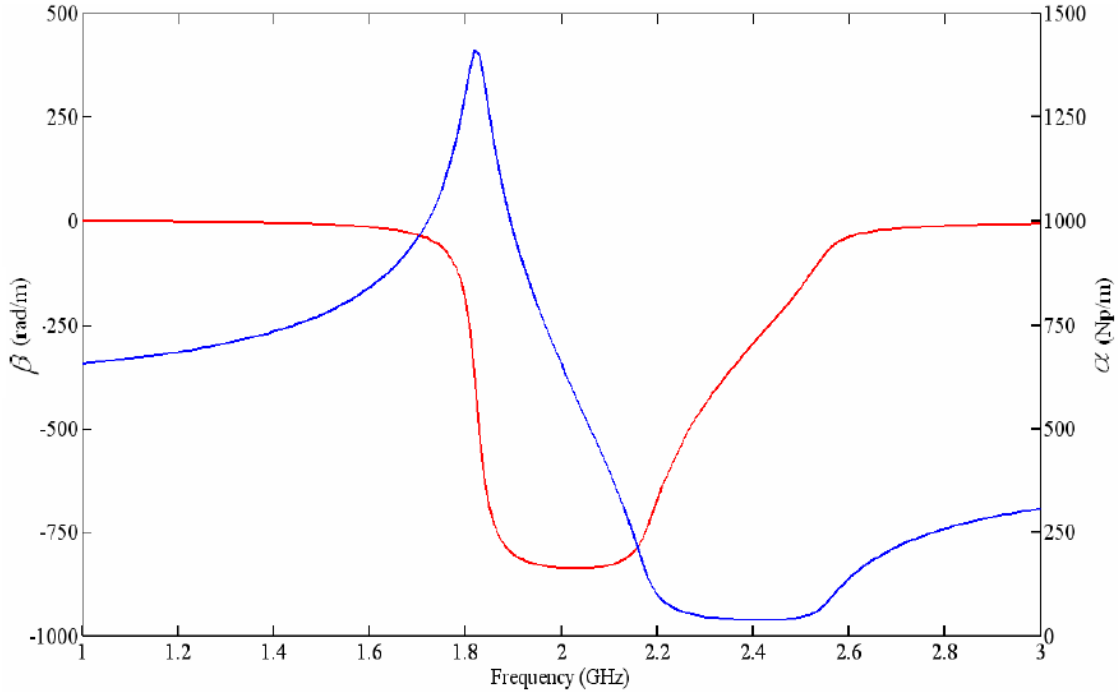

Figure 5.16c. Phase (red) and attenuation (blue) constant of wire loaded SR

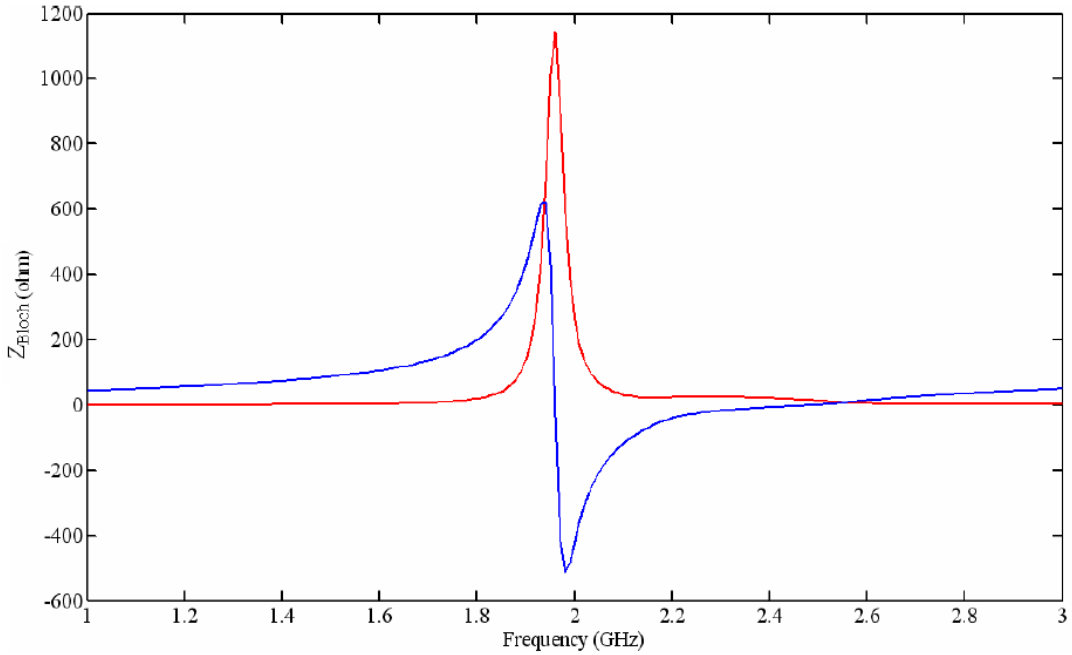

Figure 5.16d. Real (red) and imaginary (blue) part of wave impedance of wire loaded SR

There are important issues to be discussed about the frequency dependence of retrieved parameters. The retrieval procedure leads in general to the satisfying results—an expected Lorentzian type magnetic response for the effective permeability with the magnetic resonance frequency at 1.95GHz. The negative permeability region extends from 1.93GHz to 2.55GHz. Drude type permittivity response is identified upto the excitation of spiral resonator through the wire. One important remark is on the possible reason of unphysical artifacts such as positive imaginary part of permittivity and permeability at certain frequencies. One reason is that magnetic field induced polarization and electric field induced magnetization effects are not taken into account in the analytic formulation of extraction method. However, these effects are important to characterize the material. For instance, the wire can be excited with z-directed magnetic field through the spiral resonator in addition to x-directed electric field. Thus, x-directed electric field excites the spiral resonator with the resonant field distribution through the wire. In addition, the splits in the inner and outer rings and the gap region between the inner and outer rings are the other electric coupling locations for the magnetic response. In other words, both magnetic and electric fields can excite each inclusion simultaneously due to the direct connection of spiral resonator with the wire. Therefore, negative permittivity and permeability can be conveniently obtained simultaneously in a certain band in this design. The negative phase constant and negative refractive index, which is deduced from (5.4) because of negative phase shift along the propagation direction, are clearly identified in Figure 5.16c. The refractive index is therefore negative between 2.24-2.56GHz with the bandwidth of 320MHz. This LH band corresponds quite well with LH band in 1D dispersion diagram in Figure 5.15. In Figure 5.16d, the resonance in Bloch impedance is identified as in the case of wire loaded SRR in the previous section. The resonance frequency is 1.96GHz. It coincides well with the magnetic resonance frequency as expected. Bloch impedance is capacitive between the resonance frequency and higher edge of LH band, 2.56GHz. However, it is less capacitive as expected in LH band to allow plane wave transmission inside LHM array.

As a result, numerical calculations confirm negative refractive index of wire loaded spiral resonator. Because the unit cell size is approximately 1/43 of the wavelength at 2 GHz, this model can be used to design more homogeneous LH materials.

5.5 Chapter Conclusion

In this chapter, LHM design is explained. The basic design principle is based on the periodic arrangement of negative permittivity and permeability cells in the same host medium. Therefore, the eigenmode equation of periodically arranged negative permittivity and permeability materials in a rectangular waveguide is analytically calculated. The analytical calculations are confirmed by the numerical calculations with maximum error smaller than 1%. Drude type permittivity and Lorentzian type permeability responses with low electric and magnetic losses are assumed. The LH and RH bands are obtained. The possible reason of emerging RH band at the higher frequency is explained with the equivalent circuit models of negative permittivity and permeability materials. They introduce an alternative realization method of LHMs in planar microwave technology. The possible engineering applications of LHMs with both realization strategies are additionally referenced.
An LHM cell model is numerically analyzed. It is composed of same SRR and thin wire models with the geometrical dimensions indicated in Chapter 3 and Chapter 4. The main reason in selecting the same cell geometries and dimensions is to indicate that LH transmission band is the overlapping band of negative permittivity and permeability. The transmission and reflection parameters are calculated. The resonance frequency is determined. The surface current, electric and magnetic field distributions are presented. The LH band is the resulting effect of inductive loading of capacitive impedance of SRR array with the wire array. 1D Brillouin diagram is numerically calculated. LH passband is determined. The effective material parameters, Bloch impedance and complex propagation constant are additionally retrieved. At the end of the chapter, an electrically small inclusion based on the wire loading of spiral resonator is proposed as an LHM unit cell. It is numerically investigated in terms of effective permeability, permittivity, Bloch impedance and complex propagation constant. The numerical calculations confirm the effectiveness of LH cell in the design of more homogeneous composite materials with negative material parameters.

6. Metamaterial-based Antenna Design

6.1 Introduction

The fundamental theories of negative permittivity, negative permeability and left-handed metamaterials are illustrated in Chapter 3, Chapter 4 and Chapter 5. As one potential application of artificial materials in microwave communication systems, metamaterial-based antenna design is explained in this chapter. Basic concepts in electrically small antennas are introduced first. The fundamental performance limitations are explained. The minimum Q and maximum gain are the main parameters to be optimized. Therefore, these parameters are investigated to point out the effect of electromagnetic material parameters and physical dimensions on the antenna performance. The concept of artificial ground plane is additionally included as an alternative approach for directive and high gain antennas. As meta-antenna design examples, the design of broadband LHM-loaded dipole antenna is explained first. How to exploit the unit cells in the antenna design is figured out. As a second design, an alternative higher profile meta-antenna is designed. The same cell geometry in the first design is used to design a slot antenna with higher gain.

6.2 Fundamental Limits of Small Antennas

Electrically small antenna design has long been the current trend as one significant and interesting research topic in microwave community. The large dimensions of conventional $\lambda/2$ or $\lambda/4$ antennas in short-, or long-wave radio communication has further triggered to miniaturize the antenna dimensions. Especially, nowadays the demand on multifunctional complex systems imposes compact mobile terminals. The challenging issue to be overcome in the design is not only to miniaturize their physical dimensions but also not to degrade the radiation performance. The small antennas have an additional advantage especially in wireless/contactless measurement systems. They allow more reliable measurements to be done due to insignificant influence on the measured field. Hence, to design compact, high efficient/gain, broadband antennas is the main design target in any high performance wireless system.

An electrically small antenna is commonly defined as an antenna occupying a small fraction of one radiansphere, which circumscribes the maximum antenna dimension [78,79]. The radiansphere is by definition the spherical volume having the radius of $\lambda/2\pi$. This defines logically the maximum dimension to be smaller than λ/π (0.318λ) where λ is the free space wavelength. A conventional upper limit for the greatest dimension is less than one-quarter wavelength (including any image resulting from the ground plane). This results the electrically small antenna to have maximum ka value of 0.785. k is the free space wave number and a is the radius of the imaginary enclosing sphere. The main reason to have the radiansphere as a logical reference is that this radius is also the distance at which the reactive part of wave impedance is equal to the resistive part for infinitesimal electric and magnetic dipoles [80,81]. Because the radiansphere volume is larger than the near field volume for electrically small antennas, they can be modelled as a capacitive electric or an inductive magnetic dipole.

At larger distances than the radian distance, the real part of complex power dominates the imaginary part. This leads the radiating field to have more plane wave form like in the transition from the Fresnel to the Fraunhofer regime in electrically large antennas.
The operation bandwidth of any antenna for each mode can be calculated from the impedance formulation with reference to the modal equivalent circuits on the sphere of radius, a [82]. The modal impedance has the form of $Z(\omega) = R(\omega) + j\, X(\omega)$ at the reference terminal for the excited mode current, I_n . It can be derived from Poynting formulation in the form of

$$\frac{1}{2}\oint_S \left(\vec{E} x \overrightarrow{H^*}\right).\overrightarrow{dA} = -j2\omega \int_V \left(\frac{1}{4}\mu\left|\vec{H}\right|^2 - \frac{1}{4}\varepsilon\left|\vec{E}\right|^2\right)dV - \frac{1}{2}\int_V \left(\vec{E}\bullet\overrightarrow{J^*}\right)dV = \frac{1}{2} I_n{}^2 Z(\omega) \tag{6.1}$$

The real part consists of both the radiation and losses. The imaginary part is proportional to the difference of time averaged stored magnetic and electric energy outside the spherical volume.
The impedance bandwidth is often characterized by Q factor at the resonance frequency. The antenna Q is inversely proportional to the fractional bandwidth. It has a theoretical lower bound. Therefore, no electrically small antenna can exhibit a Q value less than its theoretical lower bound or bandwidth larger than a specific upper bound. The antenna Q is generally defined as in (6.2). W_e and W_m are the time average stored electric and magnetic energy. P_{loss} is the sum of total radiated and metallic loss power at the resonance frequency, ω_0 [82,83].

$$Q = \begin{cases} 2\omega_0 \dfrac{W_e}{P_{loss}}, W_e > W_m \\ 2\omega_0 \dfrac{W_m}{P_{loss}}, W_m > W_e \end{cases} \tag{6.2}$$

This formulation is actually the same formulation, which can be derived from the Poynting formulation in (6.1). It is the ratio of imaginary and real part of complex power for high Q antennas. In the lower bound calculation of Q, an arbitrary current distribution is assumed on a wire antenna. The near field distribution is then calculated in terms of a series expansion of all higher order spherical modes excited by I_n. The modal Q_n can then be calculated in the terms of modal tangential field quantities on the spherical surface of radius a as [82],

$$\begin{aligned} Q_n &= \frac{2\omega W_n}{P_n} = \frac{1}{2}\left|\rho h_n(\rho)\right|^2 \left[\rho \frac{d}{d\rho} X_n(\rho) - X_n(\rho)\right] \\ X_n &= \left[\rho j_n(\rho)\left(\rho j_n(\rho)\right)' + \rho n_n(\rho)\left(\rho n_n(\rho)\right)'\right] \left|\rho h_n(\rho)\right|^{-2} \end{aligned} \tag{6.3}$$

where h_n is the nth order spherical Hankel function of second kind. It is defined as $h_n = j_n - j.n_n$. j_n and n_n are the spherical Bessel functions of the first and second kind.

ρ is ka. The above relation is plotted in Figure 6.1. In Figure 6.1, for a specific antenna size and excited mode, with increasing operational frequency the stored energy decreases and radiation resistance increases. This is consistent with the complex power calculations on elementary electric dipole and can be derived [80].

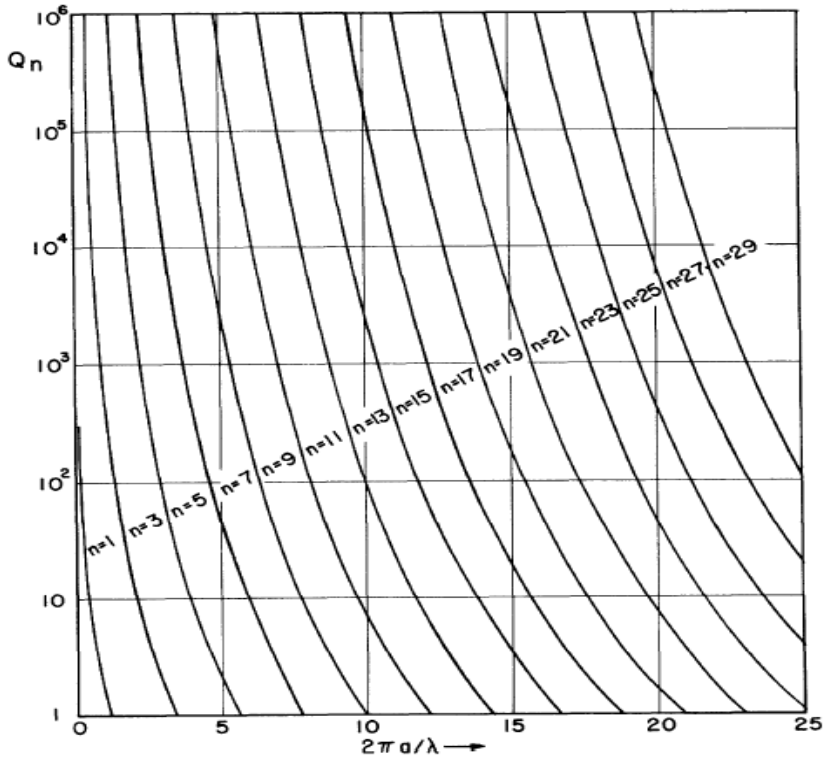

Figure 6.1. Modal Q_n of vertically polarized omnidirectional antenna [82]

On the other hand, higher order modes result the antenna to have higher Q. However, to excite higher order modes is in practice quite challenging. It is because of the difficulty in matching high reactive impedance. Therefore, the main conclusion in minimum Q calculation is that Q can only be minimized under one mode excitation without multimode operation. Because Q of lowest order mode is minimum, the antenna in the form of an infinitesimally small dipole has potentially the broadest bandwidth [82]. Therefore, the optimum method to obtain broad bandwidth is to operate the antenna with the lowest of all possible modes. The theoretical lower bound for small directional and omnidirectional antennas is expressed as in [83]

$$Q_{\text{small}}^{\min} = \left(\frac{1}{2(ka)^3} + \frac{1}{ka} \right) \tag{6.4}$$

Q can be alternatively calculated from the input impedance of a tuned antenna exhibiting a single resonance frequency as [84]

$$Q(\omega_0) = \frac{\omega_0}{2R(\omega_0)} \sqrt{\left(R'(\omega_0)\right)^2 + \left(X'(\omega_0) + \frac{|X(\omega_0)|}{\omega_0} \right)^2} \tag{6.5}$$

where $R^{'}(\omega_0)$ and $X^{'}(\omega_0)$ are the frequency derivatives of real and imaginary parts of feed point impedance at the resonance frequency, ω_0. As implied from (6.5), one method to minimize Q can be to increase the radiation resistance by using self-resonant radiators. This has an additional advantage of no matching network requirement. This reduces not only the antenna size but also the matching losses. It is an important issue. The loss resistance within the matching network often exceeds the radiation resistance in electrically small antennas. This degrades the overall efficiency [85]. Thus, one strategy could be to design self resonating structures to increase the radiation resistance and enhance the operation bandwidth.

In gain optimization, it is well known that there is no mathematical limit in the maximum gain [82],[86]. However, a small antenna with extremely high gain produces high field intensity in the vicinity of the antenna. The antenna gain is therefore limited with an upper bound in practice. The maximum gain obtainable is calculated as $G_{max}= N(N+2)$ with the maximum excited mode order N [86]. As N increases, the maximum gain increases with a disadvantage of practical difficulty in the design of matching network. In other words, the excitation of higher order modes to increase the radiation resistance results total stored energy to increase in the antenna near field as in Figure 6.1. Due to this trade-off between gain and Q, there is one additional parameter to be maximized for the optimum antenna design. This parameter is the ratio of gain (G) to Q. The maximum G/Q ratio for the small antennas is expressed as [83],

$$\max \left.\frac{G}{Q}\right|_{dir}^{small} = \frac{6(ka)^3}{2(ka)^2+1}$$
$$\max \left.\frac{G}{Q}\right|_{omni}^{small} = \frac{3(ka)^3}{2(ka)^2+1} \qquad (6.6)$$

Antenna gain can be alternatively expressed with an additional parameter [81],[87]. It is called radiation power factor (PF). It is an alternative description relating the radiating energy with the stored reactive energy inside the antenna near field. It is a valid parameter for either kind of electrically small electric or magnetic antennas. It is equal to 1/Q. It can be expressed in terms of input impedance as the ratio of the input resistance to the reactance at the resonance frequency. For any shape and type of electrically small antenna, the radiation PF at one frequency is proportional to its physical volume. Moreover, the radiation PFs of electric and magnetic dipoles are approximately same for similar physical volume.

The main difference of radiation PF from the radiation parameters introduced previously is the definition of the calculation volume. The near field distribution of any small electric or magnetic antenna can be assumed to be confined in an effective spherical volume of V' with radius a'. The radiation PF can then be calculated in terms of V' and volume of radiansphere, Vs as [81],[87]

$$PF = \frac{2}{9}\frac{V'}{Vs} = \frac{2}{9}\left(\frac{2\pi a'}{\lambda}\right)^3 \qquad (6.7)$$

Thus, one method to enhance the radiation PF is to increase the effective volume of electric and magnetic dipoles. This can be achieved by decreasing the substrate permittivity or increasing the core permeability, respectively. The logical approach in this method is to eliminate or minimize the avoidable stored energy inside the core or substrate by leaving unavoidable amount of stored energy outside the core or substrate. The enhancement of radiation resistance with low permittivity and high permeability is also consistent with the radiation resistance formulations of Hertzian electric and magnetic dipoles.

In addition, the design of high permeability materials has an additional potential application. They can be used in the realization of artificial ground planes to increase the gain and directivity. [6]. In general, the performance of low profile wire antennas is degraded by their ground plane backings. It is because of out-off phase image current when the antenna is horizontally oriented in close proximity to the ground. If the separation distance between the antenna and ground is $\lambda/4$, the ground plane reflects the antenna radiation in phase with an approximately 3 dB increase in the antenna gain. The radiation degradation occurs if the ground plane-antenna separation distance is smaller than $\lambda/4$. It can not provide gain increase. The reflected back-radiation interferes destructively with the antenna forward-radiation. Therefore, the antenna can be attributed to be partially "short circuited". A second problem especially in the microstrip antenna design is the generation of surface waves. The field distribution on the feeding line and antenna near field excite the propagating surface wave modes of the ground-substrate-air system. This results into the radiation efficiency degradation. The guided waves can deteriorate the antenna radiation pattern by reflecting from and diffracting at the substrate edges and other metallic parts. To solve these problems, a Perfect Magnetic Conductor (PMC) would be an ideal solution for low profile antennas. The antenna radiation is reflected from PMC without a phase-shift due to high surface impedance as in negative permeability materials at the resonance frequency. They can be designed by introducing artificial magnetic materials on the substrate surface. These surfaces are called alternatively as Electromagnetic Bandgap (EBG) surfaces or Artificial Magnetic Conductors (AMC) [6],[88]. There are two regions in such structures. The first one is caused as a result of array resonance and array periodicity. This is the region where the surface waves are suppressed and reflected within an electromagnetic bandgap. The second region is obtained due to the cavity resonance formed by the ground plane and structures on the substrate. This is the region where the radiating waves are reflected with no phase shift as in the case of high impedance surfaces. The most commonly known EBG surface is the mushroom EBG [89]. It consists of an array of metal patches. Each of them is connected with a via to the ground through the substrate. The capacitively coupled metal patches and inductive vias create a grid of LC resonators. A planar EBG can also be designed, which does not have any vias and acts as a periodic frequency selective surface (FSS). A widely used EBG surface is the Jerusalem-cross [90,91]. It consists of metal pads connected with narrow lines to create an LC network. On the other hand, the negative permeability metamaterials have also been frequently used in AMC design [92].

After the explanation of small antenna fundamentals, two metamaterial-based compact antenna designs are proposed and numerically investigated in the next sections.

6.3 LHM-based Broadband Dipole Antenna

In this section, the design of a metamaterial-based microstrip antenna is explained [76]. The antenna is composed of six LHM unit cells, which are directly connected to the dipole. These cells have the same geometry in Section 5.4. The input impedance is matched to 50Ω with the stepped impedance transformer and rectangular slot in the truncated ground. The configuration and operation principle of the dipole antenna are explained in Section 6.3.1. The simulated and measured return losses, radiation pattern and numerically computed radiation parameters are illustrated in Section 6.3.2.

6.3.1 Antenna Design

The antenna model is shown in Figure 6.2a and Figure 6.2b. In the first step, how to interconnect LHM cells has to be figured out to design broadband load for the dipole. The front and back side resonators in Figure 5.13 are connected symmetrically with the adjacent cells in the x-direction. They are then connected in a periodic form with the ones in the y-direction. This interconnection form is implied from the boundary conditions in the eigenmode calculation in Section 5.4. Six cells are used and arranged in a 2x3 array. The front sides are directly connected to the dipole in order to increase the field coupling. This results additionally the impedance of LH load to be transformed by the dipole. The ground plane is a truncated ground plane with a rectangular slot. This results the dipole to radiate more effectively due to lack of out-off phase image current. In addition, tuning the slot size makes the antenna to be better impedance matched. The rectangular slot can be modeled by a shunt element as a parallel LC resonator in series with the capacitance [93]. The width of the slot is appreciably smaller than half of the wavelength in the substrate. The fabricated prototype is shown in Figure 6.2c. The geometrical parameters are tabulated in Table 6.1.

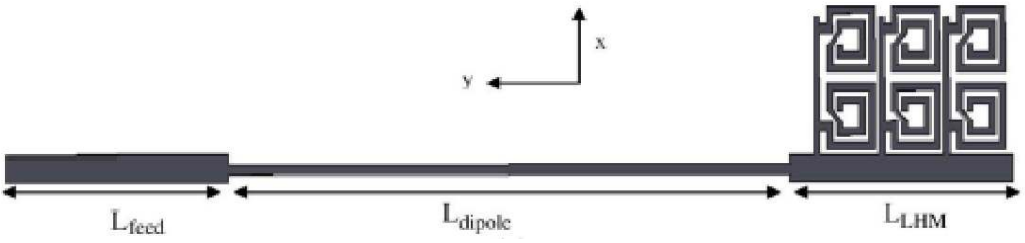

(a)

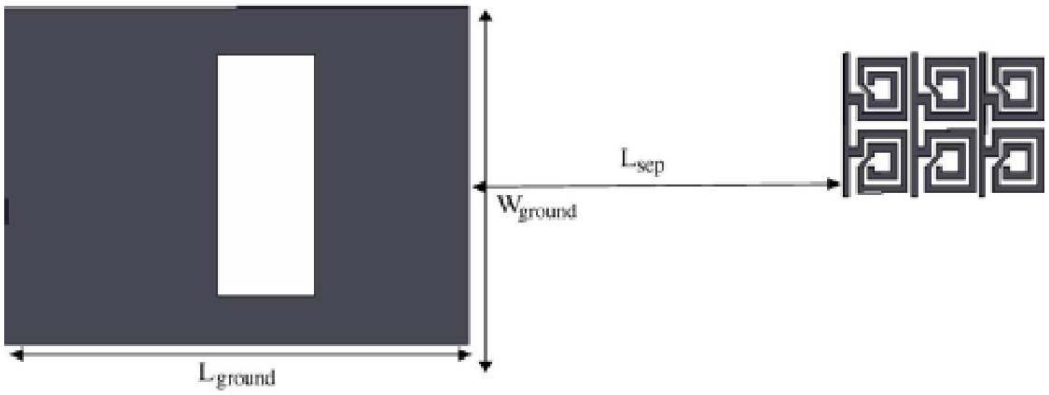

(b)

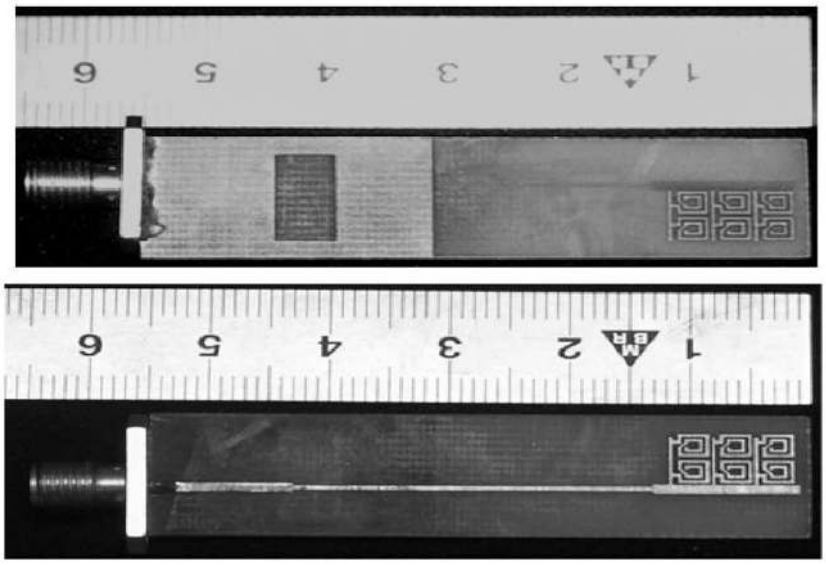

(c)

Figure 6.2. (a) Top (b) bottom geometry and (c) prototype of LHM loaded dipole antenna

Table 6.1 Geometrical Parameters of LHM loaded Dipole Antenna (mm)

Length of substrate	55
Width of substrate	14
Length of feeding line (L_{feed})	12
Width of feeding line	1
Length of dipole line (L_{dipole})	30
Width of dipole line	0.4
Dipole-LHM coupling length (L_{LHM})	12
Length of ground plane (L_{ground})	24
LHM-ground separation length (L_{sep})	19.3
Slot width	5
Slot length	10

The overall size of the dipole antenna is 55x14 mm. The size of the main radiating section is 30x14 mm. The operation principle is based on the radiation of the dipole and excitation of LHM cells with the dipole field. The cell excitation in their modal currents couples the electric and magnetic dipoles in the same way as in the eigenmode calculation in Section 5.4. These dipoles are also the radiation sources in addition to the exciting dipole antenna. The magnetic and electric dipole moments are expressed by the surface current density, $\overrightarrow{J_e}$ as [94].

$$\overrightarrow{p_m} = \frac{\mu_0}{2}\int_S \vec{r} x \overrightarrow{J_e}(\overrightarrow{r'})ds'$$
$$\overrightarrow{p_e} = \frac{j}{\omega}\int_S \overrightarrow{\nabla} \bullet \overrightarrow{J_e}(\overrightarrow{r'})\overrightarrow{r}\,ds' \qquad (6.8)$$

where $\vec{r}$ is the displacement vector directed from the surface current element to the observational point. $\vec{r}'$ is the current element position. ds' is the current carrying surface element.
Therefore, the electric and magnetic dipoles are in principle simultaneously excited at each cell. However, the magnetic dipoles are more effectively excited than the electric dipoles. The first reason is that magnetic dipole fields do not cancel in the far field because of the electric coupling among the cells. In addition, the current on the back side wire is partially oppositely directed to the current on the front side wire. This is the second reason why the electric dipoles can not be excited as effectively as the magnetic dipoles. As a last reason, the surface current on the back side cell spirals in the same direction as the surface current on the front side cell. In that respect, the front and back side cells are mainly magnetically coupled. However, as stated in the design principle, the antenna radiates mainly in the dipole mode. This is the reason why it is called as an LHM-loaded dipole antenna.

6.3.2 Experimental and Numerical Results

The return loss is measured with the vector network analyzer HP 8722C. It is shown in Figure 6.3 together with the numerical result. The operation band extends from approximately 1.3 GHz to 2.5 GHz with the center frequency of 1.9 GHz. The impedance bandwidth is 63.16 % of the center frequency. Three cell resonances can be clearly identified from the numerical calculation. However, there are resonance frequency shifts between the measured and simulated return losses. The uncertainty in the substrate permittivity and loss tangent is one reason of these frequency shifts. The deviations of the actual values from the model values result the input impedance not to be 50 Ohm. This degrades the impedance matching at the antenna feeding point. The low frequency ripples can be attributed to the impedance mismatch and inaccurate modeling of the coax-microstrip line transition. In summary, the measured and simulated return losses are in good agreement.

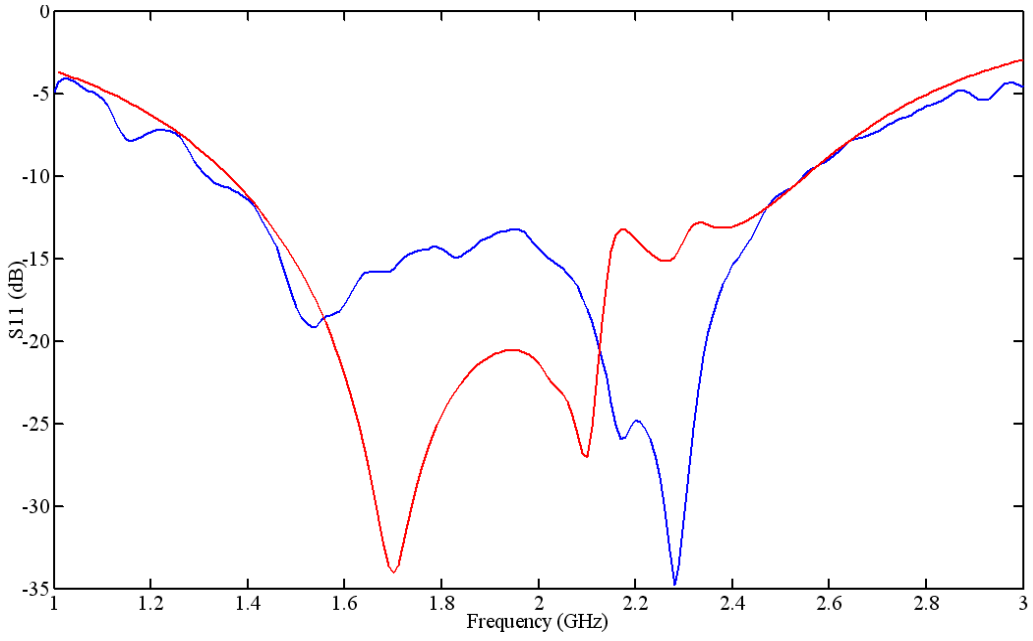

Figure 6.3. Measured (blue) and simulated (red) reflection coefficients of LHM-loaded dipole antenna

There are nevertheless some other issues to be discussed about the measured and simulated results. First of all, in the numerical result, there are lower resonance frequencies than the LH resonance frequencies in Section 5.4. These lower frequencies are due to the direct coupling between the dipole and LHM cells. They are not emerging from LH resonances. The LH resonances can be clearly identified from the foot-point impedance shown in Figure 6.6. In order to prove this reasoning, the surface current distributions at 1.72 GHz and 2.07 GHz are shown in Figure 6.4 and Figure 6.5.

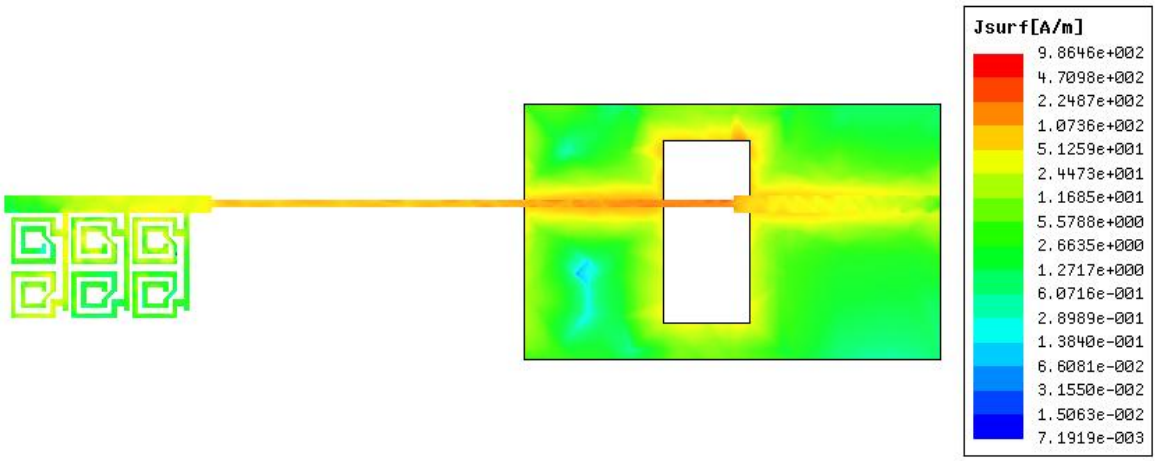

(a)

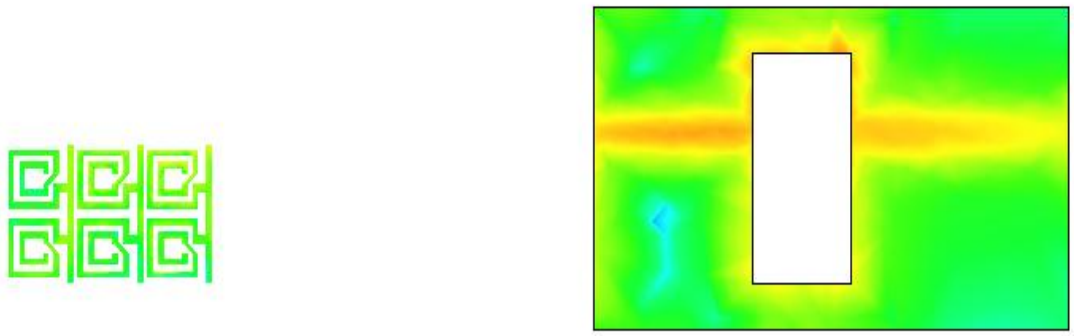

(b)

Figure 6.4. Surface current distribution on the (a) top and (b) bottom side of LHM-loaded dipole antenna at 1.72GHz

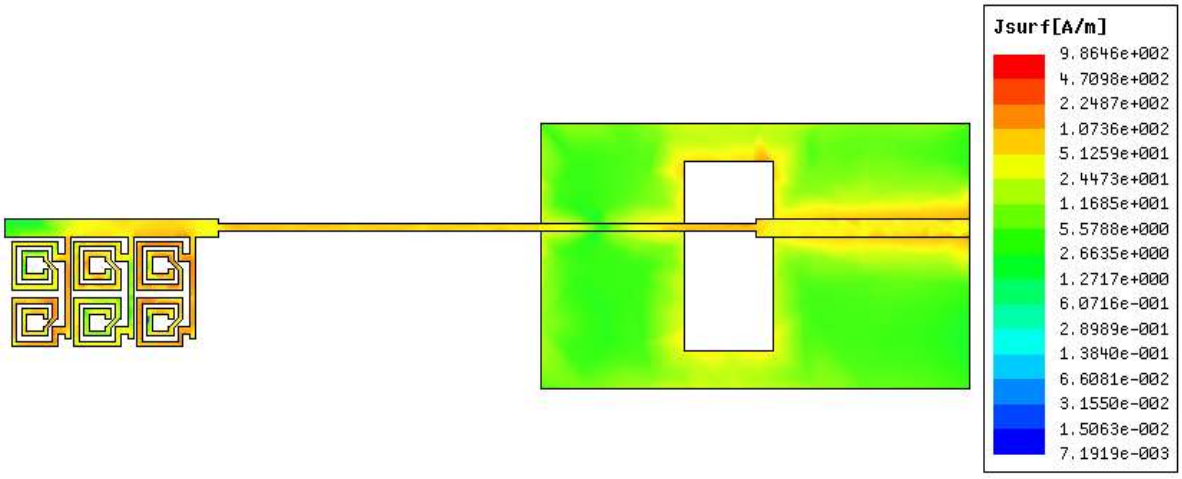

(a)

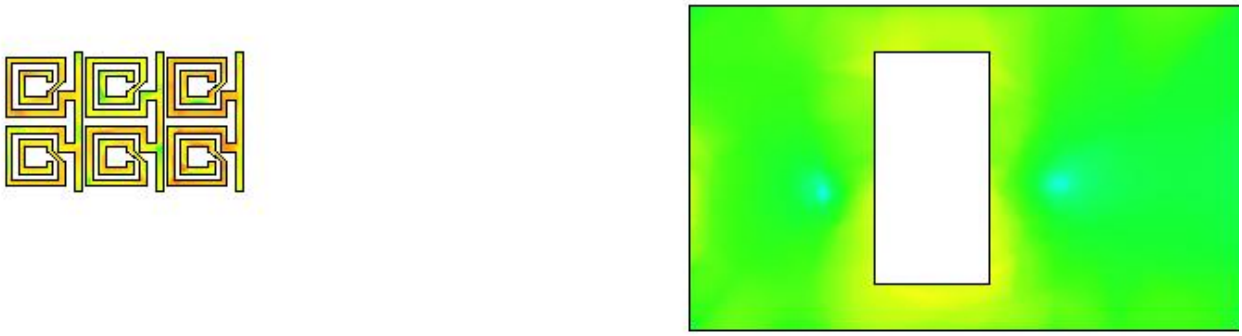

(b)

Figure 6.5. Surface current distribution on the (a) top and (b) bottom side of LHM-loaded dipole antenna at 2.07GHz

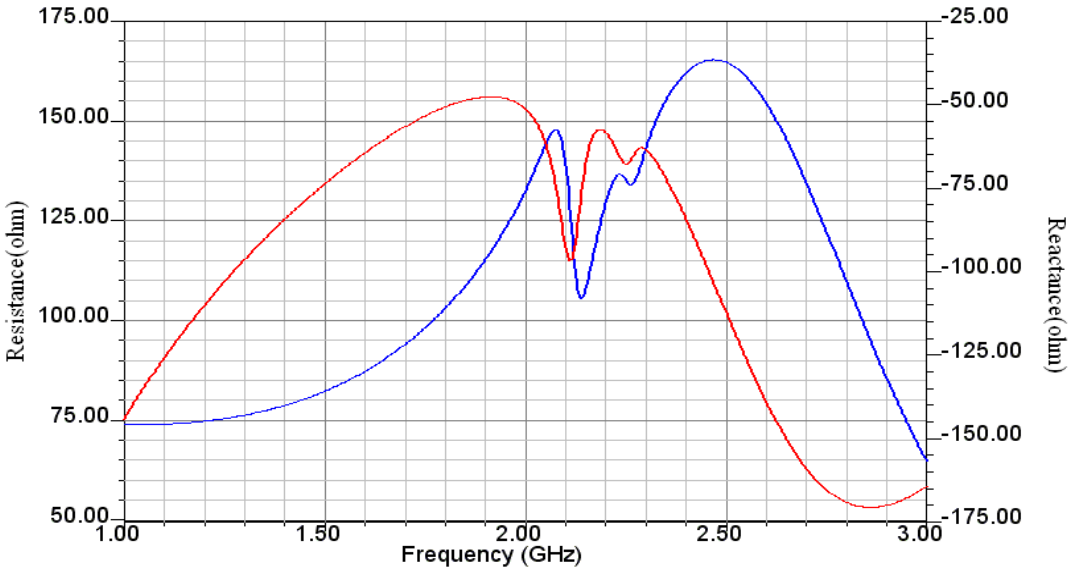

Figure 6.6. Real (blue) and imaginary (red) parts of the foot-point impedance of LHM-loaded dipole antenna

In Figure 6.4, the dipole line is excited more effectively than LH cells at 1.72GHz. It is an expected result because the lowest LH frequency is higher than 1.72GHz. In Figure 6.5, LH load is effectively excited with the dipole at 2.07GHz. In other words, the resonance frequency, 1.72 GHz is the result of impedance transformation of LH load through the dipole with the stepped impedance and rectangular slot in the ground. It is not an LH resonance. However, LH load is important for broadband operation. The simultaneous excitation of different LHM and dipole sections in the operation band is the reason why the antenna has broad bandwidth. The LH resonances at the lower frequencies are closer than the ones at the higher frequencies. This unique property is one reason of broadband feature at the lower frequencies. This is not the case in RHM-based antennas [5]. The same reasoning can also be confirmed from the dispersion diagram in Figure 5.15. Therefore, the coupled resonance feature of LHM cells results the antenna input impedance to have smooth frequency dependence. The third important issue is the radiation of LHM cells. It could be verified not only from the current distribution and return loss but also from E- and H-plane radiation patterns. Therefore, the normalized radiation patterns in y-z and x-z planes at 1.72 GHz and 2.07 GHz are shown in Figure 6.7. They are mainly dipole-like co-polarization radiation patterns. This is the reason why to call the microstrip antenna as an LHM-loaded dipole. The radiation of LHM cells is verified from the radiation pattern at 2.07 GHz.

The radiation patterns of cross-polarization in y-z and x-z planes are similar to the co-polarization radiation patterns of the magnetic and electric dipoles with shifted phase centers, respectively. The radiation intensity of cross-polarization in y-z plane at 2.07GHz is 4.77 dB more than that at 1.72 GHz due to the excitation of electric and magnetic dipoles. The gain is unfortunately small. The maximum gain and directivity are -1 dBi and 3 dB. The radiation efficiency is 40% at 2.5 GHz. The directivity, gain and radiation efficiency in whole operation band are shown in Figure 6.8. In addition, the gain is higher than that of the different kinds of miniaturized and narrow band antennas in the literature [95-97].

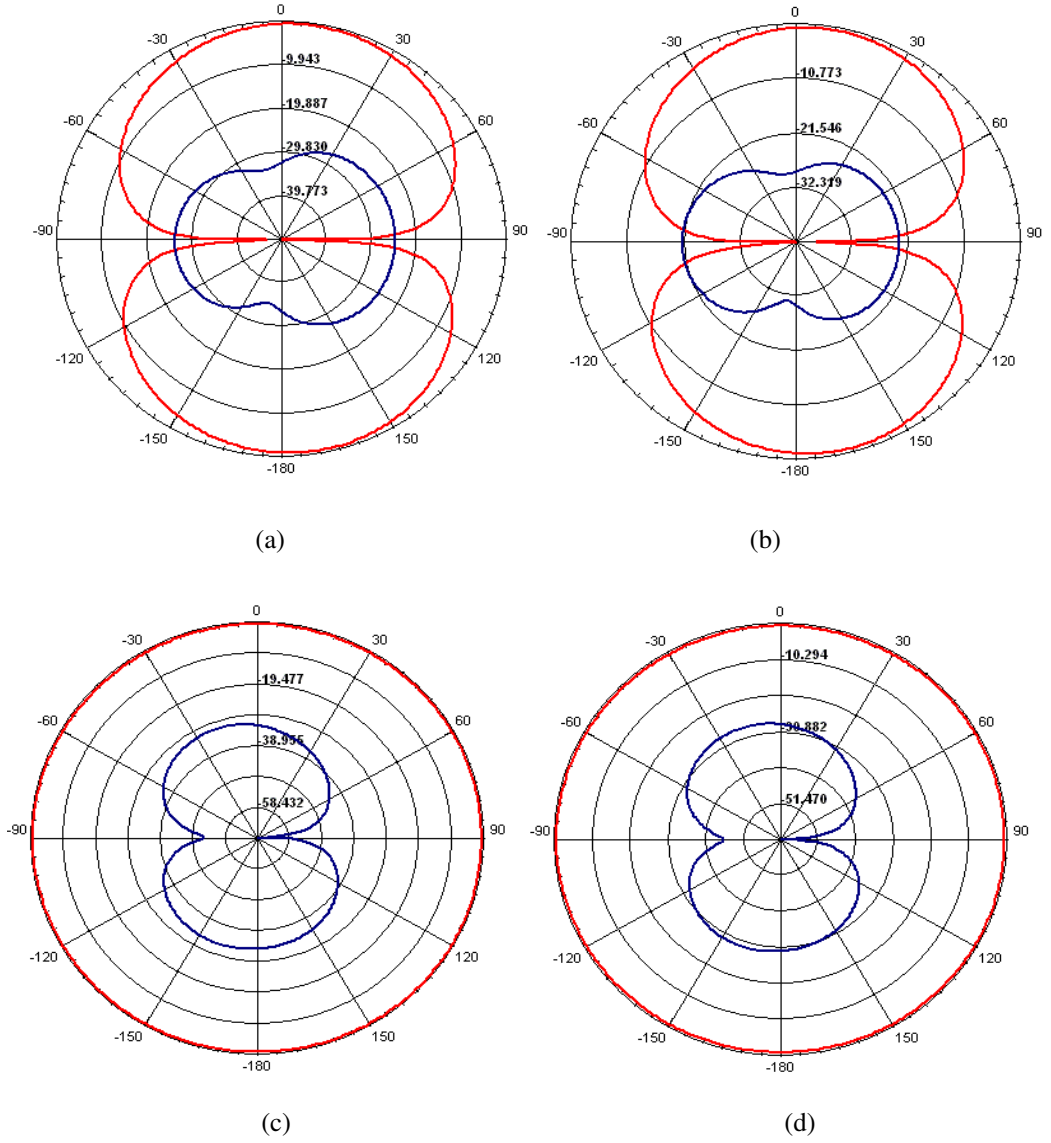

Figure 6.7. Normalized cross-polarization (blue) and co-polarization (red) radiation patterns at 1.72 GHz in (a) y-z and (c) x-z plane, and at 2.07 GHz in (b) y-z and (d) x-z plane

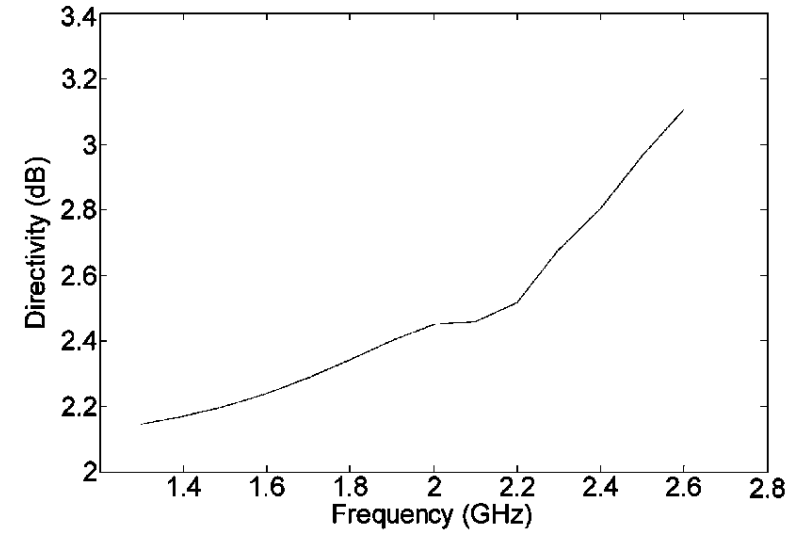

(a)

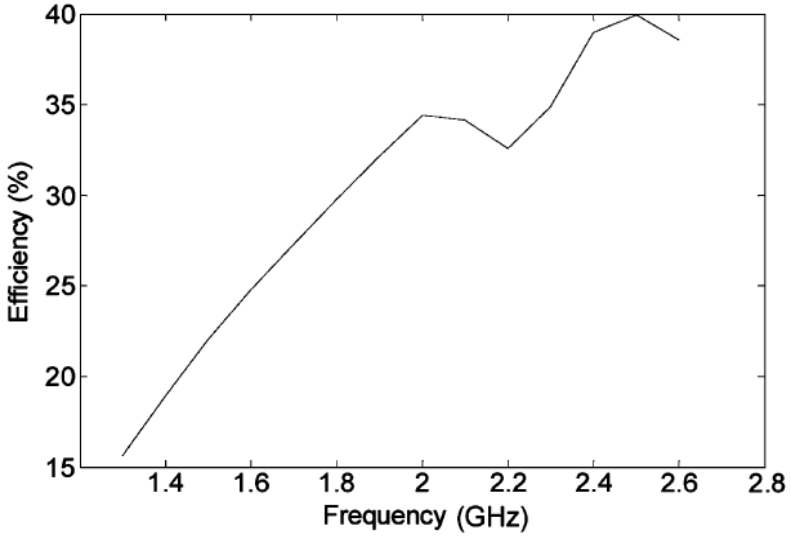

(b)

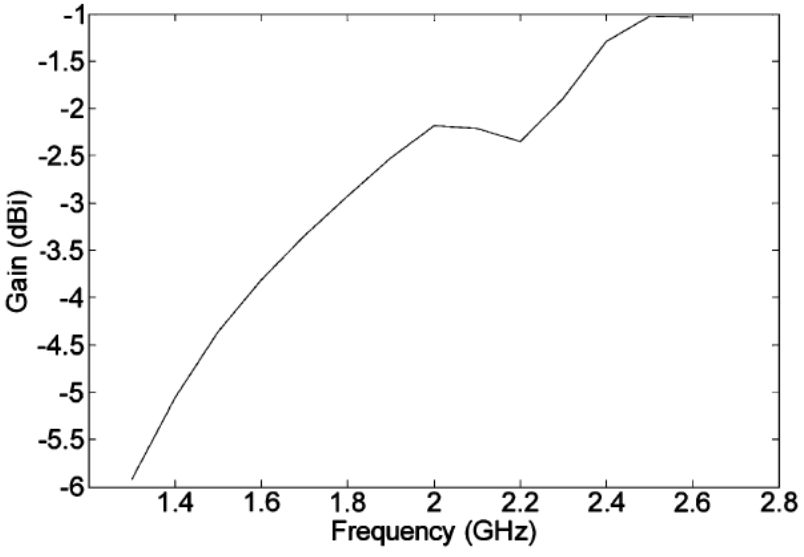

(c)

Figure 6.8. Directivity, radiation efficiency and gain of LHM-loaded dipole antenna

On the other hand, there are alternative design techniques instead of loading a narrowband dipole antenna with LHM cells for broadband operation. Some of these techniques are to increase the substrate thickness, use different shaped slots or radiating patches [98], stack and load different radiating elements with the antenna laterally or vertically [99,100], utilize magnetodielectric substrates [101] and engineer the ground plane as in the case of EBG structures [6]. These techniques result additionally into the gain improvement of microstrip antennas. The main reasons of low gain in the current design are the substrate/copper loss and the horizontal orientation of the radiating section over the ground. It is like in the case of gain reduction of the horizontal dipole with a small separation distance with the ground. Another reason is that the increasing phase difference per cell with decreasing frequency results LHM cells not to radiate effectively. This is the reason why there is a gain and efficiency improvement at the increasing frequencies in Figure 6.8.b and Figure 6.8.c.
In the next section, a metamaterial-inspired slot antenna is introduced to illustrate how to design a high gain antenna with LHM cells.

6.4 Metamaterial-Inspired Slot Antenna

In this section, a high profile metamaterial-inspired antenna is explained [102]. It consists of LHM-based slot radiator and a T-formed feeding line. The slot radiator is composed of four slotted cells of the same form as in the previous antenna. In Section 6.4.1, the geometrical model of the slot radiator is introduced. In Section 6.4.2, the antenna geometry is explained along with the design and operation principles. In Section 6.4.3, the numerically calculated return loss and radiation patterns are illustrated.

6.4.1 Metamaterial Slot Radiator Design

The radiating section of the antenna is a slotted metal plate as shown in Figure 6.9. It is designed by perforating four resonators in the same form of LH cells as in Section 6.3. The electrical length of each resonator is increased by the direct connection with the adjacent resonator. It is in principle in the form of two coupled $\lambda/2$ slot resonators. This perforated structure is located horizontally with an optimum separation distance from the ground. Therefore, the feeding line has to be located vertically to the ground plane for optimum field coupling to the radiator. The overall size of the slot radiator is 14 mm x 6 mm. The separation distance between each pair of the resonators is 0.4 mm.

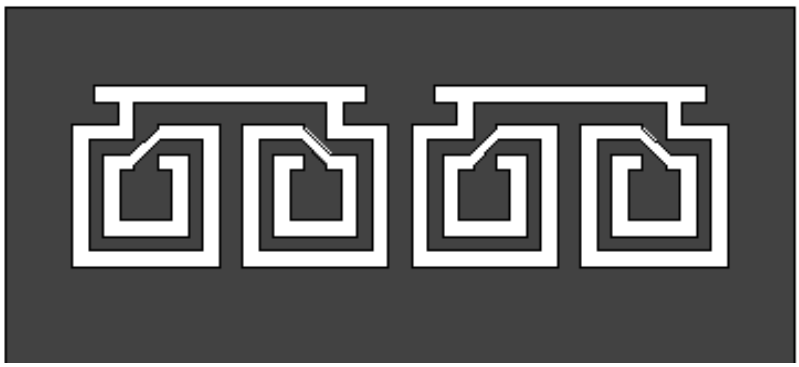

Figure 6.9 Metamaterial slot radiator geometry

6.4.2 Antenna Design

The metamaterial-inspired slot antenna is shown in Figure 6.10. In the model, the inner conductor of SMA is connected with a T-formed feeding line. It is shown in Figure 6.10a and 6.10b. The length of the extended inner conductor is 2 mm. The substrate is FR4 with the relative permittivity of 4.4 and loss tangent 0.02. The width, length and thickness of the substrate are 14 mm, 8 mm and 0.5 mm, respectively. The ground plane length, L_{grn}, is 6 mm. There is a small coupling gap, w_{gap} between the slot radiator and feeding line. It improves the impedance matching and capacitive coupling from the feeding line to the slot resonators. The width and length of coupling gap are 0.2 mm and 14 mm, respectively. The arm width, W_{mat} and length, L_{mat} of T-formed feeding line are 6.5 mm and 6 mm, respectively. The feeding line is located exactly at the middle position of the resonators as shown in Figure 6.10c. Therefore, two pairs of slot resonators are always coupled magnetically with each other. This feeding method has two main advantages. The first advantage is that the substrate of T-formed feeding line is a supporting material on which the slot radiator is located as shown in Figure 6.10a. The second advantage is that it allows the matching network to be adequately designed without increasing the antenna size as shown in Figure 6.10b.

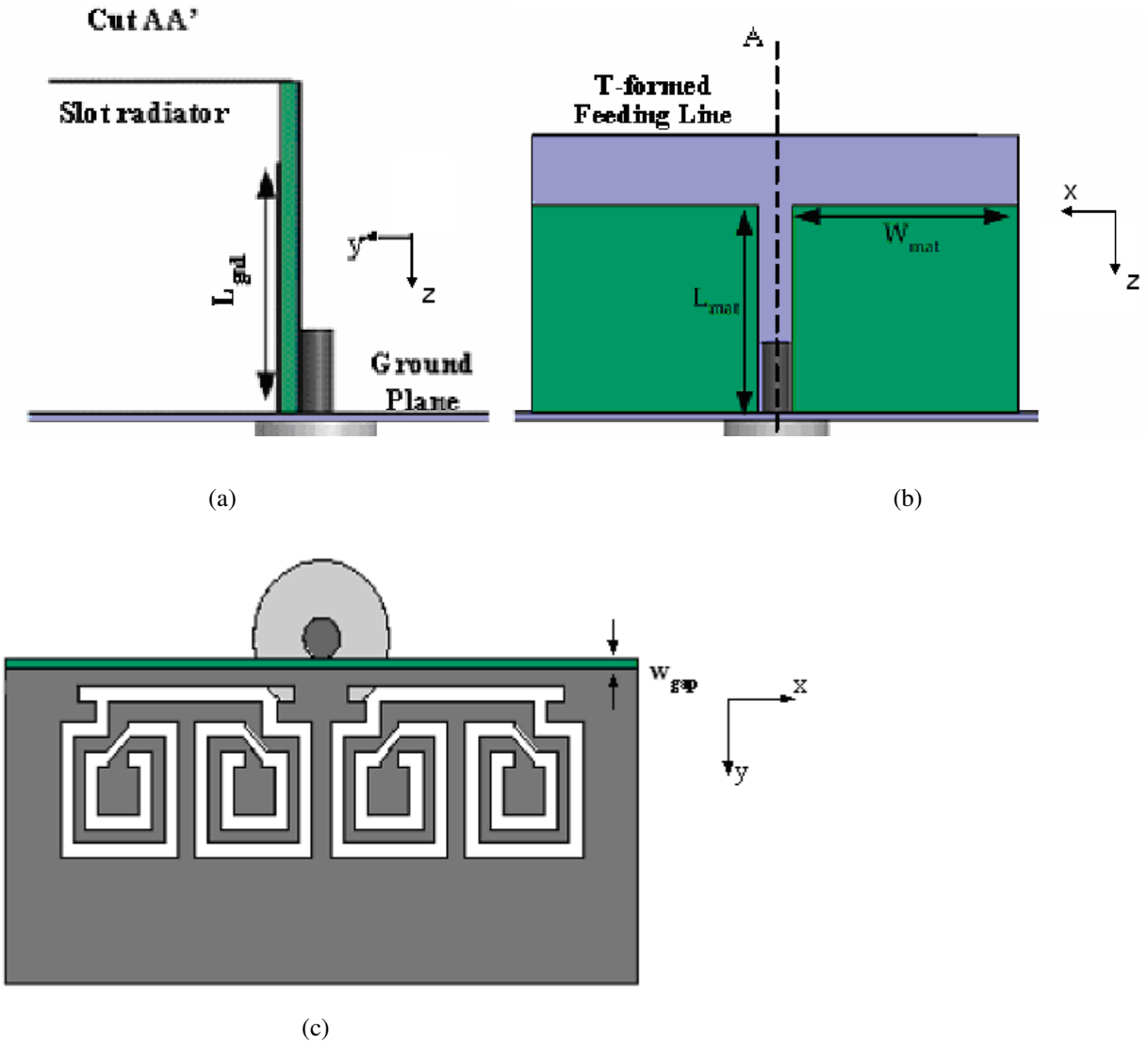

Figure 6.10 (a-b) Side and (c)top views of metamaterial-inspired slot antenna

The design principle is based on the simultaneous excitation of slotted spiral resonators and slotted wires in LH cells at the resonance frequency. In this design, slotted spiral resonators can be regarded as vertical electric dipoles due to spiralling magnetic current, whereas straight slots can be regarded as horizontal magnetic dipoles. Because vertical electric and horizontal magnetic dipoles have image dipoles in the same direction due to underlying ground plane, the proposed antenna can radiate effectively in the far field.

6.4.3 Simulation Results

The return loss is numerically calculated and shown in Figure 6.11. The resonance frequency is 5.25 GHz.

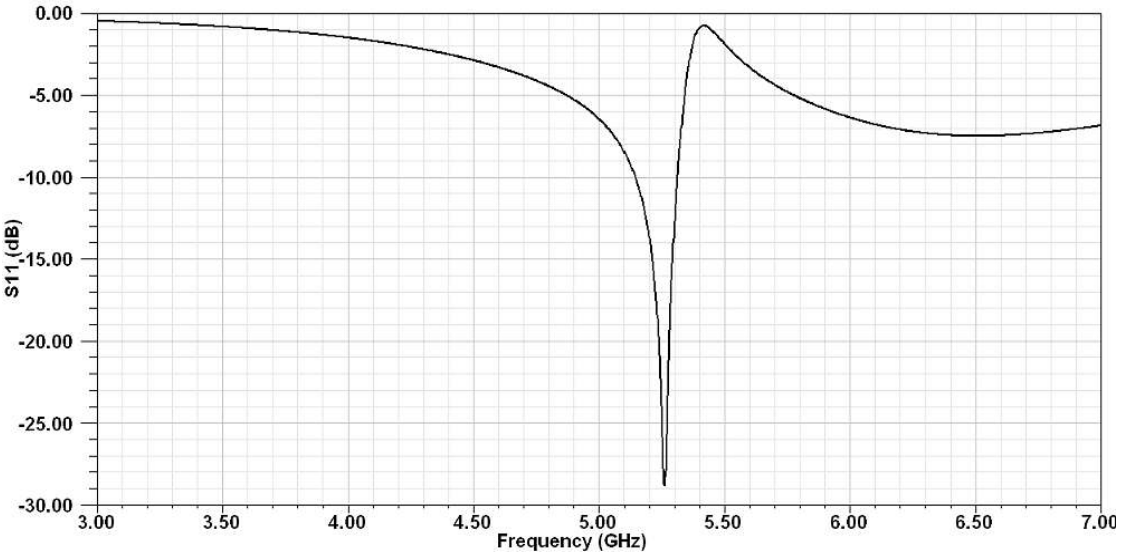

Figure 6.11. Return loss of the metamaterial-inspired slot antenna

The truncated ground plane of feeding line increases the field coupling from the transmission line to the slot resonators. Therefore, the antenna is better impedance matched. Another advantage of the ground plane is the effective coupling of the incoming field from SMA connector to the slot radiators without any leakage to the larger ground. The current distribution at the resonance frequency is shown in Figure 6.12. In Figure 6.12a, the slot resonators are excited with eigenmode field distributions through the feeding line.
The normalized radiation patterns on horizontal and vertical planes at 5.25 GHz are shown in Figure 6.13. In Figure 6.13, the co-polarization radiation pattern on horizontal plane is similar to horizontal plane radiation pattern of elementary electric dipole. It is because of the excitation of the slotted form of spiral resonator in the form of virtual magnetic current. Spiralling magnetic current results the near field distribution to be in the form of the electric dipole due to Babinet's principle and duality. However, the radiation pattern on vertical plane is not similar to the radiation pattern of electric dipole. Two possible reasons of enhanced radiation on the dipole axis are the superposition of the dipole fields in four element array and the shift of phase center. The third reason can be the excitation of another radiator in addition to the slotted wires connecting the spiral resonators. The small gap region between the feeding line and slot resonators is another excitation source in the form of magnetic dipole due to the electric field. The cross-polarization levels are better than -90dB on vertical and -80dB on horizontal plane.

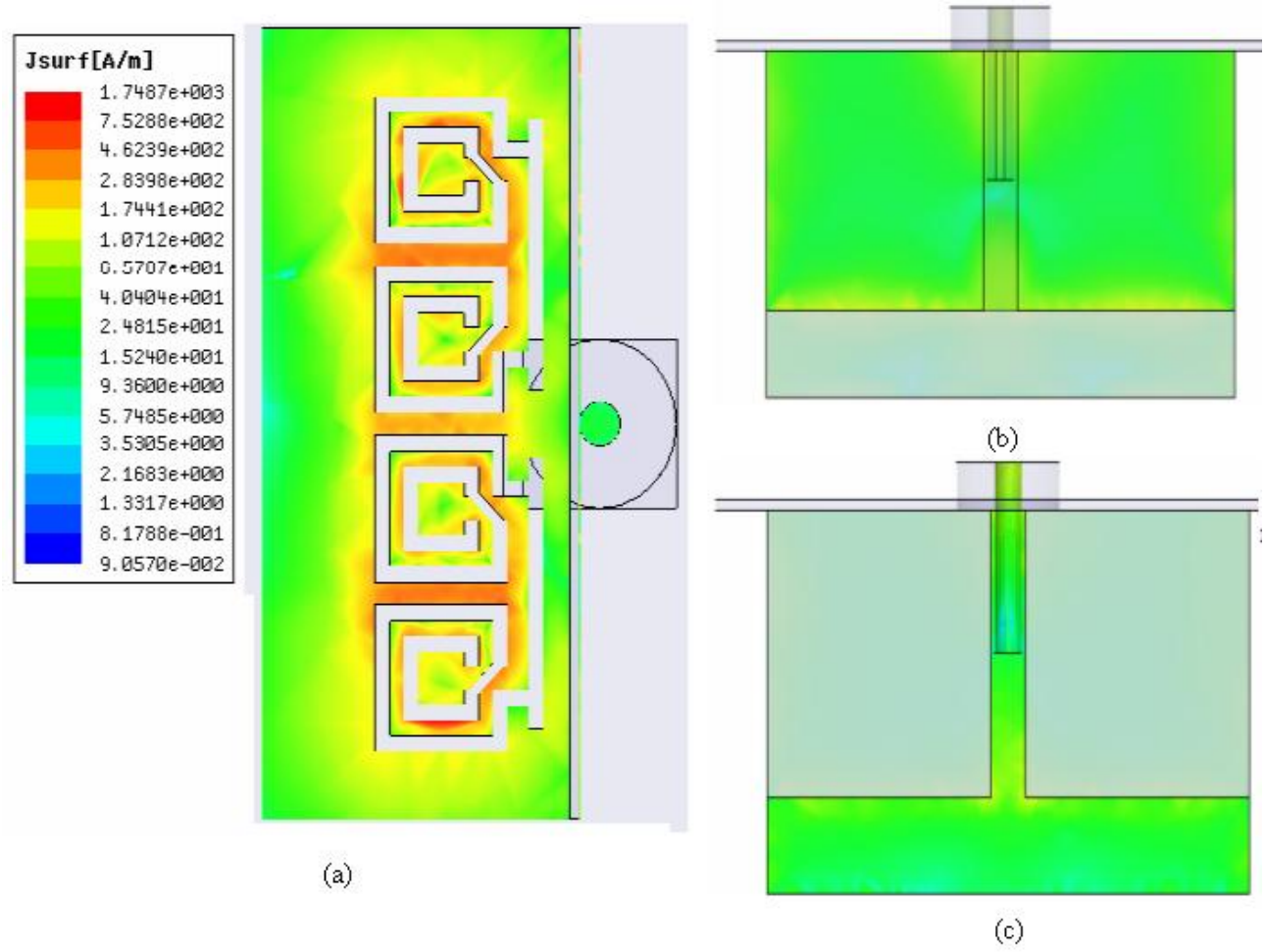

Figure 6.12. Resonant current distribution of (a) slot resonators, (b) ground plane of the feeding line and (c) T-formed transmission line of metamaterial-inspired slot antenna

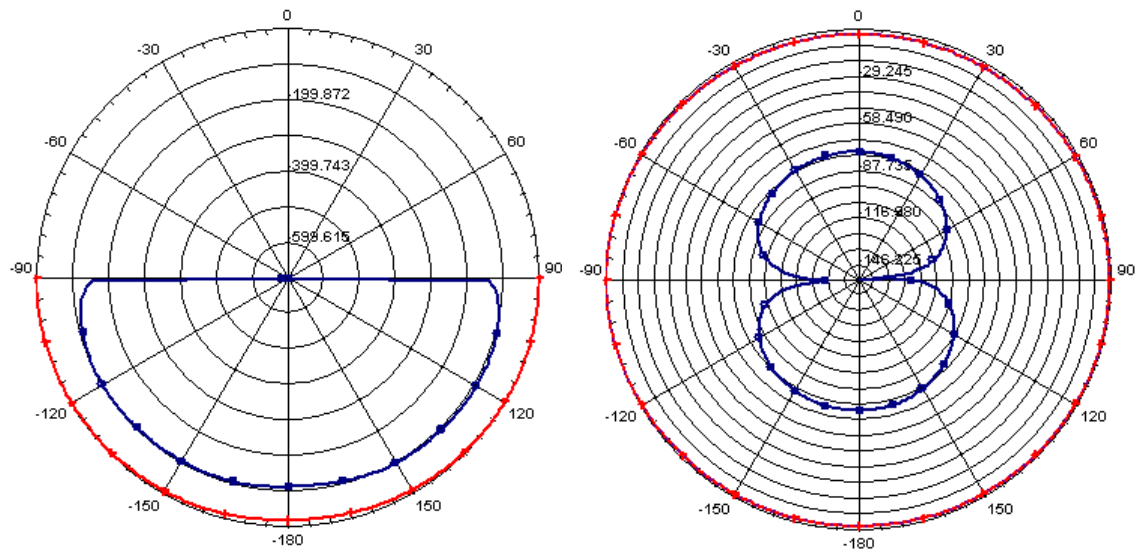

Figure 6.13 Co-polarization (red) and cross-polarization (blue) radiation patterns on (a) vertical and (b) horizontal planes at the resonance frequency

The antenna gain is 5.5 dBi. The overall efficiency is more than 90%. There are two main reasons why it is a quite efficient radiator. The first reason is the simultaneous excitation of vertical electric and horizontal magnetic dipoles over the ground plane. The second reason is the reduced level of field leakage through the feeding line from SMA to the slot resonators. The overall antenna size is 0.24λ x 0.1λ x 0.14λ with ka value of 1.16. It is slightly larger than the radiansphere at the resonance frequency. Some alternative compact antenna designs in the literature are [102-107].

6.5 Chapter Conclusion

In this chapter, the fundamental radiation parameters of small antennas are introduced. The basic performance limitations are explained. They are quite important parameters to have realizable radiation parameters in a limited volume. The formulations of minimum Q and maximum gain are presented. The effect of electromagnetic material parameters and physical dimensions on the antenna radiation is pointed out. It is concluded that the minimum radiation Q can only obtained with the excitation of the lowest order mode without multimode operation. In contrary to the minimum Q limit, there is no mathematical limit in the maximum gain. However, the excitation of higher order modes in a small antenna results high field intensity in the vicinity of the antenna. In practice, this increases the stored electric and magnetic energy with an additional increase in the losses and degradation in the radiation efficiency. Therefore, maximum gain is limited by the gain of lowest order mode for possibly broad bandwidth. In the next sections, two meta-antenna design examples are illustrated. The first design is the broadband LHM-loaded dipole antenna. The antenna design is based on the broadband loading of narrowband dipole with LHM cells in Section 5.4. The reflection coefficient is numerically calculated and experimentally verified. The surface current distribution and radiation patterns are illustrated. The radiation of LHM cells is confirmed. The maximum gain and directivity are -1 dBi and 3 dB. The radiation efficiency is 40% at 2.5 GHz. The directivity, gain and radiation efficiency are illustrated. It has the overall dimension of 0.34λ x 0.08λ with the main radiating section of 0.19λ x 0.08λ at the center frequency. The possible reasons of low radiation efficiency are highlighted. An alternative metamaterial-inspired slot antenna is introduced as a second meta-antenna. It consists of four slotted forms of the same cell as the main radiator. The slot resonators are excited capacitively with T-formed feeding line. The antenna is narrowband. The gain is 5.5dBi with an overall efficiency of better than 90%. The effective excitation of the vertical electric and horizontal magnetic dipoles formed in the slot resonators makes the antenna to radiate quite efficiently. The overall antenna size is 0.24λ x 0.1λ x 0.14λ with ka value of 1.16 at the resonance frequency.

7. Metamaterial-based Filter Design

7.1 Introduction

In Chapter 6, as a potential application of artificial materials, two different compact antennas are proposed. In this chapter, metamaterial-based filter design is investigated. It is an another important microwave application of artificial materials. The fundamental design approaches are explained first with representative filter designs in the literature. Compact, narrowband/wideband, band-stop/band-pass filters are presented. Important geometrical parameters are discussed in these illustrative examples. These parameters are important to tune the frequency band and improve the filter selectivity. As a next step, the design of a compact band-stop filter (BSF) is numerically and experimentally studied. The design approach how to excite the compact resonators in an effective manner is discussed. As a second design example, a compact band-pass filter (BPF) is designed with the same cell geometry as in the first design. The important design parameters are indicated. The main reason to use the same cell geometry is to point out its effectiveness in different filter designs.

7.2 Fundamental Principles of Metamaterial-based Filter Design

The metamaterial cells are electrically small and frequency selective as illustrated in Section 3.4, Section 4.4 and Section 5.4. The self-resonant nature allows them to be conveniently used in the design of compact filters. These filters are in principle designed by loading of a host transmission line with different combinations of electrically small resonators as LHM with negative permittivity and permeability materials [3-5]. In which filter type they can be utilized is deduced from 1D dispersion diagram. The unit cells of negative permittivity, negative permeability and LH materials can be used in BPFs at the bandpass frequencies. They can be alternatively used in BSFs at the bandgap frequencies. The high potential of metamaterial cells in compact filter design can also be deduced from the circuit models. In Section 5.2, LH cells are modeled as series capacitance and shunt inductance loaded with series inductance and shunt capacitance. This property points out an additional potential of LHM cells. They can be used in the design of compact broadband filters, which operate both in RH and LH bands.

In this section, representative filter examples in the literature are presented. They are mainly SRR and CSRR based designs. However, alternative designs composed of different resonator geometries are also referenced. Most microwave filters in this section are composed of small number of cells. In that respect, taking the effective parameters of these structures into account for the filter design has no meaning [14]. Therefore, to attribute these filters as “meta-filters” is the right approach. Sub-wavelength resonance features allow also to model the filters as series or parallel resonance circuits with discrete elements. In meta-filters, the filter parameters can be tuned by the resonator geometry, size and relative location in the host medium. This controllable manipulation of electrical characteristics makes them to be quite promising alternatives to the conventional designs [3-5].

The first design approach is based on how to improve the filter parameters of conventional designs with the metamaterial inclusions. In that respect, as a meta-filter example, SRRs are inserted into a conventional low pass filter for out-of-band rejection improvement [108,109].

They can be alternatively located close to the coupled line sections of a conventional coupled-line filter without entailing a considerable area increment. If they are properly geometrically tuned, the spurious bands can be eliminated. The out-of-band rejection level is additionally improved. The detailed design considerations are in [110].
In the second design approach, the design of narrowband LH BPF is investigated. It is shown in Figure 7.1. SRRs and metallic parts of CPW are in black and gray, respectively.

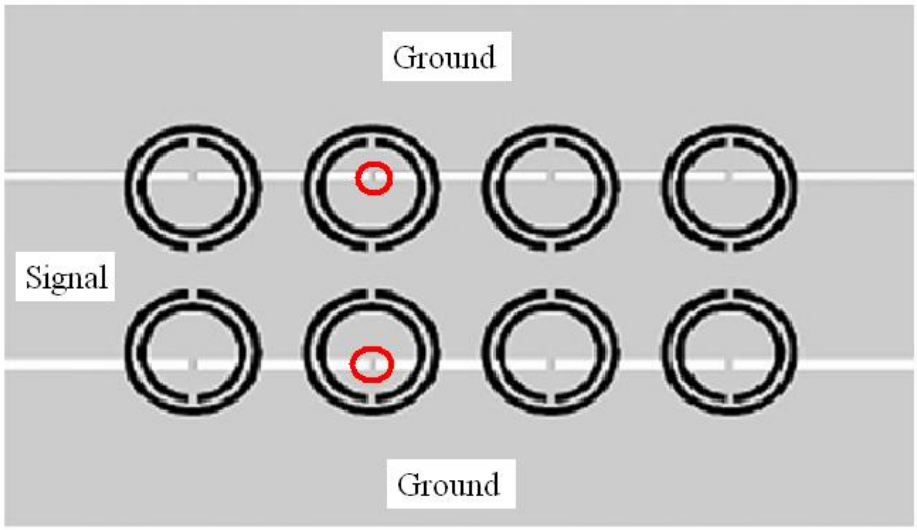

Figure 7.1. SRR based LH transmission line [111]

In Figure 7.1, four pairs of SRRs are located in a periodic manner at the back side of a short-circuited CPW. The short-circuited sections are shown in red. These sections excite SRRs effectively at the resonance frequency through the magnetic field. Therefore, optimum SRR positioning with respect to the shorting wires is an important design parameter. The wave transmission is based on the loading of capacitive SRRs with inductive shorting wires. Therefore, the transmission medium has narrow LH passband [3],[14],[111]. In analogy to bulk LH realizations, the short-circuiting lines are planar realizations of infinitely long wires in artificial plasma. This can be deduced from the wave impedance of short-circuited CPW, which is inductive as the wave impedance of periodic wire array under plane wave excitation derived in Section 4.2. The measured and numerically calculated filter parameters are extensively investigated with an equivalent circuit model in [111]. This design approach is applied in other filter realizations [112-115]. BPFs can be alternatively realized with different cell geometries [116-118]. Two cell geometries to be conveniently used in microstrip technology are shown in Figure 7.2. The ground plane and signal line are in gray and black, respectively.

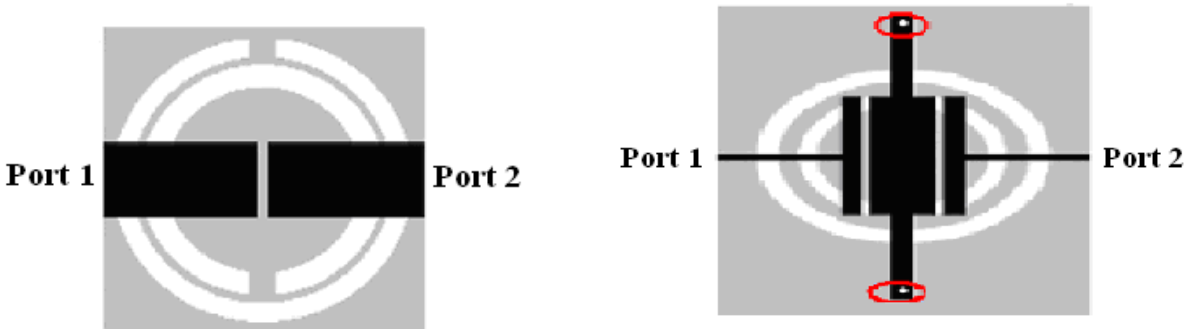

(a) (b)

Figure 7.2. (a) Purely resonant and (b) hybrid CSRR-based LHM cell geometry [116],[119]

These cells are basically composed of CSRR etched in the ground plane and capacitive gaps etched in the microstrip line. The main difference inbetween is that hybrid cell is contacted to the ground with the vias at the left and rights sides of the signal line as indicated in red in Figure 7.4. In CSRR-based hybrid cell, the signal transmission can be obtained at a lower band due to the additional shunt inductance loading. Therefore, it is an improved version of the purely resonant type [14]. They have one important design advantage.The bandgap between RH and LH bands can be compensated with the appropriate geometrical parameters [14],[120]. They can be therefore used conveniently in the broadband filter design [3].
The third design approach is based on broadband filter realizations with these LHM cells. As a design example, broadband BPF with purely resonant cell is shown in Figure 7.3.

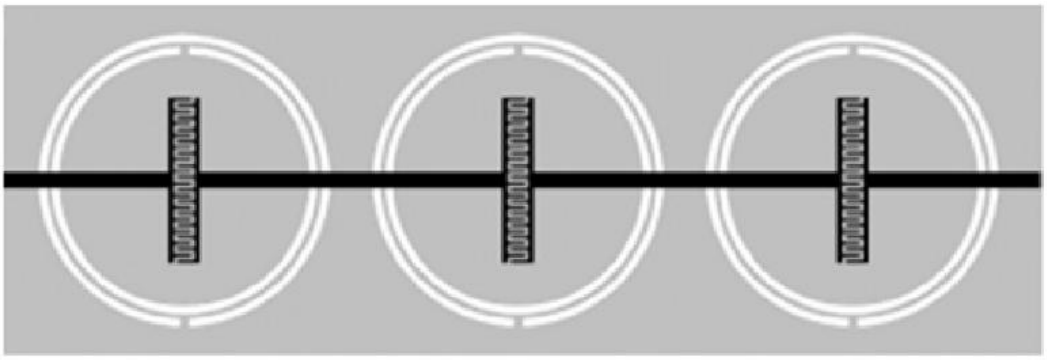

Figure 7.3. Broadband LHM BPF geometry [120]

In Figure 7.3, CSRRs are etched in the ground plane. Because they can be modeled as shunt parallel resonance circuits, the shunt inductive loading is obtained for the frequencies lower than the resonance frequency [3]. The series capacitive loading for LH transmission is realized by the interdigital capacitances in the gap region. Thus, the operation principle relies on the series loading of the interdigital capacitances with inductive CSRRs. Measurement and simulation results are included in [120]. There are similar filter realizations with the same design approach in [3],[121-123].
The fourth design approach is a frequently addressed methodology in narrowband filter realizations [124-126]. It is based on the alternating arrangement of RH and LH cells along the wave propagation direction. This alternating loading enhances the filter selectivity by LH and RH cells at the lower and higher edge of the passband, respectively. It does not degrade the insertion loss significantly. One exemplar BPF is shown in Figure 7.4.

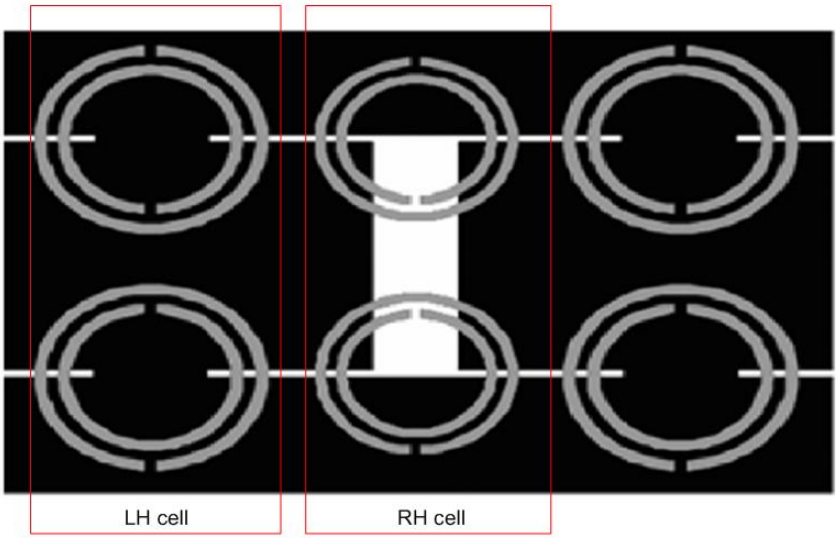

Figure 7.4. Narrowband two LH and one RH alternating BPF geometry [124]

In Figure 7.4, SRRs and metallic parts of CPW are in gray and black, respectively. LH and RH cells are indicated in red. RH lines are formed by smaller SRRs loaded with the capacitive gaps etched in CPW signal line. LH lines are formed by larger SRRs loaded with the short-circuited CPW line as in Figure 7.1. To use smaller SRRs in RH and larger SRRs in LH is important. The frequencies lower than the resonance frequency of SRRs in LH line are suppressed with high rejection level. Additionally, the frequencies higher than the resonance frequency of SRRs in RH line are suppressed with high selectivity. Therefore, the resulting filter is a narrow band, high selective, composite RH/LH filter [124]. If it is compared with a conventional coupled line filter of the similar filter characteristics, the total filter length is roughly three times shorter than the conventional filter [14]. The same design approach can be conveniently implemented in microstrip technology. For this case, RH lines are designed by CSRRs etched in the ground plane loaded with the shunt inductances. LH lines are formed by CSRRs etched in the ground plane loaded with the series capacitances [3].
In the fifth design approach, the realization of ultra-wide pass-band filters (UWBPF) is explained. This approach allows the upper frequency limit to be controlled and the spurious bands to be rejected at the specific frequencies. One UWBPF is shown in Figure 7.5.

Figure 7.5. Ultra-wide band-pass filter geometry [127]

In Figure 7.5, the signal line and ground plane of microstrip line are in black and gray, respectively. This filter is the ultra-wideband version of the broadband filter in Figure 7.3 In this design, there is no control on the upper limit of RH passband without smaller CSRRs. Therefore, the upper frequency limit is controlled with the additional CSRRs of the smaller radius inside the CSRRs of the larger radius. The higher resonance frequency of smaller CSRRs limits the upper frequency with a high rejection level near the resonance frequency. The geometrical dimensions can be accordingly adjusted for the desired resonance frequency. Therefore, the upper frequency limit can be conveniently tuned. The upper frequency and frequency selectivity can be optimized in a controlled manner with the relative placement to the larger CSRRs and interdigital capacitances. The design and operation principles are studied more extensively in [127]. This design principle can be conveniently modified for improved filter realizations. Additional resonators can be included to reject unwanted interfering signals. Two filter realizations with controlled frequency notches in the passband are shown in Figure 7.6a and Figure 7.6b.

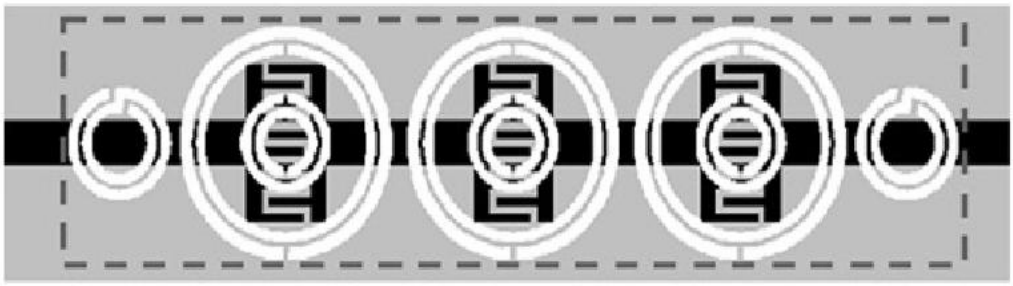

Figure 7.6a. UWB filter geometry with CSRR and complementary spiral resonators [127]

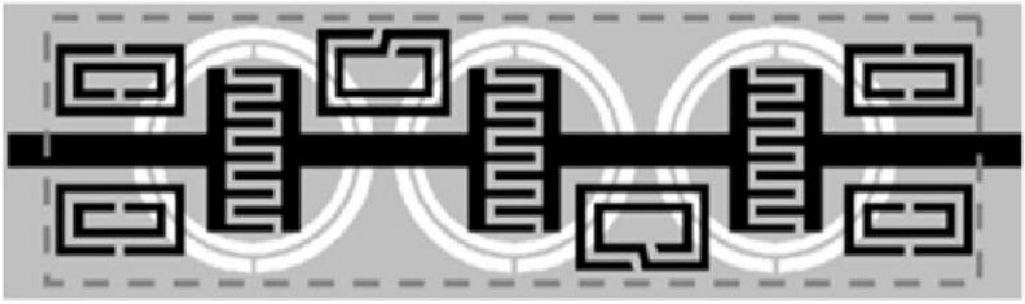

Figure 7.6b. UWB filter geometry with SRR and spiral resonators [128]

The filter in Figure 7.6a is a modified version of the filter in Figure 7.5. In Figure 7.6a, the complementary spiral resonators (CSR) are etched in the ground plane under the feeding line. They are located at the beginning and ending parts of the filter to have attenuation poles in the passband [127]. They can be tuned precisely to eliminate the spurious signals at the desired frequencies. The filter in Figure 7.6b is a modified version of the filter in Figure 7.3. In Figure 7.6b, all the additional resonators inserted into the host line are metallic. They are located on the top layer of the substrate. Four SRRs located near the filter extremes are designed to control the upper frequency limit with high selectivity. Two SRs are located in the central part to have desired attenuation poles in the passband [128]. As in the previous filters, the notch frequency and upper frequency limit can be adjusted conveniently by the geometrical dimensions of SR and SRR. The relative displacements of each resonator from the other resonators and LH/RH host line are also optimization parameters [3], [124-128].
In these typical design approaches, the design of pure resonant CSRRs is quite important for the optimum filter performance. Hybrid cells can be alternatively applied in the filter design. The design flexibility of hybrid cells leads not only UWBPFs to be implemented, but also standard filters to be designed. A complete methodology for the design of planar BPFs based on CSRRs was introduced in [129]. These filters can be modeled as in Figure 7.7a. In this model, the admittance inverters with normalized admittance of $\bar{J}=1$ are cascaded with alternating shunt resonators. These resonators can be designed as parallel LC resonant tanks shown in Figure 7.7b. As long as the admittances of the resonant elements match with those of LC tanks at least around the resonance frequency, the targeted approximation (Chebyshev and Butterworth) can be applied in the filter design. The admittance inverters can be implemented by cascading the hybrid cells. The filter realizations based on this design methodology are illustrated in [130-133].

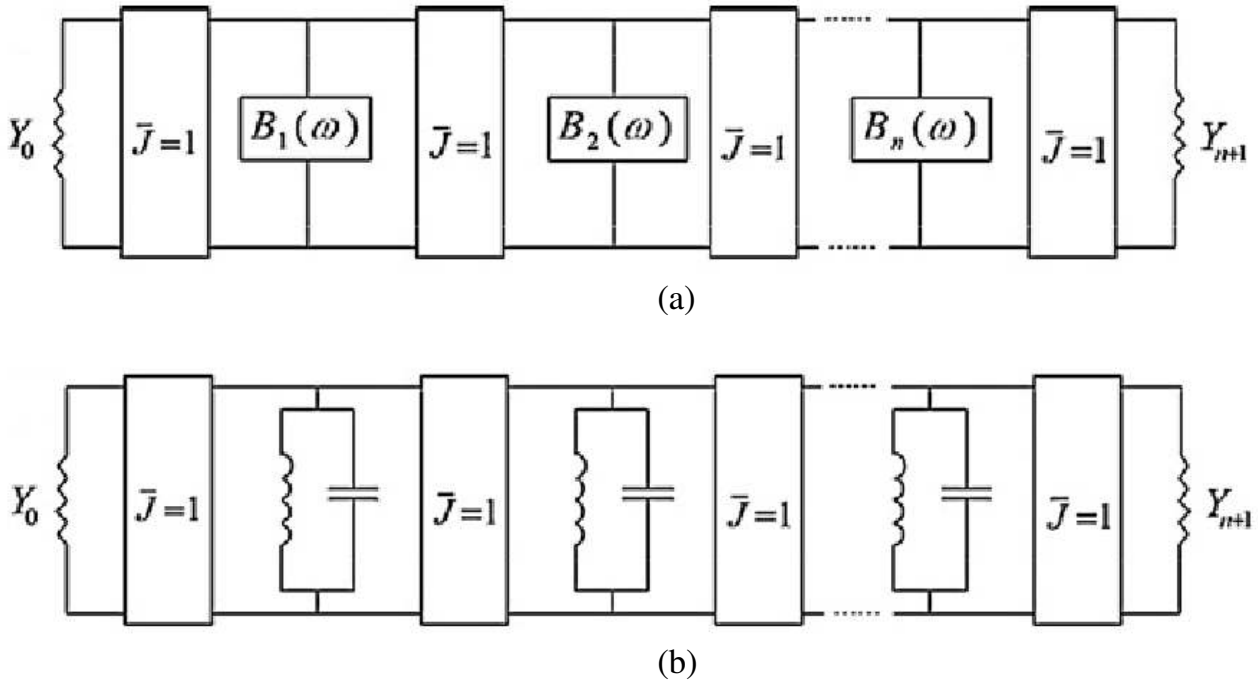

Figure 7.7 (a) BPF model consisting of impedance inverters and shunt resonators (b) BPF model with LC resonant tanks as shunt resonators [129]

7.3 Metamaterial-based Band-Stop Filter

In this section, a compact, high selective BSF is explained [134]. The filter is composed of four LHM cells as shown in Figure 7.8. One cell in each pair is anti-symmetrically connected with its mirror image. Two identical resonator pairs are located anti-symmetrically along the propagation direction. This filter topology is selected for symmetric return losses at both ports. The compact resonators are the same cells introduced in Section 5.4. This cell geometry is utilized to point out the use of same cell topology in the design of versatile microwave components. In Section 7.3.1, the geometrical model is introduced at first. The important parameters to be optimized are pointed out. The design principle is explained. In Section 7.3.2, the numerical and experimental results are presented. The operation principle is described. The numerical calculations on the geometrical parameters are illustrated.

7.3.1 Band-Stop Filter Design

LHM-based BSF is shown in Figure 7.8. In the filter model, the separation distance between each of two x-direction oriented cells is 0.4 mm. Each resonator pair is arranged in y-direction with the gap distance of 0.2 mm. The filter width ($W_{f)}$ and length (L_f) are 6.5 mm and 7.6 mm, respectively. The width of each metallic line is 0.3 mm except the width of feeding line. The feeding line width is 0.9 mm to have 50 Ω line impedance. The length of transmission line sections from the feeding ports is 6.2mm. The substrate is FR4 with the thickness of 0.5mm. The relative permittivity and loss tangent are set as 4.4 and 0.02, respectively. The total width and length of the filter are 7.7 mm and 20 mm, respectively.
In the filter design, two cells are connected anti-symmetrically on the either side of the transmission line. This results the current distribution in each pair to be symmetrical at all frequencies.

The resulting confinement of field lines in each pair reduces the possible radiation losses. Each resonator pair is directly connected with the feeding line. The direct connection enhances the field coupling from the feeding line to the resonators for high field rejection at the resonance frequency. It results also the resonant current distribution to have similar form with the current distribution in eigenmode calculation in Section 5.4.2.2. The cells in the proposed filter are therefore electrically (red circle) and magnetically (blue circle) coupled with the feeding line through the wires and spiral resonators. One resonator pair is arranged as the mirror image of the other resonator pair in the propagation direction. Therefore, the same return losses at both ports are obtained. In conventional BSFs, resonator shaped slots are structured in the ground plane to have high rejection at the resonance frequency. However, it requires an additional concern how to suppress the resulting back radiation of the slotted ground. Therefore, this type of feeding method is a good alternative to the conventional feeding method.

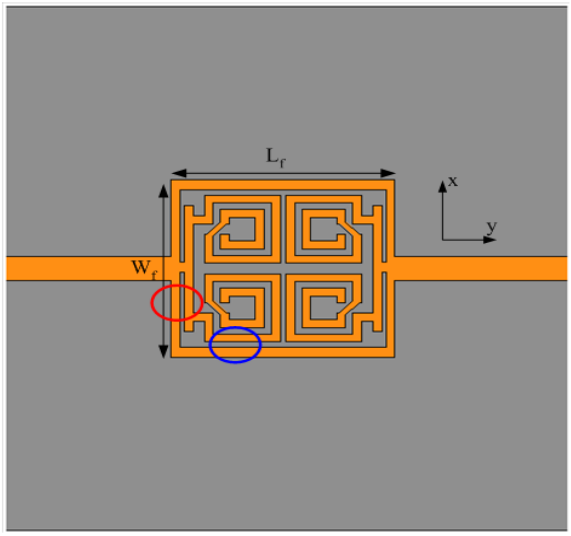

Figure. 7.8 LHM based Band-Stop Filter

However, there are important geometrical parameters to be optimised in the filter design. These parameters are

- separation distance of one resonator pair from the other resonator pair along y-direction
- separation distance of both resonator pairs from the feeding line along x-direction
- separation distance of both resonator pairs from the feeding line along y-direction

In Section 6.3, the uncertainty of the substrate permittivity is indicated as a possible reason for the discrepancy between the measured and simulated resonance frequency of the meta-antenna. It is therefore important to investigate the effect of substrate permittivity to have better arguments for the possible deviations between the numerical and experimental results.

7.3.2 Experimental and Numerical Results of Band-Stop Filter

The performance of BSF is numerically calculated by using FEM based commercial software HFSS. The transmission and reflection parameters are also measured by the vector network analyser 8722C. The simulated and measured transmission parameters are shown along with the reflection parameters in Figure 7.9.

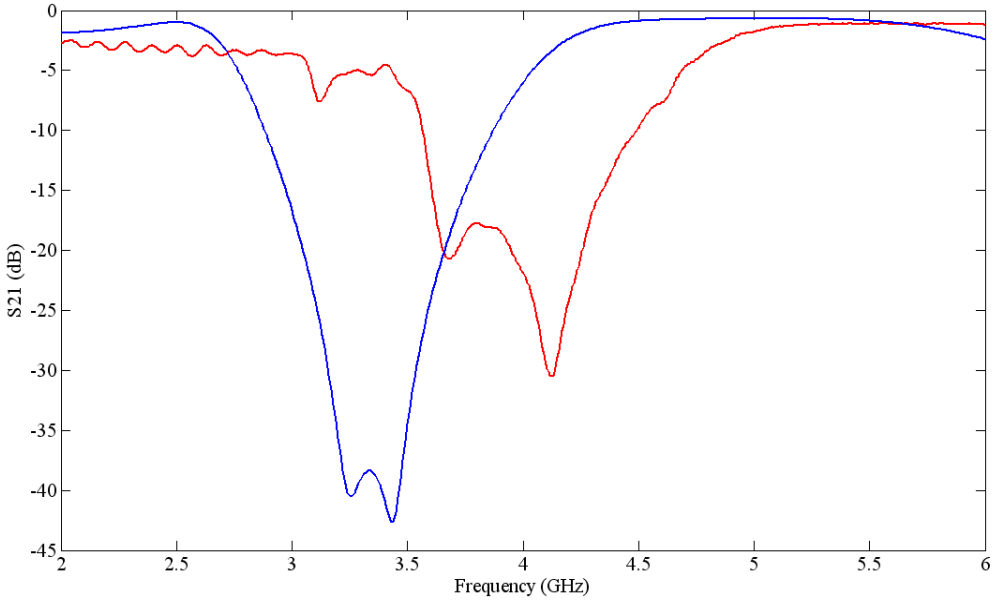

Figure 7.9a. Measured (red) and calculated (blue) transmission parameters of band-stop filter

In Figure 7.9a, two coupled stop-band frequencies can be identified at 3.26 and 3.44 GHz in the numerical calculation. It is an expected result of near field coupling from one resonator pair to the other resonator pair and feeding line. The measured stopband frequencies are 3.67GHz and 4.12 GHz. They are shifted by 410 MHz and 680 MHz from the numerically calculated lower and upper stop-band frequencies. There are two main reasons of frequency shifts. The first reason is the geometrical deviations between the numerical model and fabricated prototype. There are some metallic lines, which are not well-resolved in the fabrication process. This can be verified from the discrepancy in the measured return losses at both ports. The reflection parameter at port 1 must be same as the reflection parameter at port 2. However, they are not the same as shown in Figure 7.9b. Therefore, measured reflection parameter is different from calculated reflection parameter in Figure 7.9c. There are some other effects of cables and even calibration errors, which can be implied from low frequency ripples.

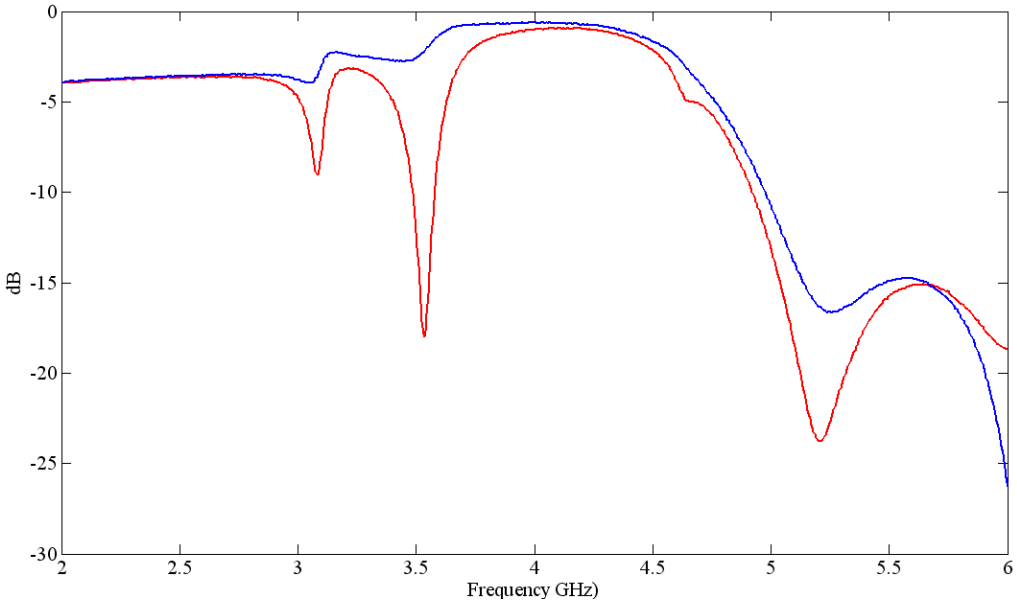

Figure 7.9b. Measured S11 (red) and S22 (blue) of band-stop filter

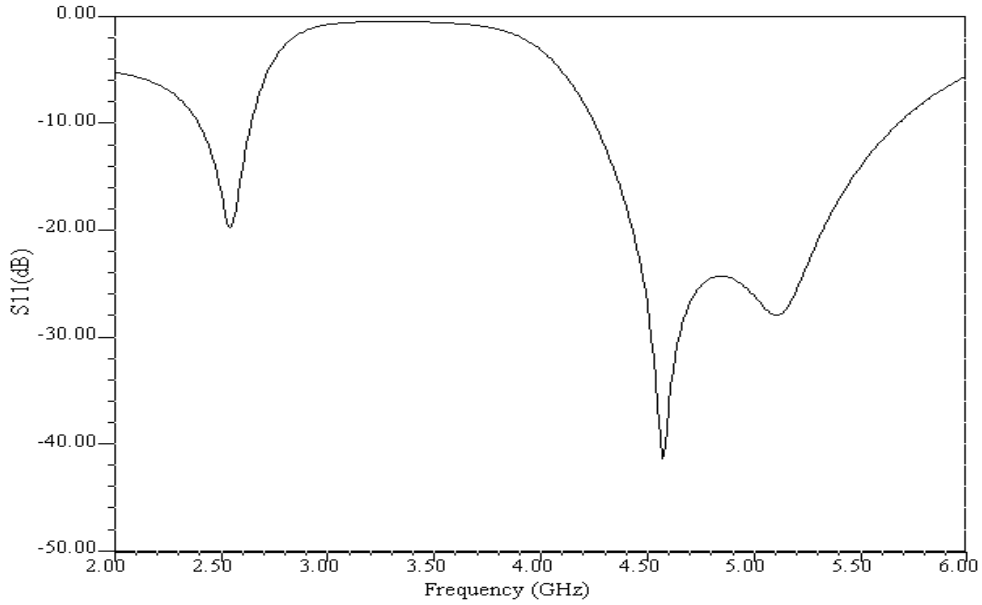

Figure 7.9c. Calculated reflection parameter of band-stop filter

The second reason is the uncertainty in the substrate permittivity. As pointed out in Section 6.3, this was a possible reason of resonance frequency shift in the experimental results. In order to identify the effect of substrate permittivity, the transmission parameter is numerically calculated for different permittivity values. It is shown in Figure 7.10.

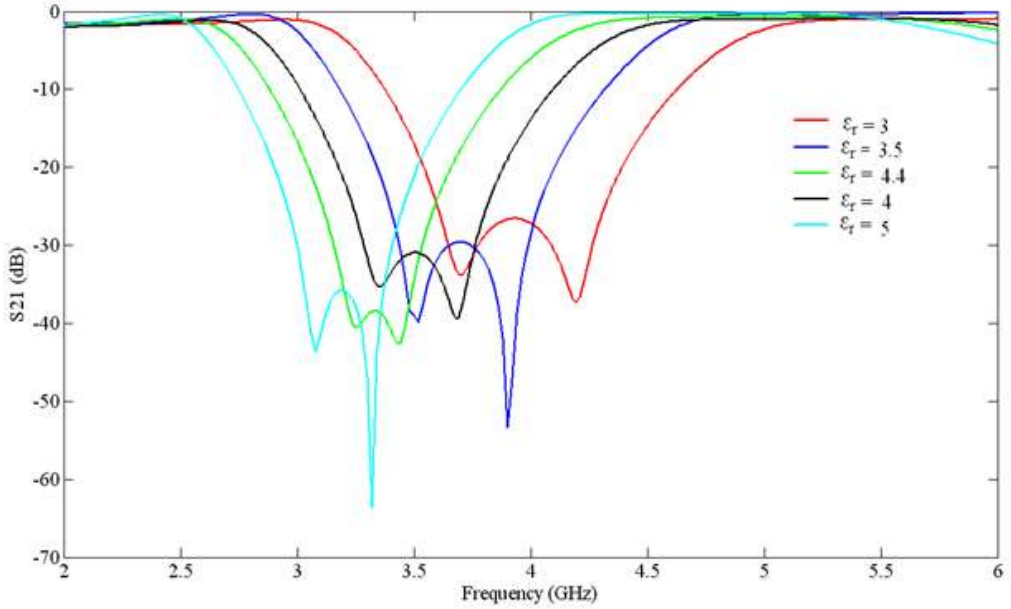

Figure 7.10. Transmission parameter of band-stop filter for different substrate permittivity

In Figure 7.10, the stopband frequencies shift to the higher frequencies for lower permittivity. The higher coupling among both resonator pairs and enhanced magnetic coupling with the feeding line are the main reasons. In addition, this uncertainty changes the input impedance from the designed value. Therefore, unwanted resonances can be observed as in Figure 7.9a.

As a result, the numerically calculated return loss is larger than 10 dB in two frequency bands of 2.41- 2.65 GHz and 4.26-5.72 GHz as shown in Figure 7.9c. The calculated insertion loss is larger than 30 dB in the frequency band of 3.16-3.54 GHz. However, the experimental results indicate signal suppression level better than 15dB between 3.6 GHz and 4.34 GHz with 740MHz stopband. The surface current distribution at the higher resonance frequency, 3.44 GHz is shown in Figure 7.11.

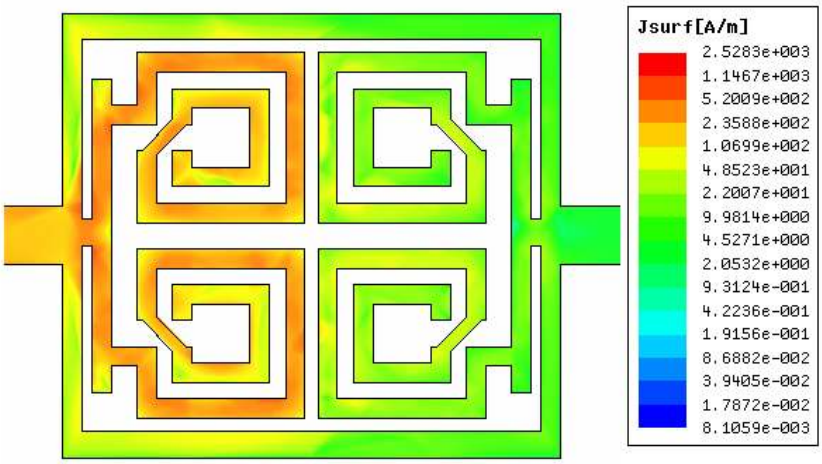

Figure 7.11. Surface current distribution of band-stop filter at 3.44 GHz

The current distribution on each of two resonators on the left side indicates λ/4 resonance at this frequency. High impedance at the open end of these resonators is transformed into the low impedance at this frequency. Thus, the incoming field is coupled electrically to the wire and magnetically to the spiral resonator to excite coupled λ/4 resonance as in the case of eigenmode calculation in Section 5.4.2.2. The magnetic coupling among the resonators can be deduced from the symmetric current distribution. The magnetic coupling between the feeding line and resonator pairs affects both upper and lower resonance frequencies. However, the frequency shift at the lower stopband frequency is higher than that at the higher stopband frequency. The transmission parameters are shown in Figure 7.12 for different separation distances in x-direction between the feeding line and resonator pairs.

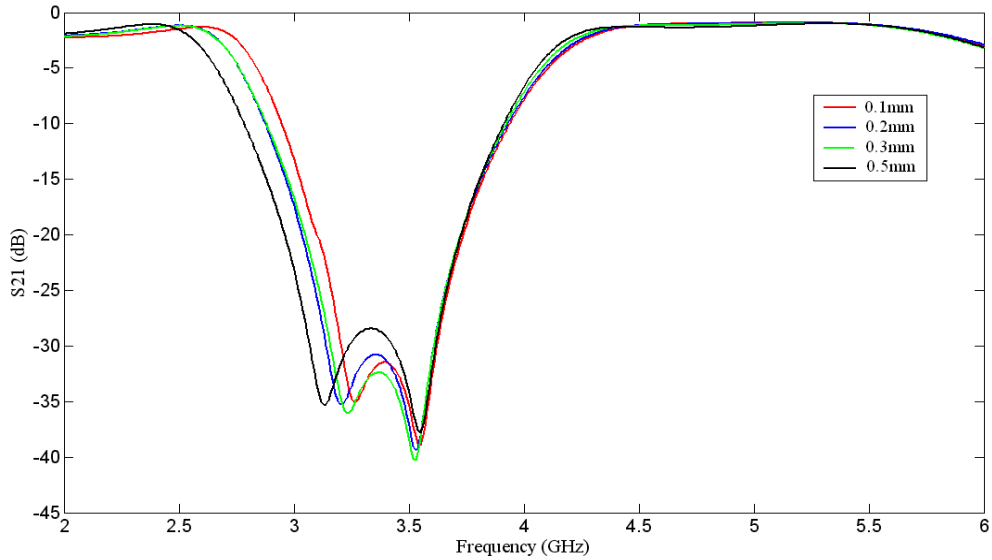

Figure 7.12. Transmission parameter of band-stop filter for different magnetic coupling distances

Why the lower resonance frequency is more dependent on the magnetic coupling is explained in the following manner. The higher stop-band frequency is the resonance frequency of two magnetically coupled resonators. This can be implied from the additional numerical calculation without second resonator pair. The resonance frequency without second resonator pair is negligibly different from the higher resonance frequency. However, the lower resonance frequency is due to the magnetic coupling between the first and second resonator pairs along the propagation direction. The higher magnetic coupling between the feeding line and excited resonator pair reduces the magnetic field from the first resonator pair to the second one. This is the reason why stop-bandwidth is smaller with the smaller separation distance between the feeding line and resonator pairs.
In this section, a design approach for compact BSF with LHM cells is explained. The dimensions of main filtering section are $\lambda o/12.57$ x $\lambda o/10.75$ at the lower stopband frequency. The filter selectivity is approximately 40 dB/GHz at the higher stopband frequency.

7.4 Metamaterial-based Band-Pass Filter Design

In this section, the design of a compact, LHM-based BPF is explained [73]. BPF is composed of two LHM cells, which have the same geometry of thin wire loaded spiral resonators as in Section 5.4. The design principle is based on direct connection of each resonator to the feeding line and a certain coupling distance between two resonators. This separation distance affects the inductive and capacitive coupling of each resonator with the other resonator and feeding line. The field coupling among the resonators at the resonance frequency results them to be effectively excited through the feeding line. In Section 7.4.1, the geometrical model is introduced. The design parameters to be optimized are discussed. The design principle is explained. In Section 7.4.2, the numerical results are presented. Surface current density and effects of geometrical parameters are illustrated. The operation principle is explained.

7.4.1 Band-Pass Filter Design

The BPF is shown in Figure 7.13. Two LHM resonators are located antisymmetrically along the x-axis. They are directly connected with the feeding line to excite each resonator. The excited resonator has to be coupled to the other resonator in an effective manner for low insertion loss. The separation distance of two x-direction oriented cells is 0.2 mm. The separation distance between one cell and feeding line section in y-direction, L_{sep} is 0.2 mm. One resonator is shifted from the other one along y-direction with a distance of 0.2 mm. This is an important design parameter to be investigated. Instead of using high lossy FR4, low loss Rogers 5880 material is used. The relative permittivity and loss tangent are 2.2 and 0.0009. Low-loss substrate is advantageous to reduce the insertion loss by enhancing the field coupling from one resonator to the other resonator. The lengths of extended feeding line in x- (L_{extx}) and y-directions (L_{exty}) are 2.5mm and 4.3mm, respectively. The width and length (L_{feed}) of feeding line are 1.5mm and 7.5mm, respectively. The direct connection length of the feeding line, ($L_{extfeed}$) in the extended sections is 1.9mm. The substrate width and length are 30 mm and 18.8mm, respectively. The total filter size is 6.4mm x 4.8 mm.

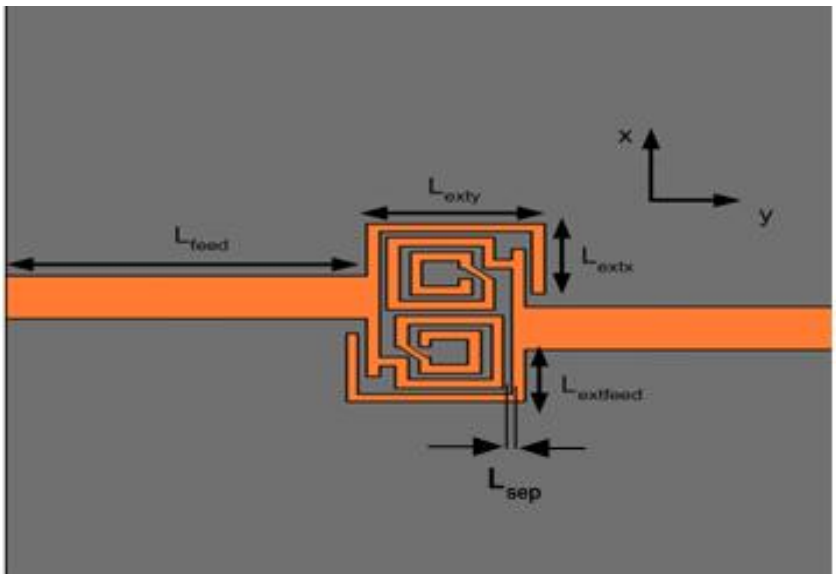

Figure 7.13. Thin wire loaded spiral resonator based BPF

The design principle is to feed one resonator directly through the feeding line. The highly concentrated field results the directly excited resonator to couple to the other resonator. The excited field in the first resonator is also enhanced by the magnetic field of the extended section of the feeding line. The magnetic and electric intercoupling as in the case of 0 and л resonant modes among the resonators result the incoming field at the first port to transmit with different phase shifts to the second port. How effectively these resonators are excited and coupled is quite important. This affects the filter selectivity significantly. Therefore, some geometrical parameters have to be investigated to figure out the field coupling strength.

These parameters are mainly

1-) separation distance of one resonator from the other resonator along x-direction
2-) shift of one resonator from the other resonator along y-direction
3-) separation distance of both resonators from the feeding line sections

This feeding method results the resonators to couple with the feeding line in an optimal manner. As a next step, the return and insertion losses are numerically calculated. The resonant current distribution is illustrated. The effects of geometrical parameters on filter performance are discussed.

7.4.2 Numerical Results of Band-Pass Filter

To validate the filter design principle, the reflection and transmission parameters are numerically calculated. They are shown in Figure 7.14. The return loss is larger than 10 dB with the insertion loss smaller than 1 dB between 4.58GHz and 5.24GHz. The lowest insertion loss is 0.4 dB at 4.7GHz. The filter selectivities are approximately 124.25 dB/GHz and 36.71 dB/GHz at the lower and higher edge of the passband, respectively.

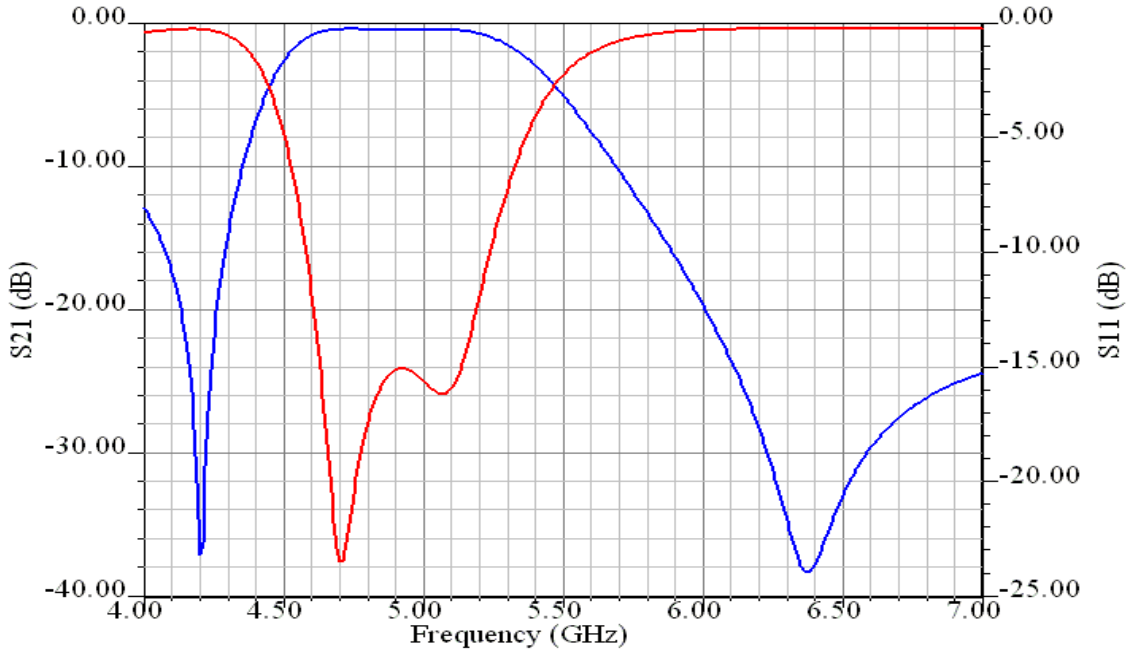

Figure 7.14 S21(blue) and S11 (red) parameters of band-pass filter

In the design process, the geometrical parameters are optimized for low insertion loss. How the resonators have to be arranged along y-direction is an important design parameter. In Figure 7.15, the transmission parameters for different shift of these resonators along y-direction are shown.

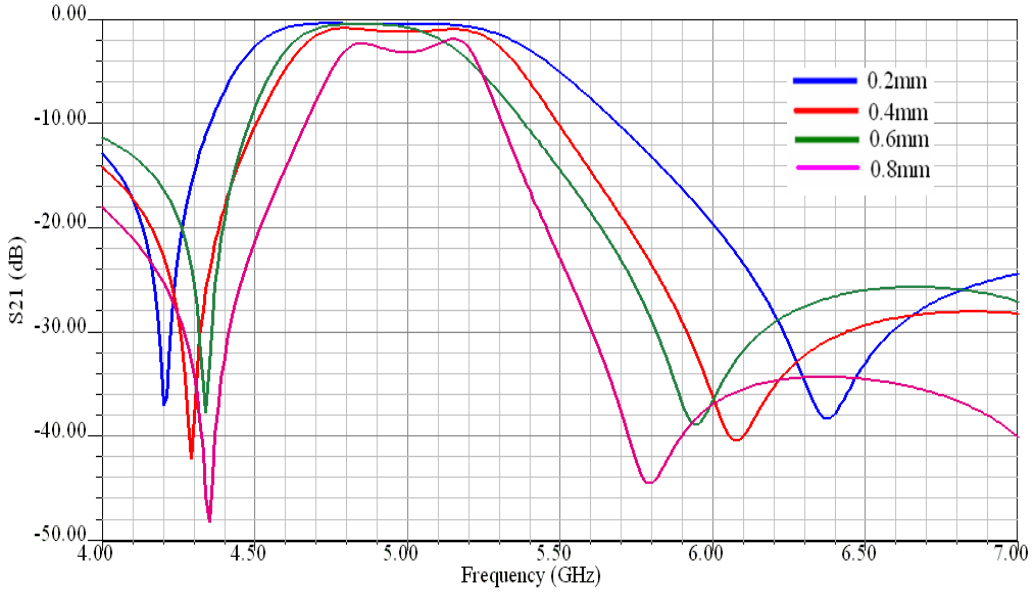

Figure 7.15 Transmission parameter of band-pass filter for different resonator shift along y-direction

In Figure 7.15, higher field coupling among the resonators with smaller shift results the bandwidth to be broader. The insertion loss is lower. The filter selectivity at the lower and higher edges of the passband are degraded. In addition, the field coupling from one resonator to the another resonator is enhanced through the magnetic coupling from the feeding line. Therefore, another design parameter is the separation distance between extended feeding line in y-direction and resonators along x-direction. The transmission parameters are shown in Figure 7.16 for different separation distances between each resonator and feeding line.

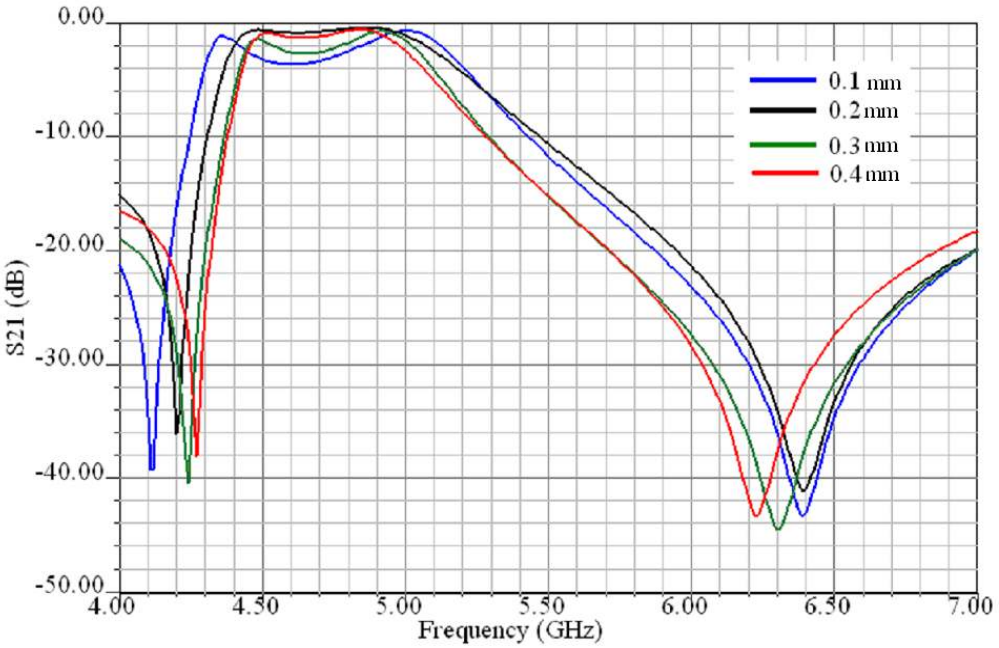

Figure 7.16. Transmission parameter of band-pass filter for different resonator separation distances from the feeding line

In Figure 7.16, the higher field coupling with small separation distance increases the bandwidth. The lower stopband frequency decreases and higher stopband frequency increases. These frequencies are the resonance frequencies of two coupled resonators. They can be modelled as parallel or series resonators at these frequencies. In analogy to the band diagram, these are the lower and higher edge of the passband in the first Brillioun zone. The surface current distributions at 4.2GHz and 6.36GHz in the optimum filter design illustrate the above mentioned remarks in Figure 7.17. In Figure 7.17, the first resonator is directly excited through the feeding line on the left side. The second resonator is excited through the field coupling from the first resonator and feeding line. In Figure 7.17a and Figure 7.17b, the field distributions of the excited resonator and feeding line couple the resonators electrically in 0 mode at 4.2GHz and magnetically in л mode at 6.36 GHz. However, in the passband, the incoming field is transmitted at different phase shifts by the excitation of second resonator through the electric and magnetic coupling from the first resonator.

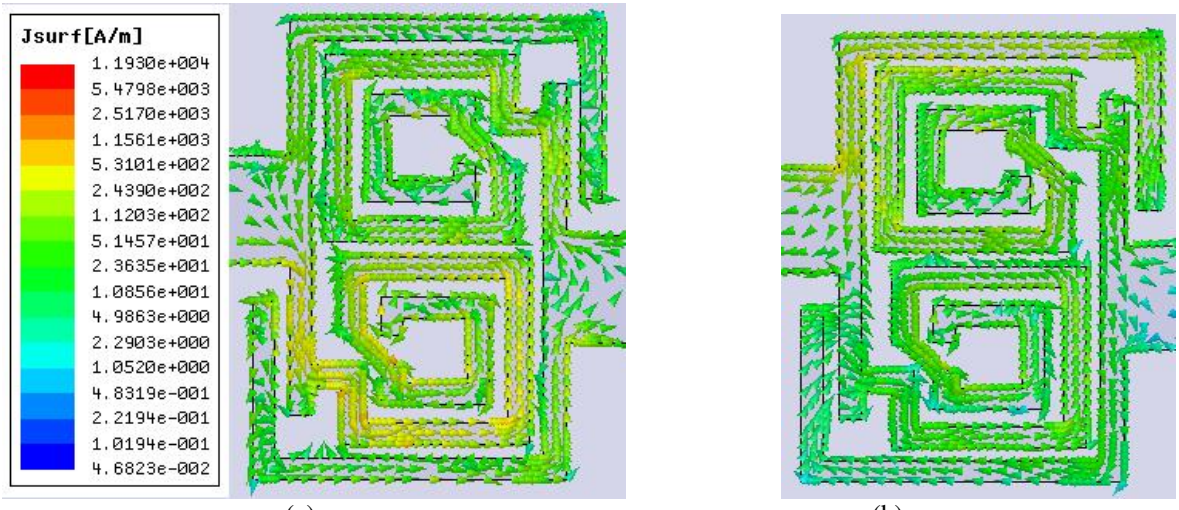

(a) (b)

Figure 7.17: Surface current distribution of band-pass-filter at (a) 4.2GHz and (b) 6.36GHz

In this section, the design of a compact BPF composed of two LHM cells is explained. The filter size without the feeding line sections is λo/10.23 x λo/13.64 at the lower passband frequency, 4.58GHz. It is quite compact in comparison to the conventional stepped impedance or coupled line filter designs [3],[14],[135]. One important advantage is no need of an additional matching network. This reduces the filter size significantly. The proposed filter has satisfactory insertion loss. It is smaller than 1 dB in the frequency band between 4.58 GHz and 5.24 GHz with the bandwidth of 660 MHz. The filter selectivities with reference to 3dB insertion loss are 124.25 dB/GHz and 36.71 dB/GHz at the lower and higher edge of the passband, respectively.

7.5 Chapter Conclusion

In this chapter, basic design approaches of metamaterial-based filters are highlighted. Representative filter designs in the literature are illustrated. Compact broadband/ narrowband BPF and UWBPF realizations are explained because of their design challenges in wireless communication systems. The bandgap separating LH band from RH band can be conveniently eliminated by purely resonant and hybrid CSRR cells. This is very important in broadband filter realizations. SRR and CSRR-based filter designs have inherently narrow stop-band characteristics with high selectivity. Therefore, BSFs can be realized in a straightforward manner by cascading SRR/CSRR cells. This property can be used in the design of high selective narrowband filters. How to suppress the unwanted spurious frequencies in UWBPFs is explained with design examples.

A compact LHM-based BSF is experimentally and numerically studied. The design and operation principles are explained in detail. The experimental results indicate signal suppression level better than 15dB between 3.6 GHz and 4.34 GHz with 740MHz stopband. The possible reasons of the deviation between the measured and calculated transmission parameters are discussed. The filter selectivity is approximately 40 dB/GHz at the higher stopband frequency. The dimensions of main filtering section are λo/12.57 x λo/10.75 at the lower stopband frequency. As a second meta-filter, a compact BPF composed of two LHM cells is designed. The insertion loss is smaller than 1 dB in the frequency band between 4.58 GHz and 5.24 GHz with the bandwidth of 660 MHz. The filter selectivities are numerically calculated with reference to 3dB insertion loss. They are 124.25 dB/GHz and 36.71 dB/GHz at the lower and higher edge of the passband, respectively. The size of main filtering section is λo/10.23 x λo/13.64 at the lower passband frequency. It is quite compact in comparison to the conventional stepped impedance or coupled line filter designs. The important advantage of both filter designs is no need of additional matching network. This reduces the filter physical size significantly.

8. Conclusion

The main goal of this thesis is to understand and investigate the design and operational principles of metamaterial-based antennas and filters with the focus on compact microwave realizations. Therefore, unit cells of negative permeability, permittivity and Left-Handed materials are extensively studied with numerical and analytical calculations. These calculations are important in order to understand the underlying physical mechanism in the design of artificial materials. For each of these metamaterial classes, one novel cell design with improved homogeneity is proposed. In Chapter 2, a short overview is given to understand the design principles.

In Chapter 3, artificial magnetism resulting from periodic metallic cylinders with/without splits is studied analytically and numerically. Analytical calculations for transmission and reflection parameters of concentric cylinders with splits are confirmed by numerical simulations and are in good agreement. The effective permeability formulation is compared with the original formulation of Pendry and approximates the resonance frequency better. A conventional negative permeability cell, Split Ring Resonator, is numerically analyzed in order to understand the principle of resonant negative permeability. The source for the demagnetization of the incoming magnetic field is the excitation of electrically small magnetic dipoles. Therefore, the Split Ring Resonator array has a capacitive impedance in the negative permeability region between the magnetic resonance and the plasma frequency. A 1D Brillouin diagram is numerically calculated to verify the bandgap region with negative permeability. An alternative parameter retrieval method, based on Bloch's Theorem for infinitely periodic structures is proposed. At the end of this chapter, a novel geometry based on fractal spiral resonator is proposed. The cell has dimensions, $\lambda_0/40$ x $\lambda_0/100$ x $\lambda_0/40$ at the magnetic resonance frequency and shows a more homogeneous behaviour of the composite material.

In Chapter 4, artificial dielectrics based on periodic metallic wires are analyzed first to study non-resonant negative permittivity materials. The effective permittivity is analytically calculated under plane wave excitation and agrees well with numerical values. An equivalent circuit model based on the reflection parameter is derived and a Drude type permittivity function is confirmed by numerical calculations. The analytical calculations of the permittivity of a wire array make no assumptions on the frequency dispersion unlike the one of Pendry. A wire strip model in planar technology on a low loss substrate is numerically analyzed. The transmission and reflection parameters are calculated in order to understand the principle of negative permittivity. The incoming electric field is depolarized due to excitation of electrically small electric dipoles, formed from the wire currents. Thus, the wire array has inductive impedance in the negative permittivity region as in the case of a short-circuited transmission line. At the end of the chapter, a novel geometry based on fractal anti-spiral resonators is proposed. The cell dimensions are $\lambda_0/55$ x $\lambda_0/22$ x $\lambda_0/22$ at the electric resonance frequency. More homogeneous composite materials with negative permittivity could be therefore designed.

In Chapter 5, the design of Left Handed Materials, based on the periodic arrangement of negative permittivity and permeability cells in the same host medium, is studied. The eigenmode equation of a loaded rectangular waveguide is analytically and numerically calculated. They are in good aggrement. The negative refractive index and subwavelength resonance phenomenon are confirmed. Drude type electric and Lorentzian type magnetic parameters with low losses are assumed to observe LH and RH bands.

The reason of a high frequency RH band is explained by equivalent circuit models of negative permittivity and permeability materials. An LHM unit cell is numerically analyzed and confirms that the LH transmission band is the overlapping region of negative permittivity and permeability. It is due to inductive loading of the capacitive impedance of SRRs by thin wires. Thus, the stored electric energy in the near field of SRR is compensated with the stored magnetic energy in the near field of thin wire. At the end of the chapter, a novel geometry based on wire loading of spiral resonators is proposed as LH cell. The cell dimensions are $\lambda_0/51$ x $\lambda_0/44$ x $\lambda_0/77$ at the LH resonance frequency. It can be used in the design of more homogeneous LH materials.

In Chapter 6, the design principle of metamaterial-based compact antennas is studied. The first design is a broadband dipole antenna loaded with LHM cells. The reflection coefficient is numerically calculated and experimentally confirmed. The radiation of electrically small LHM cells is confirmed by the surface current distribution and radiation patterns. The maximum gain and directivity are -1 dBi and 3 dB with 40% radiation efficiency at 2.5 GHz. Possible reasons for the low antenna gain are the inherent substrate/copper loss, the horizontal orientation of the radiating section over the ground plane and the increasing phase difference per unit cell with the decreasing frequency. Higher phase differences cause the successive LH cells to radiate destructively in the far field due to out-of-phase excitation. This is the reason why there is a certain gain and efficiency improvement with increasing frequencies. The overall dimensions of the antenna are 0.34λ x 0.08λ with the main radiating section of 0.19λ x 0.08λ at the center frequency. The second design is a metamaterial-based slot antenna. This antenna consists of four slotted cells as the main radiator. The slot resonators are excited capacitively with T-shaped electrically small monopoles. The antenna is a narrowband antenna with a gain of 5.5dBi and overall efficiency better than 90%. The effective excitation of vertical electric and horizontal magnetic dipoles formed by the slot resonators is the reason for the high efficieny. The overall antenna size is 0.24λ x 0.1λ x 0.14λ with ka value of 1.16 at the resonance frequency.

Finally, in Chapter 7, the design principles of metamaterial-based compact filters are studied with two compact filter designs. The first filter is a Band Stop Filter, which is studied experimentally as well as numerically. The experimental results indicate a signal rejection level better than 15dB between 3.6 GHz and 4.34 GHz with a 740MHz stopband. Possible reasons for the differences between the measured and calculated transmission parameters are discussed. The filter selectivity is 40 dB/GHz at the higher stopband frequency. The dimensions are λo/12.57 x λo/10.75 at the lower stopband frequency. The second design is a Band Pass Filter with two unit cells of same LHM geometry as for the Band Stop Filter. The numerically calculated insertion loss is smaller than 1 dB in the frequency band between 4.58 GHz and 5.24 GHz with the bandwidth of 660 MHz. The filter selectivities at 3dB insertion loss are 124.25 dB/GHz and 36.71 dB/GHz for the lower and higher edge of the passband, respectively. The physical size without the feeding line is λo/10.23 x λo/13.64 at the lower passband frequency, 4.58GHz. It is quite compact as compared to conventional stepped impedance or coupled line filter designs. Both filter designs do not require any matching network, which reduces the physical size significantly.

References

[1] D. R. Smith, W. J. Padilla, D. C. Vier, S. C. Nemat-Nasser, and S. Schultz, "Composite medium with simultaneously negative permeability and permittivity," Phys Rev Lett 84, 4184-4187 (2000).

[2] G. Veselago, "The electrodynamics of substances with simultaneously negative values of permittivity and permeability," Sov. Phys. Usp. 10, 504-509 (1968).

[3] Ricardo Marqués, Ferran Martín , Mario Sorolla, Metamaterials with Negative Parameters: Theory, Design and Microwave Applications Wiley Series in Microwave and Optical Engineering

[4] G. V. Eleftheriades and K. G. Balmain, Negative Refraction Metamaterials: Fundamental Principles and Applications. New York:Wiley Interscience, 2005

[5] Caloz and T. Itoh, Electromagnetic Metamaterials: Transmission Line Theory and Microwave Applications Piscataway, NJ: Wiley- IEEE, 2005.

[6] N. Engheta and R. W. Ziolkowski, Metamaterials Physics and Engineering Explorations, Eds.New York: Wiley/IEEE, 2006.

[7] Pendry, J.B, Holden, A.J. ; Robbins, D.J. ; Stewart, W.J. "Magnetism from conductors and enhanced nonlinear phenomena", IEEE Transactions on Microwave Theory and Techniques, Vol. 47, No. 11 ,Nov 1999

[8] J. Pendry, A. Holden, W. Steward, and I. Youngs, "Extremely low frequency plasmons in metallic mesostructures," Phys. Rev. Lett., vol. 76, no. 25, pp. 4773-4776, 1996

[9] J. B. Pendry, A J Holden, D J Robbins and W J Stewart,"Low frequency plasmons in thin-wire structures ", J. Phys.: Condens. Matter, 10, 4785, 1998

[10] Z. W. Liu, H. Lee, Y. Xiong, C. Sun, and X. Zhang, "Far-field optical hyperlens magnifying sub-diffraction-limited objects," Science 315, 1686-1686 (2007).

[11]X. Zhang, and Z. Liu, "Superlenses to overcome the diffraction limit," Nature Mater 7, 435-441 (2008).

[12] J. B. Pendry, D. Schurig, and D. R. Smith, "Controlling electromagnetic fields," Science 312, 1780-1782 (2006).

[13] N. Engheta, "An idea for thin subwavelength cavity resonators using metamaterials with negative permittivity and permeability," IEEE AntennasWireless Propag. Lett., vol. 1, no. 1, pp. 10–13, 2002.

[14] M. Gil, J. Bonache, F. Martín, "Metamaterialfilters: A review", Metamaterials, Volume 2, Issue 4, December 2008, Pages 186–197

[15] A. Alù and N. Engheta,"Guided modes in a waveguide filled with a pair of single-negative (SNG), double-negative (DNG), and/or double-positive (DPS) layers," IEEE Trans. Microw. Theory Tech., vol. 52, no. 1, pp. 199–210, Jan.2004.

[16] A. Alù and N. Engheta, "An overview of salient properties of guided-wave structures with double-negative and single-negative metamaterials," in Negative Refraction Metamaterials: Fundamental Properties and Applications,2005

[17] A. Grbic and G. V. Eleftheriades, "Overcoming the diffraction limit with a planar left-handed transmission lines," Phys. Rev. Lett., vol. 92, no. 11, p. 117 403, Mar. 2004..

[18] J. B. Pendry, "Negative refraction makes a perfect lens," Phys. Rev. Lett., vol. 85, pp. 3966–3969, Oct. 2000.

[19] A. A. Grbic and G. V. Eleftheriades, "Experimental verification of backward- wave radiation from a negative refractive index metamaterial," J.Appl. Phys., vol. 92, pp. 5930–5935, Nov. 2002.

[20] R.W. Ziolkowski and A. Kipple, “Application of double negative metamaterials to increase the power radiated by electrically small antennas,” IEEE Trans. Antennas Propag., vol. 51, no. 10, pp. 2626–2640, Oct. 2003.
[21]M. Schüßler, J. Freese, and R. Jakoby, “Design of compact planar antennas using LH-transmission lines,” in Proc. IEEE MTT-S Int. Microw. Symp., 2004, vol. 1, pp. 209–212.
[22] C.-J. Lee, K. M. K. H. Leong, and T. Itoh, “Design of resonant small antenna using composite right/left handed transmission line,” in Antennas Propag. Soc. Int. Symp., 2005,
[23] A. Sanada, M. Kimura, I. Awai, C. Caloz, and T. Itoh, “A planar zeroth-order resonator antenna using a left handed transmission line,” in 34th Eur. Microw. Conf., Amsterdam, The Netherlands, 2004,
[24] M. C. K. Wiltshire, J. B. Pendry, and J. V. Hajnal, "Sub-wavelength imaging at radio frequency," J Phys-Condens Mat 18, L315-L321 (2006).
[25] K. Aydin, K. Guven, C. M. Soukoulis, and E. Ozbay, "Observation of negative refraction and negative phase velocity in left-handed metamaterials," Appl Phys Lett 86, 124102 (2005).
[26] M. Gokkavas, K. Guven, I. Bulu, K. Aydin, R. S. Penciu, M. Kafesaki, C. M. Soukoulis, and E. Ozbay, "Experimental demonstration of a left-handed metamaterial operating at 100 GHz," Phys Rev B 73, 193103 (2006).
[27] T. J. Yen, W. J. Padilla, N. Fang, D. C. Vier, D. R. Smith, J. B. Pendry, D. N. Basov, and X. Zhang, "Terahertz magnetic response from artificial materials," Science 303, 1494-1496 (2004).
[28] S. Linden, C. Enkrich, M. Wegener, J. F. Zhou, T. Koschny, and C. M. Soukoulis, "Magnetic response of metamaterials at 100 terahertz," Science 306, 1351-1353 (2004).
[29] V. M. Shalaev, "Optical negative-index metamaterials," Nature Photonics 1, 41-48 (2007).
[30] W. S. Cai, U. K. Chettiar, H. K. Yuan, V. C. de Silva, A. V. Kildishev, V. P. Drachev, and V. M. Shalaev, "Metamagnetics with rainbow colors," Opt Express 15, 3333-3341 (2007).
[31] W. Kock, "Metallic delay lenses," Bell Syst. Tech. J., vol. 27, pp. 58{82, 1948.
[32] W. Rotman, "Plasma simulations by artificial dielectrics and parallel-plate media," IRE Trans. Ant. Propag., vol. 10, pp. 82-95, 1962.
[33] R. King, D. Thiel, and K. Park, "The synthesis of surface reactance using an artificial dielectric," IEEE Trans. Antennas and Propagat., vol. 31, pp. 471-476, 1983.
[34] H. Schneider and P. Dullenkopf, "Slotted tube resonator: A new nmr probe head at high observing frequencies," Rev. Sci. Instrum., vol. 48, no. 1, pp. 68-73, 1977.
[35]M. Wiltshire, J.B.Pendry, I. Young, D. Larkman, D. Gilderdale, and J. Hajnal, "Microstructured magnetic materials for radio frequency operation in magnetic resonance imaging (mri)," Science, vol. 291, pp. 849-851, 2001.
[36] M. Wiltshire, J. Hajnal, J.B.Pendry, and D. Edwards, "Metamaterial endoscope for magnetic field transfer: near field imaging with magnetic wires," Optics Express, vol. 11, pp. 709{715, 2003.
[37]S. A. Ramakrishna, J. B. Pendry, M. C. K. Wiltshire, and W. J. Stewart, "Imaging the near field," Journal of Modern Optics, vol. 50, pp. 1419-1430, 2003.
[38] Antoniades, M.A.,Eleftheriades, G.V. "Compact linear lead/lag metamaterial phase shifters for broadband applications" IEEE Antennas and Wireless Propagation Letters, Volume: 2 , Issue: 1 pg: 103 - 106, 2003

[39]Caloz, C.,Sanada, A. ; Itoh, T. "A novel composite right-/left-handed coupled-line directional coupler with arbitrary coupling level and broad bandwidth " IEEE Transactions on Microwave Theory and Techniques, Volume: 52 , Issue: 3 ,pg: 980 – 992, 2004
[40] Juan D. Baena, Ricardo Marqués, and Francisco Medina ,"Artificial magnetic metamaterial design by using spiral resonators" Phys. Rev. B 69, 014402 (2004)
[41] R. Marqués, F. Medina†, and R. Rafii-El-Idrissi, "Role of bianisotropy in negative permeability and left-handed metamaterials" Phys. Rev. B 65, 144440 (2002)
[42] Shamonin, M.,Shamonina, E. , Kalinin, V. , Solymar, L. "Properties of a metamaterial element: Analytical solutions and numerical simulations for a singly split double ring" Journal of Applied Physics, vol. 95, No. 7, Apr 2004
[43] M. Shamonin,E. Shamonina,V. Kalinin, L. Solymar, "Resonant frequencies of a split-ring resonator: Analytical solutions and numerical simulations" Microwave and optical technology letters, Vol. 44, No. 2, Jan 2005
[44] B. Sauviac, C. R. Simovski, S. A. Tretyakov, "Double Split-Ring Resonators: Analytical Modeling and Numerical Simulations" , Vol. 24, No. 5, Electromag 24, 2004
[45] Marques, R.,Mesa, F., Martel, J. , Medina, F. "Comparative analysis of edge- and broadside- coupled split ring resonators for metamaterial design - theory and experiments "IEEE Transactions on Antennas and Propagation, Vol. 51, No. 10, Oct. 2003
[46] I. Bahland, P. Bhartia, Microwave Solid state circuit Design, wiley, new york, 1988
[47]Bilotti, F.,Toscano, A. , Vegni, L.,"Design of Spiral and Multiple Split-Ring Resonators for the Realization of Miniaturized Metamaterial Samples " IEEE Transactions on Antennas and Propagation, Vol. 55, No. 8, Aug. 2007
[48] Ekmekci, E., Turhan-Sayan, G. "Reducing the electrical size of magnetic metamaterial resonators by geometrical modifications: a comparative study for single-sided and double-sided multiple SRR, spiral and U-spiral resonators " IEEE Anten. Prop. Society Sym., AP-S 2008.
[49] R. Marqués, J. D. Baena, J. Martel, F. Medina, F. Falcone, M. Sorolla, and F. Martín, "Novel small resonant electromagnetic particles for metamaterial and filter design," in Proc. Int. Conf. Electromagnetics Advanced Applications (ICEAA'03), Turin, Italy, Sept. 2003.
[50]Crnojevic-Bengin, V.,Radonic, V. ; Jokanovic, B."Fractal Geometries of Complementary Split-Ring Resonators " IEEE Transactions on Microwave Theory and Techniques, Vol. 56, No. 10, oct. 2008
[51] Palandoken, M.,Henke, H. "Fractal spiral resonator as magnetic Metamaterial " Applied Electromagnetics Conference (AEMC), 2009
[52] Zeng Hui-yong, Wang Guang-ming, Liang Jian-gang, Gao Xiang-jun "Complementary split ring resonators using equilateral triangular Koch fractal curves" , IEEE International Symposium on Microwave, Antenna, Propagation and EMC Technologies for Wireless Communications, 2009
[53]Crnojevic-Bengin, Radonic, V., Jokanovic, B "Complementary Split Ring Resonators Using Square Sierpinski Fractal Curves " 36th European Microwave Conference, 2006.
[54]Radonic, V., Jokanovic, B, Crnojevic-Bengin, "Different approaches to the Design of metamaterials" MTT-Serbia, 2007
[55]Bilotti, F.,Toscano, A., Vegni, L., Aydin, K., Alici, K.M., Ozbay, E. "Theoretical and experimental analysis of magnetic inclusions for the realization of metamaterials at different frequencies" IEEE/MTT-S International Microwave Symposium, 2007.

[56] H. Chen, J. Zhang, Y. Bai, Y. Luo, L. Ran, Q. Jiang, and J. A. Kong, “Experimental retrieval of the effective parameters of metamaterials based on a waveguide method,” Opt. Express, vol. 14, no. 26, pp. 12944–12949, Dec. 2006.
[57] D. R. Smith, D. C. Vier, T. Koschny, and C. M. Soukoulis, “Electromagnetic parameter retrieval from inhomogeneous metamaterials,” Phys. Rev. E, vol. 71, pp. 0366171–03661711, 2005.
[58] N. G. Alexopoulos, C. A. Kyriazidou, and H. F. Contopanagos, “Effective parameters for metamorphic materials and metamaterials through a resonant inverse scattering approach,” IEEE Trans. Microw. Theory Tech., vol. 55, no. 2, pp. 254–267, Feb. 2007.
[59] X. Chen, T. M. Grzegorczyk, B.-I.Wu, J. Pacheco, Jr., and J. A. Kong, “Robust method to retrieve the constitutive effective parameters of metamaterials,” Phys. Rev. Lett. E, vol. 70, pp. 0166081–0166087, 2004.
[60] D. R. Smith, D. C. Vier, N. Kroll, and S. Schultz, “Direct calculation of permeability and permittivity for a left- handed metamaterial,” App. Phys. Lett., vol. 77, no. 14, pp. 2246–2248, Oct. 2000.
[61] W. X. Tang, H. Zhao, X. Y. Zhou, J. Y. Chin, and T. J. Cui, "Negative index material composed of menader lines and SRRS", Progress In Electromagnetics Research B, Vol. 8, 103–114, 2008
[62] Palandoken, M.; Henke, H., "Fractal negative-epsilon metamaterial ", International Workshop on Antenna Technology (iWAT), 1-4, 2010
[63]J. D. Baena, J. Bonache, F. Martín, R. Marqués, F. Falcone, T. Lopetegi, M. A. G. Laso, J. García-García, I. Gil, M. F. Portillo, and M. Sorolla, “Equivalent-circuit models for split-ring resonators and complementary split-ring resonators coupled to planar transmission lines,” IEEE Trans. Microw. Theory Tech., vol. 53, no. 4, pp. 1451–1461, Apr. 2005.
[64]Ozbay, E.,Soukoulis, C.M.,"Observation of Negative Refraction and Negative Phase Velocity in True Left-Handed Metamaterials " ,36th European Microwave Conference,Pg: 959 - 962, 2006.
[65] R. A. Shelby, D. R. Smith, and S. Schultz, "Experimental verification of a negative index of refraction," Science 292, 77-79 (2001). BIBLIOGRAPHY 104
[66] S. Foteinopoulou, E. N. Economou, and C. M. Soukoulis, "Refraction in media with a negative refractive index," Phys Rev Lett 90, 107402 (2003).
[67] Aydin, K.,Ozbay, E., "Negative refraction and focusing by a left-handed material slab in free space ", Quant. Elect. and Laser Science Conference, pg: 1-2 2006
[68] Eleftheriades, G.V., "Analysis of Bandwidth and Loss in Negative-Refractive-Index Transmission-Line (NRI–TL) Media Using Coupled Resonators ",IEEE Microwave and Wireless Components Letters, Vol: 17 , No: 6, pg: 412-414, 2007
[69]Karamanos, T.D.,Dimitriadis, A.I. ; Kantartzis, N.V., "Compact Double-Negative Metamaterials Based on Electric and Magnetic Resonators ", IEEE Antennas and Wireless Propagation Letters,Volume: 11, Pg: 480 - 483, 2012
[70] N. Engheta, “Ideas for potential applications of metamaterials with negative permittivity and permeability,” in Advances in Electromagnetics of Complex Media and Metamaterials. ser. NATO Sci., S. Zouhdi, A. H. Sihvola, and M. Arsalane, Eds: Kluwer, 2002, pp. 19–37.
[71] I. S. Nefedov and S. A. Tretyakov, “Waveguide containing a backward-wave slab,” ArXiv.org, Nov. 2002 [Online]. Available:http://arxiv.org/pdf/cond-mat/0211185.

[72] B.-I.Wu, T.M. Grzegorczyk, Y. Zhang, and J. A. Kong, “Guided modes with imaginary transverse wave number in a slab waveguide with negative permittivity and permeability,” J. Appl. Phys., vol. 93, no. 11, pp.9386–9388, Jun. 2003.
[73] Xun-Ya Jiang, "Metamaterial", ISBN 978-953-51-0591-6, InTech, May 16,2012 DOI: 10.5772/2319
[74]Abielmona, S.,Nguyen, H.V. ; Caloz, C.,"CRLH zeroth order resonator (ZOR): Experimental demonstration of insensitivity to losses and to size" Asia-Pacific Microwave Conference, pg: 657 - 662, 2006
[75]Nader Engheta, Ziolkowski, R.W.,"A positive future for double-negative metamaterials” IEEE Transactions on Microwave Theory and Techniques,Volume: 53 , Issue: 4, Pg: 1535 - 1556 ,2005
[76] Palandoken, M.,Grede, A., Henke, H., "Broadband Microstrip Antenna With Left-Handed Metamaterials ", IEEE Transactions on Antennas and Propagation, Volume: 57 ,Issue: 2 , pg 331-338, 2009
[77] T. Koschny, P. Markos, D. R. Smith, and C. M. Soukoulis, “Resonant and antiresonant frequency dependence of the effective parameters of metamaterials,” Phys. Rev. E, pp. 0656021–0656024, 2003.
[78]Wheeler, H.A, “Small Antennas,” IEEE Trans. Antennas Propagat. , vol . AP-23, July 1975, pp.462-469
[79] Wheeler, H.A, “The radiansphere around a small antenna,” Proc. Of the IRE, vol.47, pp.1325-1331, Aug. 1959.
[80]Constantine A.Balanis, Antenna Theory and Design. John Wiley & Sons, Inc., 1997.
[81] R. C. Johnson, Antenna Engineering Handbook, 3rd ed. New York: McGraw-Hill.
[82] J. Chu, “Physical limitations on omnidirectional antennas,” J. Appl. Phys., vol. 19, pp. 1163–1175, Dec. 1948
[83]Geyi, W. , “Physical limitations of antenna,”, Antennas and Propagation, IEEE Transactions on pp. 2116 - 2123 , Volume: 51 Issue: 8, Aug. 2003
[84]A.D. Yaghjian and S.R. Best, Impedance, bandwidth, and Q of antennas, Trans IEEE, AP-53 (2005), 1298–1324.
[85] Steven R. Best, "A study of the performance properties of small antennas", Mitre coorperation technical papers
[86] R. F. Harrington, "Effect of antenna size on gain, bandwidth, and efficiency", J. Res. Nat. Bureau Stand., vol. 64D, pp. 1 - 12, 1960.
[87]Wheller , H.A.: ‘Fundamental limitations of small antennas’, Proc IRE, December 1947, pp. 1479–1488
[88]G. Goussetis, A.P. Feresidis, J.C. Vardaxoglou, Tailoring the AMC and EBG Characteristics of Periodic Metallic Arrays Printed on Grounded Dielectric Substrate. IEEE Transactions on Antennas and Propagation, vol. 54, no. 1, January 2006.
[89]Sievenpiper, L. Zhang, R. Broas, N.G. Alexopolous, and E. Yablonovitch, Highimpedanceelectromagnetic surfaces with a forbidden frequency band, IEEE Trans Microwave Theory Tech MTT-47 (1999), 2059–2074.
[90]F. Yang, K. Ma, Y. Qian, T. Itoh, A Uni-planar Compact Photonic-Bandgap (UCPBG) Structure and Its Applications for Microwave Circuits. IEEE Transactions on Microwave Theory and Techniques, vol. 47, no. 8, August 1999.
[91]F-R. Yang, K-P. Ma, Y. Qian, and T. Itoh, A novel TEM waveguide using uniplanar compact photonic-bandgap (UC-PBG) structure, IEEE Trans Microwave Theory Tech MTT-47 (1999), 2092–2098

[92]Soon-Soo Oh, Lotfollah Shafai, “Artificial magnetic conductor using split ring resonators and its applications to antennas,” Microwave and Techn. Letters, vol. 48, no.2, pp.329–334, Feb. 2006.
[93] M. Gil, J. Bonache, J. Garcia-Garcia, J. Martel, and F. Martin, “Composite right/left-handed metamaterial transmission lines based on complementary split-rings resonators and their applications to very wideband and compact filter design,” IEEE Trans. Microw. Theory Tech., vol. 55, no. 6, pp. 1296–1304, Jun. 2007.
[94]L. Li, H. Yao, Q. Wu, and Z. Chen, “Broad-bandwidth and low-loss metamaterials: Theory, design and realization,” J. Zhejiang Univ. Science A, vol. 7, no. 1, pp. 5–23, Jan. 2006.
[95]C.-J. Lee, K. M. K. H. Leong, and T. Itoh, “Composite right/left-handed transmission line based compact resonant antennas for RF module integration,” IEEE Trans. Antennas Propag., vol. 54, no. 8, pp. 2283–2291, Aug. 2006.
[96]A. K. Skrivervik, J. -F. Zürcher, O. Staub, and J. R. Mosig, “PCS antenna design: The challenge of miniaturization,” IEEE Antennas Propag. Mag., vol. 43, no. 4, pp. 12–27, Aug. 2001.
[97]H. Iizuka and P. S. Hall, “Left-handed dipole antennas and their implementations,” IEEE Trans. Antennas Propag., vol. 55, no. 5, pp. 1246–1253, May 2007.
[98] K. F. Lee, K. M. Luk, K. F. Tong, S. M. Shum, T. Huynh, and R. Q. Lee, “Experimental and simulation studies of the coaxially fed U-slot rectangular patch antenna,” Proc. Inst. Elect. Eng. Microw. Antennas Propag., vol. 144, no. 5, pp. 354–358, Oct. 1997.
[99] B.-L. Ooi, S. Qin, and M.-S. Leong, “Novel design of broad-band stacked patch antenna,” IEEE Trans. Antennas Propag., vol. 50, no. 10, pp. 1391–1395, Oct. 2002.
[100] C. L. Lee, B. L. Ooi, and X. D. Zhou, “A broadband air filled stacked U-slot patch antenna,” Elect. Lett., vol. 35, no. 7, pp. 515–517, Apr. 1999.
[101]K. Sarabandi, R. Azadegan, H. Mosallaei, and J. Harvey, “Antenna miniaturization techniques for applications in compact wireless transceivers,” in Proc. URSI, 2002, pp. 2037–2040.
[102] Nasimuddin Nasimuddin,"Microstrip Antennas", ISBN 978-953-307-247-0, InTech, April 04, 2011, DOI: 10.5772/609
[103] J. Zhu and G.V. Eleftheriades, “Dual-band metamaterial-inspired small monopole antenna for WiFi applications”, Electronics Letters, October 2009 Vol. 45, No. 22
[104] Cuong Tran Manh, Habiba Hafdallah Ouslimani, Geraldine Guida, Alain Priou, Herve Teillet and J. Y. Daden, “Metamaterial Structures for Compact Millimeter Wave Antenna Applications”, PIERS Proceedings, Hangzhou, China, March 24-28, 2008
[105] H L Zhang, H Xin, R Bortolin, J Kudva, “ A compact metamaterial-inspired multilayered slot antenna“, Microwave Opt. Techn. Letter (2011), Vol: 53, Issue: 1, Pg: 219-223
[106] V. A. Tamma, T E Wang, E F Kuester, W Park, C L Holloway, J Zhou, “Metamaterial inspired electrically small patch antenna“, Antennas and Propagation, APS-URSI 2011 IEEE International Symposium on (2011)
[107] Erentok, A., and Ziolkowski, R.W.: “Metamaterial-inspired efficient electrically small antennas”, IEEE Trans. Antennas Propag., 2008, 56, (3), pp. 691–707
[108] J. García-García, J. Bonache, F. Falcone, J.D. Baena, F. Martín, I. Gil, T. Lopetegi, M.A.G. Laso, A. Marcotegui, R. Marqués, M. Sorolla, “Stepped-impedance low pass filters with spurious passband suppression”, Electronics Letters 40 (2004) 881–883.

[109] A. Ali, M.A. Khan, Z. Hu, “High selectivity lowpass filter using negative-epsilon metamaterial resonators”, Electronics Letters 43 (2007) 528–530.
[110]S. S. Karthikeyan and R. S. Kshetrimayum, “Harmonic suppression of parallel coupled microstrip line bandpass filter using CSRR”, Progress In Electromagnetics Research Letters, Vol. 7, 193–201, 2009
[111] F. Martín, F. Falcone, J. Bonache, R. Marqués, M. Sorolla, “Split ring resonator based left handed coplanar waveguide”, Applied Physics Letters 83 (2003) 4652–4654.
[112]F. Falcone, F. Martín, J. Bonache, R. Marqués, T. Lopetegi and M. Sorolla, “Left handed coplanar waveguide band pass filters based on bi-layer split ring resonators”, IEEE Microwave and Wireless Components Letters, vol. 14, pp. 10-12, January 2004.
[113] J. Bonache, F. Martín, F. Falcone, J. García, I. Gil, T. Lopetegi, M.A.G. Laso, R. Marqués, F. Medina, M. Sorolla, “Super compact split ring resonators CPW band pass filters”, IEEEMTT- S International Microwave Symposium Digest, Fort Worth (TX), USA, pp. 1483-1486, June 2004.
[114] J. García-García, J. Bonache, I. Gil, F. Martín, M.C. Velazquez- Ahumada and J. Martel, “Miniaturized microstrip and CPW filters using coupled metamaterial resonators”, IEEE Transactions on Microwave Theory and Techniques, vol. 54, pp. 2628-2635, June 2006.
[115] J. Bonache, I. Gil, J. García-García, F. Martín, “Novel Microstrip Band Pass Filters Based on Complementary Split Rings Resonators”, IEEE Transactions on Microwave Theory and Techniques, vol. 54, pp. 265-271, January 2006.
[116] J. Bonache, I. Gil, J. García-García, F. Martín, “Novel microstrip band pass filters based on complementary split rings resonators”, IEEE Transactions on Microwave Theory and Techniques 54 (2006) 265–271.
[117] M. Gil, J. Bonache, F. Martín, “Synthesis and applications of new left handed microstrip lines with complementary split-ring resonators etched on the signal strip”, IET Microwaves Antennas and Propagation 2 (4) (2008) 324–330.
[118] F. Falcone, T. Lopetegi, M.A.G. Laso, J.D. Baena, J. Bonache, R. Marqués, F. Martín, M. Sorolla, “Babinet principle applied to the design of metasurfaces and metamaterials”, Physical Review Letters 93 (2004) 197401–197404.
[119]F Aznar, M Gil, J Bonache,"Modelling metamaterial transmission lines : a review and recent developments" OptoElectronics Review (2008) Volume: 16, Issue: 3, Publisher: Springer, Pages: 226-236
[120] M. Gil, J. Bonache, J. Selga, J. García-García, F. Martín, Broadband resonant type metamaterial transmission lines, IEEE Microwave and Wireless Components Letters 17 (2007) 97–99.
[121]Bin Li, Xi-Wang Dai, Bian Wu, Chang-Hong Liang, “Ultra wideband filter design based on composite right-/left-handed transmission line”, Microwave and Optical Technology Letters Volume 49, Issue 10, pages 2379–2381, October 2007
[122]H. Wang, L. Zhu and W. Menzel, “Ultra-Wideband Bandpass Filter with Hybrid Microstrip/CPW Structure,” IEEE Microwave And Wireless Components Letters, vol. 15, pp. 844-846, December 2005
[123]Li Bin Xi'an Electron. Eng. Res. Inst., Xi'an Li Xu-ping , “Ultra wideband filter design based on right/left-handed transmission line” , Antennas, Propagation and EM Theory, 2008. ISAPE 2008. 8th International Symposium on, 481 - 484 ,2-5 Nov. 2008

[124] J. Bonache, F. Martín, F. Falcone, J. García, I. Gil, T. Lopetegi, M.A.G. Laso, R. Marqués, F. Medina, M. Sorolla, "Super compact split ring resonators CPW band pass filters", Proceedings of the IEEE-MTT International Microwave Symposium Digest, FortWorth, TX, USA, June 2004, pp. 1483–1486.
[125] J. Bonache, F. Martín, F. Falcone, J.D. Baena, T. Lopetegi, J.García-García, M.A.G. Laso, I. Gil, A. Marcotegui, R. Marqués, M. Sorolla, "Application of complementary split rings resonators to the design of compact narrowband pass structures in microstrip technology", Microwave and Optical Technology Letters 46 (2005) 508–512.
[126] P. Mondal, M.K. Mandal, A. Chaktabarty, S. Sanyal, "Compact bandpass filters with wide controllable fractional bandwidth", IEEE Microwave and Wireless Components Letters 16 (2006) 540–542.
[127] F. Martín, M. Gil, J. Bonache, J. García-García,"Composite right/left handed (CRLH) transmission lines based on complementary split rings resonators (CSRRs) and applications", Proceedings of the International Congress on Advanced Electromagnetic Materials in Microwaves and Optics (Metamaterials 2007), Rome, Italy, October 2007, pp. 872–875.
[128] M. Gil, J. Bonache, F. Martín, "Metamaterial filters with attenuation poles in the pass band for ultra wide band applications", Microwave and Optical Technology Letters 49 (2007) 2909–2913.
[129] J. Bonache, I. Gil, J. García-García, F. Martín, "Novel microstrip band pass filters based on complementary split rings resonators", IEEE Transactions on Microwave Theory and Techniques 54 (2006) 265–271.
[130] M. Gil, J. Bonache, F. Martín, "Ultra compact band pass filters implemented through complementary spiral resonators (CSRs)", Proceedings of the IEEE-MTT International Microwave Symposium Digest, Atlanta, USA, June 2008, pp. 1119–1122.
[131] J. Bonache, F. Martín, J. García-García, I. Gil, R. Marqués, M. Sorolla, "Ultra wide band pass filters (UWBPF) based on complementary split rings resonators", Microwave and Optical Technology Letters 46 (2005) 283–286.
[132] H.V. Nguyen, C. Caloz, "Broadband highly selective bandpass filter based on a tapered coupled-resonator (TCR) CRLH structure", Proceedings of the European Microwave Association, vol. 2, March 2006, pp. 44–51.
[133] C. Tseng, T. Itoh, "Dual-band bandpass and bandstop filters using composite right/left-handed metamaterial transmission lines", Proceedings of the IEEE-MTT International Microwave Symposium Digest, San Francisco, CA, USA, June 2006, pp. 931–934.
[134] Palandoken, M.,Henke, H., "Compact LHM-based band-stop filter ", 2010 Mediterranean Microwave Symposium (MMS),229-231, 25-27 Aug. 2010
[135] David Pozar, Microwave Engineering, John Wiley Sons, ISBN 0-471-17096-8

APPENDIX A

Quasi-Static Analysis of Negative Permeability Cells

The effective permeability of periodic long cylinders can also be derived with an equivalent inductance, L and resistance, R of the cylinder in one unit cell. The total induced current, I is calculated from the magnetic induction law in the form of

$$\oint_C \vec{E}.\vec{dl} = -j\omega \int_F \mu_0 \vec{H}.\vec{dF} \tag{A1.1}$$

$$(R + j\omega L)I = -j\omega\mu_0 H_0 \pi r^2 \tag{A1.2}$$

$$I = \frac{-j\omega\mu_0 H_0 \pi r^2}{R + j\omega L} \tag{A1.3}$$

The magnetization vector , $\vec{M}$, can then be calculated from I in terms of $\vec{H_o}$ and χ_m as

$$\vec{M} = \frac{1}{a^2\, l_{cyr.}} I\pi r^2 \vec{e_z} = \frac{1}{a^2\, l_{cyr.}} \left(\frac{-j\omega\mu_0 \left(\pi r^2\right)^2}{R + j\omega L} \right) \vec{H_0}$$

$$\vec{M} = \chi_m \, \vec{H_0} \tag{A2.1}$$

where $l_{cyr.}$ is the cylinder length.
Therefore, the effective permeability has the form of

$$\mu_{eff} = \mu_0 \left(\frac{1}{a^2\, l_{cyr.}} \left(\frac{-j\omega\mu_0 \left(\pi r^2\right)^2}{R + j\omega L} \right) + 1 \right) \tag{A2.2}$$

In (A2.2), R can be expressed as

$$R = \frac{1}{\kappa} \, \frac{\text{Length}}{\text{Cross Section Area}} = \frac{1}{\kappa} \frac{2\pi r}{\Delta r \, l_{cyr.}} \tag{A2.3}$$

L is formulated by calculating the magnetic field from Amper's Law in Figure A1

$$\oint_C \vec{H}.\vec{dl} = I$$

$$\vec{B} = \mu_0 \frac{I}{l_{cyr.}} \vec{e_z}$$

$$L = \frac{\Phi_m}{I} = \frac{\int_F \vec{B}.\vec{dF}}{I} = \mu_0 \frac{\pi r^2}{l_{cyr.}} \tag{A2.4}$$

where Φ_m is the magnetic flux

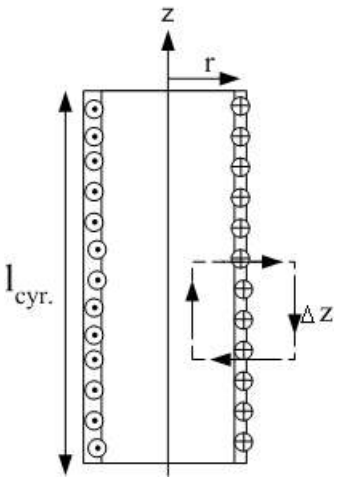

Figure A1 Metallic cylinder cell with the radius, r and length, $l_{cyr.}$

After the substitution of L and R into (A2.2), the effective permeability is formulated as

$$\mu_{eff} = \mu_0 \left(\frac{1}{a^2} \left(\frac{-j\omega\mu_0 \left(\pi r^2\right)^2}{\frac{1}{\kappa}\frac{2\pi r}{\Delta r} + j\omega L\, l_{cyr.}} \right) + 1 \right) \tag{A2.5}$$

$$= \mu_0 \left(1 - \frac{\pi r^2}{a^2} \left(\frac{r\Delta r}{-j\frac{2}{\omega\mu_0\kappa} + r\Delta r} \right) \right) \tag{A2.6}$$

In this formulation, the cell size in z-direction has to be sufficiently long to reduce the edge effects at the cylinder ends. (A2.5) and (A2.6) are the same formulations of (3.7b) and (3.7a) after the substitution of skin depth into (3.7a).
Effective permeability formulations in terms of equivalent circuit elements in (A2.2) makes the resonant permeability of concentric slotted cylinder array to be conveniently obtained. The equivalent circuit is then in the form of series loading of L with an equivalent capacitance of slotted cylinder, C in Figure 3.3. The effect of C can be taken into account by the modification of L in the following form.

$$Z_{total} = R + j\omega L + \frac{1}{j\omega C}$$

$$Z_{total} = R + j\omega L_{eq}$$

$$L_{eq} = L\left(1 - \frac{1}{\omega^2 LC}\right) \tag{A3.1}$$

Thus, the most important point in the resonant permeability formulations is to calculate the capacitance of one cell with longitudinal slots, C in terms of quasi-static analysis. C can be calculated from the capacitance of two concentric cylinders without longitudinal slots, C_o in Figure A2. C_o is formulated by calculating the electrical field and resulting potential difference, $\Delta\phi$ as in the following form,

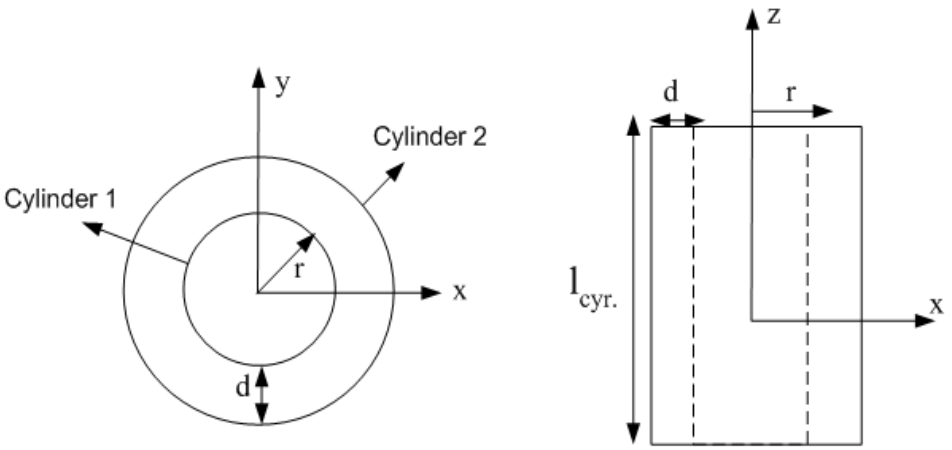

Figure A2 Two concentric metallic cylinders with inner radius r and outer radius r+d and length $l_{cyr.}$

$$\vec{E} = \frac{q_l}{2\pi\varepsilon_0\rho}\vec{e_\rho}$$

$$\phi_2 - \phi_1 = \Delta\phi = -\int_r^{r+d} E_\rho d\rho = \int_r^{r+d} -q_l \frac{1}{2\pi\varepsilon_0\rho} d\rho$$

$$|\Delta\phi| = \left|\frac{q_l}{2\pi\varepsilon_0}\ln\left(\frac{r+d}{r}\right)\right| = \frac{|q_l|\, l_{cyr.}}{C_0}$$

$$C_0 = \frac{2\pi\varepsilon_0\, l_{cyr.}}{\ln\left(\frac{r+d}{r}\right)} \qquad \text{(A3.2)}$$

where q_l is the total charge density per unit length, r and d are the radius of the inner cylinder and the separation distance between two concentric cylinders, respectively.
In the formulation of SRR resonance frequency, L is assumed to be approximately same as L in (A2.4). It is due to the effect of high magnetic coupling between the cells in the axial direction. However, the equivalent capacitance is no more the same as the one calculated in (A3.2) due to axial dependence of field lines. It can be calculated approximately from the capacitance of two infinitely long rectangular lines of width w and separation distance d in Figure A3.

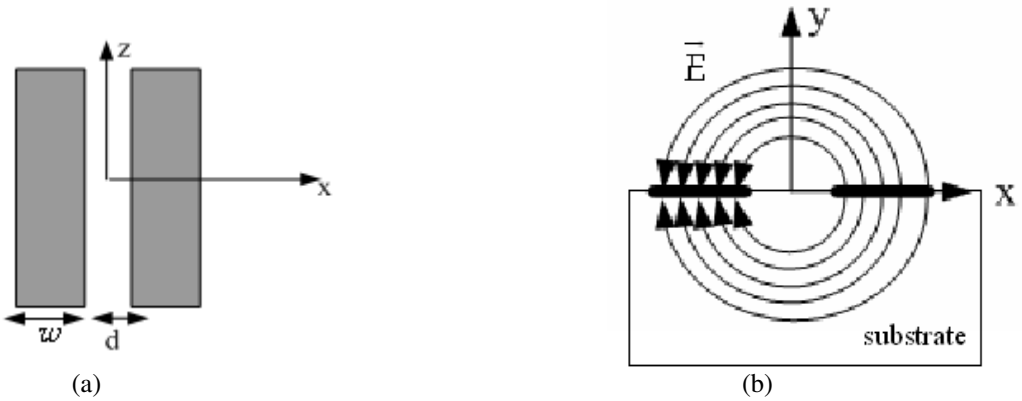

Figure A3 (a) Two parallel rectangular lines with width w and separation distance d (b) approximate electric field lines

The rotation symmetrical electric field can be formulated from the potential difference, ϕ_o in the form of

$$\vec{E} = \frac{\phi_o}{\pi\rho}\vec{e_\phi} \qquad y>0$$

$$\vec{E} = -\frac{\phi_o}{\pi\rho}\vec{e_\phi} \qquad y<0 \qquad \text{(A4.1)}$$

The total charge per unit length, Q'_{total} on the upper and lower sides of one rectangular plate and total capacitance per unit length, C'_{SRR} are calculated as

$$Q'_{total} = \int_{\frac{d}{2}}^{w+\frac{d}{2}} \varepsilon_0 \ \vec{E}.\vec{e_y}dx + \int_{\frac{d}{2}}^{w+\frac{d}{2}} -\varepsilon_s \ \vec{E}.\vec{e_y}dx$$

$$Q'_{total} = (\varepsilon_0 + \varepsilon_s)\int_{\frac{d}{2}}^{w+\frac{d}{2}} \frac{\phi_o}{\pi x}\ dx = (\varepsilon_0 + \varepsilon_s)\frac{\phi_o}{\pi}\ln(\frac{2w+d}{d})$$

$$C'_{SRR} = \frac{(\varepsilon_0 + \varepsilon_s)}{\pi}\ln(\frac{2w+d}{d}) \qquad \text{(A4.2)}$$

where ε_s is the substrate permittivity. Thus, total C_{SRR} is in the form of

$$C_{SRR} = 2\, r_{avg}(\varepsilon_0 + \varepsilon_s)\ln(\frac{2w+d}{d}) \qquad \text{(A4.3)}$$

with an average radius, r_{avg} .

In this formulation, d has to be sufficiently small in comparison to w to reduce the edge effects for rotational symmetrical field distribution.

Appendix B

List of Author's Publications

Journal/ Conference Papers

1. M. Palandöken, M. Aksoy und M. Tümay," A fuzzy-controlled single-phase active power filter operating with fixed switching frequency for reactive power and current harmonics compensation", Electrical Engineering, Volume 86, Number 1, 2003

2. Merih Palandöken, Murat Aksoy and Mehmet Tümay,"Application of fuzzy logic controller to active power filters", Electrical Engineering Vol: 86 No:4, (2004)

3. Merih Palandöken, Mehmet Tümay and Murat Aksoy, " A novel approach to active power filter control", Electrical Engineering Vol: 87 No: 1 , (2005)

4. M. Palandoken, H. Henke, "Fractal Spiral Resonator as Magnetic Metamaterial", IEEE Applied Electromagnetics Conference (AEMC), 2009

5. Merih Palandoken, Andre Grede, and Heino Henke, "Broadband Microstrip Antenna With Left-Handed Metamaterials", IEEE Transactions on Antennas and Propagation, Vol. 57, No. 2, 2009
6. M. Palandoken, H. Henke, "Fractal Negative-Epsilon Metamaterial", IEEE International Workshop on Antenna Technology (iWAT), 2010

7. Merih Palandöken, Heino Henke, "Compact LHM-based Band-Stop Filter", IEEE Mediterranean Microwave Symposium (MMS), 2010

8. Merih Palandöken, Heino Henke, "Miniaturized Self-resonant Metamaterial-based Antenna",International Journal of Microwave and Optical Technology, Vol.6, No., 2011

9. Merih Palandöken, "Compact LHM-inspired Microstrip Antenna", International Journal of Microwave and Optical Technology, Vol.6, No.6, 2011

10. Merih Palandöken, "Dual-Band Epsilon-Negative Material Inspired Fractal Antenna", International Journal on Science and Technology, Volume 2, Issue 1, 2011

11. B. Bouhlal, S. Lutzmann, M. Palandöken, V. Rymanov, A. Stöhr, T. Tekin, "Integration platform for 72 GHz photodiode-based wireless transmitter", SPIE Photonics West 2012, San Francisco, Jan. 21-26, Proc. SPIE 8259, 82590H, 2012

12. M. Palandöken, B. Bouhlal, S. Lutzmann, V. Rymanov, A. Stöhr, T. Tekin, "Integration platform for 1.55 µm waveguide-photodiode based 71-76 GHz wireless transmitter", International Forum on Terahertz Spectroscopy and Imaging, 5th Workshop on Terahertz Technology, Kaiserslautern, March 6-7, Paper Identity No. 47, 2012

13. V. Rymanov, S. Babiel, A. Stöhr, S. Lutzmann, M. Palandöken, B. Bouhlal, T. Tekin, " Integrated E-Band Photoreceiver Module for Wideband (71-76 GHz) Wireless Transmission", European Microwave Week 2012, European Microwave Conference, EUMC 2012, Amsterdam,The Netherlands, 29 October - 1 November, paper no. 1751, 2012, (accepted)

14. V. Rymanov, S. Lutzmann, M. Palandöken, T. Tekin, A. Stöhr, "Wideband 1.55 µm Waveguide Photodiodes Employing Planar Resonant Circuits for E-band (60-90 GHz) Operation" , Progress In Electromagnetics Research Symposium, PIERS 2012, Moscow, Russia, 19-23 August, 2012, (accepted)

15. V. Rymanov, M. Palandöken, S. Lutzmann, B. Bouhlal, T. Tekin, A. Stöhr, "Integrated Photonic 71-76 GHz Transmitter Module Employing High Linearity Double Mushroom-Type 1.55 µm Waveguide Photodiodes", IEEE International Topical Meeting on Microwave Photonics, MWP 2012, Noordwijk, The Netherlands, 11-14 September, paper no. 2594588, 2012, (accepted)

16. Merih Palandöken, Sascha Lutzmann, Vitaly Rymanov, Andreas Stöhr, and Tolga Tekin, "Grounded CPW-WR12 Transition Design for 1.55 µm Photodiode Based E-band Transmitter", PIERS 2012 , (accepted)

17. Merih Palandöken, Vitaly Rymanov, Andreas Stöhr, and Tolga Tekin, "Compact Metamaterial-based Bias Tee Design for 1.55 µm Waveguide-photodiode Based 71-76 GHz Wireless Transmitter", PIERS 2012 , (accepted)

Book Chapters

18. Merih Palandöken, "Artificial Materials based Microstrip Antenna Design", in *Microstrip Antennas*, ISBN 978-953-307-247-0, InTech, 2011

19. Merih Palandöken, "Metamaterial-Based Compact Filter Design", in *Metamaterial*, ISBN 978-953-51-0591-6, InTech, 2012